

*Supermassive binary black hole  
systems in active galaxies*

**Inaugural-Dissertation**

zur

Erlangung des Doktorgrades  
der Mathematisch-Naturwissenschaftlichen Fakultät  
der Universität Köln.

vorgelegt von

**Mar Mezcua Pallerola**

aus Lleida, Spanien

Berichtersteller:

Prof. Dr. Andreas Eckart

Prof. Dr. Anton Zensus

Tag der mündlichen Prüfung: 18. Oktober 2011

*Pots arribar fins on tu vulguis*

*A la mama, al papa, a l'Àlex, i al Pau*





# Contents

<b>Zusammenfassung</b>	<b>1</b>
<b>Resumen</b>	<b>5</b>
<b>Abstract</b>	<b>9</b>
<b>1 Introduction</b>	<b>13</b>
1.1 Galaxy classification . . . . .	13
1.1.1 The AGN engine . . . . .	15
1.1.2 AGN classification . . . . .	18
1.1.3 Basic physics . . . . .	21
1.2 Galaxy evolution . . . . .	28
1.2.1 Binary black hole evolution . . . . .	30
1.2.2 Observational evidence of supermassive binary black hole systems . . . . .	35
1.3 This thesis . . . . .	36
<b>2 Observational methods</b>	<b>39</b>
2.1 Optical spectroscopy . . . . .	39
2.1.1 Overscan trimming . . . . .	41
2.1.2 Bias subtraction . . . . .	41
2.1.3 Cosmic rays . . . . .	41
2.1.4 Flat-field correction . . . . .	41
2.1.5 Wavelength calibration . . . . .	42
2.1.6 Flux calibration . . . . .	44
2.2 Radio interferometry . . . . .	44
2.2.1 Fundamentals . . . . .	45

2.2.2	Calibration . . . . .	47
2.2.3	Synthesis imaging . . . . .	53
2.2.4	Model fitting . . . . .	55
2.2.5	Interferometer arrays . . . . .	56
<b>3</b>	<b>X-shaped radio galaxies</b>	<b>59</b>
3.1	Introduction . . . . .	59
3.2	The sample . . . . .	61
3.2.1	Spectroscopic observations . . . . .	62
3.3	Data analysis . . . . .	63
3.3.1	Stellar absorption lines . . . . .	64
3.3.2	Starburst histories . . . . .	65
3.3.3	Optical continuum . . . . .	66
3.3.4	Black hole masses . . . . .	68
3.3.5	Dynamic age of radio lobes . . . . .	68
3.4	Results . . . . .	69
3.4.1	Spectroscopic observations . . . . .	69
3.4.2	Luminosity matching . . . . .	77
3.4.3	Host type . . . . .	77
3.4.4	Black hole masses . . . . .	78
3.4.5	Starbursts . . . . .	79
3.5	Discussion . . . . .	82
<b>4</b>	<b>Ultraluminous X-ray sources</b>	<b>87</b>
4.1	Introduction . . . . .	87
4.2	Uncovering the compact radio emission of ULXs . . . . .	89
4.2.1	Samples . . . . .	90
4.2.2	Observations and data reduction . . . . .	91
4.2.3	Results . . . . .	92
4.2.4	Discussion . . . . .	97
4.3	Mass limits of ULXs . . . . .	102
4.3.1	Data . . . . .	104
4.3.2	Analysis . . . . .	104
4.3.3	Discussion . . . . .	106
4.4	The shell-like structure of the extragalactic supernova remnant SNR 4449-1 . . . . .	114
4.4.1	Observations and data reduction . . . . .	116
4.4.2	Results . . . . .	117
4.4.3	Discussion . . . . .	120

---

4.5	Summary . . . . .	124
<b>5</b>	<b>Double nucleus galaxies</b>	<b>127</b>
5.1	Introduction . . . . .	127
5.2	The binary black hole evolution-luminosity relation . . . . .	129
5.3	The sample . . . . .	131
5.4	Data analysis . . . . .	131
5.4.1	PSF fitting . . . . .	131
5.4.2	Nuclear and host galaxy luminosities . . . . .	132
5.4.3	Parameters of the model . . . . .	134
5.5	Results . . . . .	134
5.5.1	The AGN-host connection . . . . .	135
5.5.2	Tidal enhancement . . . . .	135
5.5.3	Accretion disk disruption . . . . .	138
5.5.4	Extinction . . . . .	141
5.6	Discussion . . . . .	143
5.6.1	The black hole-bulge correlation . . . . .	144
5.6.2	Tidal enhancement and accretion disk disruption . . . . .	144
5.6.3	Sub-kpc AGN pairs . . . . .	145
5.6.4	Relation to the ULX objects . . . . .	146
<b>6</b>	<b>Conclusions and future work</b>	<b>149</b>
6.1	Summary of results . . . . .	150
6.2	Future work . . . . .	155
	<b>Appendices</b>	<b>159</b>
<b>A</b>	<b>Kinematic black hole mass estimates</b>	<b>161</b>
A.1	Introduction . . . . .	161
A.2	Analysis . . . . .	162
A.2.1	Black hole masses . . . . .	162
A.2.2	Emission lines . . . . .	162
A.3	Results . . . . .	163
<b>B</b>	<b>Atlas of stellar population analysis and starburst histories</b>	<b>167</b>
<b>C</b>	<b>PSF fitting of double nucleus post-merger galaxies</b>	<b>203</b>
	<b>Bibliography</b>	<b>217</b>

<b>Acknowledgements</b>	<b>237</b>
<b>Curriculum Vitae</b>	<b>245</b>

# Zusammenfassung

Nach dem hierarchischen Galaxienentstehungsmodell wachsen Galaxien durch Fusionen, die Sternentstehung erhöhen und aktiven galaktischen Kernen (AGN) Aktivität verleihen. Wenn fast alle Galaxien ein supermassives Schwarzes Loch (SMBH) in ihrer Mitte aufweisen, ist davon auszugehen, dass Paare von SMBHs im Zuge einer Verschmelzung ('Merger') gebildet werden. Der Nachweis und die Anzahl von binären Schwarzen Loch (BBH)-Systemen können uns somit helfen, zu verstehen, wie Galaxien entstehen und wachsen und die Evolutionsmodelle, die das Universum regieren, zu erhellen. Zu diesem Zweck verfolgen wir in dieser Arbeit drei verschiedene Ansätze für den beobachtbaren Nachweis von BBH-Systemen: in X-förmigen Radiogalaxien, in ultrahellen Röntgenquellen und in Doppel-Kern Post-Merger-Galaxien.

X-förmige Radiogalaxien sind eine besondere Klasse von Radioquellen. Sie besitzen zwei Paare von Radiokeulen, die symmetrisch durch das Zentrum der Galaxie gehen und der Galaxie ein X-förmiges Aussehen in den Radiobeobachtungen verleihen. Diese Morphologie wurde vorgeschlagen, um entweder einer vor kurzem erfolgten Fusion von zwei SMBHs oder das Vorhandensein eines zweiten aktiven BH in den galaktischen Kern wiederzugeben. Dieses Szenario ist in dieser Arbeit durch eine facettenreiche Studie, die Messungen der Leuchtkraft im Radio und im Optischen mit Schätzungen der BH Masse, des Alters der Radiokeulen und der Sternentstehungsgeschichte in den X-förmigen Radioquellen und deren Muttergalaxie kombiniert, getestet worden. Die Studie umfasst eine Stichprobe von 38 X-förmigen Radiogalaxien und einer Kontrollprobe von 36 radiolauten aktiven Kernen mit ähnlicher Rotverschiebung und Helligkeiten im Radio und Optischen Bereich. Die optischen Spektren der Galaxien werden modelliert unter Verwendung einer linearen Kombination von synthetischen stellaren Populationen, welche die stellare Geschwindigkeitsdispersion (aus dem die BH Masse abgeleitet werden

kann), den Licht und Massenanteil sowie die Metallizität der stellaren Populationen liefert. Von diesen wird die Sternentstehungsgeschichte der Galaxien abgeleitet. Das dynamische Alter der aktiven Radiokeulen wird über ihre Winkelgröße in den Radio Karten abgeschätzt. Eine statistische Untersuchung aller dieser Eigenschaften zeigt, dass alle X-förmige Quellen in der Probe in elliptischen Galaxien zu finden sind, ihre BH-Massen im Durchschnitt höher sind als die in einer Kontrollprobe von radiolauten AGN und sie weisen eine verbesserte Sternbildungsrate innerhalb von Zeitskalen, die in galaktischen Fusionen zu erwarten sind, auf. Diese Ergebnisse liefern weitere Untermauerung für das Merger Szenario als den Ursprung der besonderen X-förmigen Radio Morphologie.

Ultrahelle Röntgenquellen (ULX) sind ebenfalls vorgeschlagen worden, im Zusammenhang mit BBH-Systemen in Post-Merger-Galaxien zu stehen. Die hohe Röntgenleuchtkraft der ULXs kann nicht durch Sternentwicklungsmodelle erklärt werden, sofern sie nicht Röntgendoppelsterne mit super-Eddington Akkretion, starken strahlenden Effekten oder in einem ultrahellen Zustand waren. Alternativ wurden ULXs vorgeschlagen, mittelschwere Schwarzer Löcher (IMBH), die mit sub-Eddington Rate wachsen, jungen Supernovae oder sekundären BHs, die entstehen im Zuge einer Verschmelzung mit dem ULX Galaxie, zu sein. Um zu erklären, welches das wahrscheinlichste Szenario ist, wurde die BH Masse der ULXs mit beobachteten Radio Pendants von der Lage des ULXs in der Schwarzen-Loch-Fundamentalebene abgeschätzt. Wir fanden, dass die 19 studierten ULXs BH-Massen im Bereich von  $10^3$ - $10^8 M_{\odot}$  besitzen und dass 58% von ihnen eine geschätzte BH Masse aufweisen, die für IMBHs erwartet wird. Wir führen auch hochauflösende VLBI Beobachtungen im Radiobereich von drei ULXs mit Radio Pendants durch. Dies führt zu einer besseren Einschränkung der BH Masse von zwei von ihnen und zu der aufgelösten Struktur eines der jüngsten bekannten Supernovaüberreste.

Die dritte Klasse von Objekten für mögliche BBH Host-Systeme sind die Galaxien mit Doppelkernen. Nach den Modellen, die die Entwicklung der BBH Systeme beschreiben, wird angenommen, dass die Leuchtkraft der beiden Kerne durch eine Erhöhung der Akkretionsrate aufgrund von Gezeiteneffekten und auch durch Akkretionsscheibenstörung beeinflusst wird. Dies testen wir in dieser Arbeit mit dem Studium der optischen Leuchtkraft von 54 Post-Merger-Galaxien mit Doppelkernen. Die Leuchtkraft der einzelnen Kerne und ihr relative Abstand wird aus der Modellierung der Zentren der Post-Merger-Galaxien aus den  $g$ ,  $r$ , und  $u$ -Band-Bilder mit zwei Gauss-förmigen Komponenten bestimmt (PSF Fitting), während die Leuchtkraft der Galaxie

von der optischen Photometrie des SDSS ermittelt wird. Als Ergebnis des PSF Fitting finden wir, dass in 19 Post-Merger-Galaxien die beiden Kerne mit  $\leq 1$  kpc getrennt sind. Diese Quellen sind damit potenzielle sub-kpc Skala AGN-Paare. Zweitens finden wir, dass die nukleare Leuchtkraft mit der Leuchtkraft der Galaxie durch eine Gezeitenerhöhung der Akkretionsrate korreliert ist, jedoch beeinflusst ein weiterer Mechanismus die beobachteten Leuchtkraftverläufe. Wir vermuten das Zerbrechen der Akkretionsscheibe und schätzen, dass es bei einem Bindungsradius zwischen 1 und 3 kpc stattfindet. Eine Modellierung mittels eines BBH-Modells, welches eine Erhöhung der Gezeitenwechselwirkung sowie Akkretionsscheibenstörungen berücksichtigt, unterstützt diese Ergebnisse und zeigt, dass die Akkretionsscheibe des primären und des sekundären Kernes in allen Quellen gestört ist. Das Modell ergibt auch, dass die beiden Kerne gravitativ gebunden sind, wenn sie sich bei einem projizierten Abstand von 2,3 kpc befinden, was für 60% der studierten Galaxien gilt. Wir finden auch, dass der spektrale Index der Akkretionsscheibe, bestimmt aus der Modellierung, in Übereinstimmung mit denen der AGN, die ihren Maximum in der spektralen Energieverteilung im optischen-UV-Band ("big blue bump") besitzen, übereinstimmt.

Um das BBH-Szenario in den ULXs mit Radio Pendants zu testen, wenden wir die Ergebnisse der BBH Modellierung für Doppel-Kern Post-Merger-Galaxien auf die Beziehung zwischen Röntgenleuchtkraft der ULXs und dem Kernabstand zu ihrer Muttergalaxie an. Der beobachtete Trend zwischen der ULX Leuchtkraft und ihrem Kernabstand ist in Übereinstimmung mit dem BBH-Modell. Dies unterstützt das BBH-Szenario für die studierten ULX Quellen.

Insgesamt zeigen die Ergebnisse unserer Studie, dass die Aktivität der sekundären Schwarzen Löcher rasch in Post-Merger-Galaxien abklingt, was die sehr niedrige Erkennungsrate für die sekundären BH erklärt. Basierend auf den Ergebnissen unserer Studie sind effektivere Ansätze zur Erfassung der sekundären BH entwickelt worden und diese Ansätze werden nun in einer Reihe von optischen und Radioastronomischen Einrichtungen, einschließlich des VLT, des EVLA und des VLBA angewendet.





# Resumen

Según el modelo jerárquico de formación galáctica, las galaxias crecen a través de fusiones que aumentan la formación estelar y desencadenan actividad en el núcleo galáctico activo (AGN). Si casi todas las galaxias contienen un agujero negro supermasivo (SMBH) en su centro, se espera que pares de SMBHs se formen en el transcurso de una fusión. La detección y estimación del número de agujeros negros binarios (BBH) pueden, por lo tanto, ayudarnos a entender cómo se forman y crecen las galaxias así como arrojar luz sobre los modelos evolutivos que rigen el Universo. Con este objetivo, en esta tesis seguimos tres líneas distintas de estudio para obtener pruebas observacionales de sistemas de BBH: en las radio galaxias en forma de X, en fuentes ultraluminosas de rayos X, y en galaxias en post-fusión con núcleo doble.

Las galaxias en forma de X son una clase de radio fuentes peculiares que presentan dos pares de lóbulos en radio que pasan simétricamente por el centro de la galaxia, lo cual da a la galaxia la morfología en radio en forma de X. Se ha sugerido que esta morfología podría reflejar una fusión reciente de dos SMBHs o la presencia de un segundo agujero negro (BH) activo en el núcleo galáctico. En esta tesis, esta hipótesis se ha probado mediante un estudio multifacético que combina mediciones de la luminosidad óptica y de radio, estimaciones de las masas del agujero negro y las edades de los lóbulos en radio, y evaluaciones de las historias de formación estelar en las radio fuentes en forma de X y sus galaxias anfitrionas. El estudio abarca una muestra de 38 radio galaxias en forma de X y una muestra de control de 36 núcleos activos radio-fuertes con similares desplazamientos hacia el rojo y similares luminosidades ópticas y de radio. Los espectros ópticos de las galaxias son modelados mediante una combinación lineal de poblaciones estelares sintéticas que proporciona la dispersión de velocidades estelares (a partir de la cual se puede obtener la masa

del BH) así como la fracción de la luz, fracción de la masa y la metalicidad de las poblaciones estelares. A partir de éstas se puede obtener la historia de formación estelar de las galaxias. La edad dinámica de los lóbulos activos se estima por su tamaño angular en los mapas de radio. Un estudio estadístico de todas estas propiedades revela que todas las fuentes en forma de X de la muestra se encuentran en galaxias elípticas, sus masas de BH son en promedio superiores a los de la muestra de control de AGN radio-fuertes, y presentan una mayor actividad de formación estelar a las escalas de tiempo esperadas en fusiones galácticas. Estos resultados apoyan la hipótesis de la fusión como origen de la peculiar morfología de las radio galaxias en forma de X.

También se ha sugerido que las fuentes ultraluminosas de rayos X (ULX) pueden estar relacionadas con los sistemas de BBH en galaxias post-fusión. La alta luminosidad en rayos X de las ULXs no puede explicarse mediante los modelos de evolución estelar, a menos que sean binarias de rayos X con acrecimiento súper-Eddington, con fuertes efectos de colimación, o en un estado ultraluminoso. Por otra parte, se ha sugerido que las ULXs son agujeros negros de masa intermedia (IMBH) con una tasa de acrecimiento sub-Eddington, supernovas jóvenes, o BHs secundarios en el curso de una fusión con la galaxia anfitriona de la ULX. Con el fin de aclarar cuál es la situación más probable, la masa de BH de las ULXs con contrapartidas en radio detectadas se estima a partir de la ubicación de las ULXs en el plano fundamental de los agujeros negros. Encontramos que las 19 ULXs estudiadas tienen masas de BH estimadas en el rango de  $10^3$ – $10^8 M_{\odot}$ , y que el 58% de ellas tienen masas de BH en el rango de  $10^2$ – $10^5 M_{\odot}$  esperado en IMBHs. También llevamos a cabo observaciones en radio de alta resolución con VLBI de tres ULXs con contrapartidas en radio conocidas. Esto resulta en una mayor estimación de la masa de BH de dos de ellos y la obtención de la estructura resuelta de uno de los restos de supernova más joven conocido.

La tercera clase de objetos propensos a alojar sistemas de BBH son las galaxias con doble núcleo. De acuerdo con los modelos que describen la evolución de los sistemas de BBH, se espera que la luminosidad de los dos núcleos se vea afectada por un aumento de la tasa de acrecimiento debido a efectos de marea y por la rotura del disco de acrecimiento. Esta tesis demuestra esta hipótesis mediante el estudio de la luminosidad óptica de una muestra de 54 galaxias post-fusión con núcleo doble. La luminosidad de cada uno de los núcleos y su separación relativa se obtiene a partir del ajuste de dos componentes gaussianas (PSF fitting) a las imágenes en banda  $g$ ,  $r$ , y  $u$  del centro de estas galaxias post-fusión, mientras que la luminosidad de la galaxia

anfitriona se obtiene a partir de la fotometría óptica del SDSS. Como resultado del PSF fitting, encontramos que en 19 de las galaxias post-fusión los dos núcleos están separados físicamente por menos de 1 kpc. Estas fuentes son, por lo tanto, candidatas a contener pares de AGN a escalas inferiores al kpc. En segundo lugar, encontramos que la luminosidad nuclear se correlaciona con la luminosidad de la galaxia debido a un aumento de la tasa de acrecimiento por causas de marea, pero que otro mecanismo está afectando también a la tendencia observada en la luminosidad. Sugerimos que la rotura del disco de acrecimiento desempeña también un papel, y estimamos que éste debería ocurrir en un radio de ligadura de entre 1 y 3 kpc. El ajuste de un modelo de BBH, que tiene en cuenta tanto el incremento en luminosidad debido a las mareas así como la rotura del disco de acrecimiento, apoya estos resultados e indica que el disco de acrecimiento, tanto del núcleo primario como del secundario, está siendo rasgado en todas las fuentes. El modelo indica también que los dos núcleos se encuentran gravitacionalmente unidos cuando están a una distancia proyectada de 2.3 kpc, que es el caso del 60% de las galaxias estudiadas. Así mismo, encontramos un valor del índice espectral de la ley de potencias del disco de acrecimiento que está de acuerdo con el de AGNs con un pico en la banda óptica/UV (“big blue bump”) en su distribución espectral de energía.

Con el fin de probar el escenario BBH en las ULXs con contrapartidas detectadas en radio, los resultados del ajuste de BBH obtenidos para las galaxias con núcleo doble se aplican también a la dependencia de la luminosidad en rayos X de las ULXs con la separación nuclear a su galaxia anfitriona. La tendencia observada entre la luminosidad de las ULX y la distancia nuclear está de acuerdo con el modelo de BBH, apoyando la hipótesis de BBH para las fuentes ULX estudiadas.

En general, los resultados de nuestro estudio indican que la actividad del agujero negro secundario se apaga rápidamente en las galaxias post-fusión, lo que explica la baja tasa de detección de secundarios. Nuestro estudio muestra una manera más efectiva de abordar el estudio observacional de estos objetos, que se continuará con observaciones en el visible y en radiofrecuencia utilizando, entre otros, el VLT, el EVLA, y el VLBA.



# Abstract

According to the hierarchical galaxy formation model, galaxies grow through mergers that enhance star formation and trigger active galactic nucleus (AGN) activity. If nearly all galaxies host a supermassive black hole (SMBH) in their center, it is expected that pairs of SMBHs will be formed in the course of a merger event. The detection and number estimates of binary black hole (BBH) systems can, thus, help us to understand how galaxies form and grow, and shed light on the evolutionary models that rule the Universe. With this purpose, we pursue, in this thesis, three different lines of observational evidence for BBH systems: in X-shaped radio galaxies, in ultraluminous X-ray sources, and in double nucleus post-merger galaxies.

X-shaped radio galaxies are a class of peculiar radio sources which exhibit two pairs of radio lobes that pass symmetrically through the center of the host galaxy, giving the galaxy the X-shaped morphology seen on radio maps. This morphology has been suggested to reflect either a recent merger of two SMBHs or the presence of a second active BH in the galactic nucleus. This scenario is tested in this thesis by a multifaceted study that combines measurements of radio and optical luminosity, estimates of the black hole masses and ages of the radio lobes, and assessments of the starburst histories in the X-shaped radio sources and their host galaxies. The study covers a sample of 38 X-shaped radio galaxies and a control sample of 36 radio-loud active nuclei with similar redshift and optical and radio luminosities. The optical spectra of the host galaxies are modeled using a linear combination of synthetic stellar populations that provides the stellar velocity dispersion (from which the BH mass can be derived) and the light fraction, mass fraction, and metallicity of the stellar populations. From these, the starburst history of the galaxies is derived. The dynamic age of the active lobes is also estimated, from their angular size on the radio maps. A statistical study of all these properties reveals that all the X-

shaped sources in the sample are found in elliptical galaxies, their BH masses are on average higher than those in a control sample of radio-loud AGN, and they exhibit enhanced star formation activity on timescales expected in galactic mergers. These results yield further support to the merger scenario as the origin of the peculiar X-shaped radio morphology.

Ultraluminous X-ray sources (ULX) have also been suggested to be related to BBH systems in post-merger galaxies. The high X-ray luminosity of ULXs cannot be explained by stellar evolution models, unless they were X-ray binaries with super-Eddington accretion, strong beaming effects, or in an ultraluminous state. Alternatively, ULXs have been suggested to be intermediate-mass black holes (IMBH) accreting at sub-Eddington rates, young supernovae, or secondary BHs in the course a merger event with the ULX host galaxy. In order to clarify which is the most likely scenario, the BH mass of those ULXs with radio counterparts detected has been estimated from the location of the ULXs in the black hole fundamental plane. We find that the 19 ULXs studied have estimated BH masses in the range  $10^3$ – $10^8 M_{\odot}$ , and that 58% of them have estimated BH masses in the range  $10^2$ – $10^5 M_{\odot}$  expected for IMBHs. We also perform high-resolution VLBI radio observations of three ULXs with radio counterparts. This yields a better constraint of the BH mass of two of them and the resolved structure of one of the youngest known supernova remnants.

The third class of objects likely to host BBH systems are the galaxies with double nucleus (double nucleus galaxies). According to the models that describe the evolution of BBH systems, the luminosity of the two nuclei is expected to be affected by an enhancement of the accretion rate due to tidal effects and by accretion disk disruption. This is tested, in this thesis, with the study of the optical luminosities of a sample of 54 post-merger galaxies with double nucleus. The luminosity of each of the nuclei and their relative separation is derived from the fit of two gaussian components (PSF fitting) to the  $g$ ,  $r$ , and  $u$ -band images of the center of these post-merger galaxies, while the luminosity of the host galaxy is obtained from SDSS optical photometry. As a result of the PSF fitting, we find that in 19 post-merger galaxies the two nuclei are physically separated by  $\leq 1$  kpc. These sources are, thus, potential sub-kpc scale AGN pairs. Secondly, we find that the nuclear luminosity is correlated with the luminosity of the host galaxy due to a tidal enhancement of the accretion rate, but that another mechanism is also affecting the luminosity trends observed. We suggest that accretion disk stripping is also at play, and estimate that it should take place at a binding radius between 1 and 3 kpc. A

fit by a BBH model, which takes into account tidal enhancement as well as accretion disk disruption, supports these results, obtaining that the accretion disk of both the primary and the secondary nucleus are being disrupted in all the sources. The model also finds that the two nuclei become gravitationally bound when they are at a projected separation of 2.3 kpc, which is the case for 60% of the galaxies studied. We also find that the value of the power-law spectral index of the accretion disk derived from the fit is in agreement with the ones of AGN with a peak in the optical-UV band (big blue bump) of their spectral energy distribution.

In order to test the BBH scenario in the ULXs with radio counterparts detected, the results of the BBH fit obtained for double nucleus post-merger galaxies are also applied to the X-ray luminosity dependence of the ULXs on the nuclear separation to their host galaxy. The observed trend between ULX luminosity and nuclear distance is in agreement with the BBH model, supporting the BBH scenario for the ULX sources studied.

Overall, the results of our study indicate that the activity of the secondary black holes is rapidly quenched in post-merger galaxies, which explains the very low detection rate for the secondaries. Based on the results of our study, more effective approaches for detecting the secondaries have been derived, and these approaches will be now pursued at a number of optical and radio astronomical facilities, including the VLT, the EVLA, and the VLBA.





# 1

---

## Introduction

*Unus pro omnibus,  
omnes pro uno.*  
(One for all, all for one)  
Alexandre Dumas (1844)

*Understanding how galaxies form and grow is one of the major challenges that Astronomy faces today. It is widely accepted that galaxies are not isolated objects expanding in a flat Universe, but that they interact, changing their morphological appearance and properties, and merge, resulting often into a different type of galaxy. This evolutionary scheme has been found to be strongly related to the presence of a supermassive black hole (SMBH) in the nucleus of, possibly, every galaxy. In active galaxies, the SMBH and its surroundings form an active galactic nucleus (AGN), one of the brightest and most powerful objects in the Universe. Given that galaxies merge and that a SMBH resides at the center of (nearly) all galaxies, it is expected that pairs of SMBHs form for a certain period of time before they finally coalesce. The evolution of this binary black hole (BBH) system is not yet clear, mainly owing to the low number of BBH systems detected. This chapter provides an introduction to how galaxies are classified, giving special emphasis to AGN and their physics, and to how they and their SMBH evolve. The chapter concludes with a presentation of the three observational evidence for BBH systems studied in this thesis.*

### 1.1 Galaxy classification

The existence of galaxies other than the Milky Way was established in the 1920s using the period-luminosity relation of variable stars (Leavitt & Pickering 1912). Galaxies were classified according to their morphology into elliptical, spiral, lenticular, and irregular (Hubble 1936) in the so-called Hubble diagram (Fig. 1.1). Elliptical galaxies are smooth, ellipsoidal and almost featureless. The Hubble diagram categorizes them according to their

ellipticity, from E0 being nearly spherical to E7 being highly elongated. They have little cool gas and consequently a reduced rate of star formation and few young blue stars. They are instead populated by older, more evolved, stars that orbit the galaxy center in random directions. Spiral galaxies are formed by bright spiral arms containing hot young stars and dusty gas from which these stars form, together with a central bulge of older stars. Along the sequence from Sa spirals to Sc and Sd in the Hubble classification scheme, the spiral arms become more open and the fraction of gas and young stars increase. Lenticular galaxies (categorized as type S0) have intermediate properties of both elliptical and spiral galaxies. They possess a central elliptical bulge and a rotating disk, but the disk is devoid of spiral arms. Galaxies that do not fit in any of these categories are classified as irregulars. They are small blue galaxies lacking any structure as spiral arms. The nomenclature ‘early-type’ and ‘late-type’ is often used to refer to the position of galaxies along the Hubble sequence, from ellipticals to spirals.

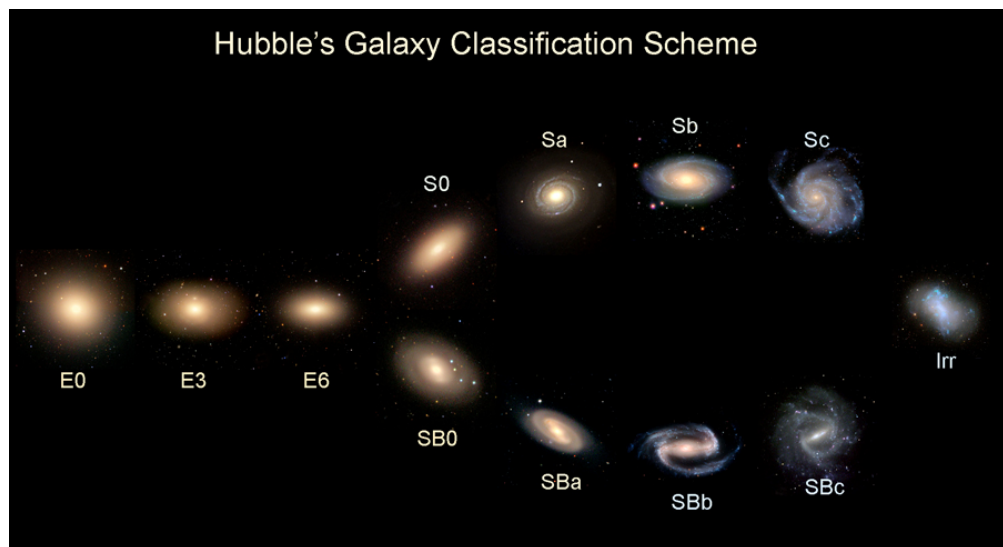


FIGURE 1.1— Hubble diagram of galaxy classification. Constructed from Sloan Digital Sky Survey pictures (John Kormendy's Web Page)

Early in the twentieth century, galaxy spectroscopy revealed some galaxies to show nuclear emission lines of ions that could not be excited by photons coming from young stars (Fath 1909; Slipher 1917). Seyfert (1943) published a first catalog of galaxies in which the nuclear spectrum showed strong

broad emission lines. The major breakthrough came in the 1950s with the development of the radio astronomy. Many of the strongest radio sources were associated with luminous elliptical galaxies (Reber 1944; Bolton & Stanley 1948; Bolton et al. 1949; Ryle et al. 1950). Some galaxies were found to have radio-bright compact nuclei and huge radio lobes extending outwards from the central cores (Hanbury Brown et al. 1952; Morris et al. 1957). The origin of this radio emission could not be thermal, but was argued to be produced by energetic particles moving along magnetic fields (Alfvén & Herlofson 1950). The study of active galactic nuclei (AGN) had begun.

### 1.1.1 The AGN engine

Active galaxies are powered by a bright nucleus able to produce monochromatic luminosities ranging all the way from  $\sim 10^{42}$  to  $\sim 10^{48}$  erg s<sup>-1</sup>, as much as  $10^4$  times the luminosity of a normal galaxy. This radiation covers the whole electromagnetic spectrum, spreading over a broad range of frequencies, from the gamma-rays and X-rays to the radio regime (a typical galaxy emits almost all its energy within one decade of frequency). These makes AGN some of the most powerful objects ever observed in the Universe. For many years, scientists have sought after a mechanism able to explain the AGN emission. The nuclear fusion taking place in the stellar interiors is not efficient enough to produce the high luminosities observed. The most effective way of releasing such enormous amounts of energy is via accretion of matter onto a supermassive black hole (SMBH; Salpeter 1964; Zel'Dovich 1964). According to the current accepted model or Standard Model (Antonucci 1993; Urry & Padovani 1995), the main components of an AGN are (see Fig 1.2):

- **Central engine.** The central engine is formed by a SMBH ( $10^6$ - $10^{10}$   $M_{\odot}$ ) accreting the surrounding material. During the accretion process the infalling matter loses angular momentum, forming an accretion disk of several astronomical units. Viscosity causes the disk gas to spiral inward and heat up, emitting continuum radiation that peaks in the optical-ultraviolet waveband (the so-called 'big blue bump'). The flow of hot ionized gas pulls magnetic field lines inward. A corona of hot material forms above the accretion disk and scatters photons via inverse-Compton scattering up to X-ray energies.
- **Broad line region.** The Broad Line Region (BLR) consists of a collection of thousands of dense gas clouds (with a density of  $N_H \sim 10^{10}$

$\text{cm}^{-3}$ ) orbiting the central engine at a distance of about 0.1–1 pc from the nucleus. The gas clouds have an effective temperature of  $\sim 10^4$  K and are ionized by the continuum emission coming from the accretion disk, producing broad emission lines at optical wavelengths. The typical width of these lines is  $\sim 3000 \text{ km s}^{-1}$ , which reflects the large Keplerian velocity of the gas clouds.

- **Torus.** An obscuring torus of cold gas and dust surrounds the central engine at a distance of up to 10 pc. This torus constitutes the source of material used by the accretion disk to feed the SMBH. Its dust grains absorb the optical radiation coming from the nucleus and re-radiate it at infrared (IR) wavelengths, where it can be observed in nearby AGN using high-spatial-resolution IR interferometers (Jaffe et al. 2004; Tristram et al. 2007). The torus has a non-uniform, clumpy structure with a temperature  $\leq 1500$  K (e.g., Krolik & Begelman 1988; Beckert 2005; Höning et al. 2006), which is the sublimation temperature of dust grains and defines the innermost radius of the torus (e.g., Barvainis 1987; Laor & Draine 1993).
- **Narrow line region.** The Narrow Line Region (NLR) is formed by low-density gas clouds ( $N_{\text{H}} \sim 400\text{-}1000 \text{ cm}^{-3}$ ) located at a distance of about 100 pc, extending out to 4 kpc, from the SMBH. The NLR is ionized by the accretion disk and massive stars nearby, producing intense narrow forbidden lines such as  $[\text{OII}]\lambda 3727\text{\AA}$ ,  $[\text{OIII}]\lambda\lambda 4959, 5007\text{\AA}$ ,  $[\text{NII}]\lambda 6583\text{\AA}$ ,  $[\text{SII}]\lambda\lambda 6716, 6731\text{\AA}$ . The clouds have a typical velocity of  $\sim 500 \text{ km s}^{-1}$  and a temperature of  $T \sim 10^4$  K.
- **Jets.** In some AGN, a pair of highly collimated relativistic plasma outflows emerge in opposite directions from the proximity of the SMBH. These jets are believed to form within 10-100 Schwarzschild radii from the black hole, where the twisting of magnetic fields in the accretion disk and the rotating black hole collimates a mixture of electrons, positrons, and protons, extracting angular momentum from the accreting matter (see Beckwith et al. 2009 and references therein). Jets can extend beyond the host galaxy, several kpc (or even Mpc) out from the core. The best way to observe them is at radio wavelengths, but they radiate in all wavebands from the radio to the gamma-rays via synchrotron and inverse-Compton emission processes (see Sect. 1.1.3).

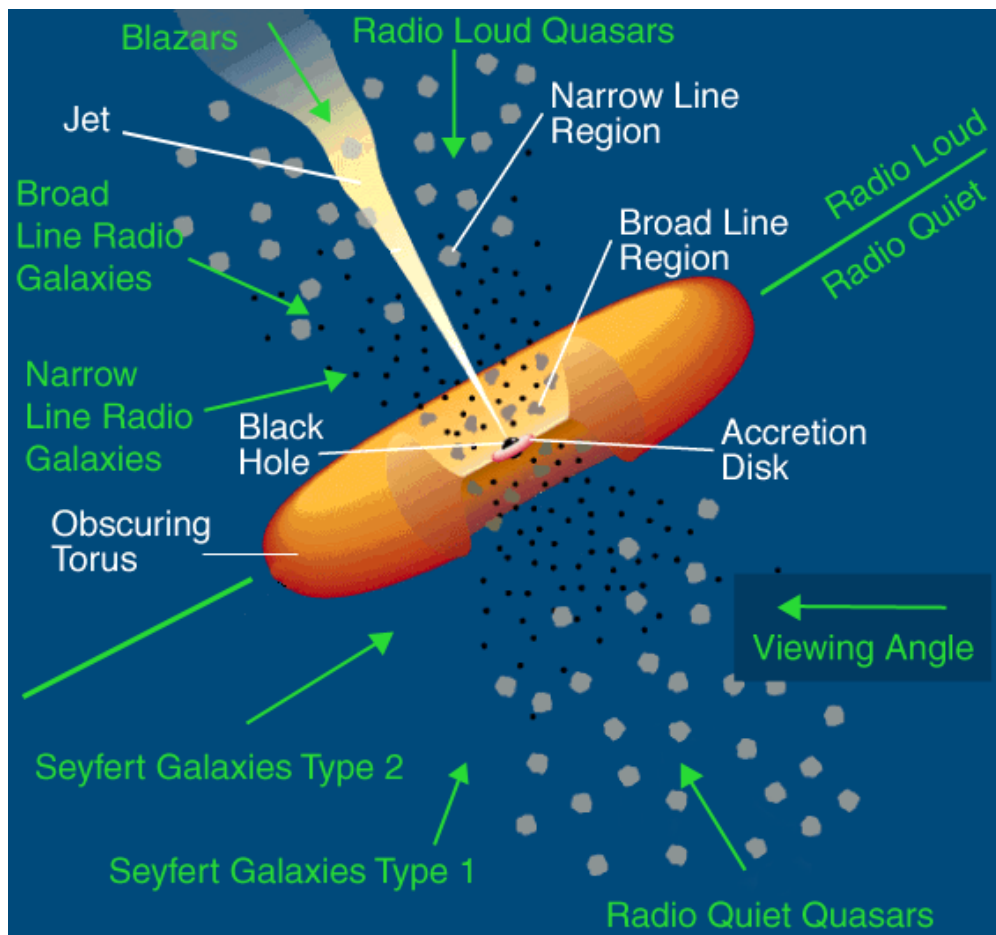


FIGURE 1.2— Standard model of active galactic nuclei. The supermassive black hole in the center is surrounded by an accretion disk and clouds of cold gas that constitute the Broad Line Region. Further out, colder gaseous clouds orbit the central engine emitting narrow emission lines, hence called Narrow Line Region. The SMBH, the accretion disk, and the BLR reside within a donut-shaped dusty torus that is responsible of the AGN dichotomy due to obscuration affecting different viewing angles. In the case of radio-loud quasars, radio galaxies, and blazars, a radio jet that can extend far out of the NLR is observed. Figure reproduced from Urry & Padovani (1995).

### 1.1.2 AGN classification

After the detection of the first extragalactic radio sources in the early 1950s, the earliest way to classify AGNs was based on their radio emission. The radio-loudness,  $R$ , was defined as a measure of the relative contribution of the radio emission to the overall radiative emission, but in practice it is calculated as the ratio of radio flux density (5 GHz) and optical flux density (4400 Å),  $R = S_{5\text{GHz}}/S_{4400\text{Å}}$  (Kellermann et al. 1989). A source is classified as radio-loud if  $R \geq 10$ , and radio-quiet otherwise. A compilation of all AGN types is shown in Table 1.1.

**Radio-quiet AGN.** In this group we find Seyfert galaxies (which can be as well radio-faint), radio-quiet quasars, and LINERs.

- Seyfert galaxies constitute  $\sim 1\%$  of all AGN. They have relatively low luminosities ( $L_{\text{opt}} \sim 10^{41} - 10^{44} \text{ erg s}^{-1}$ ) and their spectrum is characterized by strong emission lines. A sub-classification is done depending on the presence (Seyfert 1) or absence (Seyfert 2) of broad emission lines. They can show strong nuclear X-ray emission and sometimes a weak small-scale radio jet. Their host galaxies are usually spiral and irregular galaxies.
- Radio-quiet quasars are a brighter version of Seyfert galaxies, on average two orders of magnitude more powerful. The distinction between them is made in terms of a limiting optical magnitude. Their high luminosity outshines their host galaxy starlight, giving them a point-like ‘quasi-stellar’ appearance (hence their name, quasi-stellar objects or QSO). They show strong optical continuum emission, X-ray continuum emission, and broad and narrow optical emission lines. They populate the most massive galaxies (usually ellipticals, Dunlop 2001) at very high redshifts.
- Low-ionization nuclear emission-line regions (LINERs) constitute the lowest-luminosity class of AGN ( $L \leq 10^{42} \text{ erg s}^{-1}$ ) and can be found in  $\sim 60\%$  of all nearby galaxies (Osterbrock 1989). They show only weak nuclear emission-line regions but no other signatures of AGN emission, which locates them in the limit of applicability of the standard AGN scenario. This led to a major debate concerning the source of energy that excites the ionized gas at the center of these galaxies, with some astronomers asserting that the emission is powered by star formation regions rather than an AGN (e.g., Terlevich & Melnick 1985; Shields 1992; Cid Fernandes et al. 2004a).

**Radio-loud AGN.** Here we can find radio-loud quasars, blazars, and radio galaxies.

- Radio-loud quasars (RLQ) are differentiated from their radio-quiet counterparts by the addition of emission from a jet. They show thus strong optical continuum emission, broad and narrow emission lines, and strong X-ray emission, together with nuclear and often extended radio emission. For small inclination viewing angles, RLQ jets show superluminal motion due to relativistic and projection effects (e.g., Porcas 1983; Zensus et al. 1987; Zensus & Pearson 1990; Ros et al. 1998). Depending on the shape of their radio spectrum, they are further classified into steep-spectrum RLQ and flat-spectrum RLQ.
- Blazars are characterized by rapid continuum variability at all frequencies, high optical polarization ( $\geq 3\%$ ), and radio and X-ray emission. They are usually compact and show a flat radio spectrum. Blazars are sub-classified into BL Lac objects and ‘optically violently variable’ (OVV) quasars. BL Lacs are named after the prototype object BL Lacertae, which was initially thought to be a variable star. They present a featureless spectrum, lacking any emission or absorption lines. Both radio and optical emission are strongly polarized. Their extremely rapid variability (of a few hours or days) shows often correlation at different wavelengths. OVV objects present the same pattern of variability as BL Lacs, but their spectrum shows stronger emission lines and they have higher level of polarization.
- Radio galaxies show powerful radio emission and extended structure. Their emission comes from a pair of highly collimated jets that extend beyond the nucleus up to Mpc scales, forming two radio-bright lobes on either side of the galaxy. The stronger the radio source, the bigger the lobes tend to be (the largest known reach 3 Mpc across). Radio galaxies are sub-classified into broad-line radio galaxies (BLRG, or type 1 radio galaxies) and narrow-line radio galaxies (NLRG, or type 2 radio galaxies) depending on the presence of broad and narrow optical emission lines, respectively. The luminosity and morphology of the radio jets and lobes gives rise to another type of classification, introduced by Fanaroff & Riley (1974). Radio galaxies with a radio luminosity  $L_{178\text{MHz}} \leq 10^{42} \text{ erg s}^{-1}$  and well collimated jets that end as faint radio lobes are categorized as Fanaroff-Riley type I (FRI). On the other hand, Fanaroff-Riley type II (FR II) radio galaxies have  $L_{178\text{MHz}} \geq 10^{42} \text{ erg s}^{-1}$  and show even more

TABLE 1.1— AGN dichotomy

Type	Host	Broad lines	Narrow lines	Radio jets	Variability	Polarization
Radio loud quasars	all	yes	yes	strong	some (days)	some
Radio quiet quasars	all	yes	yes	weak	weak	weak
Broad line radio galaxies (FRII only)	elliptical	yes	yes	strong	weak (months)	weak
Narrow line radio galaxies (FRI and FRII)	elliptical	no	yes	strong	no	no
BL Lac objects	elliptical	no	no	yes	yes (days)	yes
OVV quasars	elliptical	yes	yes	yes	yes (days)	yes
Seyferts type I	spiral/irregular	yes	yes	weak	some (months)	weak
Seyferts type II	spiral/irregular	no	yes	weak	no	some
LINERs	all	no	yes	weak	weak	no

Main observed characteristics of the different AGN types. Adapted from Krolik (1998), Table 1.2; A. Müller, MPE.

collimated and fainter jets but very bright hot spots and radio lobes in their extremes. NLRG can be either FRI or FRII radio galaxies, while BLRG are always FRII.

This wide diversity of AGN types is well explained by the Unified Model introduced in Sect. 1.1.1 (Antonucci 1993; Urry & Padovani 1995). According to this model, the different AGN types observed correspond simply to different viewing angles<sup>1</sup> of the same unique AGN (see Fig. 1.2). When the AGN is viewed edge-on (inclination angle  $\sim 90$  degrees), the dusty torus obscures the internal BLR and the observer sees an AGN type 2 source (either a Seyfert 2 or a type 2 radio galaxy) featuring narrow optical emission lines in its spectrum but lacking broad emission lines. As the viewing angle decreases towards a face-on view, the accretion disk and BLR become visible and the observer sees type 1 radio galaxies (BLRG) and Seyfert 1 AGN showing both broad and narrow spectral emission lines. At small inclination angles, close to the jet axis (inclination  $< 5$  degrees), the AGN emission is dominated by the highly beamed continuum radiation of the jet. In this case the observed AGN is a

<sup>1</sup>The viewing angle or inclination angle is defined as the angle between the line of sight and the rotation axis of the accretion disk



blazar. The origin of its variable emission is the relativistic jet being oriented close to the line of sight. Relativistic effects amplify both the luminosity of the jet and the amplitude of variability. For an extensive review on nuclear activity, see Ho (2008).

### 1.1.3 Basic physics

We have seen that a major contribution to the powerful AGN luminosity comes from the accretion disk and the relativistic jets. In this section we will dig a bit deeper into the physical mechanisms responsible for their emission.

The spectral energy distribution of the black body radiation in thermodynamic equilibrium is given by Planck's law:

$$B_{\nu}(T) = \frac{2h\nu^3}{c^2} \frac{1}{e^{h\nu/kT} - 1}, \quad (1.1)$$

where  $h$  is the Planck's constant,  $\nu$  is the frequency of emission,  $T$  is the temperature of the system,  $c$  is the speed of light, and  $k$  is the Boltzmann's constant.

In the Rayleigh-Jeans regime ( $h\nu \ll kT$ ), the equation above can be reduced to

$$B_{\nu}(T) = \frac{2\nu^2}{c^2} kT. \quad (1.2)$$

$B_{\nu}$ , also called brightness or specific intensity, has units of  $\text{J s}^{-1} \text{m}^{-2} \text{Hz}^{-1} \text{sr}^{-1}$ . To obtain the total flux of a source,  $B_{\nu}$  must be integrated over the total solid angle subtended by that source:

$$S_{\nu} = \int_{\Omega_s} B_{\nu}(\theta, \varphi) \cos\theta d\Omega, \quad (1.3)$$

and the flux density  $S_{\nu}$  is measured in units of  $\text{J s}^{-1} \text{m}^{-2} \text{Hz}^{-1}$ .

Since radio sources usually present very small fluxes, these are measured in units of Jansky (Jy), defined as

$$1\text{Jy} = 10^{-26} \text{J s}^{-1} \text{m}^{-2} \text{Hz}^{-1}. \quad (1.4)$$

The intensity of the radiation can be expressed as well in terms of the brightness temperature,  $T_{\text{B}}$ , which is equivalent to the temperature of a black body radiating the same amount of flux as the source. In the Rayleigh-Jeans

approximation,  $T_B$  is defined as

$$T_B = \frac{c^2 B_\nu}{2k\nu^2}. \quad (1.5)$$

Observationally, the brightness temperature is given by (Ghisellini et al. 1993):

$$T_B = 1.77 \times 10^{12} \left( \frac{S_m}{\nu^2 \theta^2} \right) (1+z) \text{ K}, \quad (1.6)$$

where  $S_m$  is the observed synchrotron flux (in Jy) at a frequency  $\nu$  (in GHz),  $z$  is the redshift of the source, and  $\theta$  is the angular size of the source (in milliarcseconds).

**Accretion disk.** The radiation generated by the central AGN is so intense that it exerts an outward pressure on the gas around it. If this radiation pressure is too strong, the gas cannot come close enough to feed the SMBH. There is a limit on the amount of luminosity radiated by the gas so that the SMBH does not run out of fuel. If we assume a time-steady spherically symmetric accretion flow (Bondi accretion; Bondi 1952) of fully ionized gas, then the outward pressure is due to Thomson scattering by the electrons in the gas (the proton contribution to the scattering is not significant due to their larger mass). The central source emits photons of luminosity  $L$ , so an electron at radius  $r$  will receive a radiation force  $\sigma_T L / 4\pi^2 r^2 c$ , where  $\sigma_T$  is the Thomson cross section. The radiation pressure balances the gravitational force when

$$\frac{GM(m_e + m_p)}{r^2} \simeq \frac{GMm_p}{r^2} = \frac{\sigma_T L}{4\pi^2 r^2 c}, \quad (1.7)$$

where  $m_e$  and  $m_p$  are the electron and proton mass, respectively, and  $M$  is the mass of the central SMBH. The Eddington luminosity  $L_{\text{Edd}}$  is then defined as the larger value of  $L$  that still allows material to fall inward:

$$L_{\text{Edd}} = \frac{4\pi GMm_p c}{\sigma_T} \simeq 1.51 \times 10^{38} \frac{M}{M_\odot} \text{ erg s}^{-1}. \quad (1.8)$$

So for  $L > L_{\text{Edd}}$  (super-Eddington luminosities), the radiation pressure overpowers the gravitational force of the infalling matter. On the contrary, the radiation force cannot support gravity at sub-Eddington luminosities ( $L_{\text{Edd}} < L$ ).

If the accretion flow produces radiation with a certain efficiency  $\eta$ , the

central black hole sets a mass accretion rate:

$$\dot{M} = \frac{L}{c^2 \eta}, \quad (1.9)$$

and the Eddington accretion rate:

$$\dot{M}_{\text{Edd}} = \frac{L_{\text{Edd}}}{c^2 \eta} = 3 \times 10^8 \left( \frac{\eta}{0.1} \right)^{-1} M_{\odot} \text{yr}^{-1}, \quad (1.10)$$

where the radiative efficiency is of the order of  $\eta \sim 0.1$ . The Eddington ratio is then defined as  $\dot{M}/\dot{M}_{\text{Edd}}$ .

So far we have assumed a simple spherically symmetric accretion. But accretion of matter toward the central black hole requires eliminating not only gravitational energy but also most of the matter's initial angular momentum. Since the total angular momentum must be conserved, angular momentum should be transported outwards for matter to accrete. We expect then the material to accrete not spherically, but to form a disk (Krolik 1998). The local change of angular momentum is described by the torque, which is created by local viscosity between adjacent rings in the disk. Viscosity can heat up and radiate away part of the gravitational energy, but it is not strong enough to transport angular momentum to the outer parts of the disk. It was suggested that the existence of an enhanced viscosity generated by turbulence in the disk could be able to redistribute the angular momentum (Shakura & Sunyaev 1973). A parameter  $\alpha$  was introduced ( $\alpha \leq 1$ ; no accretion for  $\alpha=0$ ) to describe the effective increase of viscosity due to turbulent eddies within the disk. Assuming subsonic turbulence, the disk viscosity  $\nu$  can be then estimated as:

$$\nu = \alpha c_s H, \quad (1.11)$$

where  $c_s$  is the sound speed or velocity of the turbulent cells, and  $H$  is the disk height which is assumed to be the largest size of the turbulent cells. The disk height is related to the Keplerian orbital angular velocity  $\Omega$ ,  $H = c_s/\Omega$ , where  $\Omega = \frac{\sqrt{GM}}{r^{3/2}}$  and  $r$  is the radial distance from the central black hole of mass  $M$ . This Shakura-Sunyaev  $\alpha$ -disk model assumes that the disk is in Local Thermal Equilibrium (LTE) and that it radiates away the viscous heat efficiently, becoming geometrically thin. This geometrically thin accretion disk made of relatively cold gas forms when the accretion rate is sub-Eddington (e.g.,  $\dot{M}/\dot{M}_{\text{Edd}} \gtrsim 0.1$ ) and the matter opacity is very high (Shakura & Sunyaev

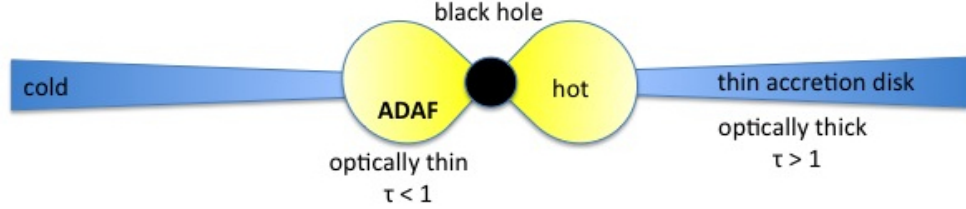


FIGURE 1.3— Accretion disk of an AGN with an Advection Dominated Accretion Flow (ADAF). The disk is geometrically thin and optically thick when the opacity is very high ( $\tau > 1$ ), but it puffs up into an optically thin torus when the opacity is very low ( $\tau < 1$ ). Sketch adapted from A. Müller, MPE.

1973). Thin disks have a quite luminous thermal electromagnetic spectra, similar to a sum of black bodies, and their radiatively cooling efficiency is very high. In the outer regions of the disk, the local spectrum of radiation follows a Planck distribution (Eq. 1.1) with a surface temperature profile  $T_s \propto r^{-3/4}$  (Shakura & Sunyaev 1973). The accretion disk luminosity can be then derived from:

$$L_\nu = 2\pi \int F_\nu(r) r dr, \quad (1.12)$$

where  $F_\nu(r) \propto r^{-\beta}$  is the radial distribution of spectral intensity and  $\beta$  a power-law index that depends on the observing band.

When the Eddington ratio moves to smaller values ( $\dot{M}/\dot{M}_{\text{Edd}} \lesssim 0.1$ ) and the opacity is very low, the disk puffs up into a torus or Advection Dominated Accretion Flow (ADAF; see Fig.1.3). ADAFs are cooled by advection rather than radiation, and they are very radiatively inefficient. Their non-thermal radiation is much less luminous than the Shakura-Sunyaev thin disk, and they show a power-law Spectral Energy Distribution (SED). ADAFs are as well called radiative inefficient accretion flows (RIAFs; Quataert 2003), and they might help to the formation and collimation of the relativistic jets (Rees et al. 1982).

**Jet physics.** The main emission mechanism in AGN jets is the synchrotron radiation. The synchrotron emission is produced when charged particles (i.e., electrons) moving at relativistic velocities are accelerated by strong magnetic fields (see Fig. 1.4, top left). If we consider a charged particle gyrating with velocity  $\mathbf{v}$  in a magnetic field  $\mathbf{B}$ , the emission of the particle has a gyromagnetic

frequency:

$$\nu_g = \frac{\gamma^2 e B}{2\pi m c}, \quad (1.13)$$

where  $e$  is the particle charge,  $m$  its mass, and  $\gamma$  is the Lorentz factor defined as  $\gamma = \frac{1}{\sqrt{1 - \left(\frac{v}{c}\right)^2}}$ .

Since the mass of the electron is much smaller than the proton mass (by a factor  $\sim 2000$ ), the acceleration of the electrons is much larger than the protons. Hence, the contribution of the protons to the radiation is insignificant and the synchrotron emission is attributed only to electrons and positrons. It is usually assumed that the energy distribution of the charged particles responsible for the synchrotron emission follows a power-law of the form:

$$N(E)dE \sim E^{-p}dE, \quad (1.14)$$

where  $N(E)$  is the number of charged particles with energies between  $E$  and  $E+dE$  and  $p$  is the slope of the distribution. The superposition of the spectra of the individual particles results into the observed AGN radio spectrum, which is a power-law described by  $S_\nu \sim \nu^{+\alpha}$ , where  $S_\nu$  is the flux density,  $\nu$  is the observed frequency, and  $\alpha$  is the power-law index  $\left(\alpha = \frac{1-p}{2}\right)$ .

The most compact and dense regions in AGN show usually a flat or inverted spectrum owing to synchrotron self-absorption. This happens when the same electrons responsible for the emission of the synchrotron photons start to absorb their own emission. As a result, the radio spectrum of the source shows a peak at a certain frequency  $\nu_{\text{peak}}$  (see Fig. 1.5). This turnover frequency separates the two regimes in which the medium becomes optically-thick ( $\nu < \nu_{\text{peak}}$ ) or optically-thin ( $\nu > \nu_{\text{peak}}$ ) to the synchrotron radiation. Hence, for frequencies below  $\nu_{\text{peak}}$ , the radio spectrum will drop ( $\alpha \sim 5/2$ ; Rybicki & Lightman 1979) because the absorbed photons do not contribute to the observed flux density. Free-free absorption (or bremsstrahlung self-absorption) can contribute as well to the optically-thick part of the spectrum. This mechanism takes place in an ionized medium when a charged particle (i.e., an electron) changes its kinetic energy due to the presence of an ionized atom and absorbs a photon (see Fig. 1.4, top right), and it is expected to produce a power-law spectrum of slope  $\alpha = 2$ .

At higher frequencies, the loss of energy of the emitting particles owing to

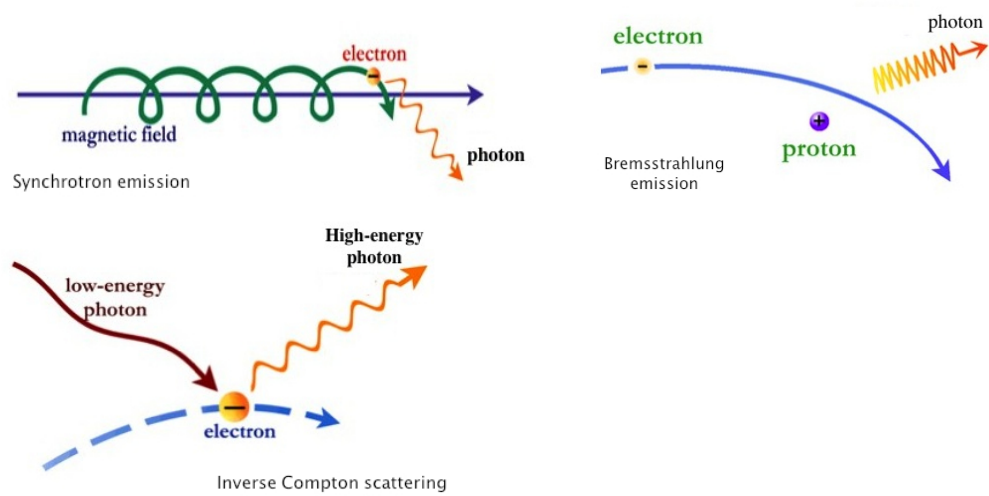


FIGURE 1.4— Radiation processes in AGN jets. When a charged particle is accelerated, radiation is emitted. Top left: The synchrotron emission is a non-thermal mechanism that occurs when charged particles are accelerated around magnetic field lines. Top right: Thermal bremsstrahlung or free-free emission occurs when charged particles (i.e., electrons) are accelerated in the presence of an ionized atom. Free-free absorption is the absorption of photons by these electrons. Bottom: Inverse Compton scattering takes place when photons gain energy upon scattering by relativistic electrons. This process is the inverse of the Compton scattering, where the scattering of a photon results in a decrease of energy (and increase of wavelength).

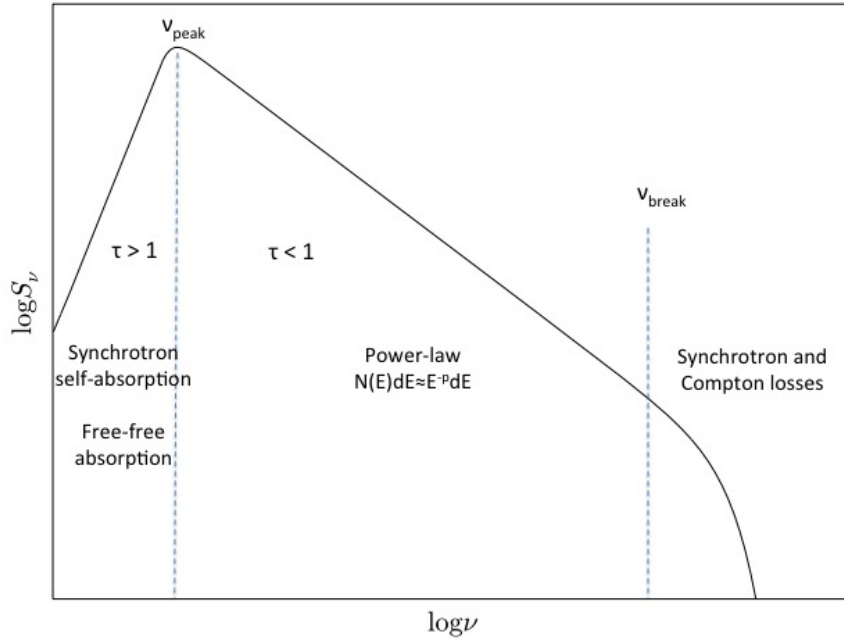


FIGURE 1.5— Sketch of the radio spectrum of an AGN. The peak of the spectrum corresponds to the transition between the optically thick ( $\tau > 1$ ), and optically thin ( $\tau < 1$ ) regimes. At frequencies below  $\nu_{peak}$ , synchrotron self-absorption and free-free absorption processes contribute to the radio emission. The central region corresponds to the power-law regime, which extends through several decades in frequency. At higher frequencies, a broken slope due to synchrotron and inverse Compton losses can be seen. The break frequency is related to the age of the emitting particles. Courtesy of C. Fromm.

the synchrotron radiation itself and inverse Compton losses produces a broken slope in the observed radio spectrum (at a break frequency  $\nu_{break}$ , see Fig. 1.5). In the inverse Compton scattering, photons are scattered to higher energies by the relativistic electrons (see Fig. 1.4, bottom left), gaining an energy proportional to  $\gamma^2$ . Depending on the value of  $\gamma$ , photons in the radio and IR can be scattered up to X-rays and  $\gamma$ -rays.

The more extended sources present a complex spectrum with a steeper slope. This is explained by the superposition of different parts of the source, each with a different turnover frequency. The parts become optically-thick at different frequencies so that the spectral energy distribution of the source has contributions from all the parts.

## 1.2 Galaxy evolution

According to the current paradigm of galaxy evolution in a  $\Lambda$  cold dark matter Universe, galaxies grow in a hierarchical or ‘bottom-up’ way through mergers (Searle & Zinn 1978), combining smaller systems to build larger and more massive galaxies (Toomre & Toomre 1972). Starting with the ‘Toomre’ sequence of 11 interacting galaxies chronologically arranged to show how spirals can merge to produce ellipticals (Toomre 1977), an extensive list of on-going merger systems associated to different observational properties (Ultraluminous Infrared Galaxies, ULIRGs; post-starburst galaxies; submillimeter galaxies, SMG; etc.) have been studied in detail across the whole electromagnetic spectrum (e.g., Sanders et al. 1988; Sanders & Mirabel 1996; Colina et al. 2001; Genzel et al. 2001; Naab et al. 2006; Brassington et al. 2007; Hopkins et al. 2008b, Hopkins et al. 2008a). The evolution from late-type to early-type galaxies has a significant impact on the galaxy morphology and kinematics, in the form of inflows of gas, galaxy winds that can clear the galaxy of its gas (e.g., Springel et al. 2005b), and a significant increase of the star formation, as has been shown by several numerical simulations (e.g., Mihos & Hernquist 1996; Cox 2004; Di Matteo et al. 2007, Di Matteo et al. 2008).

Compelling observational evidence indicate that SMBHs can be found at the center of nearly all galaxies (Richstone et al. 1998). It was found that the mass of the black hole is linked to the host galaxy through the central stellar velocity dispersion ( $M_{BH} - \sigma$  relationship; e.g., Ferrarese & Merritt 2000; Gebhardt et al. 2000; Tremaine et al. 2002), the bulge luminosity (e.g., McLure & Dunlop 2002; Marconi & Hunt 2003), and the central concentration of light (or Sersic index; e.g., Graham et al. 2001; Graham & Driver 2007), indicating that some common growth process or feedback between the SMBH and the host galaxy may exist. If nearly all galaxies host a SMBH at their center and galaxies grow through frequent galaxy merging, a pair of SMBHs is expected to be found at the center of galaxies that have recently undergone a merger (e.g., Begelman et al. 1980; Volonteri et al. 2003). If enough gas is available for accretion onto one (or both) SMBHs, the gas funneled towards the galactic centers during the merger may initiate and fuel AGN activity, triggering strong quasar accretion (e.g., Hernquist 1989; Kauffmann & Haehnelt 2000; Hopkins et al. 2008b). Observational evidence and simulations indicate that AGN feedback expels gas from the galaxy centers, shutting down accretion onto them, quenching star formation, and playing a key role in transforming late-type into early-type galaxies (e.g., Di Matteo et al. 2005; Springel et al. 2005a; Croton et al. 2006). A cyclic model was proposed to link



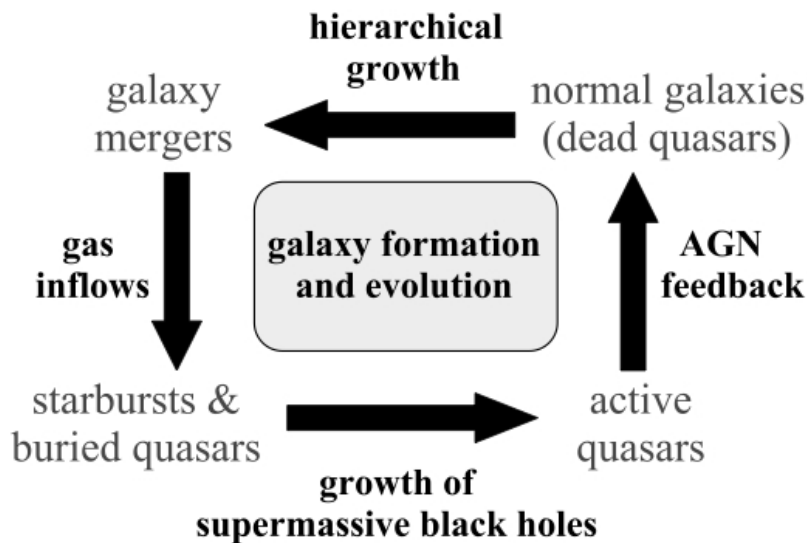


FIGURE 1.6— Formation and evolution of galaxies through the cosmic cycle. When normal galaxies merge, inflows of gas towards the center enhance star formation and AGN activity, triggering the SMBH growth. The gas is expelled from the galactic nuclei during the active AGN phase, shutting down the accretion on the SMBH and resulting into a non-active normal galaxy again. The cycle restarts when a new merger event between non-active galaxies occur. Image taken from Hopkins et al. (2006).

all the different processes and episodes that take place during the evolution of galaxies, from gas inflow and triggered starburst during the galactic merger leading to the growth of SMBHs, to quasar activity, AGN feedback, and back to the hierarchical growth (Fig. 1.6; Hopkins et al. 2006).

Despite the wide recognition of this hierarchical evolutionary model, other evolution schemes are gaining momentum nowadays. It has been shown that gas-free ('dry') mergers are not able to assemble more than half the present-day mass of early-type galaxies (Nipoti et al. 2009), nor to reproduce the structural and kinematic features observed in some of them (Jesseit et al. 2007; Hopkins et al. 2009). The accretion/merging of massive satellite galaxies can provide the required gas mass of elliptical galaxies to evolve (e.g., Struve et al. 2010), although other mechanisms such as the infall of small gas clouds from the halo could also be able to fuel the galaxy (e.g., Kereš et al. 2005). Several studies do also not find any apparent correlation between nuclear activity and merger interactions (e.g., Virani et al. 2000; Li et al. 2008), while the formation of disk galaxies and pseudobulges can be naturally explained by alternative models as the secular evolution (e.g., Kormendy & Kennicutt 2004).

### 1.2.1 Binary black hole evolution

As we have seen above, the formation of supermassive binary black holes (BBHs) seems to be a natural consequence of the merging of two galaxies. The formation, evolution, and final coalescence of the SMBH pair proceeds basically in three stages (Begelman et al. 1980). In a first stage, after the merging galaxies, violently distorted by their mutual interaction, have merged into a single system, the nuclei of both galaxies approach each other and lose energy via dynamical friction between the black holes and the surrounding stars. In a characteristic dynamical time scale of  $\sim 10^8$  years, the black holes sink toward the center of the new galaxy where they form a gravitationally bound binary (Fig. 1.7). The black holes spiral together under dynamical friction until the binary system becomes hard, this is, when the distance between the BHs has shrunk to about the cusp radius and the velocity dispersion of the stars in the core equals their Keplerian velocity. In this stage, some of the orbital angular momentum of the binary system is transferred to the stars orbiting the binary, which gain sufficient energy so that they are ejected from the galactic core at velocities comparable to the binary's orbital velocity (slingshot effect). The energy loss through ejection of stars is the dominant process when the separation of the black holes is between a few parsecs and one tenth of a parsec, and causes the binary to harden and increase its binding energy. At this point, there is a major hurdle (called the 'final parsec problem'; Milosavljević & Merritt 2001), namely that the binary ejects all the stars on intersecting orbits and the loss-cone is depleted at timescales significantly shorter than it is replenished, that is, the black holes stall. The extraction of energy and angular momentum from the binary system can continue via several processes, e.g., accretion of gas onto the binary (e.g., Armitage & Natarajan 2002) or refilling the loss-cone via cloud-star/star-star encounters (Milosavljević & Merritt 2001). These interactions refill the stellar orbits in the center of the galaxy so that no stalling occurs and the binary separation continues to decrease. In the final stage, the compact binary arrives to the point where the emission of gravitational wave radiation carries away the last remaining angular momentum and the two black holes coalesce. This last phase has received considerable attention because it would constitute the largest source of gravitational waves detectable with future gravitational wave space interferometers (e.g., Merritt et al. 2004; Sesana et al. 2005).

In the case that each of the nuclei of the two merging galaxies harbors an AGN, the properties of the two AGN (e.g., the accretion disks and jet activity)

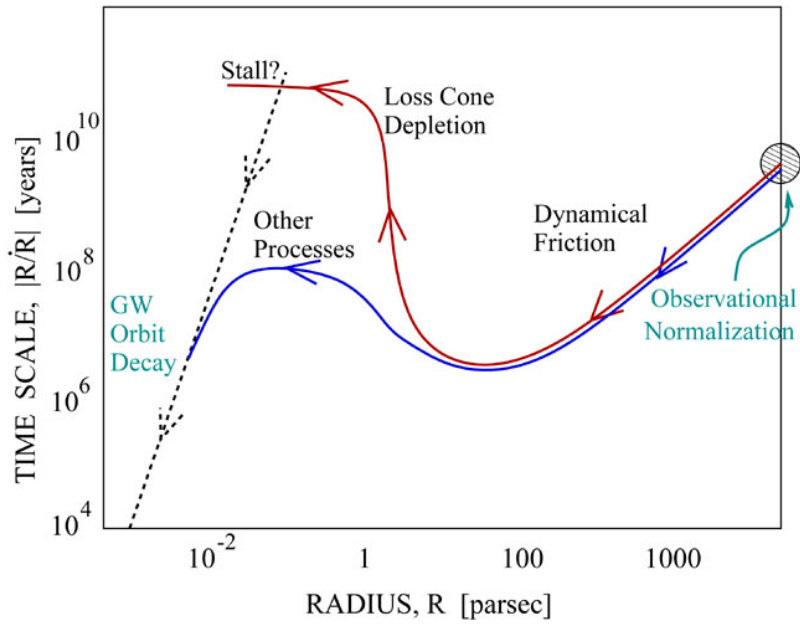


FIGURE 1.7— Evolution of the binary black hole separation in a merged galaxy. Dynamical friction brings the two black holes close together forming a gravitationally bound system. The separation decrease slows down as stars are ejected from a loss-cone. If the loss-cone is depleted, the black holes stall (red line). If star and gas clouds encounters are able to refill the loss-cone, the binary separation decreases until the loss of orbital momentum due to gravitational wave emission becomes efficient and ultimately leads to black hole coalescence (blue line). Image taken from Backer et al. (2004).

will evolve with the merger, from a first stage where the nuclei are not yet gravitationally bound to a final one just before they coalesce. The evolution of the two AGN can be divided into four stages (Lobanov 2005):

- Stage I or ‘Low-power AGN’: each black hole has an accretion rate  $\dot{M} \leq 10^{-3} \dot{M}_{\text{Edd}}$  and supports a luminosity  $L \leq L_{\text{Edd}} \times \dot{M} \sim 10^{43} M_8 \text{ erg s}^{-1}$ , where  $M_8$  is the BH mass in units of  $10^8 M_\odot$ . The accretion disks of the two AGN remain intact, and the nuclei present weak pc-scale and kpc-scale jets, and weak broad line regions. The system shows a weak variability, with long-term changes, and stays in this phase  $\sim 10^8$  years.
- Stage II or ‘High-power AGN’: the two BHs are gravitationally bound at a distance  $\leq 10$  pc, which is reduced to  $\sim 0.1$  pc via dynamical friction. In this stage, which lasts around  $10^8 - 10^9$  years, the secondary BH loses its accretion disks and disrupts the nuclear environment of the primary. The fuelling rate of each BH increases to  $\dot{M} \leq (0.1 - 1) \dot{M}_{\text{Edd}}$ , and the luminosity to  $L \leq L_{\text{Edd}} \times \dot{M} \sim 10^{46} M_8 \text{ erg s}^{-1}$ . The AGN show strong pc-scale and kpc-scale jets (resembling FR II radio galaxies) and strong broad line regions. The variability is strong as well, with timescales of  $\sim 10^2 - 10^4$  days.
- Stage III or ‘Radio-quiet AGN’: at this stage the accretion disk around the primary black hole is destroyed and the BHs orbit at a separation of  $\sim 10^{-2} - 1$  pc. There are no signs of collimated outflows, and the activity in the nuclear region is very turbulent. Each BH has a fueling rate of  $\dot{M} \leq 0.1 \dot{M}_{\text{Edd}}$  and luminosity  $L \sim 10^{45} M_8 \text{ erg s}^{-1}$ . The variability increases to a timescale of  $\sim 1 - 10^3$  days. This phase lasts less than  $10^8$  years.
- Stage IV or ‘Intraday variable AGN’: in this final state the orbital separation of the binary decreases to less than  $10^{-2}$  pc due to gravitational radiation losses. An accretion disk around the binary system may be re-formed, and the jet activity re-started. The luminosity expected is  $\leq 10^{45} M_8 \text{ erg s}^{-1}$ , and the system shows a very high variability of between 0.1 and 100 days. This period lasts around  $10^7$  years, until the two black holes finally merge.

The evolution of the AGN power can also be described as a function of the reduced mass and orbital separation,  $r$ , of the two black holes in the BBH system (Lobanov 2007; Lobanov 2008). The reduced mass is defined as:

$$\tilde{M} = \frac{2M_2}{M_1 + M_2}, \quad (1.15)$$

where  $M_1, M_2$  are the masses of the two black holes, with  $M_1 > M_2$  ( $\tilde{M}=1$  for  $M_1 = M_2$ ;  $\tilde{M}=0$  for  $M_2=0$ ). The reduced separation,  $\tilde{r}$ , is given by:

$$\tilde{r} = 1 - \frac{r_c}{r + r_c} = \frac{r}{r + r_c}, \quad (1.16)$$

where  $r_c$  is the distance at which the two black holes become gravitationally bound (this happens when  $r = r_c$  and, thus,  $\tilde{r}=1/2$ ). Binary systems have  $\tilde{r} \leq 1/2$ , while unbound pairs have  $\tilde{r} > 1/2$ .

The model assumes that in the early stage of the merger each of the two SMBHs has an active accretion disk around it, and that there is a central stellar bulge of radius  $r_b$ , mass  $M_b$ , and velocity dispersion  $\sigma_b$ . The two black holes will then become bound to each other when  $r_c = r_b \left( \frac{M_1 + M_2}{M_b} \right)^{1/3}$  (Begelman et al. 1980). The disruption distance  $r_d$  at which the accretion disks will be disrupted and eventually destroyed can be estimated, for the primary and the secondary black hole respectively, as (Lobanov 2008):

$$r_{d1} = \left( 1 + \frac{\varepsilon_1}{\tilde{M}^2(2 - \tilde{M})} \right)^{-1} \quad (1.17)$$

and

$$r_{d2} = \left( 1 + \frac{\varepsilon_1}{(2 - \tilde{M})^3} \right)^{-1}, \quad (1.18)$$

where  $\varepsilon_1 = M_1/M_{\text{eq}}$  and  $M_{\text{eq}}$  is the critical mass for which an equal mass binary BH system will undergo disk destruction at the time of gravitational binding (when  $\tilde{r}_d = \tilde{r}_c$ ). In systems with  $M_1 < M_{\text{eq}}$ , the destruction of the accretion disk around the secondary BH will occur before the formation of the gravitationally bound system. Since typical values of  $M_{\text{eq}}$  can reach  $10^9$ - $10^{10}M_\odot$ , in most galactic mergers the disk around the secondary BH will be destroyed before or during the formation of the gravitationally bound system (Lobanov 2008).

Assuming that the accretion rate increases proportionally to the tidal

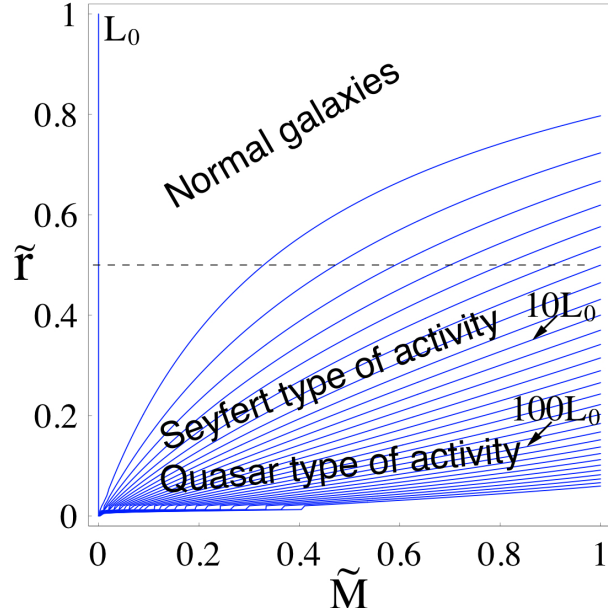


FIGURE 1.8— AGN peak luminosity of a binary black hole system in function of  $\tilde{r}$  and  $\tilde{M}$ . The peak luminosity increases with increasing  $\tilde{M}$  and  $\tilde{r}$ , and it reaches  $L_{\text{peak}} = 1000L_{\odot}$  for an equal mass binary ( $\tilde{M}=1$ ) at  $r \simeq 0.03r_c$ . This would correspond to the most powerful quasars. At the same reduced separation, an unequal mass binary with  $\tilde{M}=0.15$  will only produce  $L_{\text{peak}} = 10L_{\odot}$ , which would correspond to a Seyfert nucleus. Figure and caption taken from Lobanov (2007).

forces acting on stars and gas on scales comparable to the accretion radius,  $2GM_{\text{BH}}/\sigma_b^2$ , the peak luminosity from an AGN can be estimated from (Lobanov 2007; Lobanov 2008):

$$L_{\text{peak}} = L_0 \left( 1 + \frac{\tilde{M}}{2 - \tilde{M}} \frac{\tilde{M}}{\tilde{r}^2} \right), \quad (1.19)$$

where  $L_0$  is the luminosity of a typical single, inactive galactic nuclei. AGN peak luminosities calculated for a range of values of  $\tilde{M}$  and  $\tilde{r}$  are shown in Fig. 1.8:  $\sim 70\%$  of all galaxies would be classified as inactive if they were distributed homogeneously in the  $\tilde{M}$ - $\tilde{r}$  domain, while Seyfert galaxies (with  $L_{\text{peak}}=10\text{-}100L_{\odot}$ ) would constitute 15% of the galaxy population and quasars (with  $L_{\text{peak}} > 100L_{\odot}$ ) the 10%. The estimates of the peak luminosity, thus, correctly predicts the relative fractions of different types of AGN.

### 1.2.2 Observational evidence of supermassive binary black hole systems

The importance of finding and studying supermassive BBH systems stems not only from the role they play in the evolution of galaxies, and thus the Universe, but also from the relevance they may have in explaining different types of AGN. Several authors suggested a possible link between BBHs and radio-loud AGN types (e.g., Basu et al. 1993; Wilson & Colbert 1995; Valtonen & Heinämäki 2000; Britzen et al. 2001; Merritt & Ekers 2002; Karouzos et al. 2010). In particular, Villata & Raiteri (1999) suggested that BL Lacs and FRI radio galaxies would represent the late stages in the evolution of the binary system, when the pair is closely bound and has low mass accretion, while FRII radio galaxies would be the result of a widely separated BBH with long orbital period. Zier & Biermann (2001) and Zier (2006) proposed that a torus of molecular gas could form from the winds of the stars orbiting the BBHs, when the stars are ejected due to the orbital angular momentum transferred to the BBH system. Since this torus is believed to be ubiquitous in AGN, BBHs would play a key role in the Unified Model of AGN (e.g., Antonucci 1993).

The detection and number estimates of supermassive BBHs is thus of pivotal importance when studying models of galaxy formation and evolution. Many observational evidence have been suggested in the last decades in order to detect (or infer) the presence of supermassive BBH systems in galaxies. In the case of spatially unresolved BBHs, most of these evidence are related to jet structures. The most acknowledged systems with peculiar jet morphology are X-shaped radio galaxies (Leahy & Williams 1984; Parma et al. 1985; Leahy & Parma 1992) and double-double radio galaxies (Schoenmakers et al. 2000), which have both been long under study due to their possible link to supermassive binary black hole systems. X-shaped radio sources owe their name to two pair of radio lobes (the high-surface-brightness ones and the low-surface-brightness ones) that pass symmetrically through the center of the host galaxy forming an X-shaped or winged pattern. The suggested connection between X-shaped radio sources and galaxy mergers is studied in detail in this thesis and is presented in Chapter 3. Double-double radio galaxies, on the other hand, exhibit two pairs of symmetric radio lobes aligned along the same axis. The lack of radio emission between the inner and outer lobes suggests some interruption and re-starting of the jet formation, which could be related to the presence of a merged BBH system (Liu et al. 2003).

Other peculiar phenomena suggested to be a manifestation of the presence of supermassive BBHs are the observation of helical distortions and bending of jets in several sources (PKS 0420–014, Britzen et al. 2001; 3C 345, Lobanov

& Roland 2005; BL Lac S5 1803+784, Roland et al. 2008), and the quasi-periodic changes in lightcurves (e.g., OJ 287; Sillanpaa et al. 1988, 1996; Valtaoja et al. 2000). Several studies have focused as well on observations of double-peaked emission line profiles, both broad (e.g., Gaskell 1996; Eracleous & Halpern 1994, 2003; Strateva et al. 2003, Strateva et al. 2006; Boroson & Lauer 2009; Chornock et al. 2010; Shen & Loeb 2010) and narrow (e.g., Liu et al. 2010a,b; Smith et al. 2010; Fu et al. 2011), which are interpreted as the presence of two broad line regions associated to two black holes. This double-horned profile can, however, be as well explained by several other models (e.g., Chen & Halpern 1989; Zheng et al. 1990, 1991; Eracleous et al. 1997; Popović et al. 2009; Shapovalova et al. 2010).

Despite the numerous observational evidence that could yield the detection of a pair of supermassive black holes, only in a few cases have supermassive BBHs been directly observed (NGC 6240, Komossa et al. 2003; 0402+379, Rodriguez et al. 2006; 3C 75, Hudson et al. 2006; kpc-scale binary AGN, Liu et al. 2010a) or are suggested as quasar pairs (see review from Komossa 2006).

### 1.3 This thesis

The detection and study of supermassive BBHs and of their contribution to the formation of galaxies constitute the major aim of this thesis. Detecting or inferring the presence of supermassive BBHs in active galaxies and studying their imprint on the hosts can help us understand the role they play in the formation of galaxies, of different AGN types, and of the Universe, providing significant constraints on the current hierarchical evolutionary model.

Three major observational evidence of supermassive BBHs have been studied and are presented in this thesis, structured in 3 independent chapters.

- In Chapter 3 the optical spectra and the starburst and jet activity of a sample of X-shaped radio galaxies are analyzed and compared to those of a control sample of FR II radio galaxies that have similar properties but no signs of X-shaped jet morphology. Implications of the obtained results are discussed for the black hole merger scenario as the possible origin of the observed X-shaped morphology, and for the potential presence of active secondary black holes in post-merger galaxies.
- Chapter 4 presents a millisecond-scale study of the compact radio emission coming from selected Ultraluminous X-ray sources (ULX). ULXs are another type of objects suggested to harbor the secondary black hole of a BBH system in the course of a galactic merger. The study



is aimed at unveiling the physical nature of these objects and has been initiated, for the first time, in this thesis. The results include the shell-like resolved structure of an extragalactic supernova remnant and two ULXs being potential intermediate mass black hole candidates.

- In Chapter 5 the luminosity of sample of post-merger galaxies with double nucleus is studied. The nuclear activity in post-merger galaxies was suggested to be closely connected to the evolution of binary SMBH systems formed in the course of a merger (Lobanov 2007; Lobanov 2008). The estimates connected well the galactic types and strength of the nuclear activity, and explained the luminosity evolution in the secondary supermassive BH in post-merger galaxies. However, the connection had not yet been studied systematically in a sample of post-merger galaxies. The study has been started, for the first time, in this thesis by testing a possible relation between the luminosity of the individual nuclei of such galaxies and the distance between the two nuclei. The chapter presents a model that explains satisfactorily the luminosity trend observed not only in the double nucleus post-merger galaxies, but also in the ULX sources of Chapter 4.

Throughout this thesis, a  $\Lambda$ -CDM cosmology with parameters  $H_0 = 73 \text{ km s}^{-1} \text{ Mpc}^{-1}$ ,  $\Omega_\Lambda = 0.73$ , and  $\Omega_m = 0.27$  is assumed.



# 2

---

## Observational methods

*Fiat lux.*  
(Let there be light)  
Book of Genesis

*This thesis has made combined use of optical spectroscopy and photometry, and radio interferometry. This chapter presents the main characteristics of the spectroscopic observations in the optical, and the fundamentals of the interferometric radio observations. The data reduction steps followed for each technique are as well explained.*

### 2.1 Optical spectroscopy

Since Newton dispersed the light of the Sun with a prism for the first time in the 17th century, the use of spectroscopy in astronomy has grown as the best tool to identify the elements from which stars, gas, and galaxies are formed and give us a direct probe for the actual physical processes at play. The spectroscopic technique allows us to obtain both spatial and spectral information of an object at the same time. The radiation coming from an astronomical source is typically dispersed by a prism or a diffraction grating that decomposes the light into its different wavelengths (see Fig. 2.1). The photons are collected by a Charge Coupled Device (CCD), which is a two-dimensional array of light-sensitive elements or silicon chips called *pixels* that convert the incoming photons into an electric charge. The accumulated charge in each pixel is read out as an electrical signal, digitized, and stored. The result is a digital image where the value in each image pixel is proportional to the number of incident photons on the detector pixel.

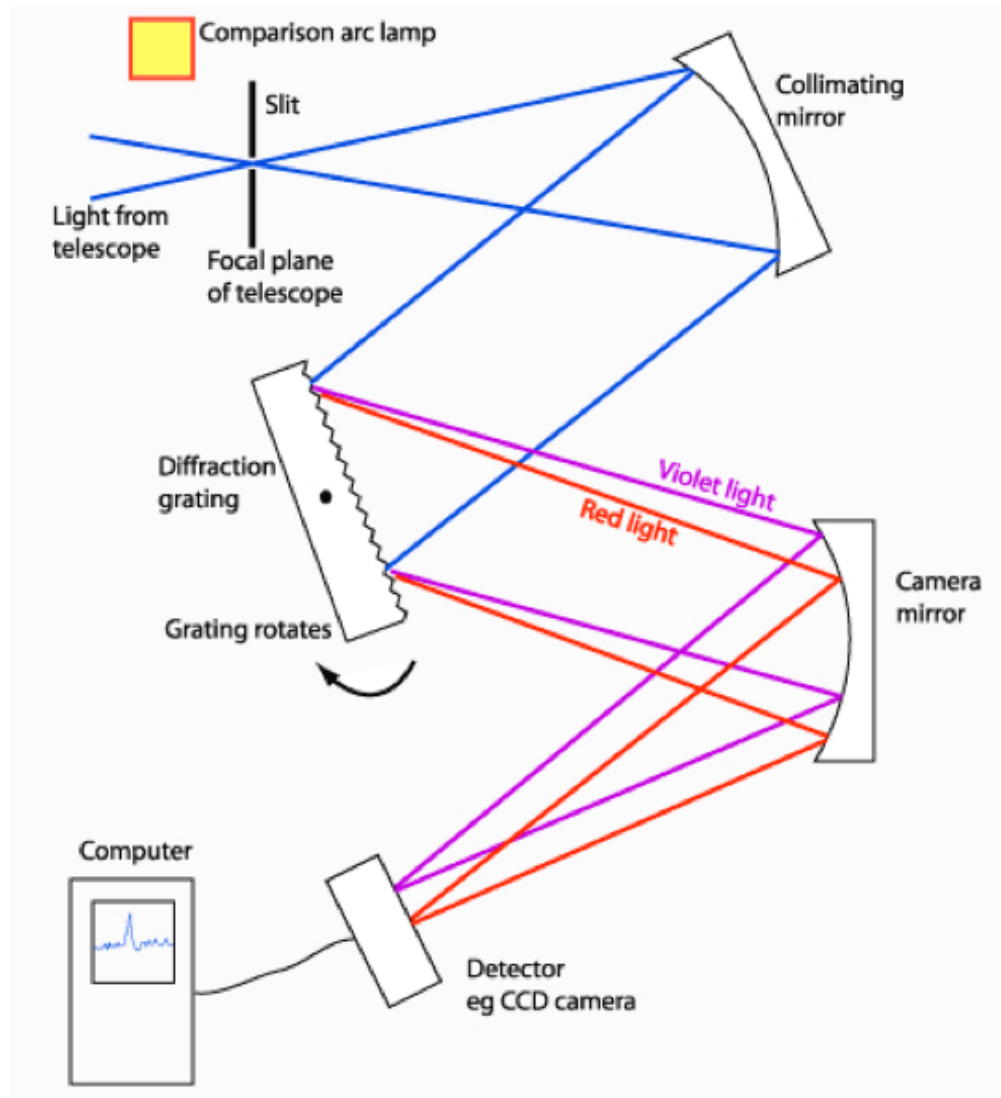


FIGURE 2.1— Schematic diagram of a slit spectrograph. The light from an astronomical source or from a comparison lamp enters the slit of the spectrograph, which acts as a point source of light. Light is then collimated by a mirror before hitting the diffraction grating. The grating disperses the light into its component wavelengths, which are focused by a camera mirror into a CCD detector. Adapted from Kaler (1989).

Before the spectrum of the astronomical source can be extracted from the CCD image, the data must be corrected for instrumental effects and calibrated in wavelength and flux. The main steps necessary to reduce the raw images are: bias subtraction, removal of cosmic rays, and flat-field correction. One of the best tools to perform these steps is the software IRAF (Image Reduction and Analysis Facility)<sup>1</sup>. The commands that IRAF uses are called ‘tasks’. Tasks that perform similar functions are grouped together into packages (see <http://iraf.noao.edu> for details).

### 2.1.1 Overscan trimming

The digital images have a zone, called ‘overscan’, that is not illuminated by the CCD and has thus the lowest level of incident photons. This region is identified by a sudden drop of flux at the end of the images and is trimmed using the task `imcopy`.

### 2.1.2 Bias subtraction

An offset, *bias*, or zero-level signal is introduced electronically during the digitalization of the CCD data to maintain the measured digital values positive. This bias can vary across the detector and as well during the night. To correct for this offset signal, exposures of zero-length are taken with the shutter closed at the beginning and at the end of the night. A median bias image is generated by stacking all the zero-length exposures using the IRAF task `imcombine` and is subtracted from all the images using the task `imarith`.

### 2.1.3 Cosmic rays

Cosmic rays are highly energetic particles detected by the CCD as abnormal high values confined to a single pixel or a few adjacent pixels. Automatic tasks as `cosmicrays` can be used to eliminate the ones that are above a certain threshold by interpolating using adjacent pixel values. However, it is safer to edit the images interactively using the task `imedit` (see Fig. 2.2, top).

### 2.1.4 Flat-field correction

The quantum efficiency (number of electrons produced per incident photon) is not the same for all the pixels within the CCD. To correct for this non-uniform pixel-to-pixel sensitivity, a flat image that contains the response of each pixel to

---

<sup>1</sup>IRAF is distributed by the National Optical Astronomy Observatories operated by the Association of Universities for Research in Astronomy, Inc. under cooperative agreement with the National Science Foundation.

a uniformly illuminated source must be obtained. Flat-field images are usually obtained exposing the CCD for a short period of time (some seconds) to the twilight sky or to the uniform illumination of the dome of the telescope. They are afterward combined to produce a single flat image. In spectroscopy, flat-field images present a different structure along the spatial (i.e., vertical) and the spectral (i.e., horizontal) direction (see Fig. 2.2, left). The variation along the spectral direction depends on the illumination used for the flat-field exposure (e.g., color of light), the transmission of the dispersing spectrograph, and the spectral response of the CCD. This structure is removed by fitting a smooth curve (usually a spline function) to the averaged signal of all columns along the spatial direction and dividing the value of the flat-field at each pixel by the value of the smooth curve. This is done using the task `response`, which is found in the package `twospec.longslit`. As a result, a final flat-field image that contains only the spatial variation across the CCD is obtained. The target images are then divided by this final flat image (task `imarith`) in order to correct for the pixel-to-pixel variations in sensitivity along the spatial direction.

Once the spectrum has been corrected for instrumental effects, it must be calibrated in wavelength and flux.

### 2.1.5 Wavelength calibration

The spectrum of a standard emission line source or comparison lamp (i.e., CuHeNeAr lamp; Fig. 2.2, right) is usually taken after the observations in order to assign wavelength values to the spectral axis of the target images. The wavelength calibration starts by interactively identifying the position of the most prominent emission lines in the lamp spectrum using the task `identify`. The file created by this task is then used by the task `reidentify` to identify the rest of the lines along the whole image. Using the output from `reidentify`, a spline function is fitted to determine the dispersion function (wavelength to pixel correspondence) using the task `fitcoords`. The dispersion function is finally applied to the spectrum of the lamp to transform coordinates in pixels to angstroms (task `transform`). This calibration is then applied to the target spectrum obtaining a spectrum calibrated in wavelength. After the wavelength calibration is done, the spectrum can be extracted from the image. In order to extract the spectrum, an aperture or range of rows of the CCD containing the spectrum must be selected. The pixels along each short column of the CCD over these rows are then summed to produce a single row. This is done with

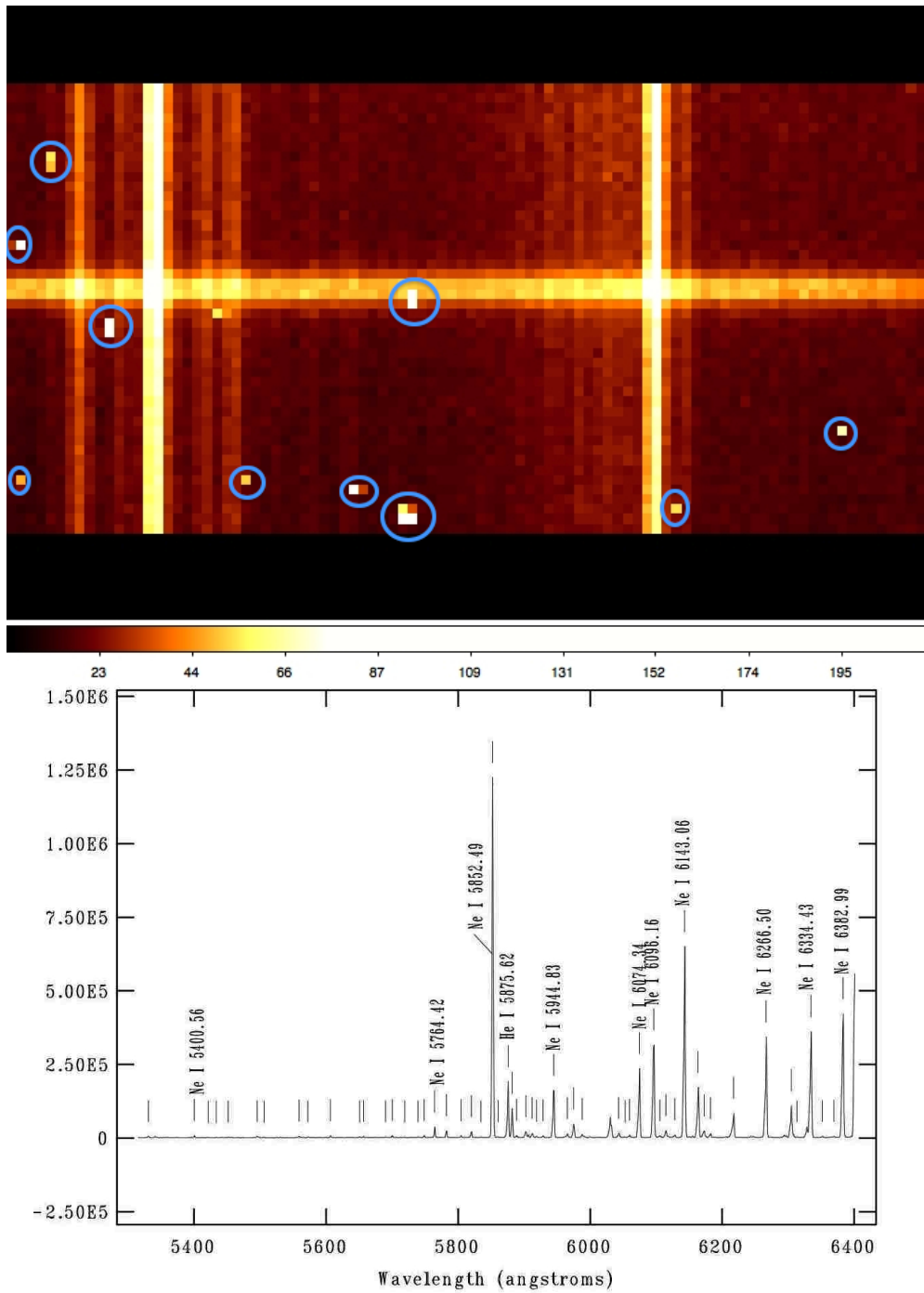


FIGURE 2.2— Top: Raw spectrum of the X-shaped radio galaxy J1008+0030, debiased and flat-field corrected. The horizontal axis corresponds to the spectral direction and the vertical axis to the spatial direction. Cosmic rays are marked with blue circles and are removed interactively using the task `imedit`. The vertical lines correspond to the sky contribution. Bottom: Spectrum of the CuHeNeAr calibration lamp used for the line identification. The horizontal axis has been calibrated in wavelength, the vertical axis corresponds to the flux, in counts (Michael Richer, OAN-SPM).

the task `apall`. The spectrum of the sky is also extracted in the same way, but selecting an aperture that does not encompass the spectrum. The sky spectrum is subtracted from the target spectrum with the task `background`.

### 2.1.6 Flux calibration

The spectrum of a spectrophotometric standard star, whose flux is known, must be observed in order to finally calibrate the target spectrum of the source and correct for atmospheric extinction. The observed spectrum of the calibration star is compared to its catalogued flux using the task `standard` contained in the package `onedspec`. A sensitivity function, or instrumental response as a function of wavelength, is then determined using the task `sensfunct`. The target spectrum is finally divided by the instrumental response using the task `calibrate`. After all these steps, the final flux calibrated spectrum of the target is obtained (see Fig. 3.5 for an example).

## 2.2 Radio interferometry

Active galactic nuclei can be observed at different wavelengths of the electromagnetic spectrum. However, their core and jets emit most of their radiation in the radio domain (e.g., via synchrotron processes; see Sect. 1.1.3) and are thus most often studied in this regime, also because of the high angular resolution achieved at this long wavelengths.

The angular resolution  $\theta$  of a radio telescope is determined by the wavelength,  $\lambda$ , of the radiation received and the diameter,  $D$ , of the telescope:

$$\theta \propto \frac{\lambda}{D} \quad (2.1)$$

Since it is not technically feasible to construct steerable radio antennas much bigger than  $\sim 100 \text{ m}^2$ , radio astronomers use groups of radio telescopes forming an interferometer array to achieve resolutions down to the order of milliarcseconds.

This section gives an introduction to the interferometric technique used in radio astronomy, in particular the Very Long Baseline Interferometry (VLBI) technique (Rogers et al. 1983; Walker 1986), and presents the two interferometric arrays of different baseline lengths used in this thesis: the Giant Meterwave Radio Telescope (GMRT) and the European VLBI Network

---

<sup>2</sup>The largest single dish telescope constructed is the Arecibo Radio Telescope, which is non-steerable and has a diameter of 305 m ([http://www.naic.edu/public/the\\_telescope.htm](http://www.naic.edu/public/the_telescope.htm)).



(EVN).

### 2.2.1 Fundamentals

In the radio domain, the waves coming from an astronomical source can be collected by two radio telescopes and combined (or correlated) in the same fashion as in Young's double slit experiment, where the wavefronts passing through two slits interfere constructively (when waves are in phase) and destructively (waves nearly 180° out of phase) producing bright and dark interference fringes, respectively.

Because of the great distance traveled, the wavefronts coming from the source can be considered planar when they reach the Earth. If the two antennas, forming a two-element interferometer, point at the source with an angle  $\theta$ , the astronomical signal will reach first one antenna (the right-hand one in Fig. 2.3) before the other, introducing a path difference or 'geometrical delay'  $\tau_g$  (Thompson 1999):

$$\tau_g = \mathbf{b} \cdot \mathbf{s} / c, \quad (2.2)$$

where  $\mathbf{b}$  is the baseline vector,  $\mathbf{s}$  is the unit vector pointing at the source, and  $c$  is the speed of light. The projected length of the baseline on the sky,  $D \cos \theta$ , changes as the Earth rotates.

The signal received in each antenna is transmitted through waveguides to an amplifier, which uses filters to select the required frequency band of width  $\Delta\nu$  centered on a frequency  $\nu$ , and produces output voltages:

$$V_1(t) = v_1 \cos 2\pi\nu(t - \tau_g), \quad V_2(t) = v_2 \cos 2\pi\nu(t) \quad (2.3)$$

The signals are then sent to the correlator, formed by a voltage multiplier and a time averaging (integrating) circuit, that combines them producing an output:

$$r(\tau_g) = \langle V_1(t)V_2(t) \rangle = v_1 v_2 \cos 2\pi\nu\tau_g$$

This output is proportional to the power received from the source by the correlator in bandwidth  $\Delta\nu$ , and can thus be expressed in terms of the radio brightness  $I(\mathbf{s})$ , in the direction  $\mathbf{s}$ , at frequency  $\nu$ , and under a solid angle  $d\Omega$ :

$$r = \Delta\nu \int_S A(\mathbf{s}) I(\mathbf{s}) \cos \frac{2\pi\nu\mathbf{b}\mathbf{s}}{c} d\Omega, \quad (2.4)$$

where  $A(\mathbf{s})$  is the effective collecting area in the direction  $\mathbf{s}$ , assumed to be the same for both antennas.

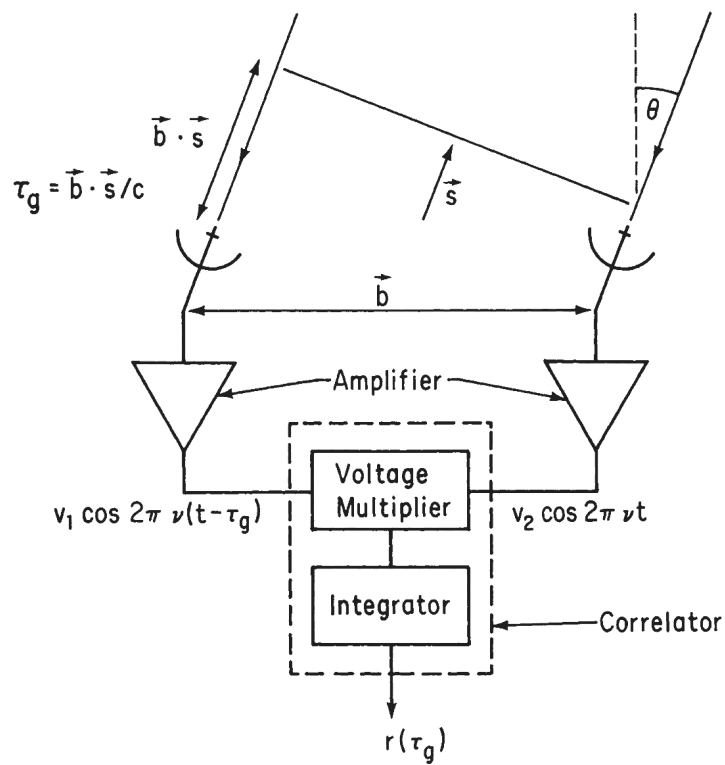


FIGURE 2.3— Schematic diagram of a two-antenna interferometer. The wavefront of a source reaches first the antenna on the right, and later the one on the left introducing a delay. The outputs of each amplifier and correlator are shown. Image taken from Thompson (1999).

When an extended source is observed with a radio interferometer, waves coming from one part of the source arrive at each antenna after having traveled a different distance than waves emitted at another part. Both signals arrive thus with a phase difference  $\Delta\phi$ , which corresponds to the Fourier transform of the physical sky separation (Burke & Graham-Smith 2002). It is usual to specify a direction  $s_0$  in the sky as the phase tracking center, on which the synthesized field of view of the interferometer is to be centered. All the nearby points on the sky are then described by a vector  $\sigma$  perpendicular to  $s_0$ , so that  $s = s_0 + \sigma$ .

Michelson (1890) introduced the term *visibility* to quantify the relative amplitude of the optical fringes observed in his interferometer. In radioastronomy the term *visibility* is used as a measure of the coherence of the electric field radiated from the source, which depends to some extent on the characteristics of the interferometer, and is defined as:

$$V = |V| e^{i\phi_V} = \int_S \mathcal{A}(\sigma) I(\sigma) e^{-2\pi i \mathbf{v} \cdot \sigma / c} d\Omega, \quad (2.5)$$

where  $\mathcal{A}(\sigma) = A(\sigma)/A_0$  is the normalized antenna reception pattern and  $A_0$  is the response at the beam center.

Separating the real and imaginary parts of the visibility and introducing them in Eq. 2.4 yields:

$$r = A_0 \Delta v |V| \cos\left(\frac{2\pi \mathbf{v} \cdot s_0}{c} - \phi_V\right). \quad (2.6)$$

The interferometer then measures the amplitude and phase of the fringe pattern (Eq. 2.6), from which the amplitude and phase of the visibility  $V$  can be derived after appropriate calibration. In the calibration process the errors owing to instrumental and environmental effects (e.g., weather, array geometry, ionosphere) are removed from the measured data (see Sect. 2.2.2). Finally, after the measurements are properly calibrated, the brightness distribution of the source can be obtained from the visibility data by applying an inverse Fourier transformation in a process called imaging (see detailed steps in Sect. 2.2.3).

### 2.2.2 Calibration

The visibilities measured by the interferometer are affected by instrumental and environmental effects that are expressed as antenna gains. The antenna gains are complex numbers that depend on frequency and time, and have amplitude terms and phase terms. The observed visibilities ( $\hat{V}_{i,j}$ ) are then the product of

the true visibilities ( $V_{i,j}$ ) and the antenna complex gains  $g_{i,j}$ :

$$\hat{V}_{i,j}(\nu, t) = g_i(\nu, t)g_j^*(\nu, t)V_{i,j}(\nu, t) \quad (2.7)$$

where  $i, j$  are antenna numbers,  $\nu$  is the frequency, and  $t$  is the time. The aim of the calibration process is then to calculate the antenna gains so that the true input visibilities can be estimated. The amplitude and phase terms of the antenna gains are calculated, respectively, in the amplitude and the phase calibration steps. The software package AIPS<sup>3</sup> can be used to edit and calibrate radio interferometric data. This software is structured into tasks, and in each task several parameters can be set. The basic policy of AIPS is to leave the original visibilities intact during the calibration process. This is achieved by creating calibration tables that contain the antenna gains (see Fig. 2.4). Before starting the calibration, the data must be carefully checked for any bad antennas, bad scans, or points with anomalous values in intensity or phase. The task UVPLT is used to examine the data, while with UVFLG the bad data are flagged and a FG table containing all the flags is created. Once the data have been examined and flagged, the calibration process can begin. The calibration consists of four main steps: amplitude calibration, phase calibration, bandpass calibration, and data averaging.

#### *Amplitude calibration*

In the amplitude or flux calibration the amplitudes of the visibility data are corrected for instrumental effects such as losses in the digitalization process of the signal, the system temperature of the receivers (i.e., noise temperature that includes the Earth's atmosphere), and the antenna gains of the telescopes (i.e., variations of the response of the antennas with time and frequency). To apply amplitude calibration, an astronomical source (the so-called *flux calibrator*) near to the target in the sky, with high flux, and compact, must be observed either at the beginning or at the end of the observations. The flux calibrator is calibrated using the task CALIB, which gives the conversion factor between the raw observed flux of the calibrator and its absolute flux by using a default point model. The flux density of secondary calibrators (e.g., phase calibrator) are determined from the primary flux calibrator (task GETJY), and the solutions are interpolated for all the sources (task CLCAL) and stored as a calibration (CL) table.

---

<sup>3</sup>The Astronomical Image Processing System of the National Radio Astronomy Observatory (NRAO).

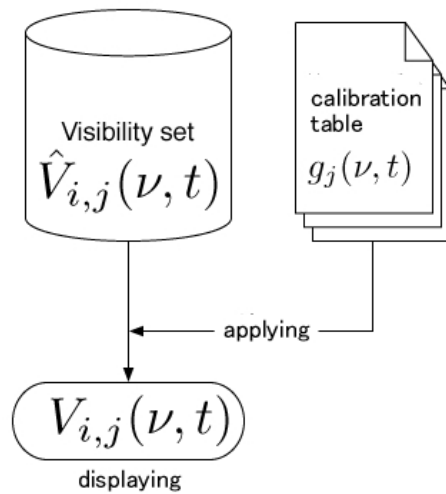


FIGURE 2.4— Treatment of the visibility the data by the software AIPS. The raw visibility set  $\hat{V}_{i,j}(\nu, t)$  remains untouched during the calibration process, but different calibration tables containing the antenna gains are created in each step of the calibration. The calibration tables are applied to the observed visibility data to obtain the true visibilities  $V_{i,j}(\nu, t)$ .

### *Phase calibration*

The phases of the measured visibilities are affected by instrumental offsets and slopes between and within the different frequency channel bands. In AIPS these channel bands are called intermediate frequencies (IFs), since they are the result of a technical down-frequency mixing. The phase offsets are due to the ionosphere of the Earth, the electronics of each antenna, and the structure of the target source. To calibrate the phase, a bright and compact phase calibrator a few degrees away from the target source is needed. The phase calibrator and the target are observed in phase-referencing mode, shifting between target and phase calibrator throughout the observation.

The fringe fitting technique is an operation that calibrates the visibility phases by correcting them from delay residuals, which are the delays (i.e., variations of the phase with frequency) remaining after the correlation process, and from time derivatives of the delay residuals (i.e., rate). These delays are caused by geometrical offsets due to the different positions and clocks of the antennas and the propagation through the Earth's atmosphere, which cannot be perfectly tracked at the correlator. If visibility phases are not constant in time and frequency, a loss of coherence and decrease of the visibility amplitudes occurs. To avoid this, we solve for the delay and rate running the task FRING

to the calibrators and applying the solution to all the sources. These solutions are stored as a second CL table, which contains also the amplitude solutions previously obtained, using the task CLCAL.

The phases on the target source can still vary rapidly with time after fringe fitting (e.g., due to an inadequate model of the source structure during the fringe fitting). These phase fluctuations can be reduced by looping through cycles of imaging and deconvolution (see Sect. 2.2.3) combined with phase self-calibration. The phase self-calibration technique (e.g., Cornwell 1995; Walker 1995; Cornwell & Fomalont 1999) minimizes the difference between the observed phases and the model phases based on a trial image, or the so-called ‘closure phase’. The closure phase is formed by summing the observed phases around a triangle of baselines. Since the phase errors associated with the individual antennas cancel completely (Pearson & Readhead 1984), the observed closure phase is unaffected by the phase errors of any of the antennas. Using four antennas, it is also possible to form ratios of the visibility amplitudes (called ‘closure amplitudes’) that are independent of the antenna gain factors. The self-calibration method calculates then the residuals that are the difference between the observed visibilities and the model visibilities (i.e., the visibilities without gain errors) and minimizes them by changing the amplitude and phase. This is done iteratively using the tasks CALIB and IMAGR (see Sect. 2.2.3). When the minimization converges, the solution of the self-calibration can be used to obtain a better recovery of the source structure. It should be noted that self-calibration is only done when the target source is sufficiently strong (i.e., has sufficient signal-to-noise ratio in the self-calibration time interval, which must be shorter than that used for the fringe fit), and if absolute positional information is not needed (since the absolute position is lost in the process of self-calibration).

#### *Bandpass calibration*

Visibilities depend on the frequency properties of the instrument. To correct for the channel to channel behavior response of the instrument, the amplitude and phase variations across the bands must be calibrated using a bandpass calibrator and the task BPASS. The result of bandpass calibration is shown in Figs. 2.5-2.6, where the visibility amplitudes and phases are plotted against frequency in the so-called *cross power spectra*. The bandpass solutions are stored as a BP calibration table.

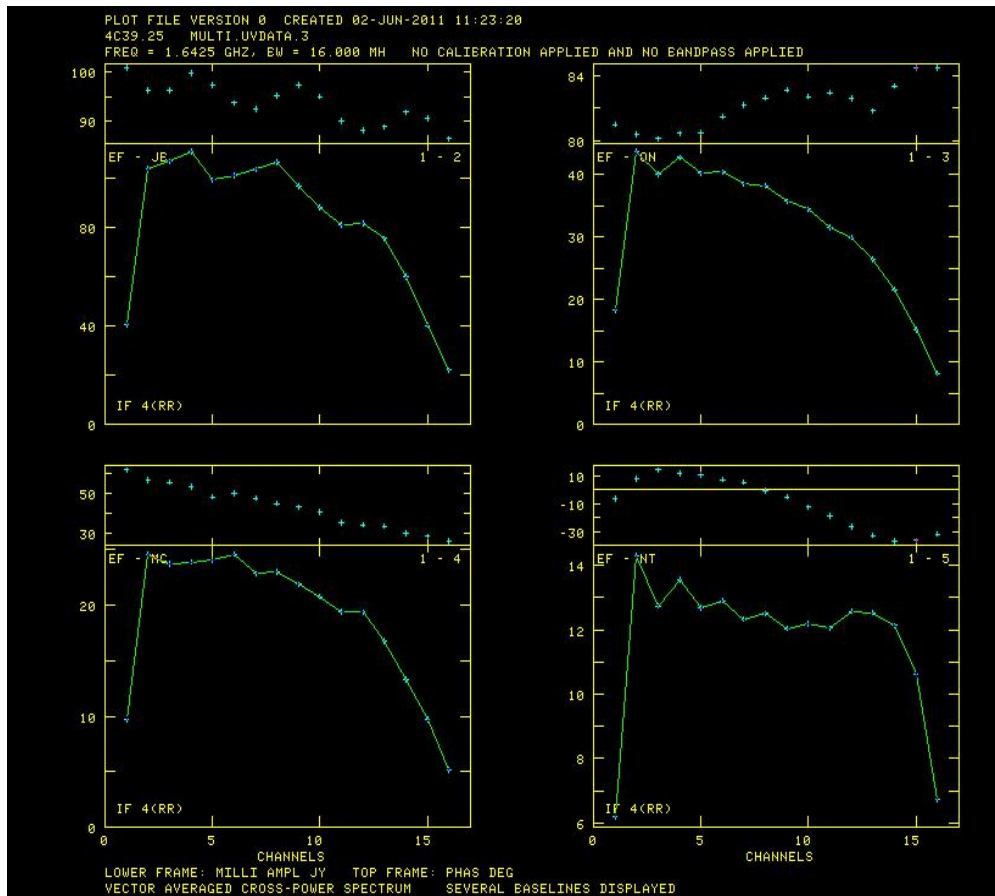


FIGURE 2.5— Cross power spectra before calibration of four different baselines for the flux calibrator 4C+39.25. The bottom and top plots of each panel correspond to the visibility amplitude and phase, respectively, as a function of frequency. Spectra are not flat, but amplitudes decrease at the edges of the bandpass and phases show slopes and variations against frequencies caused by the delay residuals.

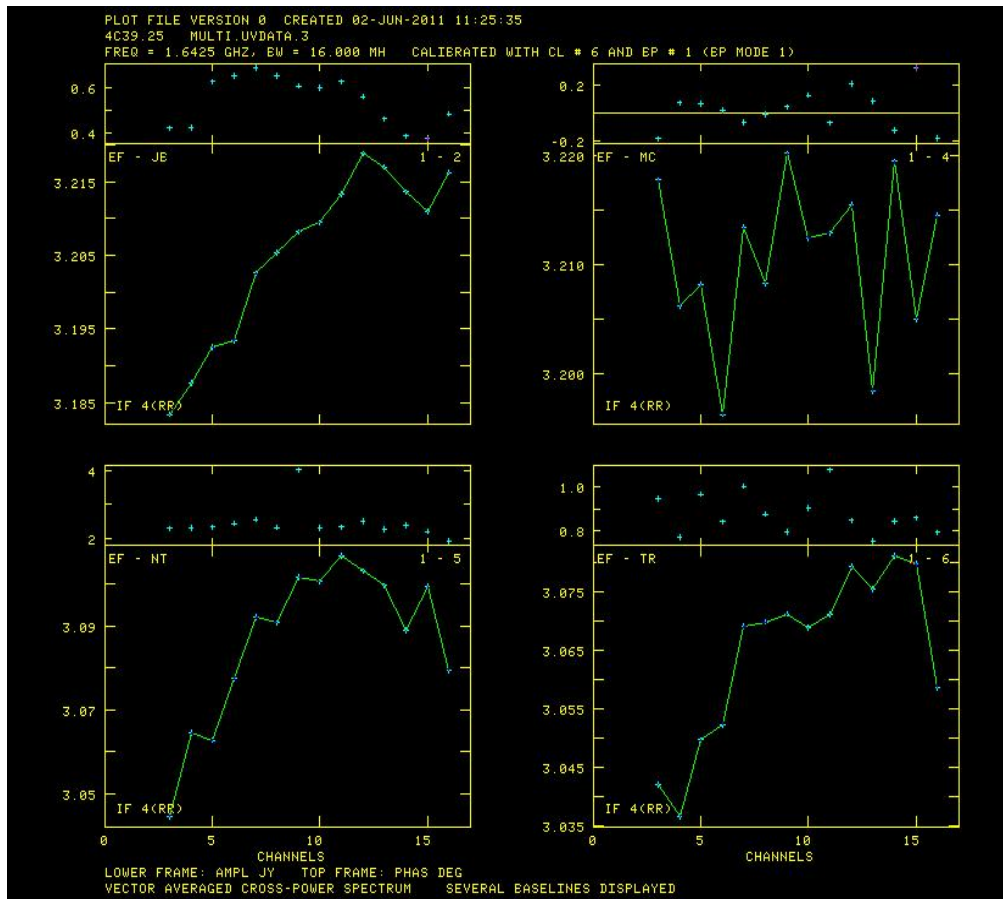


FIGURE 2.6— Cross power spectra of the four different baselines of the previous figure after calibration. The bottom and top plots of each panel correspond to the visibility amplitude and phase, respectively, as a function of frequency. After applying fringe fitting and bandpass calibration, the phases become almost flat (variations of a few degrees) and the amplitudes are nearly constant.



### Data averaging

Once amplitude, phase, and bandpass have been calibrated and all the instrumental effects corrected, single-source files can be created by splitting the multi-source data into each source with the task `SPLIT`. This task applies the calibration tables (CL and BP) obtained in the previous steps to the observed visibilities and allows also the averaging of data in time and frequency, reducing the number of channels and IFs so that the volume of data decreases and the signal-to-noise ratio (S/N) increases.

### 2.2.3 Synthesis imaging

According to the van Cittert-Zernike theorem, the brightness distribution  $I$  of a source is related to the complex visibility  $V$  via a two-dimensional Fourier transform:

$$I_{\nu}(l, m) = \int \int V_{\nu}(u, v) e^{2\pi i(ul+vm)} dudv, \quad (2.8)$$

where the  $(l, m)$  coordinates describe the source brightness distribution projected on the sky (see Fig. 2.7), while the  $(u, v)$  coordinate system expresses the distribution of the interferometer baseline coverage (the so-called *uv-plane*). In other words, radio interferometers do not measure the intensity on the sky but its Fourier transform in the *uv-plane*. Each data point sample in the *uv-plane* is called a *visibility*. To reconstruct the brightness distribution of the source we need a good sampling of the *uv-plane* (i.e., as many visibilities as possible), which we obtain by adding antennas to the interferometer to increase the number of baselines.

Performing the inverse Fourier transform of the visibility plane  $V(u, v)$  to obtain the intensity distribution  $I(l, m)$  is not so straight forward. Because the Fourier *uv-plane* is not fully sampled, the interferometer's response pattern (equivalent to a telescope's response pattern known as point spread function, PSF) leaves spurious signals in the image. To remove these effects, a sampling function  $S(u, v)$  that expresses the sparse *uv-coverage* and the beam pattern of the interferometer must be taken into account and introduced as a multiplicative factor, obtaining as a result a *dirty image*,  $I_D$  of the source:

$$I_{\nu}^D(l, m) = \int \int V_{\nu}(u, v) S(u, v) e^{2\pi i(ul+vm)} dudv \quad (2.9)$$

The Fourier inversion, thus, leads no longer to the true brightness distribution of the source but to the brightness distribution convolved with the

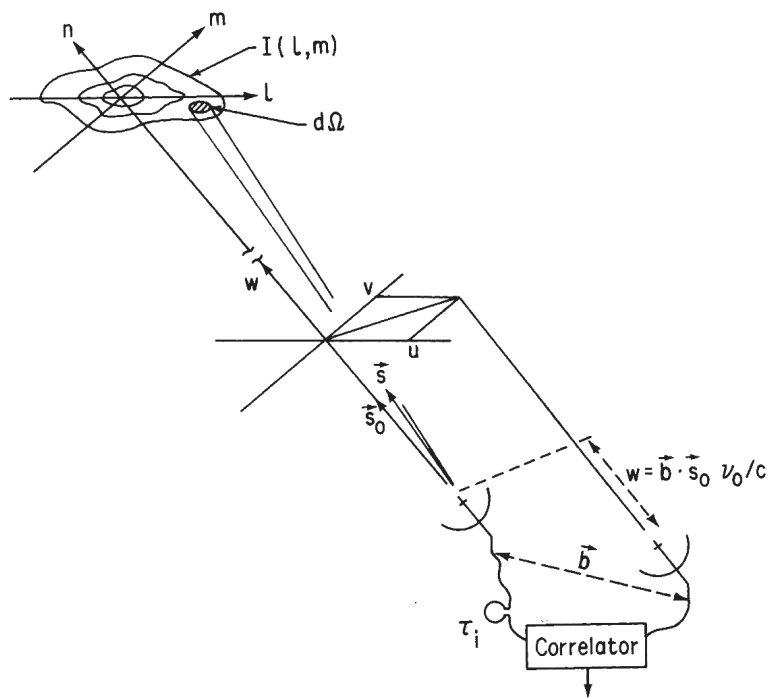


FIGURE 2.7— Coordinates used in the sampling of the brightness distribution of a source by a two-antenna interferometer.  $I(l, m)$  describes the source brightness distribution projected on the sky. The distribution of the baseline coverage of the interferometer is described by the  $uv$ -plane  $(u, v)$ . Image taken from Thompson (1999).

synthesized beam, or *dirty beam*,  $B(l, m)$ , of the interferometer:

$$I^D(l, m) = B(l, m) * I(l, m), \quad (2.10)$$

where

$$B(l, m) = \int \int S(u, v) e^{2\pi i(ul+vm)} dudv. \quad (2.11)$$

To recover the true sky brightness distribution,  $I(l, m)$ , we need to deconvolve the dirty beam from the calibrated visibility data. There are two deconvolution methods widely used nowadays: the Maximum Entropy Method (MEM; e.g., Frieden 1972) and the CLEAN (e.g., Högbom 1974). In this thesis we use the CLEAN algorithm, implemented in the AIPS task IMAGR. This algorithm is an iterative process that starts by identifying the location and strength of the strongest peak of emission in the dirty image. The algorithm then subtracts this point source and a specified fraction of the dirty beam and stores it as a *clean component* (CC), leaving a residual map of the dirty image. A second iteration starts, in which the strongest peak of emission in the residual map is identified, subtracted, and stored as a further CC. This cleaning process is repeated iteratively until the residual map reaches the noise level of the observations and is smooth and featureless. Then the temporary image that contains all the CCs is convolved with an idealized interferometer beam that has the Full Width at Half Maximum (FWHM) of the dirty beam, creating a *clean map*. The final image containing the true brightness distribution of the source results from the addition of the clean map to the residual map. A point source model can be used with the CLEAN algorithm in the IMAGR task to improve the recovery of the source structure (e.g., self-calibration; see Sect. 2.2.2).

#### 2.2.4 Model fitting

After the true brightness distribution of the source has been obtained, the source radio emission must be analyzed and interpreted physically. This can be done with the *model fitting* technique, which models the radio emission in the image plane or in the uv-plane of calibrated visibility data by fitting a two-dimensional Gaussian distribution (either circular or elliptical) to the whole or part (components) of the radio structure. The parameters of a each fitted Gaussian component that are obtained through this process are: the total flux density, the peak flux density, the post-fit root-mean-square (rms) noise, the size, and the position angle. Therefore, the radio emission of the target source can be fitted by a number of Gaussian components and characterized by the

parameters obtained from the fit.

### 2.2.5 Interferometer arrays

The rms of a radio telescope scales inversely with its collecting area. Therefore, the use of an array of several radio antennas not only increases the number of visibilities or baselines but also the sensitivity of the interferometer. Another way of covering the uv-plane effectively is using the rotation of the Earth to rotate the array relative to the sky. This technique, called 'Earth-rotation synthesis' (Ryle 1962), causes the points in the uv-plane that each baseline points at to change with time, increasing thus the coverage of the uv-plane. There are several interferometers that use this technique, e.g., the VLA (Very Large Array) or the GMRT (Giant Meterwave Radio Telescope), whose antennas are physically connected by cables or wires. In this thesis we use data from the GMRT, which is an array of 30 parabolic antennas of 45m-diameter each, located in Pune (India). The GMRT has a Y-shape configuration, with the longest baseline being of 25 km, yielding a maximum achievable resolution of 2 arcsec at the highest frequency (1420 MHz). It covers a range of declinations from  $-53$  to  $+90$  degrees and operates in 6 frequency bands, ranging from 50 MHz to 1.4 GHz.

#### *Very Long Baseline Interferometry (VLBI)*

The VLBI is one of the most powerful techniques for achieving high-resolution imaging of distant radio sources. It employs multiple radio telescopes scattered around the Earth that simultaneously record data from the same radio source. The data are stored on magnetic tapes or hard disks and sent to a central processing site where they are correlated. Recently, the use of optical fibers is converting VLBI arrays into connected interferometers (e.g., e-MERLIN). In this thesis we use observations made with the European VLBI Network (EVN), which is an interferometric array of radio telescopes spread throughout Europe and beyond (Fig. 2.8). At 18 cm (or 1.6 GHz) the longest baseline is of  $\sim 8500$  km (including antennas in China, South Africa, and Puerto Rico), which gives an achievable angular resolution of 5 milliarcseconds and a sensitivity of 7.5 mJy (with an integration time on source of 3.5 hours). The EVN operates from 90 cm to 3 mm and can be used together with other interferometers (i.e., the VLBA and the VLA) to achieve sub-milliarcsecond resolutions (the so-called Global VLBI Array).

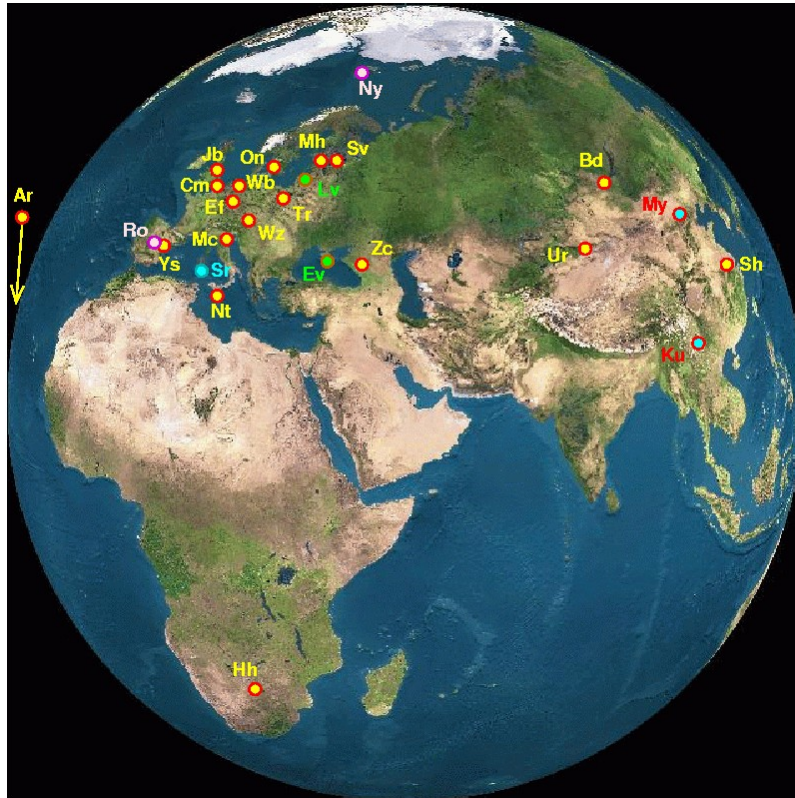


FIGURE 2.8— Location of the antennas that form the European VLBI Network (EVN). The colors indicate the operational status of the antennas: operational stations (yellow/red), new stations not yet fully participating (blue), non-EVN stations that sometimes participate (purple), and non-EVN stations with whom initial EVN-tests have been carried out (green/brown). Figure and caption taken from the EVN website (<http://www.evlbi.org/>).



# 3

---

## X-shaped radio galaxies

*The search for observational evidence for supermassive binary black holes starts with the radio-optical study of X-shaped radio galaxies. The peculiar jet morphology of these sources has long been suggested to be the result of a galactic merger and the subsequent black hole coalescence. The imprint of such a merger should be reflected not only on the jet morphology of the merged galaxy but also on its black hole mass and starburst history. This chapter shows that the sample of X-shaped radio galaxies studied has statistically higher black hole masses and older episodes of star formation than a control sample of radio-loud AGN with similar redshifts and luminosities. The data also reveal enhanced star formation in the X-shaped sample prior to the formation of the jets and at timescales expected in galactic mergers. The results obtained are discussed in the framework of the merger scenario.*

### 3.1 Introduction

X-shaped (or ‘winged’) radio galaxies are a class of extragalactic radio sources with two low-surface-brightness radio lobes (the ‘wings’) oriented at an angle to the active, or high-surface-brightness, lobes (Leahy & Williams 1984). Both sets of lobes often pass symmetrically through the center of the host galaxy, giving the galaxy an X-shaped morphology as seen on radio maps (see Fig. 3.1). Several authors have attempted to explain the unusual structure in X-shaped sources. It was suggested that the X-shaped morphology may result from a precession of the jet caused by misalignment between the angular momenta of the central supermassive black hole (SMBH) and the gas accreted onto it (Rees 1978). Subsequently, four different scenarios were proposed for the formation of this peculiar radio morphology: 1) backflow from the active lobes into the wings (Leahy & Williams 1984; Capetti et al. 2002); 2) slow conical precession of the jet axis (Parma et al. 1985; Mack et al. 1994);

3) reorientation of the jet axis during which flow continues; and 4) reorientation of the jet axis, but the jet turned off or at greatly reduced power during the change of direction (Dennett-Thorpe et al. 2002). The reorientation of a black hole spin axis owing to a minor merger may lead to a sudden flip in the direction of the associated jet (Merritt & Ekers 2002). In this case, X-shaped galaxies would be the sites of spin-flips associated with recent coalescences of pairs of supermassive black holes (Gopal-Krishna et al. 2003; Gergely & Biermann 2009). The older wings would then represent relics of past radio jets, while the active lobes would reflect the activity that ensued after the black hole merger. Hence, synchrotron aging should lead to a steeper spectral index in the wings or low-surface brightness features than in the high-surface brightness active lobes. However, in some X-shaped sources, the wings have a similar or even flatter spectral index than the active lobes (Lal & Rao 2005). To explain this discrepancy, it was suggested that at least some of the X-shaped sources may contain coalescing binary SMBH systems with two pairs of jets associated with two unresolved AGN (Lal & Rao 2005). Alternative models, assuming a pre-merger state of the two black holes, employ non-ballistic precession (Gong 2008; Gong et al. 2011). Several studies have been carried out in the optical and X-ray band, with results in some cases favoring the hydrodynamic backflow model over the merger-induced rapid reorientation scenario (e.g., Hodges-Kluck et al. 2010a; Landt et al. 2010), and in other cases favoring the merger model as the best explanation for the observed winged morphology (Hodges-Kluck et al. 2010b). See Gopal-Krishna et al. (2010) for a more detailed review of the different scenarios proposed to explain the origin of X-shaped radio galaxies.

In all schemes in which X-shaped objects are the product of galactic mergers, the properties of the nuclear region will be affected by the past SMBH merger or the presence of a secondary SMBH. This should then be reflected by statistically higher masses of the central black holes in galaxies hosting the X-shaped radio morphology. If the X-shaped morphology is indeed caused by a profound event in the nuclear region, such as a merger of two SMBH, then it may also be reflected in the starburst history of the host galaxy (e.g., Blecha et al. 2011). Investigations of the black hole masses and starburst histories can therefore address the question of the physical nature of the X-shaped sources and their difference from the “canonical” radio galaxies, if representative samples of both radio types are studied and compared against each other.

In this chapter, we determine the black hole masses, luminosities, starburst



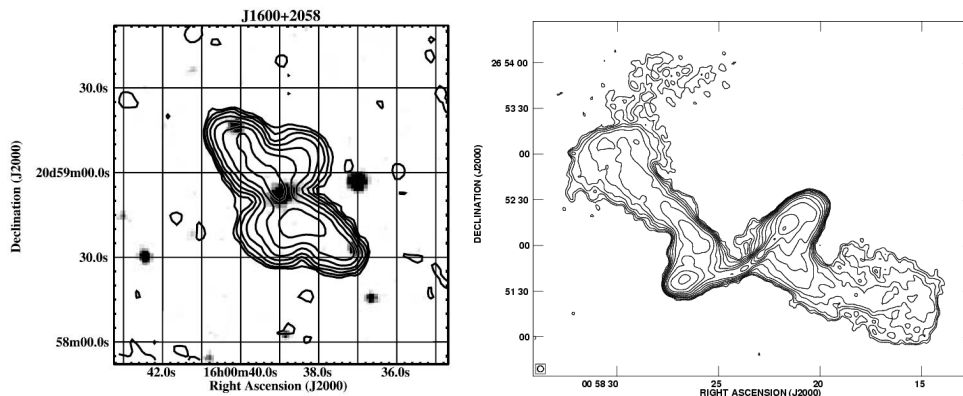


FIGURE 3.1— Two examples of X-shaped radio galaxies: J1600+2058 on the left panel (VLA FIRST 1.4 GHz contours overlaid on the optical image; Cheung 2007) and NGC 326 on the right panel (VLA 1.4 GHz in the A+C configuration; Murgia et al. 2001).

histories, and jet dynamic ages in a sample of X-shaped galaxies and compare them with a control sample of radio-loud active nuclei with similar redshifts and optical and radio luminosities.

### 3.2 The sample

The sample of AGN analyzed here is drawn from a list of known X-shaped sources and a list of 100 ‘winged’ and X-shaped radio source candidates (Cheung 2007) that were morphologically identified in the images from the VLA FIRST survey (Becker et al. 1995).

A subsample of 50 radio galaxies with bona fide X-shaped radio morphology was defined from the 100 candidate list (Cheung et al. 2009). Because this selection was based on visual inspection of the candidate objects and lacks quantifiable selection criteria, we refer to the original sample of Cheung (2007) for selecting appropriate candidates for our study. We select the X-shaped objects with optical spectra that show well-detected stellar absorption lines.

Of the 100 X-shaped candidates (Cheung 2007), 22 were found to have spectroscopic information in the Sloan Digital Sky Survey (SDSS) data release (DR6; Adelman-McCarthy et al. 2008), and optical spectra for additional 27 objects were obtained by Cheung et al. (2009) with the 9.2 m Hobby-Eberly Telescope (HET) at McDonald Observatory and the 6.5 m Multiple-Mirror Telescope (MMT) at Mt. Hopkins Observatory.

To increase the number of spectroscopically identified X-shaped radio galaxies, we observed 13 X-shaped sources included in the candidates list of

Cheung (2007).

The final sample comprises 38 X-shaped radio galaxies, namely: 12 of the 13 objects observed, 15 X-shaped radio sources with SDSS spectra, 5 of the 27 X-shaped objects with spectra presented in Cheung et al. (2009), and 6 of the previously known X-shaped radio sources: 3C192, 4C+32.25, 4C+48.29 and 1059+169 (Lal & Rao 2007), 3C223.1 (Lal & Rao 2005) and 4C+01.30 (Wang et al. 2003) with spectra also available in the SDSS.

In order to evaluate the results obtained for the X-shaped radio galaxies, we compile a control sample of 19 radio-loud sources from Marchesini et al. (2004) plus 6 Fanaroff-Riley type II (FR II) sources from de Vries et al. (2006), and 11 radio loud elliptical galaxies from González-Serrano & Carballo (2000) that have SDSS spectra, and cover the same ranges of redshift ( $z < 0.3$ ) and optical and radio luminosities as the objects in the target sample. The resulting common luminosity ranges for both samples are:  $\log \lambda L_{5100\text{\AA}} \in [43.0, 46.0]$  and  $\log \nu L_{1.4\text{GHz}} \in [39.0, 44.5]$ . The Kolmogorov-Smirnov (KS) test applied to the optical and radio luminosities of the X-shaped sample and the control sample gives a probability  $> 5\%$  that the two samples are drawn from the same parent distribution, which warrants making statistical comparisons between them.

### 3.2.1 Spectroscopic observations

The observed sample comprises 13 X-shaped radio galaxies retrieved from a list of 100 candidates (Cheung 2007). We selected objects with bright ( $m_R < 19$ ) optical counterparts for which no spectroscopic redshifts have been reported.

Optical spectroscopy observations of the sample were carried out on 20-23 March 2009 with the 2.1-meter telescope of the Observatorio Astronómico Nacional at San Pedro Mártir (OAN-SMP), Baja California, México. The Boller & Chivens spectrograph was tuned in the 4000 to 8000 Å range (grating 300 l/mm), with a resolution of 4 Å pix corresponding to 8 Å (FWHM). A 2''5 slit was used. To calibrate the spectral measurements, the spectrophotometric standard star Feige 34 was observed two times during every night of the observing run.

For each target source, two or three exposures were taken, with a typical exposure duration of 1800 s (see Table 3.1). The data reduction was carried out with the IRAF software following the standard procedures explained in Chapter 2. The spectra were bias-subtracted and corrected with dome flat-field frames. Cosmic rays were removed interactively from all images. Arc-

TABLE 3.1— Observation log

Name (1)	$m_R$ (2)	Obs. date (3)	Exp. time (4)
J0813+4347	16.1	2009 Mar 20	$2 \times 1800$
		2009 Mar 22	$2 \times 1800$
J0838+3253	16.9	2009 Mar 21	$2 \times 1800$
		2009 Mar 23	$2 \times 1800$
J0924+4233	17.8	2009 Mar 23	$2 \times 1800$
J1008+0030	15.8	2009 Mar 20	$2 \times 1800$
		2009 Mar 22	$2 \times 1800$
J1055-0707	17.6	2009 Mar 20	$3 \times 1800$
J1200+6105	18.3	2009 Mar 23	$2 \times 1800$
J1201-0703	16.4	2009 Mar 22	$2 \times 1800$
		2009 Mar 23	$2 \times 1800$
J1258+3237 <sup>a</sup>	17.0	2009 Mar 20	$2 \times 1800$
J1351+5559	15.1	2009 Mar 22	$2 \times 1800$
		2009 Mar 23	$1 \times 1800$
J1408+0225	18.4	2009 Mar 22	$3 \times 1800$
J1459+2903	16.5	2009 Mar 21	$2 \times 1800$
J1537+2648	18.3	2009 Mar 22	$2 \times 1800$
		2009 Mar 23	$2 \times 1800$
J1606+0000	15.0	2009 Mar 21	$2 \times 1800$

**Column designation:** (1) – object name based on J2000.0 coordinates; (2) – apparent magnitude R, taken from Cheung (2007); (3) observation date; (4) exposure time, in seconds. **Notes:** *a* – Optical misidentification in Cheung (2007). The spectrum of this object corresponds to a K-type star and not an X-shaped radio galaxy.

lamp (CuHeNeAr) exposures were used for the wavelength calibration. A spline function was fitted to determine de dispersion function (wavelength to pixel correspondence). Sky emission lines located at known wavelengths were removed during the calibration in wavelength.

### 3.3 Data analysis

The optical spectra of the objects in both samples have been used to measure properties of  $H\beta$  and [OIII] emission lines (see Appendix A, page 161) and a number of stellar absorption lines. These measurements were applied to

making kinematic mass estimates of the central black holes. The absorption line fits were also used to recover starburst histories in the host galaxies and to estimate the epochs of the most recent starburst. Angular sizes of active lobes and inactive wings (in X-shaped objects) were measured to determine the dynamic ages of the radio emission in the X-shaped objects and in the objects from the control sample.

### 3.3.1 Stellar absorption lines

The SDSS spectra collected for the objects in both samples contain several significant stellar absorption features (such as CaH+K  $\lambda\lambda 3969, 3934\text{\AA}$ , the MgIb  $\lambda\lambda 5167, 5173, 5184\text{\AA}$  triplet, and the CaII  $\lambda\lambda 8498, 8542, 8662\text{\AA}$  triplet, etc.) that can be matched against a combination of different synthetic stellar template spectra, yielding an estimate of the stellar velocity dispersion.

We use the stellar population synthesis code STARLIGHT (Asari et al. 2007; Cid Fernandes et al. 2004b, 2005, 2007; Mateus et al. 2006) to model the observed spectrum  $O_\lambda$ . The best fit is obtained using a linear combination of simple stellar populations (SSP) from the stellar library of Bruzual & Charlot (2003) and a power-law component representing the AGN continuum emission. In our fitting, we apply the standard stellar library consisting of 150 SSPs, and complement the fit with up to six power-law components given by  $F(\lambda) = 10^{20}(\lambda/4020)^\beta$ , where  $\beta = -0.5, -1, -1.5, -2, -2.5, -3$ . Each SSP spans across six metallicities,  $Z = 0.005, 0.02, 0.2, 0.4, 1, \text{ and } 2.5 Z_\odot$ , with 25 different ages between 1 Myr and 18 Gyr. The Galactic extinction caused by the foreground dust screen is modeled and parametrized by the V-band extinction,  $A_V$ . We adopt the extinction law of Cardelli et al. (1989).

The resulting model spectrum  $M_\lambda$  (combining an SSP and a power-law continuum components) is

$$M_\lambda(x, M_{\lambda_0}, A_V, v_*, \sigma_*) = M_{\lambda_0} \left[ \sum_{j=1}^{N_*} x_j b_{j,\lambda} r_\lambda \right] \otimes G(v_*, \sigma_*), \quad (3.1)$$

where  $b_{j,\lambda} \equiv L_\lambda^{SSP}(t_j, Z_j) / L_{\lambda_0}^{SSP}(t_j, Z_j)$  is the  $j^{\text{th}}$  template normalized at  $\lambda_0$ ,  $x$  is the population vector,  $M_{\lambda_0}$  is the synthetic flux at the normalization wavelength,  $r_\lambda \equiv 10^{-0.4(A_\lambda - A_{\lambda_0})}$  is the reddening term, and  $G(v_*, \sigma_*)$  is the line-of-sight stellar velocity distribution, modeled as a Gaussian feature centered at velocity

$v_*$  and broadened by  $\sigma_*$ . The best fit is reached by minimizing  $\chi^2$ ,

$$\chi^2(x, M_{\lambda_0}, A_V, v_*, \sigma_*) = \sum_{\lambda=1}^{N_\lambda} [(O_\lambda - M_\lambda)w_\lambda]^2, \quad (3.2)$$

where the weighted spectrum  $w_\lambda$  is defined as the inverse of the noise in the observed spectra. A more detailed description of the STARLIGHT code and its applications can be found in Asari et al. (2007); Cid Fernandes et al. (2004b, 2005, 2007); Mateus et al. (2006); and León-Tavares et al. (2010).

The fit for the X-shaped source J1424+2637 is shown as an example in Fig. 3.2. The observed spectrum is shown in black, the host galaxy model in red, and the AGN power-law continuum in blue. The residual spectrum obtained after the subtraction of the stellar light and the continuum is shown in green. An atlas of the fits for all the sources analyzed can be found in Appendix B, page 167.

In order to assess the fidelity of the STARLIGHT fit, we introduce a quality factor  $Q$  that combines the reduced  $\chi^2$  parameter of the modeled spectra, the velocity dispersion,  $\sigma_*$ , and its error,  $\delta_*$ :  $Q = (\chi^2 \delta_* / \sigma_*)^{-1/2}$ . Fits with  $Q > 10$  can be considered reliable (these are the fits with reduced  $\chi^2$  close to unity and fractional errors of the velocity dispersion of  $\leq 3\%$ ).

For some objects with a strong continuum, STARLIGHT can fail to synthesize the spectrum of the host galaxy, since the flux of the lines of the host galaxy is much fainter than the AGN continuum flux. In these cases, we apply the empirical correlation  $\sigma_* = \text{FWHM}[\text{OIII}]/2.35$  obtained by Nelson (2000) assuming that  $\sigma_* \approx \sigma_{\text{gas}}$ . The term  $\text{FWHM}[\text{OIII}]$  describes the full-width-at-half-maximum of the narrow component of the  $[\text{OIII}]$  emission line and is determined from a fit to the narrow lines of the  $[\text{OIII}]\lambda\lambda 4959, 5007\text{\AA}$  doublet in the residual spectrum.

### 3.3.2 Starburst histories

The STARLIGHT model for the observed spectra also yields the light fraction  $x_j$ , mass fraction  $M_{ij}$ , age  $\tau_j$ , and metallicity  $Z_j$ , of the stellar populations used in the fit. We use these parameters to derive starburst histories and estimate the epochs of the most recent starbursts in the studied galaxies. We apply Gaussian smoothing to the individual starburst events (see Fig. 3.3 for an example) and determine the epoch of the most recent starburst episode. Plots of the fits for all sources can be found in Appendix B, page 167.

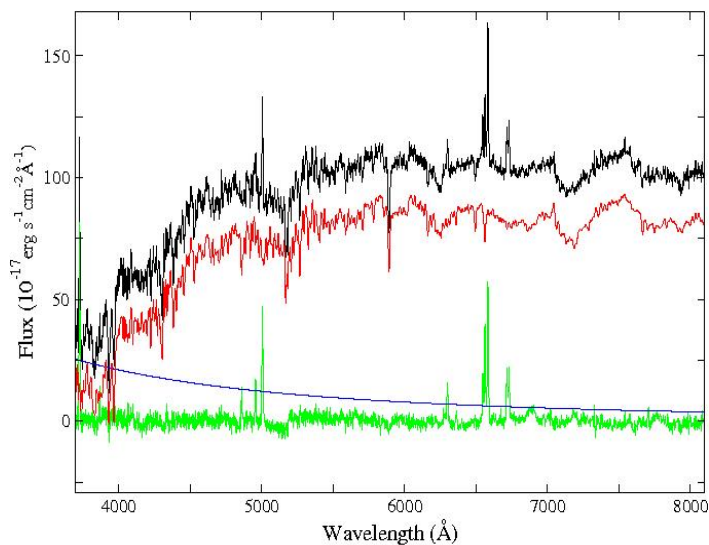


FIGURE 3.2— STARLIGHT fit for the spectrum of the X-shaped source J1424+2637. The plot shows the observed spectrum (top black line), the modeled spectrum (second red line, displaced from observed spectrum), the AGN continuum (blue line), and the residual spectrum (bottom green line). Note that the residual spectrum contains narrow and (in some objects) broad emission lines. Properties of these lines are measured separately (see Appendix A, page 161).

### 3.3.3 Optical continuum

Most of the X-shaped radio sources and some objects from the control sample are type II AGN (weakly beamed radio sources), for which STARLIGHT cannot provide reliable estimates of the AGN continuum flux. We estimate the rest-frame continuum flux at 5100 Å from the SDSS photometry, with the relation (Wu & Liu 2004)

$$f_{5100\text{\AA}}^{\circ}[\text{Jy}] = 3631 \times 10^{-0.4g} \left[ \frac{4700}{5100(1+z)} \right]^{-(g-r)/2.5 \log(6231/4770)}, \quad (3.3)$$

where  $z$  is the redshift and the  $g$  and  $r$  fiber magnitudes are obtained from the SDSS and corrected for the Galactic extinction  $A_V$  (taken from Schlegel et al. 1998). It should be noted that the flux obtained with this method also contains a contribution from the host galaxy, but this does not introduce a strong bias in our estimates.

To assess the spectral classification of the X-shaped and control host galaxies, we measure the Ca II break of their absorption optical spectrum. This break is typically seen in the spectrum of elliptical galaxies and is described

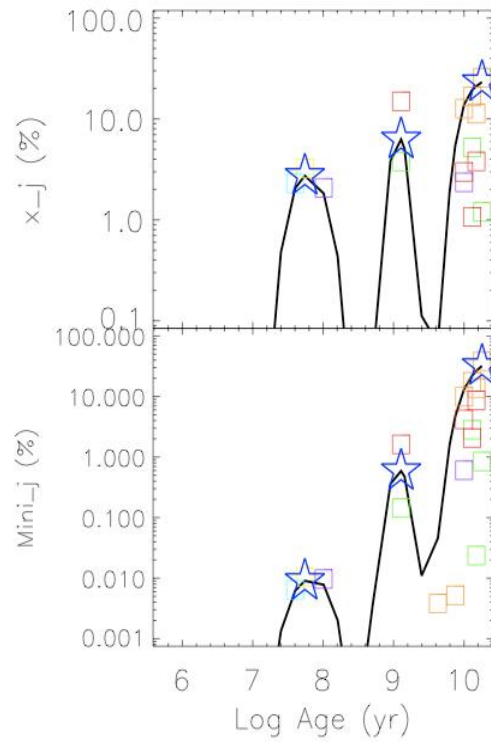


FIGURE 3.3— STARLIGHT fits for J1327–0203: the light fraction ( $x_j$ ) vs. age (top) and mass fraction  $Mini_j$  vs. age (bottom) for each stellar population used. The squares correspond to stellar populations with different metallicities: blue  $0.005 Z_{\odot}$ , purple  $0.020 Z_{\odot}$ , green  $0.200 Z_{\odot}$ , yellow  $0.400 Z_{\odot}$ , orange  $1.000 Z_{\odot}$  and red  $2.500 Z_{\odot}$ . The solid curve represents Gaussian smoothing applied to the mass and light fraction distributions of individual starbursts. The stars indicate the identified resulting starburst episodes.

by a factor  $C_{\text{CaII}} = (f_+ - f_-)/f_+$ , where  $f_-$  and  $f_+$  are the fluxes in the rest frame wavelength regions 3750–3950 Å and 4050–4250 Å, respectively (Landt et al. 2002). The Ca II break was used as an additional criterion to separate blazars from radio galaxies. Stocke et al. (1991) adopted a maximum value of  $C_{\text{CaII}} = 0.25$  for BL Lacs to ensure the presence of a substantial non-thermal jet continuum in addition to the thermal spectrum of the elliptical host galaxy. This limit was later increased to  $C_{\text{CaII}} < 0.4$  by other authors (Marcha et al. 1996; Plotkin et al. 2008).

Landt et al. (2010) provide the Ca II break values of 17 of the X-shaped sources studied here. For the rest of the X-shaped sources and control objects, we measure the  $C_{\text{CaII}}$  factor of the rest-frame optical spectra using the IRAF task `guiapps.spectool`.

### 3.3.4 Black hole masses

The measured stellar velocity dispersion,  $\sigma_*$ , can be connected with the mass,  $M_{\text{BH}}$ , of the central black hole through an empirical relation (Gebhardt et al. 2000; Tremaine et al. 2002):

$$M_{\text{BH}} = 1.349 \times 10^8 M_{\odot} \left( \frac{\sigma_*}{200 \text{ km s}^{-1}} \right)^{4.02 \pm 0.32}. \quad (3.4)$$

This relation is valid under the assumption that the kinematics of the stars in the bulge of the host galaxy is dominated by the gravitational potential of the central SMBH (Ferrarese & Merritt 2000).

### 3.3.5 Dynamic age of radio lobes

The dynamic age,  $t_a$ , of the high-surface-brightness (active) radio lobes is obtained from their angular size,  $\theta_a$ , which is defined as the separation between the center of the radio source and the most distant contour in the FIRST image. The dynamic age is then given by  $\theta_a/v_a$ , where  $v_a$  is the lobe advance speed (we adopt the commonly assumed  $v_a \approx 0.1c$ ; *cf.*, Tingay et al. 1998). Assuming that the fueling of the low-surface-brightness lobes of the X-shaped sources had stopped after the high-surface-brightness lobes were activated, the dynamic age of the passive lobes  $t_p$  during their active stage can be estimated as

$$t_p = \frac{\theta_p - t_a v_p}{v_a}, \quad (3.5)$$



where  $\theta_p$  is the angular size of the low-surface brightness lobes and  $v_p$  is their expansion speed during the inactive stage. In the absence of an observational estimate for  $v_p$ , we use  $v_p = 0.01c$  in our calculation. It should be noted that reducing  $v_p$  further only has a small effect on the ages derived for the passive lobes. The total dynamic age of the X-shaped sources can then be obtained from the sum of the dynamic ages of the active and passive lobes.

### 3.4 Results

#### 3.4.1 Spectroscopic observations

Since most of the observed spectra of the 13 targeted sources do not show strong emission lines, we determine the redshift from the CaII H  $\lambda 3968\text{\AA}$  and K  $\lambda 3934\text{\AA}$ , G band  $\lambda 4302\text{\AA}$ , MgIb  $\lambda 5175\text{\AA}$ , and NaI d  $\lambda 5896\text{\AA}$  absorption lines.

The observations provide the first spectroscopic identifications and redshifts for 8 X-shaped radio galaxies (J1008+0030, J1055–0707, J1200+6105, J1201–0703, J1351+5559, J1408+0225, J1459+2903, and J1537+2648). New spectra are obtained for 4 X-shaped sources (J0813+4347, J0838+3253, and J0924+4233, spectroscopically identified in the SDSS Adelman-McCarthy et al. 2007; and for J1606+0000, identified by Best et al. 1999). The difference between our redshifts and the ones obtained previously are  $\delta_z < 0.002$ . With the new identifications, the total number of X-shaped radio galaxies spectroscopically identified is increased to 60. The last object of our sample, J1258+3227, shows typical stellar lines of a K-type star (G band, H $\beta$ , Mg I, Fe I, and Na I absorption lines), indicating a likely misidentification (also suggested by Cheung et al. 2009). This object is excluded from further analysis. The optical spectrum of the 12 X-shaped radio galaxies and the optical misidentification are shown in Figs. 3.4 and 3.5, respectively.

In total, an X-shaped sample of 38 sources is considered for the statistical comparison with the control sample of 36 radio-loud sources. The combined results from fitting the optical spectra, black hole mass calculations, and age measurements for the radio lobes and most recent starbursts are presented in Tables 3.2–3.3. Tables 3.2 and 3.3 list (for the X-shaped objects and the control sample, respectively) the object name based on J2000.0 coordinates (Col. 1), other common catalog names (Col. 2), stellar velocity dispersion (Col. 3), black hole mass derived from  $\sigma_*$  (Col. 4), optical luminosity of the AGN (Col. 5) and of the host galaxy (Col. 6), radio luminosity (Col. 7), dynamic age

of the radio lobes (Col. 8), most recent starburst age (Col. 9), spectroscopic redshift (Col. 10), quality factor of the STARLIGHT fit (Col. 11), the value of Ca II break factor (Col. 12), and references for the control sources (Table 3.3, Col. 13). For the X-shaped sources, the total (active + passive lobe) age of the radio emission is given in brackets in Col. 8.

For the X-shaped objects J0813+4347, J0838+3253, and J0924+4233, the fit of both the SDSS spectra and the new observed spectra is performed. The values listed in Table 3.2 are those derived from the new observed spectra. These fits have higher  $Q$  than the one derived from the SDSS spectra, and are thus used for the statistical study.

The rest-frame continuum flux at 5100 Å for two X-shaped sources (J1055–0707 and J1201–0703) cannot be estimated due to their lack of SDSS photometry. These sources are excluded from the statistical study.

The control sample objects J1220+0203, J2351–0109, J1007+1248, J1252+5634, and J1114+4037 are quasars with strong power-law continuum in their spectra. Estimates of  $\sigma_*$  for these objects are obtained from the measured width of the [OIII] line as described in Sect. 3.1. The STARLIGHT results for two X-shaped sources (J0941–0143 and J1348+4411) have provided unreliable  $\sigma_*$  fits (with values of  $\sigma_*$  below the instrumental resolution of 70 km/s in the SDSS spectra, and quality factors  $Q < 10$ ) and are excluded from further analysis.

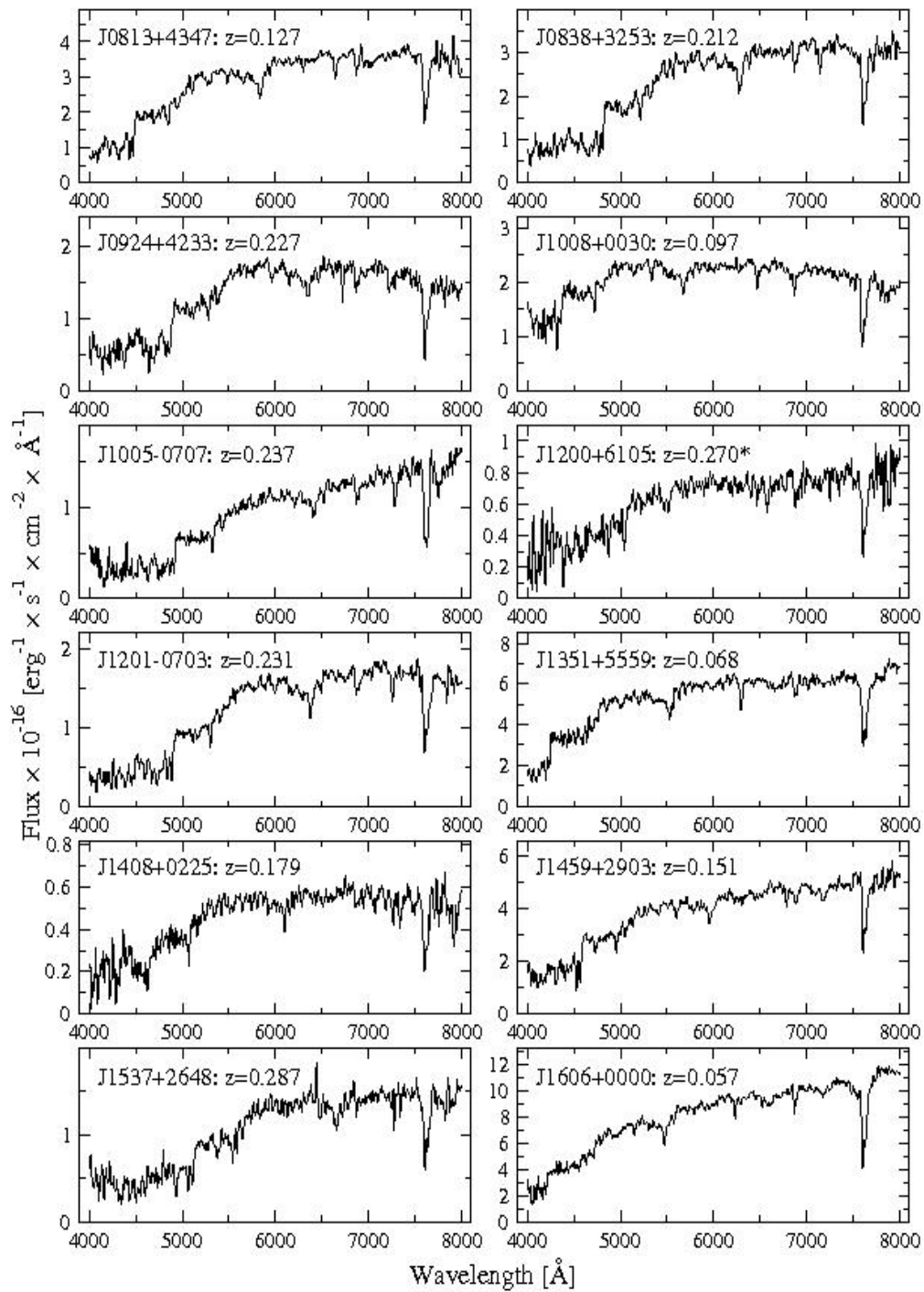


FIGURE 3.4— Optical spectrum and redshift of the targeted X-shaped radio sources. \*The noisy spectrum of J1200+6105 results in a higher uncertainty of the redshift determination for this object.

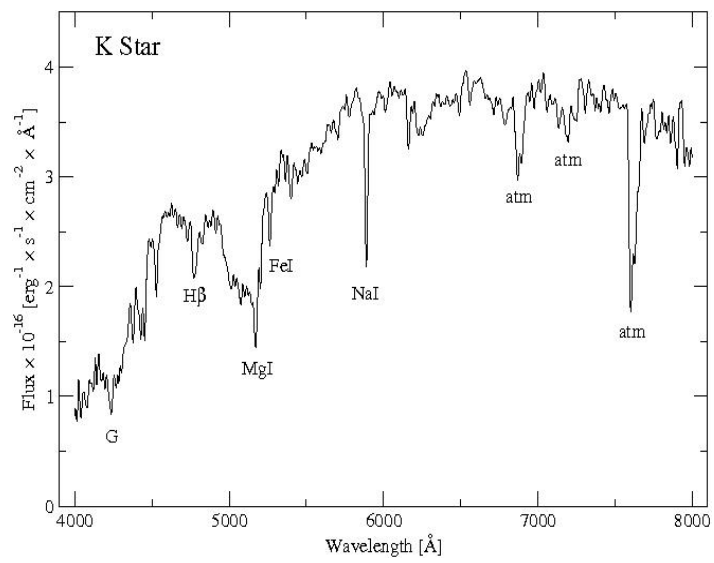


FIGURE 3.5— Spectrum of the optical counterpart of J1258+3227 showing stellar lines typical of a K-type star. This object is excluded from the analysis.

TABLE 3.2— X-shaped objects

Name		$\sigma_*$	$\log M_{\text{BH}}$	$\log \lambda L_{\text{opt}}^{\text{agn}}$	$\log \lambda L_{\text{opt}}^{\text{gal}}$	$\log \nu L_{\text{rad}}$	$\log t_a$ ( $\log t_p$ )	$\log t_{\text{sb}}$	$z$	$Q$	$C_{\text{CaII}}$
J2000	Other	[km/s]	[ $M_{\odot}$ ]	[erg/s]	[erg/s]	[erg/s]	[yr]	[yr]	(10)	(11)	(12)
(1)	(2)	(3)	(4)	(5)	(6)	(7)	(8)	(9)	(10)	(11)	(12)
J0001–0033		277.32 ± 4.55	8.70 ± 0.03	– <i>b</i>	43.77	41.27	6.37 (6.60)	6.50	0.247	83.94	0.43 <sup>f</sup>
J0049+0059		282.23 ± 9.64	8.73 ± 0.06	– <i>b</i>	43.43	41.84	6.68 (6.83)	9.20	0.304	31.07	–
J0808+2409	3C192	209.94 ± 7.97	8.21 ± 0.07	– <i>b</i>	43.85	41.82	6.52 (6.71)	6.70	0.060	41.46	0.36
J0813+4347		405.10 ± 4.63	9.36 ± 0.02	– <i>b</i>	44.11	41.31	6.29 (6.49)	9.11	0.127	382.25	0.45 <sup>f</sup>
J0831+3219	4C+32.25	194.80 ± 6.21	8.08 ± 0.06	42.42 ± 0.14	43.97	41.26	6.69 (6.85)	6.50	0.051	59.44	0.44 <sup>f</sup>
J0838+3253		361.29 ± 7.72	9.16 ± 0.04	– <i>b</i>	43.92	41.37	6.59 (6.76)	8.71	0.212	134.67	0.50
J0859–0433		250.37 ± 12.90	8.52 ± 0.09	42.33 ± 2.65	– <i>c</i>	42.13	6.08 (6.65)	8.00	0.356	24.55	–
J0924+4233		408.81 ± 7.37	9.38 ± 0.03	– <i>b</i>	43.58	41.84	6.54 (6.77)	9.11	0.227	180.24	0.42 <sup>f</sup>
J0941–0143		154.92 ± 20.61	7.68 ± 0.23	42.48 ± 5.15	43.19	42.84	6.14 (6.64)	7.00	0.384	4.92 <sup>e</sup>	–
J0941+3944	3C223.1	196.90 ± 9.14	8.10 ± 0.08	42.30 ± 0.87	43.94	41.88	6.44 (6.78)	9.11	0.107	35.30	0.38 <sup>f</sup>
J1005+1154		272.88 ± 6.46	8.67 ± 0.04	– <i>b</i>	44.12	41.37	6.43 (6.67)	9.10	0.166	66.08	0.48 <sup>f</sup>
J1008+0030		405.05 ± 3.61	9.36 ± 0.02	41.73 ± 1.37	44.02	41.19	5.61 (5.93)	6.00	0.097	844.74	0.32
J1020+4831	4C+48.29	194.30 ± 7.94	8.08 ± 0.07	42.28 ± 0.19	43.78	41.22	6.72 (7.02)	8.46	0.053	38.82	0.44 <sup>f</sup>
J1040+5056		211.57 ± 15.88	8.23 ± 0.13	– <i>b</i>	43.77	41.24	6.44 (6.65)	9.20	0.154	20.74	0.42
J1043+3131		195.27 ± 8.24	8.09 ± 0.07	41.15 ± 1.15	43.63	40.49	5.80 (6.09)	6.80	0.036	32.66	0.41
J1055–0707		321.02 ± 13.17	8.96 ± 0.07	– <i>b</i>	– <i>c</i>	42.24	6.14 (6.30)	7.40	0.237	87.96	0.47
J1101+1640	1059+169	220.98 ± 6.42	8.30 ± 0.05	41.01 ± 5.18	43.69	41.02	6.62 (6.98)	6.00	0.069	60.03	0.45 <sup>f</sup>
J1111+4050		254.75 ± 4.96	8.55 ± 0.03	– <i>b</i>	44.17	41.19	6.16 (6.43)	6.50	0.074	74.31	0.43
J1130+0058	4C+01.30	151.86 ± 6.78	7.65 ± 0.08	43.12 ± 0.15	44.10	41.65	6.24 (6.61)	9.40	0.132	24.88	0.26 <sup>f</sup>
J1140+1057		196.37 ± 7.80	8.10 ± 0.07	40.51 ± 20.11	43.61	41.09	6.28 (6.51)	6.00	0.081	40.99	0.41 <sup>f</sup>
J1200+6105		258.51 ± 5.80	8.58 ± 0.04	43.27 ± 0.20	43.69	42.01	6.08 (6.31)	6.70	0.270	180.70	0.29
J1201–0703		377.39 ± 9.52	9.24 ± 0.04	– <i>b</i>	– <i>c</i>	41.71	5.94 (6.25)	8.71	0.231	185.36	0.50
J1207+3352		181.28 ± 3.79	7.96 ± 0.04	41.85 ± 0.84	44.13	41.02	6.19 (6.44)	6.00	0.079	51.36	0.28 <sup>f</sup>
J1210–0341		221.29 ± 9.90	8.30 ± 0.08	42.14 ± 2.94	43.90	41.62	5.97 (6.56)	8.70	0.178	33.61	0.40 <sup>f</sup>
J1210+1121		223.51 ± 9.41	8.32 ± 0.07	– <i>b</i>	43.96	41.35	6.66 (6.78)	7.60	0.196	33.55	0.42
J1327–0203		237.30 ± 9.27	8.43 ± 0.07	– <i>b</i>	44.01	42.22	6.39 (6.65)	7.70	0.183	38.98	0.48 <sup>f</sup>
J1330–0206		219.35 ± 7.72	8.29 ± 0.06	– <i>b</i>	44.04	40.59	6.35 (6.61)	7.00	0.087	42.40	0.40
J1339–0016		323.77 ± 4.55	8.97 ± 0.02	– <i>b</i>	44.15	41.22	6.55 (6.81)	8.50	0.145	88.09	0.44
J1348+4411		108.42 ± 27.71	7.05 ± 0.45	41.67 ± 10.43	43.28	41.63	5.87 (6.53)	6.90	0.267	2.95 <sup>e</sup>	–
J1351+5559		342.05 ± 4.61	9.07 ± 0.02	– <i>b</i>	43.96	40.53	5.42 (5.71)	7.00	0.068	174.43	0.49
J1408+0225		352.63 ± 13.18	9.12 ± 0.07	41.53 ± 1.24	43.35	41.45	5.67 (6.01)	10.26	0.179	415.19	0.39
J1424+2637		174.99 ± 6.53	7.90 ± 0.07	40.48 ± 6.37	43.97	40.58	6.13 (6.37)	6.50	0.037	45.36	0.40
J1444+4147		226.06 ± 9.35	8.34 ± 0.07	– <i>b</i>	43.74	41.74	6.60 (6.80)	8.50	0.188	35.89	0.44 <sup>f</sup>

J1455+3237		$224.17 \pm 5.52$	$8.33 \pm 0.04$	$41.57 \pm 1.78$	43.84	40.42	6.10	(6.31)	6.50	0.084	68.39	0.39
J1459+2903		$249.18 \pm 2.43$	$8.51 \pm 0.02$	$41.97 \pm 4.57$	44.00	41.51	5.98	(6.12)	6.94	0.151	231.34	0.38
J1537+2648		$288.63 \pm 15.20$	$8.77 \pm 0.09$	$-^b$	43.49	42.03	6.05	(6.33)	9.11	0.287	42.94	0.40
J1606+0000	4C+00.58	$287.30 \pm 9.04$	$8.76 \pm 0.05$	$42.84 \pm 0.27$	44.08	41.39	5.50	(5.71)	6.00	0.057	64.28	$0.41^f$
J1614+2817		$344.13 \pm 6.21$	$9.08 \pm 0.03$	$41.32 \pm 2.65$	44.02	41.24	5.59	(6.22)	6.00	0.108	25.85	$0.42^f$

**Column designation:** (1) – object name based on J2000.0 coordinates; (2) – other common catalog names; (3) – stellar velocity dispersion obtained from STARLIGHT; (4) – black hole mass obtained from  $\sigma_*$ ; (5) – 5100 Å continuum luminosity from STARLIGHT; (6) – 5100 Å continuum luminosity from SDSS photometry; (7) – 1.4 GHz radio luminosity; (8) – dynamic age of the active (active+passive) lobes; (9) – age of the most recent starburst; (10) – spectroscopic redshift from SDSS; (11) – quality factor; (12) value of Ca II break factor. **Notes:** *a* – velocity dispersion obtained using the correlation  $\sigma_*=FWHM [OIII]/2.35$ ; *b* – STARLIGHT could not fit the continuum luminosity; *c* – no SDSS photometry available; *d* – no STARLIGHT fit; *e* – low fidelity of the STARLIGHT fit; *f* – values of Ca II break from Landt et al. (2010).

TABLE 3.3— Control sample

Name		$\sigma_*$	$\log M_{\text{BH}}$	$\log \lambda L_{\text{opt}}^{\text{agn}}$	$\log \lambda L_{\text{opt}}^{\text{gal}}$	$\log \nu L_{\text{rad}}$	$\log t_a$	$\log t_{\text{sb}}$	$z$	$Q$	$C_{\text{CaII}}$	Ref.
J2000	Other	[km/s]	[ $M_{\odot}$ ]	[erg/s]	[erg/s]	[erg/s]	[yr]	[yr]	(10)	(11)	(12)	(13)
(1)	(2)	(3)	(4)	(5)	(6)	(7)	(8)	(9)				
J0758+3747	0755+37	251.55 ± 4.63	8.53 ± 0.03	41.58 ± 0.09	44.48	41.20	6.16	6.00	0.043	85.50	0.36	M04
J0803+2440	B2 0800+24	186.04 ± 0.13	8.00 ± 0.06	- <i>b</i>	43.85	40.06	6.42	6.50	0.043	55.56	0.42	G00
J0821+4702	3C197.1	144.35 ± 9.53	7.56 ± 0.12	42.46 ± 0.05	43.80	42.05	6.11	6.00	0.128	17.33	-	M04
J0822+0557	3C198	164.35 ± 5.76	7.79 ± 0.06	42.46 ± 0.02	43.66	41.63	6.43	6.00	0.081	51.31	-	M04
J0846+3126	B2 0843+31	183.02 ± 0.14	7.98 ± 0.07	- <i>b</i>	43.58	39.84	6.98	7.00	0.067	43.13	0.41	G00
J0921+4538	3C219	188.98 ± 8.49	8.03 ± 0.08	42.52 ± 0.07	43.96	43.07	6.94	6.00	0.174	21.14	-	M04
J0925+3627	4C36.14	256.37 ± 0.35	8.56 ± 0.04	- <i>b</i>	44.26	39.36	6.60	7.00	0.112	68.51	0.43	G00
J0939+3553	3C223	181.42 ± 8.26	7.96 ± 0.08	42.45 ± 0.06	43.81	42.47	7.06	9.40	0.137	24.50	-	M04
J0941+5751	J0941+5751	189.32 ± 7.83	8.03 ± 0.07	- <i>b</i>	43.97	40.46	6.43	6.00	0.159	29.56	-	V06
J0947+0725	3C227	112.51 ± 3.35	7.13 ± 0.05	43.63 ± 0.00	43.95	41.47	6.78	6.00	0.086	24.43	-	M04
J1006+2554	B2 1003+26	240.82 ± 0.40	8.45 ± 0.06	- <i>b</i>	44.52	40.52	7.17	9.11	0.117	38.18	0.44	G00
J1006+3454	3C236	247.41 ± 7.26	8.50 ± 0.05	- <i>b</i>	44.17	42.07	7.74	6.50	0.101	54.96	0.33	M04
J1007+1248	1004+130	167.82 <sup>a</sup> ± 1.05	7.77 ± 0.01	- <i>b</i>	45.46	42.49	6.89	- <i>d</i>	0.241	- <i>d</i>	-	M04
J1031+5225	J1031+5225	204.85 ± 11.06	8.17 ± 0.09	42.34 ± 0.10	43.69	42.01	6.42	6.00	0.166	22.09	0.28	V06
J1040+2957	4C30.19	161.97 ± 0.06	7.76 ± 0.04	- <i>b</i>	44.11	41.03	- <i>c</i>	8.01	0.091	61.46	0.18	G00
J1055+5202	J1055+5202	162.90 ± 12.40	7.77 ± 0.13	42.61 ± 0.11	43.78	41.74	6.46	6.00	0.187	12.12	-	V06
J1105+3009	B2 1102+30A	262.26 ± 0.35	8.60 ± 0.04	41.14 ± 6.59	44.35	39.22	6.35	6.50	0.072	74.22	0.43	G00
J1114+4037	3C254	234.20 <sup>a</sup> ± 3.29	8.35 ± 0.03	- <i>b</i>	45.81	44.31	1.55	- <i>d</i>	0.736	- <i>d</i>	-	M04
J1154+0238	J1154+0238	169.59 ± 11.91	7.84 ± 0.12	- <i>b</i>	43.66	40.64	6.46	6.70	0.211	18.78	0.31	V06
J1219+0549	3C270	269.46 ± 3.72	8.65 ± 0.02	- <i>b</i>	44.04	40.63	6.12	7.00	0.007	84.46	0.41	M04
J1220+0203	1217+023	174.94 <sup>a</sup> ± 1.72	7.84 ± 0.02	- <i>b</i>	45.25	42.16	6.84	- <i>d</i>	0.240	- <i>d</i>	-	M04
J1252+5634	3C277.1	235.90 <sup>a</sup> ± 0.57	8.37 ± 0.00	- <i>b</i>	44.62	43.10	5.04	- <i>d</i>	0.320	- <i>d</i>	-	M04
J1259+2757	NGC4874	251.47 ± 0.32	8.53 ± 0.04	- <i>b</i>	44.36	39.59	6.30	6.00	0.024	57.54	0.42	G00
J1319+2938	4C29.47	198.73 ± 0.17	8.12 ± 0.06	- <i>b</i>	44.09	41.45	6.35	8.01	0.073	53.97	0.39	G00
J1321+4235	3C285	162.58 ± 9.46	7.77 ± 0.10	- <i>b</i>	43.86	41.68	6.6	6.00	0.079	26.37	0.24	M04
J1332+0200	3C287.1	246.02 ± 7.86	8.49 ± 0.06	43.24 ± 0.04	44.01	40.27	6.82	6.00	0.216	32.12	-	M04
J1341+5344	J1341+5344	225.84 ± 7.07	8.34 ± 0.05	- <i>b</i>	43.87	40.02	6.55	6.00	0.141	42.80	0.31	V06
J1350+2816	B2 1347+28	209.58 ± 0.23	8.21 ± 0.06	- <i>b</i>	43.98	40.65	6.34	8.01	0.072	46.69	0.41	G00
J1430+5201	3C303	167.41 ± 9.77	7.82 ± 0.10	43.22 ± 0.01	43.96	42.32	6.28	7.20	0.141	16.86	-	M04
J1512+0203	J1512+0203	194.50 ± 10.45	8.08 ± 0.09	42.79 ± 0.09	44.01	42.30	6.52	6.00	0.219	25.33	-	V06
J1529+3042	1527+30	322.89 ± 7.49	8.97 ± 0.01	- <i>b</i>	44.29	40.12	6.38	8.20	0.114	64.60	0.46	G00
J1559+2556	B2 1557+26	223.51 ± 0.24	8.32 ± 0.05	41.09 ± 15.68	43.93	39.89	- <i>c</i>	6.00	0.045	54.67	0.40	G00
J1611+3103	B2 1609+31	199.34 ± 0.23	8.12 ± 0.08	- <i>b</i>	43.93	40.70	5.74	6.00	0.095	31.15	0.42	G00

J1615+2726	1613+27	$221.13 \pm 6.13$	$8.31 \pm 0.05$	$41.11 \pm 0.40$	43.99	40.35	5.89	6.00	0.065	58.17	0.42	M04
J1617+3222	3C332	$172.37 \pm 3.80$	$8.64 \pm 0.01$	$40.90 \pm 4.45$	44.05	42.41	6.62	6.00	0.151	33.13	-	M04
J2351-0109	2349-014	$201.97^a \pm 2.12$	$8.72 \pm 0.01$	$-^b$	44.95	42.28	6.06	$-^d$	0.174	$-^d$	-	M04

**Column designation:** (1) – object name based on J2000.0 coordinates; (2) – other common catalog names; (3) ; – stellar velocity dispersion obtained from STARLIGHT; (4) – black hole mass obtained from  $\sigma_*$ ; (5) – 5100 Å continuum luminosity from STARLIGHT; (6) – 5100 Å continuum luminosity from SDSS photometry; (7) – 1.4 GHz radio luminosity; (8) – dynamic age of the active lobes; (9) – age of the most recent starburst; (10) – spectroscopic redshift from SDSS; (11) – quality factor; (12) value of Ca II break factor; (13) – Original references. **Notes:** *a* – velocity dispersion obtained using the correlation  $\sigma_*=FWHM [OIII]/2.35$ .; *b* – STARLIGHT could not fit the continuum luminosity; *c* – not available; *d* – no STARLIGHT fit. REFERENCES.– (G00) González-Serrano & Carballo (2000); (M04) Marchesini et al. (2004); (V06) de Vries et al. (2006).



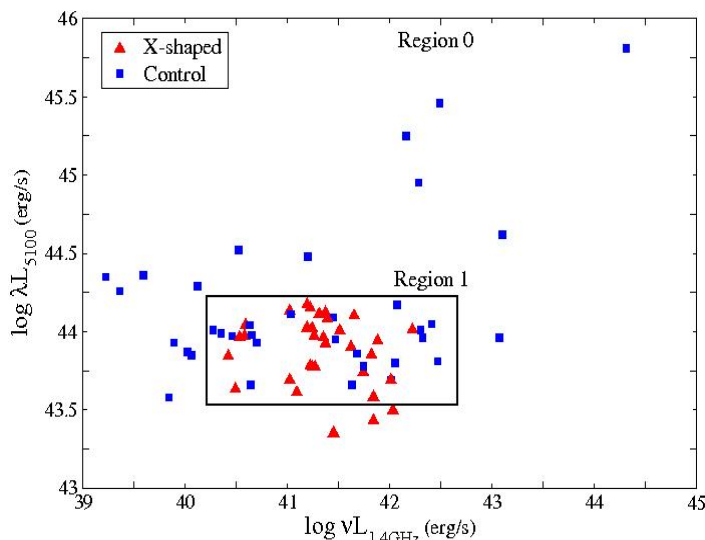


FIGURE 3.6— Optical continuum luminosity versus radio luminosity at 1.4 GHz for X-shaped (triangles) and control sources (squares). A small subregion (“Region 1” marked by a rectangle inside the plot) is identified to provide a tighter luminosity match between the two samples.

### 3.4.2 Luminosity matching

Luminosity matching between the target and control samples is illustrated in Fig. 3.6, where the continuum luminosities derived from the SDSS magnitudes (Eq. 3.3) are plotted against the radio luminosities at 1.4 GHz. The entire original radio-optical luminosity range, including all sources, is called Region 0 hereafter. To provide a tighter match between the samples (at the expense of reducing the sample sizes), we define a smaller subregion or window (shown in Fig. 3.6) called Region 1. Region 1 ranges from  $\log \lambda L_{5100\text{\AA}} \in [43.5, 44.25]$  to  $\log \nu L_{1.4\text{GHz}} \in [40.25, 42.5]$  and mainly excludes the control sources with the lowest radio luminosities and highest optical luminosities because there are no X-shaped sources with such luminosities. In Region 1, the KS-test indicates that the probability that the two samples are the same is of 87% for the optical luminosity and of 19% for the radio luminosity.

### 3.4.3 Host type

We base our spectral classification on color-color separation and on the Ca II break measurements in the target and control samples. All X-shaped sources analyzed have  $C_{\text{Ca II}} > 0.25$ , with 94% of the sources (33 out of 35) having

$C_{\text{Ca II}} \simeq 0.4$ . These values ensure that the galaxy is dominated by the thermal spectrum of the host rather than the non-thermal spectrum of an active nucleus or a relativistic jet.

For the control sample, however, the Ca II break can be determined for only 20 out of the 36 sources. Ninety percent of these sources (18 out of 20) have  $C_{\text{Ca II}} > 0.25$ , and 70% (14 out of 20) have  $C_{\text{Ca II}} \simeq 0.4$ . Only 56% of the control sources therefore have a thermal spectrum that dominates the host galaxy.

The host galaxy type of the X-shaped and control sources can be inferred using a color-color diagram. The  $g$ ,  $r$  and  $u$  magnitudes obtained from SDSS are used to plot a  $g-r$  vs  $u-g$  color-color diagram (Fig. 3.7) for the two samples. Only the sources with a spectrum dominated by the host galaxy (as determined from the Ca II break) are included in this plot. According to the distribution of galaxies in the  $u-g$  vs  $g-r$  diagram from Strateva et al. (2001), all galaxies lying above the  $u-r = 2.22$  separator line are elliptical systems. The plot shows that all the X-shaped radio sources and all the control sources for which the SDSS magnitudes are available qualify as elliptical galaxies, with only one source from each of the samples lying slightly below the  $u-r = 2.22$  separator line. The X-shaped source J0049+0059 (with  $u-g = 5.0$ ) is not plotted in Fig. 3.7, but it qualifies as an elliptical galaxy as well.

In order to better study the relation between the galactic hosts of the X-shaped and control radio sources, a control subsample of elliptical galaxies will be considered from now on. This subsample is defined according to the galactic type obtained by the SDSS color separation described above and the Ca II break, and contains the 20 control sources for which the  $C_{\text{Ca II}}$  value could be determined.

#### 3.4.4 Black hole masses

From the individual estimates of the black hole masses, we calculate the mean BH mass in the X-shaped sample,  $\langle M_{\text{BH,X-shaped}} \rangle$ , and derive its ratio to the mean BH mass in the control samples  $r_{\text{xc}} = \langle M_{\text{BH,X-shaped}} \rangle / \langle M_{\text{BH,control}} \rangle$ . The resulting ratio is  $2.30^{+0.37}_{-0.32}$  for the X-shaped/control samples and  $1.75^{+0.32}_{-0.27}$  for the X-shaped/control (ellipticals) samples. These values increase to  $2.89^{+0.62}_{-0.51}$  and  $2.24^{+0.54}_{-0.44}$ , respectively, in the tighter Region 1.

The differences of the black hole masses in the two samples are further illustrated by the distribution of BH masses in Figs. 3.8- 3.9. The histograms of the mass distributions for the X-shaped and control samples in Regions 0 and

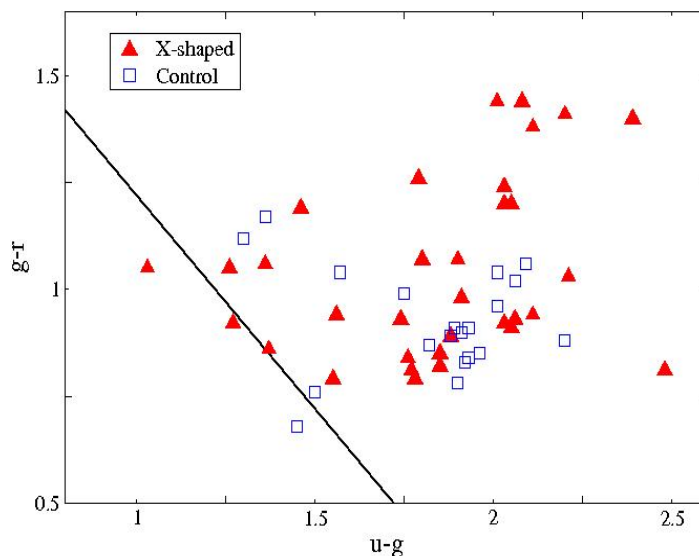


FIGURE 3.7— Color-color diagram ( $g-r$  colors versus  $u-g$  colors) for X-shaped sources (triangles), and control sources (squares). Black line:  $u-r = 2.22$  galaxy type separator from Strateva et al. (2001). Sources situated above this line are classified as elliptical galaxies.

I underline the trend of the X-shaped objects to have statistically higher black hole masses than the black hole masses obtained for the control sample. About 70% of the X-shaped sources have  $\log M_{\text{BH}} > 8.25M_{\odot}$ , both for Region 0 and Region 1. The respective percentages are 50% and 25% for the control sample objects in Region 0 and 1. The KS-test applied to the BH mass distribution of the X-shaped and control sample gives probabilities of 97% and 99% that the two samples are significantly different in Regions 0 and 1, respectively. This statistical significance remains unchanged also when the subsample of elliptical control sources is considered.

The statistically larger black hole mass of the X-shaped sample implies that these objects are possibly located in galaxies that have undergone strong major activity in the past, with either one major merger event or multiple minor mergers.

### 3.4.5 Starbursts

The starburst and radio lobe ages can be used to see whether starburst activity is different in the X-shaped objects and whether it can be related to the production

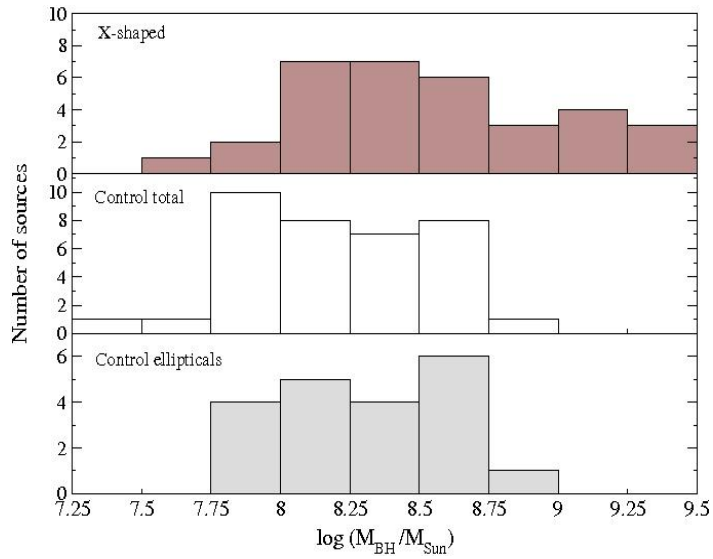


FIGURE 3.8— Histogram of the black hole mass in Region 0 for the sample of X-shaped sources (top), control all (middle), and control ellipticals (bottom).

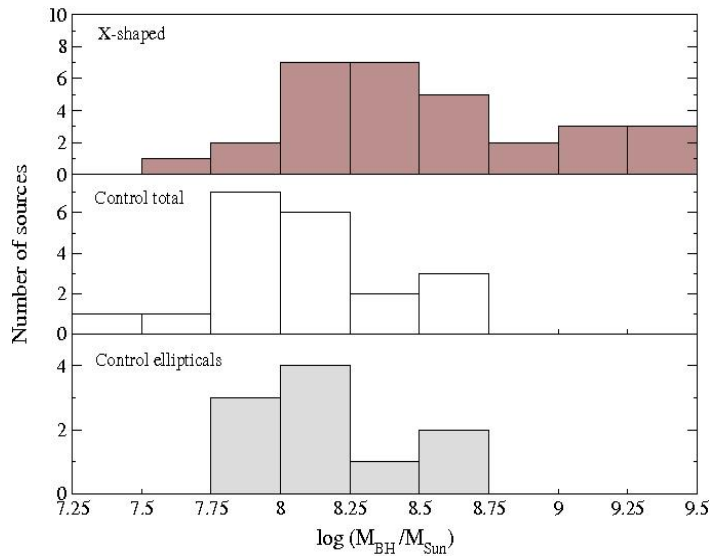


FIGURE 3.9— Histogram of the black hole mass in Region 1 for the sample of X-shaped sources (top), control all (middle), and control ellipticals (bottom).

of radio emission in both the target and control samples.

Distributions of the ages of the most recent starburst in Region 0 are compared in Fig. 3.10 for the X-shaped sample and the control samples. A sizeable fraction of objects in both samples have relatively recent starbursts, with a peak of starburst activity in the range of  $10^{6.0}$ – $10^{6.5}$  years. The distribution of starburst ages in the X-shaped sample is much broader, with 50% of the sources having a starburst activity older than  $10^8$  years. Only 19% of all the control sources and 25% of the control ellipticals exhibit these starbursts. The histogram also reveals a secondary peak between  $10^{9.0}$ – $10^{9.5}$  years in the distribution of starburst ages of the X-shaped sample (see Fig. 3.10). The most recent peak of star formation, present in all three samples, could be related to the current jet activity (e.g., Rees 1989; Labiano et al. 2008; Silk & Norman 2009). The secondary peak, only present in the X-shaped sample, cannot be linked to the active lobes as their largest dynamic age is  $\sim 10^7$  years (see Table 3.2, col. 8). Such strong starburst activity can only possibly be related to an event that occurred before the active lobes were formed. It can be speculated that these older starbursts are related to galactic mergers themselves. A delay between merger-driven starburst and AGN activity is shown in recent studies (Schawinski et al. 2010; Blecha et al. 2011). This scenario can be further tested by comparing the starburst ages to the dynamic ages of the radio lobes for both the X-shaped and control samples.

According to the KS-test, the starburst ages of the X-shaped sample and the control sample are different with a probability of 98% both in Region 0 and 1. To account for a possible dependence of this difference on the galactic type, the KS-test is applied to the X-shaped sample and the subsample of control ellipticals. Considering the subsample of only control ellipticals, the KS-test gives a probability of 95.5% for the X-shaped objects to be different from the control sample.

Histograms of the logarithmic ratio of the dynamic age and the most recent starburst age for the objects in Region 0 are shown in Fig. 3.11. The X-shaped sources tend to have starburst ages that are older than the dynamic ages of the radio lobes, while in both the control sample and the control subsample of ellipticals these ages are comparable. The mean logarithmic ratio of the X-shaped sample is  $-1.43 \pm 0.23$ , while the one of the control sample is  $-0.14 \pm 0.18$ . The starburst activity in X-shaped sources is therefore likely not related to the active lobes. This difference in the starburst/dynamic age ratios may support the scenario in which the active lobes of the X-shaped sources are due to a possible reorientation caused by a black hole merger (Merritt & Ekers

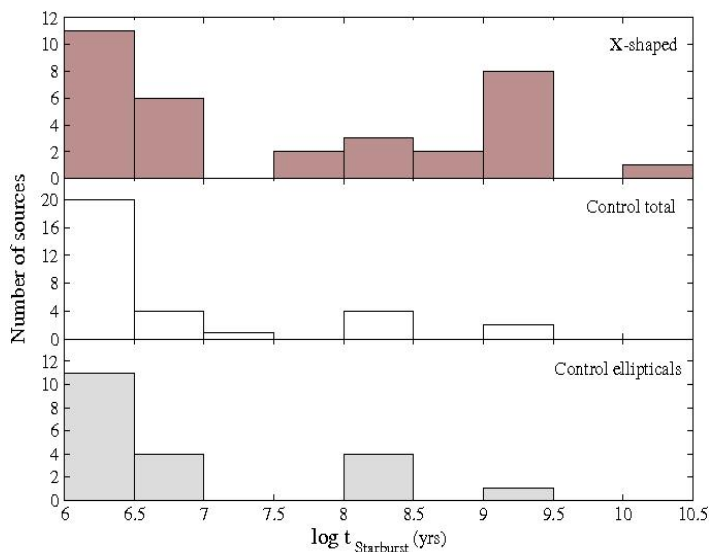


FIGURE 3.10— Histogram of the ages of most recent starburst for X-shaped sources (top), control all (middle), and control ellipticals (bottom) in Region 0.

2002) that leaves the old low-surface-brightness lobes inactive. Assuming that the low-surface-brightness lobes became inactive when the high-surface ones were activated, the dynamic age of the passive lobes during their active stage can be determined using Eq. 3.5. The ratio of the total dynamic age of the active plus passive lobes to the starburst age is plotted in Fig. 3.11 (second panel), and it indicates that the starburst age still remains older than the total dynamic age of the lobes. This suggests that the starburst activity in X-shaped sources had occurred before the possible reorientation owing to a black hole merger, and it may have been related to the galactic merger itself.

### 3.5 Discussion

The origin of the X-shaped morphology in X-shaped radio galaxies is a matter of ongoing debate. Some recent studies in the X-rays (Hodges-Kluck et al. 2010b) and some theoretical models (Gong et al. 2011) favor a recent merger of two supermassive black holes as the most plausible scenario. Other studies (Hodges-Kluck et al. 2010a; Landt et al. 2010) propose a backflow from the active lobes into the wings to explain the peculiar morphology of X-shaped radio galaxies.

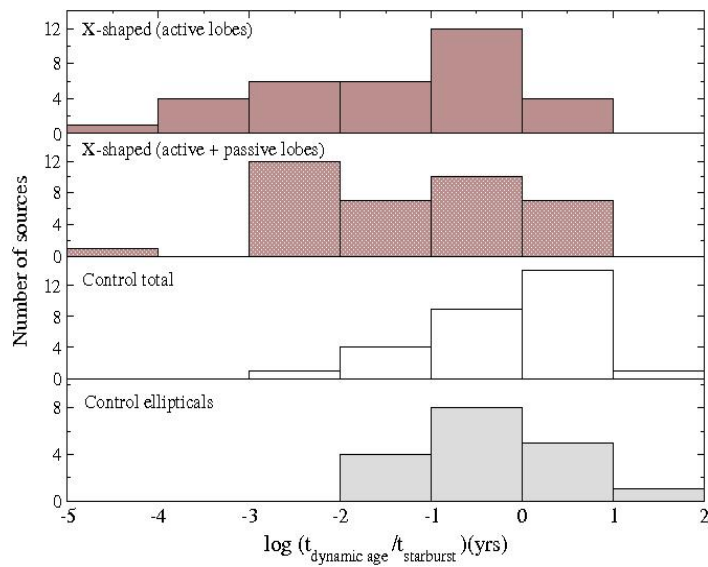


FIGURE 3.11— Logarithmic ratios of the dynamic ages of the radio emission to the age of the most recent starburst for Region 0. The top row presents the ages of active lobes in X-shaped objects, while the second row shows the sum of the ages of the active and passive lobes. The two bottom rows show distributions of the age ratios in the control sample (third row) and the control subsample of ellipticals (fourth row).

This chapter has presented the largest statistical study of the black hole mass and starburst activity in X-shaped radio sources. The properties of a sample of 38 X-shaped radio galaxies have been compared to those of a control sample of 36 radio-loud active nuclei, with stringent luminosity and color criteria applied to provide the best match between the two samples. The results suggest that a galactic merger is a more likely explanation of the origin of X-shaped sources. The merger hypothesis is further supported by the finding that all of the X-shaped objects studied are hosted by early-type galaxies, which are expected to have undergone at least one major merger event over the course of their evolution (Toomre 1977).

Histograms of the BH mass distribution for the X-shaped and control samples show that X-shaped radio galaxies tend to have higher  $M_{\text{BH}}$  than the control sample. The ratio of the mean  $M_{\text{BH}}$  between the two samples confirms the trend observed, with the X-shaped sample having a mean BH mass  $2.89^{+0.62}_{-0.51}$  times higher than the one of the control sample in a tight common range of radio and optical luminosities. The higher average black hole mass in the galaxies hosting the X-shaped radio sources may result from a major merger event and the consequent coalescence of the two central black holes, which could be the origin of the winged morphology observed in the radio maps.

To test this scenario, the age of the most recent burst of star formation and the dynamic age of the radio lobes are studied for both the X-shaped and the control samples. The most recent episodes of starburst activity are statistically older in the X-shaped sample compared to those found for the control sample, with 50% of the X-shaped sources having starburst ages older than  $10^8$  years. In the X-shaped sources, the most recent starburst occurred before the active lobes were formed. Of particular interest is the peak observed in the distribution of the most recent starburst age of the X-shaped sample at ages of  $10^9$ – $10^{9.5}$  years (1–3 Gyr). This peak suggests enhanced star formation due to a merger event, which implies a timedelay of 1–3 Gyr between the peak of starburst activity and the end of the merger. Such timescale is in agreement with the time delay of  $\sim 2$  Gyr found by hydrodynamical simulations of galaxy mergers (Lotz et al. 2008), and with timescales of 0.5–2 Gyr found observationally for individual objects (e.g., Tadhunter et al. 2005; Emonts et al. 2006). On the other hand, the jet dynamic age of  $10^6$  yrs derived for the X-shaped sources is as well in agreement with the time delay between the merger event and the onset of the radio-AGN triggered activity found by other studies to be  $10^6$  years (e.g., Emonts et al. 2006).



All these results strengthen the merger origin of X-shaped radio galaxies. More detailed studies of star formation and gas kinematics in these objects will yield stronger constraints to this scenario.



# 4

---

## Ultraluminous X-ray sources

*Ultraluminous X-ray sources (ULX) are very bright X-ray sources associated with galaxies and whose nature is unknown. It has been suggested that the high X-ray luminosities observed may come from an intermediate mass black hole (IMBH), or that ULXs could harbor secondary black holes in post-merger galaxies. The study of these sources is, thus, of potential interest in the search for evidence of binary black hole systems. With the aim of revealing the true nature of ULXs and their possible link to binary black holes, archival data of a sample of 24 ULXs are analyzed and a sample of 3 ULXs with radio counterparts detected is observed with the European VLBI Network. This chapter presents the results of these observations, which include the resolved structure of a supernova remnant and two IMBH candidates whose black hole masses have been estimated using the fundamental plane of accreting black holes. A compilation of ULX sources with detected radio counterparts is also presented and estimates of their BH mass are obtained. The nature of each one of these sources is discussed individually.*

### 4.1 Introduction

In the early 1990s, the *Einstein* observatory (Fabbiano 1989) detected a population of very luminous and unresolved X-ray sources, with luminosities exceeding  $10^{39}$  erg s<sup>-1</sup>, whose origin was unknown. The luminosities of these Ultraluminous X-ray sources (ULX) are much higher than the typical luminosities of X-ray binaries in our Galaxy ( $10^{33}$ - $10^{38}$  erg s<sup>-1</sup>) but lower than X-ray emitting active galaxies ( $\sim 10^{43}$  erg s<sup>-1</sup>). Extensive studies of ULX objects over the past 20 years have revealed the nature of a few of them, but the physical mechanism triggering the high luminosities observed in all ULXs is still under debate.

One of the most appealing scenarios suggests that ULXs are intermediate mass black holes (IMBH), with masses between 100 and  $10^5 M_{\odot}$ , accreting

at sub-Eddington rates (Colbert & Mushotzky 1999). These IMBHs could be related to the seed BHs required to explain the existence of supermassive black holes (SMBH) in the early Universe (e.g., Volonteri & Rees 2005; Volonteri et al. 2008), and evidence of their existence has already been found in nearby low-mass galaxies (Greene & Ho 2004, 2007; Georgakakis et al. 2011). Models of stellar evolution cannot explain the formation of black holes with masses above  $\sim 70M_{\odot}$  (Yungelson et al. 2008). IMBHs with masses of up to  $10^3M_{\odot}$  could be formed from very young and massive (Population III) stars (Madau & Rees 2001), while  $< 10^6M_{\odot}$  BHs could result from a direct collapse of pre-galactic gas discs (Lodato & Natarajan 2006). Indeed, ULX sources are more commonly found in late-type spiral and irregular galaxies than in early-type ellipticals, and analysis of physical and environmental properties of ULXs have shown that their X-ray luminosities are correlated with star formation rates in their host galaxies (Kilgard et al. 2002; Swartz et al. 2004).

In another scenario, ULXs are suggested to be stellar mass black holes radiating at super-Eddington luminosities. Such luminosities could be produced by pressure-dominated accretion disks with photon-bubble instabilities (Begelman 2002) or, in the case of high mass X-ray binaries (HMXBs), by beaming effects from either strong outflows (geometric beaming; e.g., King et al. 2001; King 2008; King 2009; Poutanen et al. 2007) or the jet axis (relativistic beaming; e.g., Körding et al. 2002) pointing towards the observer. Examples of such super-Eddington accretors and ‘microquasars’ can be found in our Galaxy (e.g., SS433, Begelman et al. 2006; V4641, Revnivtsev et al. 2002; GRS 1915+105, Mirabel & Rodríguez 1994), supporting the non-isotropic emission scenario for ULXs with X-ray luminosities up to  $10^{40}$  erg  $s^{-1}$  (Rappaport et al. 2005). Both this model and the IMBH scenario are in agreement with ULX sources being commonly found in star-forming galaxies, and are able to produce the extended photoionized nebulae observed around some ULX sources (e.g., Wang 2002; Kaaret et al. 2004; Pakull & Mirioni 2003; Lang et al. 2007; Kaaret & Corbel 2009; Cseh et al. 2011b; Moon et al. 2011). However, the non-isotropic radiation scenario struggles to explain ULXs with X-ray luminosities above  $10^{40}$  erg  $s^{-1}$ . On the other hand, the peculiar features of the X-ray spectra of some ULXs (i.e., a soft excess and a break at high energies) have brought a new scenario in which ULXs are in an ‘ultraluminous state’ not usually seen in X-ray binaries (Gladstone & Roberts 2009).

An alternative model suggests that ULXs could harbor the secondary black hole (BH) of the binary black hole systems formed in post-merger galaxies

(Lobanov 2007). According to the binary black hole model (e.g., Begelman et al. 1980; Volonteri et al. 2003), during a galactic merger the accretion disk around the secondary BH is disrupted by tidal forces and becomes a weak emitter. The X-ray luminosities of the secondary BH would then become comparable to the brightest ULX sources. Indeed, it was found that the luminosity dependence of a sample of ULXs with the nuclear separation to their respective host galaxies could be fit by the binary black hole scenario of a galactic merger (Lobanov 2007). IMBH candidates in active galactic nuclei have been found to have X-ray luminosities in the range  $L_{0.5-2\text{keV}} \sim 10^{41} - 10^{43} \text{ erg s}^{-1}$  (e.g., Greene & Ho 2007). This suggests a new scenario in which at least some (and probably most luminous) ULXs could be intermediate mass black holes in the course of a minor merger event. Such ULXs could be found in disk galaxies with no tails or strong tidal distortions, since strong tidal interactions arise in major merger events that evolve into elliptical systems (e.g., Toomre & Toomre 1972; Barnes & Hernquist 1992), while minor mergers may not evolve into elliptical-like bulges but rather disk-like systems (e.g., Gimeno et al. 2004; Eliche-Moral et al. 2006) leading to a rather slow evolution of a smaller mass secondary BH (e.g., Cuadra et al. 2009).

To clarify which is the most likely scenario, the radio emission of ULX sources is studied in this chapter. Sect. 4.2 presents the analysis and results of a search for ULX radio counterparts in archival data, and of VLBI observations of a sample of ULX sources with known radio counterparts. A compilation of ULX sources with detected radio counterparts and the study of their estimated black hole mass is presented in Sect. 4.3. Finally, in Sect. 4.4 we describe the results obtained from the radio observations of a ULX identified as a supernova remnant. A summary of the chapter is presented Sect. 4.5.

## 4.2 Uncovering the compact radio emission of ULXs

Radio observations of ULXs provide an excellent tool for uncovering the nature of these objects, by detecting and possibly resolving their compact radio emission, measuring its brightness temperature and spectral properties, and assessing the physical mechanism for its production. Few ULXs have been studied in the radio domain (e.g., Kaaret et al. 2003; Körding et al. 2005; Miller et al. 2005b; Lang et al. 2007; Cseh et al. 2011b) and a small sample of ULX sources has been cross-identified with existing radio catalogs (Sánchez-Sutil et al. 2006; Pérez-Ramírez et al. 2011). An increase of the number of radio detections and subsequent VLBI studies of detected radio counterparts could help to clarify the nature of ULX sources.

This section presents the analysis and results of (1) archive images of the Chandra Deep Fields taken with the Giant Meterwave Radio Telescope (GMRT) looking for faint radio counterparts of the ULX sources located in these fields; and of (2) a European VLBI Network (EVN) program initiated to detect and study the milliarcsecond-scale emission from ULX objects with known radio counterparts.

#### 4.2.1 Samples

Archival GMRT data have been used to search for radio counterparts of 24 ULX objects identified in the Chandra Deep Field North (CDFN), Chandra Deep Field South (CDFS), and Extended CDFS (ECDFS; Lehmer et al. 2006). All these ULXs have luminosities  $L_X \geq 10^{39}$  erg s<sup>-1</sup> in the 0.5-2.0 keV band, and are located in optically bright irregular and late-spiral galaxies. Ten of the 24 X-ray sources appear to be coincident with optical knots of emission, with apparent diameters of  $\sim 500$ -1000 pc and optical luminosities around  $10^{40}$ - $10^{41}$  erg s<sup>-1</sup>. These optical properties are consistent with those of giant HII regions in the local universe, suggesting that these ULX sources trace distant star formation (Lehmer et al. 2006). On the other hand, the X-ray luminosity of these ULXs is comparable to the one expected from the secondary black hole of a binary BH system in the course of a galactic merger (Lobanov 2007).

The objects targeted in our EVN observations are selected from a sample of 11 X-ray sources detected by the *ROSAT* satellite and catalogued as ULXs (Liu & Bregman 2005), with radio counterparts (Sánchez-Sutil et al. 2006) in the VLA FIRST catalog (Becker et al. 1995). From these objects, we have selected three ULXs least likely to be background AGNs, brighter than 1 mJy, and located more than 1 kpc away from the nuclear region in their respective host galaxies. The first target is N4449-X4, identified as the most luminous and distant member of the class of oxygen-rich supernova remnants (SNRs; Blair et al. 1983) and classified as a ULX source (Liu & Bregman 2005). A detailed study of this source is described in Sect. 4.7. The second target is NGC 4088-X1, a ULX located at a distance of 13.0 Mpc (Sánchez-Sutil et al. 2006) in the asymmetric spiral galaxy NGC 4088. NGC 4088-X1 is located within the extended emission of a spiral arm and is coincident with a conspicuous peak of radio emission observed at 1.4 GHz (1.87 mJy in strength), which lies within the *ROSAT* positional error ( $\sim 10''$ ), with an offset of  $3.62''$  from the X-ray peak (Sánchez-Sutil et al. 2006). The ULX has an X-ray luminosity of  $5.86 \times 10^{39}$  erg s<sup>-1</sup> measured in the 0.3-8.0 keV band (Liu & Bregman 2005), which does not rule out the possibility of it being an HII region.

TABLE 4.1— GMRT observations of the Chandra Deep Field North (CDFN) and South (CDFS)

Frequency	CDFN	CDFS	Primary beam [arcmin]	Synthesized beam [arcsec]	SEFD [Jy]	$\sigma_{\text{rms}}$ [mJy]
(1)	(2)	(3)	(4)	(5)	(6)	(7)
235 MHz	2001 Dec 17 2002 Jan 4 2002 Jan 26	—	114	$20.1 \times 16.3$	536	1.4
325 MHz	—	2003 Feb 13-17	81	$13.7 \times 11.8$	338	0.6
610 MHz	—	2007 Feb 11-12	43	$7.1 \times 4.9$	288	0.8

**Column designation:** (1) – frequency ; (2) – observation dates of the CDFN ; (3) – observation dates of the CDFS ; (4) – Primary beam size of the GMRT ; (5) – Synthesized beam size ; (6) – system equivalent flux density (SEFD; an integral measure of antenna sensitivity) ; (7) – map rms noise.

The last ULX selected for the VLBI observations is NGC 4861-X2, located 14.8 Mpc away (Sánchez-Sutil et al. 2006), in a spiral galaxy (NGC 4861) that, together with the dwarf IC3961, forms the Mrk 59 complex. The offset between the radio and the X-ray positions of this ULX is  $1.97''$ , which is well within the *ROSAT* positional uncertainty, and the X-ray luminosity is  $8.4 \times 10^{39}$  erg s<sup>-1</sup> (Liu & Bregman 2005). This ULX has been suggested to coincide with an HII region powered by massive early OB type stars (Pakull & Mirioni 2002).

#### 4.2.2 Observations and data reduction

##### *GMRT*

We use archival GMRT data for the Hubble Deep Field North (overlapping with our CDFN region of interest) at 235 MHz (experiments 01NIK04 & 11TMA01), and of the CDFS at 325 & 610 MHz (experiments 03JAA01 & 11RNA01).

The observations were carried out between December 2001 and February 2007 (see Table 4.1), in dual polarization, with an integration time of 34s, and using the GMRT standard phase calibration mode and spectral line mode with a spectral resolution of 125 kHz. The amplitude and bandpass calibrators 3C48

and 3C147 were observed, depending on the availability, either at the beginning or at the end of the observing run. The data have been analyzed with AIPS, using the standard procedure described in Sect. 2.2.2. For each frequency, we combine all the calibrated uv files with the AIPS task DBCON. We image the visibility data using the task IMAGR, with uniform weighting, and the CLEAN algorithm deconvolution method (see Sect. 2.2.3). In order to detect very faint sources, we first image the entire primary beam area and extract all strong point-like objects. The CLEAN components obtained for these objects are subtracted from the visibility data, and deeper imaging is performed. Finally, self-calibration (see Sect. 2.2.2, phase-calibration) is applied to increase the dynamic range of the final image. At 610 MHz, 3 pointings of the same field (CDFS) were observed. These 3 pointings are imaged separately.

## EVN

The EVN observations (project codes EM072A & EM072B) were made on June 1st & 2nd 2009, in two separate blocks of 12 hours in duration, using 9 antennas (Effelsberg, Jodrell Bank Lovell, Cambridge, Westerbork, Onsala, Medicina, Noto, Torun, Sheshan) at L-band (wavelength of 18 cm). The basic technical parameters of the antennas are listed in Table 4.2. In order to detect weak emission from the ULX objects, we used the phase-referencing technique, calibrating the phases of the target objects with nearby strong and point-like calibrators. We switched between target-phase calibrator with a cycle time of 10 min (see Table 4.3 for integration times). The data were recorded with a bandwidth of 16 MHz and sample rate of 1024 Mbps in dual circular polarization. The correlation was carried out at JIVE (Joint Institute for VLBI in Europe, The Netherlands), with 32 spectral channels per IF and polarization and an integration time of 2 seconds. The data reduction is performed in the standard way using AIPS. Uniform weighting is used in the imaging, and tapering of the longest baselines is applied for NGC 4088-X1 and NGC 4861-X2 to improve the detection of extended emission.

## 4.2.3 Results

### 4.2.3.1 ULX sources in the Chandra Deep Fields

In Fig. 4.1 the final GMRT images obtained at 235 MHz and 325 MHz are shown (the 610 MHz image is not shown as it barely contains any detected sources). The synthesized beam sizes are  $20.1 \times 16.3$  arcsec at 235 MHz,  $13.7$



TABLE 4.2— Technical characteristics of the EVN observations

Participating telescopes			
Antenna	$D$	SEFD	$\sigma_{\text{rms}}$
	[m]	[Jy]	[mJy]
Effelsberg (DE)	100	19	...
Jodrell Bank (UK)	76	44	0.24
Medicina (IT)	32	600	0.87
Noto (IT)	32	780	1.00
Onsala (SE)	25	320	0.64
Shanghai (CN)	25	670	0.92
Torun (PL)	32	230	0.54
Urumqi (CN)	25	270	0.58
Westerbork (NL)	83 <sup>a</sup>	30	0.20

Notes:  $D$  – antenna diameter; SEFD – system equivalent flux density (an integral measure of antenna sensitivity);  $\sigma_{\text{rms}}$  – rms noise for one minute integration on the baseline between the given antenna and Effelsberg; <sup>a</sup> – equivalent antenna diameter for a phased array of  $11 \times 25$  meter antennas used for the observations.

TABLE 4.3— EVN observations at 1.6 GHz

Date	Source		Int. time [hours]
2009 June 1	NGC 4861-X2	ULX	3.3
	J1257+3229	Phase calibrator	1.2
	4C39.25	Fringe finder & bandpass calibrator	0.13
2009 June 2	NGC 4088-X1	ULX	3.5
	J1153+4931	Phase calibrator	1.3
	4C39.25	Fringe finder & bandpass calibrator	0.13

TABLE 4.4— Upper limits on the flux densities at 235.5 MHz of the ULXs in the CDFN

Name	$S$ [mJy/beam]
CXOHDFN J123631.66+620907.3	< 3.63
CXOHDFN J123632.55+621039.5	< 2.76
CXOHDFN J123637.18+621135.0	< 2.88
CXOHDFN J123641.81+621132.1	< 3.20
CXOHDFN J123701.47+621845.9	< 2.35
CXOHDFN J123701.99+621122.1	< 3.12
CXOHDFN J123706.12+621711.9	< 2.06
CXOHDFN J123715.94+621158.3	< 4.58
CXOHDFN J123721.60+621246.8	< 3.47
CXOHDFN J123723.45+621047.9	< 4.58
CXOHDFN J123727.71+621034.3	< 4.21
CXOHDFN J123730.60+620943.1	< 2.11

$\times 11.8$  arcsec at 325 MHz, and  $7.1 \times 4.9$  arcsec at 610 MHz (see Table 4.1). The respective rms noise in the maps at each frequency are 1.4, 0.6, and 0.8 mJy/beam. No radio counterparts of the ULX sources located in the CDFs are detected in a circle radius for each ULX position of 28 arcsec, which is more than 10 times the *Chandra* positional error. Upper limits on their flux densities at each frequency are given in Table 4.4 (for ULXs located in the CDFN) and Table 4.5 (ULXs in the CDFS), obtained by estimating the local rms at the ULX locations. These upper limits range between 2–4.6 mJy at 235 MHz, 1–2.5 mJy at 332 MHz, and 0.5–2 mJy at 610 MHz. The position of only three ULX sources falls in the images at 610 MHz, thus only 3 upper limits are given at this frequency.

#### 4.2.3.2 Milliarcsecond-scale compact radio emission in ULX sources

The EVN observations of N4449-X4 confirm the earlier identification of this object as a SNR, resolving its shell-like structure and obtaining the most accurate estimates of its size and age. A detailed discussion of this object is given in Sect. 4.7.

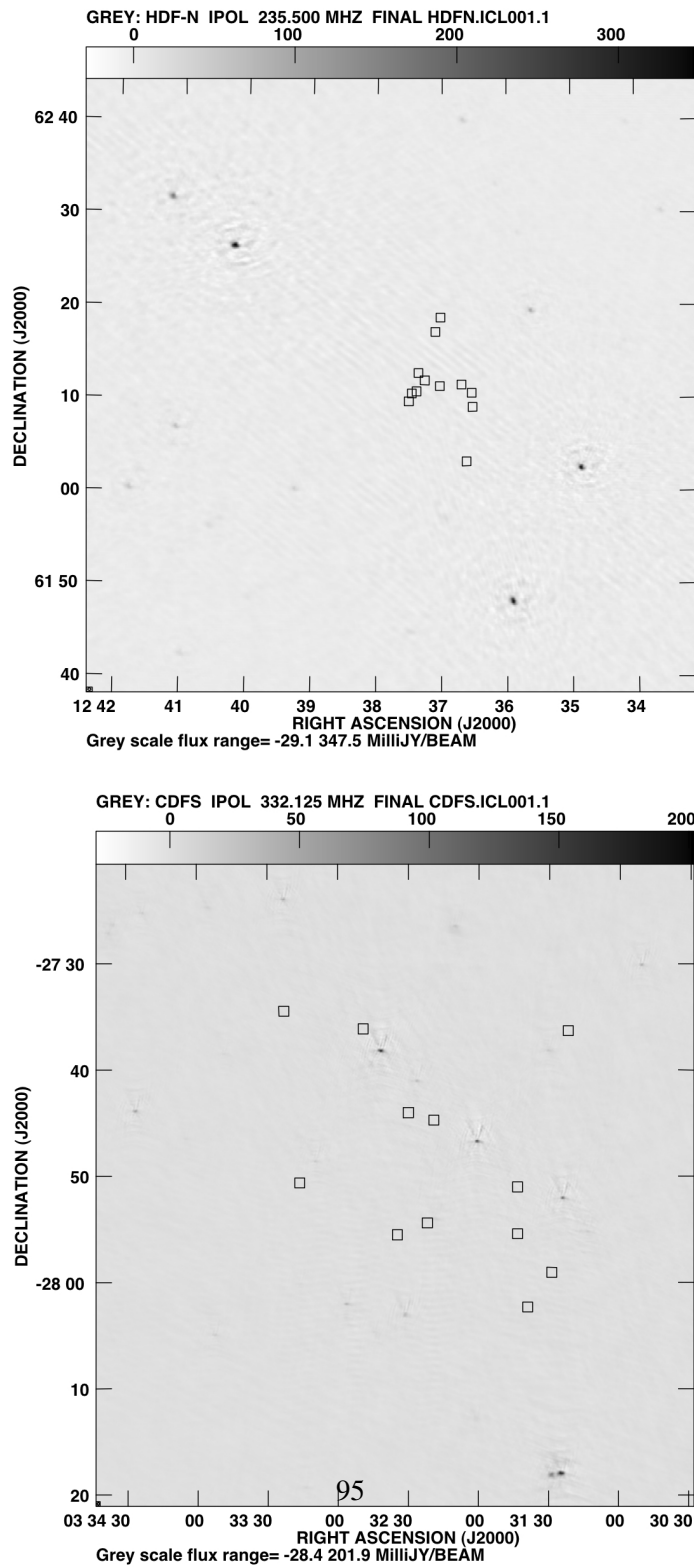


FIGURE 4.1— GMRT images of the HDFN at 235 MHz (top) and the CDFS at 325 MHz (bottom). The restoring beam sizes are  $20.1 \times 16.3$  arcsec at 235 MHz and  $13.7 \times 11.8$  arcsec at 325 MHz. The best rms sensitivities achieved are 1.4 and 0.6 mJy/beam, respectively. The ULXs positions are marked with squares.

TABLE 4.5— Upper limits on the flux densities at 332MHz and 610MHz of the ULXs in the CDFS and ECDFS

Name	$S_{332\text{MHz}}$ [mJy/beam]	$S_{610\text{MHz}}$ [mJy/beam]
CXOECDFS J033122.00-273620.1	< 1.17	...
CXOECDFS J033128.84-275904.8	< 1.38	...
CXOECDFS J033139.05-280221.1	< 1.38	< 1.62
CXOECDFS J033143.46-275527.8	< 1.45	...
CXOECDFS J033143.48-275103.0	< 1.63	...
CXOECDFS J033219.10-274445.6	< 1.85	...
CXOECDFS J033221.91-275427.2	< 2.39	...
CXOECDFS J033230.01-274404.0	< 1.63	...
CXOECDFS J033234.73-275533.8	< 1.28	...
CXOECDFS J033249.26-273610.6	< 2.98	...
CXOECDFS J033316.29-275040.7	< 0.99	< 0.66
CXOECDFS J033322.97-273430.7	< 1.08	< 0.80

The final images of NGC 4088-X1 and NGC 4861-X2 are shown in Fig. 4.2, top and bottom, respectively. The rms noises achieved are  $26\mu\text{Jy/beam}$  for NGC 4088-X1 and  $3\mu\text{Jy/beam}$  for NGC 4861-X2, and the restoring beams  $31 \times 29$  mas and  $11 \times 5$  mas, respectively. For NGC 4088-X1, we identify a compact component of flux density 0.1 mJy at a  $5\sigma$  level. The component is centered at:

$$\begin{aligned} \text{RA(J2000)} &= 12^{\text{h}}05^{\text{m}}31.7110^{\text{s}} \pm 0.0003^{\text{s}}, \\ \text{DEC(J2000)} &= 50^{\circ}32'46.729'' \pm 0.002''. \end{aligned}$$

For this component, the fit of a two-dimensional elliptical gaussian to the peak of radio emission yields an estimate of the brightness temperature of  $T_{\text{B}} > 7 \times 10^4$  K and an upper limit of  $34 \times 26$  mas for the size. Adopting a distance for NGC 4088-X1 of 13.0 Mpc yields an integrated 1.6 GHz radio luminosity of  $3.8 \times 10^{34}$  erg  $\text{s}^{-1}$ .

The ULX NGC 4861-X2 (Fig. 4.2, bottom) has a compact component A centered at:

$$\begin{aligned} \text{RA(J2000)} &= 12^{\text{h}}59^{\text{m}}00.3563037^{\text{s}} \pm 0.0000008^{\text{s}}, \\ \text{DEC(J2000)} &= 34^{\circ}50'42.87500'' \pm 0.00002''. \end{aligned}$$

It has a flux density of  $\sim 80\mu\text{Jy}$  (for which we derive a radio luminosity  $L_{1.6\text{GHz}} = 3.3 \times 10^{34}$  erg  $\text{s}^{-1}$  (assuming a distance to the host galaxy of 14.80 Mpc),

and an upper limit on the size of  $9.8 \times 3.8$  mas, corresponding to a brightness temperature  $T_B > 1.1 \times 10^6$  K. Two additional components (B and C) with a total flux density of  $\sim 70 \mu\text{Jy}$  seem to be detected, but cannot be firmly localized with the present data. If this extension were confirmed, the whole structure (including component A, B & C) would have a total flux density of 0.18 mJy, a luminosity  $L_{1.6\text{GHz}} = 7.7 \times 10^{34}$  erg s $^{-1}$ , and diameter  $D \sim 120$  mas.

#### 4.2.4 Discussion

##### 4.2.4.1 ULX sources in the Chandra Deep Fields

The 24 ULXs located in the CDFN, CDFS, and ECDFS have been suggested to be coincident with giant HII regions (Lehmer et al. 2006) or formed in star forming regions, possibly as the end product of fast evolving massive stars, and could link the ULX phenomenon with IMBHs. On the other hand, the X-ray luminosity dependence on the nuclear distance for this sample of ULXs (Lobanov 2007) suggests that ULX objects may harbor secondary black holes in post-merger galaxies. In both cases the behavior of these ULXs in the fundamental plane of accreting black holes (Corbel et al. 2003; Gallo et al. 2003; Merloni et al. 2003; Falcke et al. 2004) could help to clarify their nature. This fundamental plane is a correlation between radio core luminosity ( $L_R$ ), X-ray ( $L_X$ ) luminosity, and black hole mass ( $M_{\text{BH}}$ ), valid for both low/hard state and quiescent X-ray binaries and their equivalent low-luminosity AGN (LLAGN, i.e., FRI radio galaxies, BL Lacs and LINERs) accreting at sub-Eddington rates (e.g.,  $\sim 0.01 - 0.1 \dot{M}_{\text{Edd}}$ ):

$$\log L_R = 0.6 \log L_X + 0.78 \log M_{\text{BH}} + 7.33 \quad (4.1)$$

where a typical radio optically thick spectral index of  $\alpha_R \simeq 0.15$  and a X-ray optically thin spectral index of  $\alpha_X \simeq -0.6$  have been adopted (Falcke et al. 2004). Given the  $L_R$  and  $L_X$  of a source, an estimate of the black hole mass  $M_{\text{BH}}$  (assuming sub-Eddington accretion rate) can be obtained from the location of the source in the three dimensional  $\log L_R$ ,  $\log L_X$ ,  $\log M_{\text{BH}}$  space (parallel lines in Fig. 4.3). The location of the X-ray binary GX 339-4 (Corbel et al. 2003) and of some LLAGN (NGC 2787, NGC 3147, NGC 3169, NGC 3226, and NGC 4143; Merloni et al. 2003) are shown for comparison.

The correlation parameters of the equation above were determined using the X-ray band of 2-10 keV and the monochromatic radio luminosity at 5 GHz (Merloni et al. 2003; Falcke et al. 2004). We consequently use the spectral indices quoted above to scale to this X-ray band the 0.5-8.0 keV luminosities

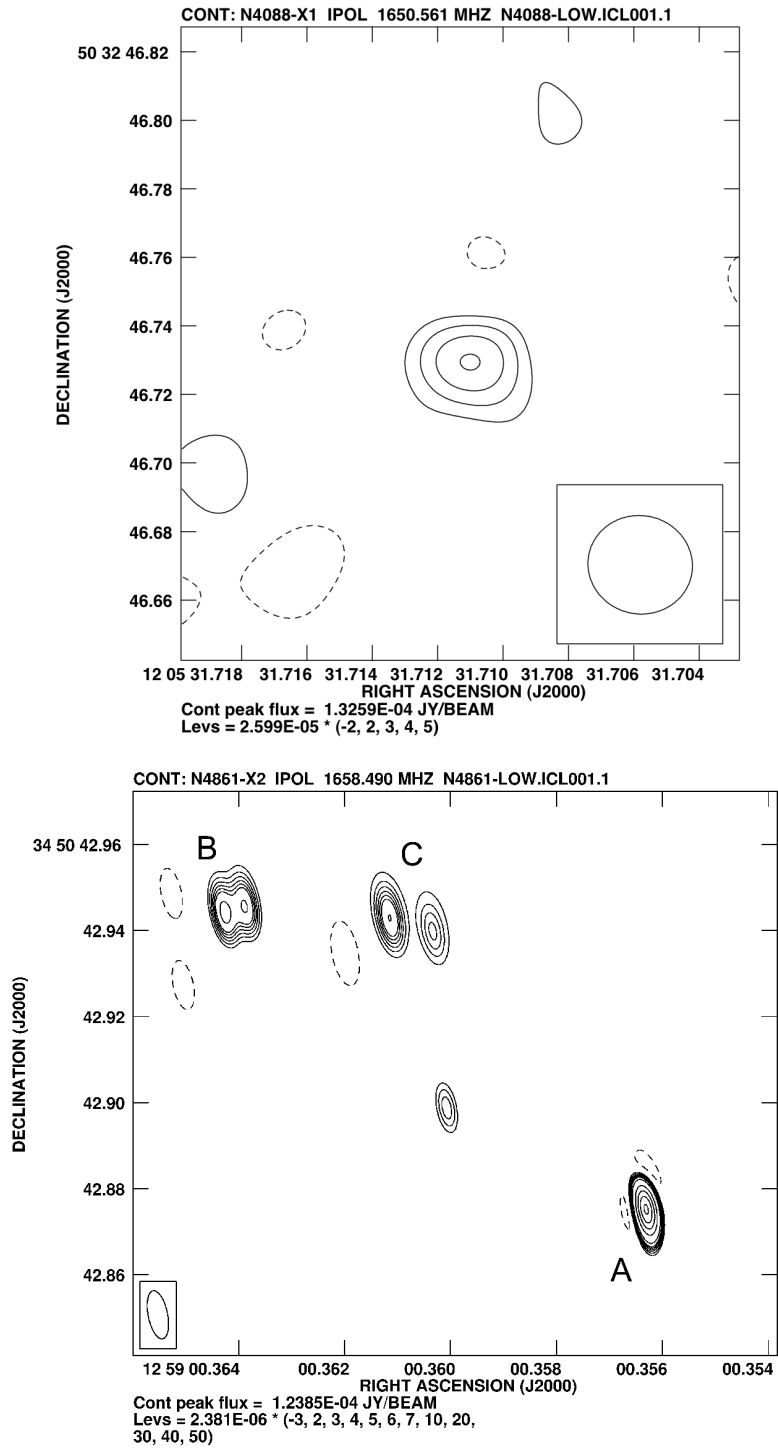


FIGURE 4.2— 1.6 GHz EVN images of the ULX sources NGC 4088-X1 (top) and NGC 4861-X2 (bottom). The restoring beam sizes are  $31 \times 29$  mas for NGC 4088-X1 and  $11 \times 5$  mas for NGC 4861-X2, with the major axis of the beam oriented along a position angle of  $21.99^\circ$  for NGC 4088-X1 and  $11.36^\circ$  for NGC 4861-X2. The contours for the top image are  $(-2, 2, 3, 4, 5) \times 26 \mu\text{Jy}/\text{beam}$ , the rms noise off-source. For the ULX at the bottom, the contours are  $(-3, 2, 3, 4, 5, 6, 7, 10, 20, 30, 40, 50) \times 3 \mu\text{Jy}/\text{beam}$ . The compact component of NGC 4861-X2 is indicated with an A. Possible extended emission may be detected in regions B and C.

of the 24 ULX sources taken from Lehmer et al. (2006) (see their Table 1), and to scale to 5 GHz the upper limits on the radio luminosities derived from the flux densities in Tables 4.4–4.5. The resulting radio and X-ray luminosities of the ULX objects in our sample are compared in Fig. 4.3 to the results of Corbel et al. (2003) and Merloni et al. (2003). The resulting upper limits on the BH masses do not provide strong constraints on the nature of these ULX objects.

Deep radio surveys of the HDFN, CDFS, and ECDFS with higher sensitivity at 1.4 GHz and 4.8 GHz have been done by several authors (e.g., Bauer et al. 2002; Rovilos et al. 2007; Kellermann et al. 2008). Some of the radio detected X-ray sources presented at these higher frequencies are coincident with the off-nuclear X-ray sources from Lehmer et al. (2006) and are thus potential radio counterparts of ULX objects. In the 40  $\mu$ Jy VLA survey at 1.4 GHz (Bauer et al. 2002), a radio counterpart to the ULX CXOHDFN J123641.8+621132 is found. A lower limit to the radio spectral slope  $\alpha_R$  (where  $S \propto \nu^{-\alpha_R}$ ) of  $\alpha_R > 0.56$  is derived using the detected 1.4 GHz flux density and an upper limit of the 8.5 GHz flux density (Bauer et al. 2002). Using their 1.4 GHz flux density and the upper limit on the flux density at 235 Mz reported in Table 4.4, we derive a spectral slope of  $\alpha_R < 2.76$ , constraining the value to  $0.56 < \alpha_R < 2.76$ . We scale the 1.4 GHz flux density to 5 GHz using a power-law spectral index of 0.56 and of 2.76, which yields a radio luminosity  $6 \times 10^{35} \text{ Jy} < L_R < 10^{37} \text{ erg s}^{-1}$ . Applying the fundamental plane of accreting BHs, an estimate BH mass range of  $10^5 < M_{\text{BH}} < 10^7 M_{\odot}$  is obtained (indicated with a double arrow in Fig. 4.3). This value is in agreement with the classification of this source as an emission-line galaxy (Bauer et al. 2002).

In the 1.4 GHz and 5 GHz VLA surveys (Kellermann et al. 2008), a radio counterpart to the ULX sources CXOECDFS J033143.46-275527.8, CXOECDFS J033143.48-275103.0, CXOECDFS J033230.01-274404.0, CXOECDFS J033234.73-275533.8, and CXOECDFS J033316.29-275040.7 is detected within an effective angular resolution of  $3.5''$ . The respective spectral indices vary from 0.1 to 1.2 and, in all cases, the radio emission is believed to be due to synchrotron emission from relativistic electrons (Kellermann et al. 2008). Using the radio luminosity at 5 GHz derived from the flux density given in Kellermann et al. (2008), and the fundamental plane of accreting black holes, a range of BH masses for these 5 ULX sources of  $(7\text{--}40) \times 10^7 M_{\odot}$  (Fig. 4.3, open squares) is estimated. These results agree with the suggestion that the radio emission comes from regions of active star formation and low-luminosity AGN (Kellermann et al. 2008). It should be noted that this radio emission accounts for the emission of the whole ULX host galaxy and not for

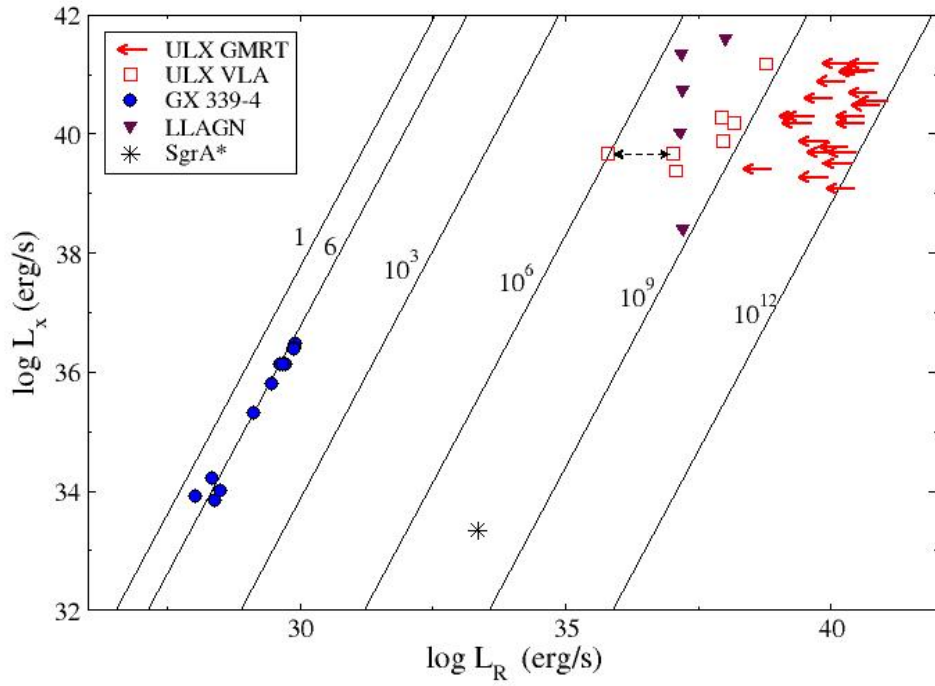


FIGURE 4.3— Location of the 24 ULXs in the fundamental plane of accreting black holes, using the GMRT upper limits on the radio flux density to derive the radio luminosities (solid arrows). Open squares: the six ULX sources with VLA radio counterparts detected (Bauer et al. 2002; Kellermann et al. 2008). The dashed double arrow indicates an estimated BH mass range of  $10^5 < M_{\text{BH}} < 10^7 M_{\odot}$  for the ULX CXOHDFN J123641.8+621132. The parallel lines correspond to the labeled black hole mass relative to that of the Sun. We show for comparison the Corbel et al. (2003) data for the X-ray binary GX 339-4 (filled circles), the Merloni et al. (2003) data for the Low Luminosity AGN (LLAGN) NGC 2787, NGC 3147, NGC 3169, NGC 3226, and NGC 4143 (inverted triangles), and Sgr A\* (asterisk).



the ULX alone. Higher resolution observations would be needed to disentangle the contribution of the ULX sources to the whole radio emission.

#### 4.2.4.2 Milliarcsecond-scale compact radio emission in ULX objects

For NGC 4088-X1, we estimate a lower limit on  $T_B$  of  $7 \times 10^4$  K. Given this lower limit on the brightness temperature and that the ULX remains unresolved, we can assume that this compact radio source is a black hole accreting at a sub-Eddington rate and apply the radio/X-ray correlation (e.g., Merloni et al. 2003; Falcke et al. 2004) to derive a hypothetical black hole mass. Scaling our radio luminosity at 1.6 GHz to 5 GHz assuming a power-law index of  $\alpha_R = 0.15$  (Falcke et al. 2004), and the X-ray luminosity to the 2-10 keV band using  $\alpha_X = -0.6$  (Falcke et al. 2004), we derive a black hole mass of  $1 \times 10^5 M_\odot$  (see Fig. 4.4, filled square). This value is in the regime of masses expected for intermediate mass black holes. The same correlation was used to locate the source in the black hole mass range  $10^6$ - $10^9 M_\odot$  (Sánchez-Sutil et al. 2006), thus suggesting that the ULX would be a background AGN unrelated to the host galaxy. However, López-Corredoira & Gutiérrez (2006) provided a clean sample of 25 ULX sources to be most probable real ULXs or to have a low probability of being contaminant foreground/background AGN/QSOs. NGC 4088-X1 is included in this sample, with a probability of being a background QSO of  $\sim 10^{-3}$ .

For NGC 4861-X2 we recover a compact component A and a possible extended structure (components B and C; see Fig 4.2 right). If this extended emission were confirmed, the whole structure would have a diameter  $D \sim 120$  mas (largest distance between A and B), which corresponds to 8.6 pc at the distance of the host galaxy. This size is in agreement with the typical size of HII regions found in our Galaxy (e.g., G18.2-0.3, which has a size of 200 mas, a luminosity of  $L_{1.4\text{GHz}} = 1.1 \times 10^{33}$  erg s $^{-1}$ , and is formed by several discrete sources; Fuerst et al. 1987). Therefore, NGC 4861-X2 could be either a clump of individual HII regions like G18.2-0.3 or an HII region of  $D \sim 8.6$  pc and  $L_{1.6\text{GHz}} = 7.7 \times 10^{34}$  erg s $^{-1}$ . Indeed, the source was already suggested to coincide or lie very close to a very intense and large HII region of diameter  $D \sim 1$  kpc (Pakull & Mirioni 2002; Pakull, private communication), but this size is much larger than our not-confirmed extended structure. On the other hand, if the whole structure consists of a very intense HII region, it would have a  $T_B \geq 10^5$  K. The minimum detectable brightness temperature with the EVN at 1.6 GHz is  $\sim 10^5$  K, therefore the extended structure should be at least barely detectable if we were dealing with such a bright HII region. This leads

to another scenario in which NGC 4861-X2 is solely formed by the compact component A, of size  $9.8 \times 3.8$  mas and  $L_{1.6\text{GHz}} = 3.3 \times 10^{34}$  erg s $^{-1}$ . If we assume that this compact radio source is a sub-Eddington accreting black hole and apply the fundamental plane (Eq. 4.1) to the consequently scaled radio and X-ray luminosities, a black hole mass of  $7 \times 10^4 M_{\odot}$  can be derived (Fig. 4.4). This mass is in agreement with an IMBH, and the source has a probability  $\sim 10^{-4}$  of being a background AGN (López-Corredoira & Gutiérrez 2006). Therefore, NGC 4861-X2 would be another candidate for an IMBH.

### 4.3 Mass limits of ULXs

Determining, or at least constraining, the ULX BH mass ( $M_{\text{BH}}$ ) is pivotal for revealing the physical mechanism producing their high X-ray luminosities. Several methods can be used to derive the  $M_{\text{BH}}$ , the most reliable one being the optical study of the stellar companion in HMXBs, either photometric (e.g., Pakull & Mirioni 2003; Patruno & Zampieri 2010) or spectroscopic (e.g., Pakull et al. 2006; Kaaret & Corbel 2009; Cseh et al. 2011a). However, due to their faintness only in a very few cases a ULX optical counterpart can be detected. Alternatively, some indirect methods can be used in the X-ray domain including: X-ray spectral fitting together with the luminosity-temperature diagram (e.g., Miller et al. 2003; Gonçalves & Soria 2006; Gladstone & Roberts 2009; Strateva & Komossa 2009), quasi-periodic oscillations (QPOs) frequency scaling with  $M_{\text{BH}}$  (e.g., Strohmayer & Mushotzky 2003; Strohmayer et al. 2007), the correlation between X-ray photon index and  $L/L_{\text{Edd}}$  (e.g., Shemmer et al. 2008), or X-ray variability (e.g., Soria et al. 2004; Heil et al. 2009).

We have seen that, under the assumption of sub-Eddington accretion, the radio luminosity can be used together with the X-ray luminosity to estimate the  $M_{\text{BH}}$  by means of the fundamental plane of accreting black holes (Corbel et al. 2003; Gallo et al. 2003; Merloni et al. 2003; Falcke et al. 2004). In this section, all the ULX sources for which a radio counterpart has been detected are compiled. These data are used to derive the  $M_{\text{BH}}$  and the radio to X-ray flux ratio, which give us a hint on the most likely nature of the ULX sources under study. A comparison of the derived  $M_{\text{BH}}$  with the ones obtained by other means (in the optical and X-ray domains) is discussed.

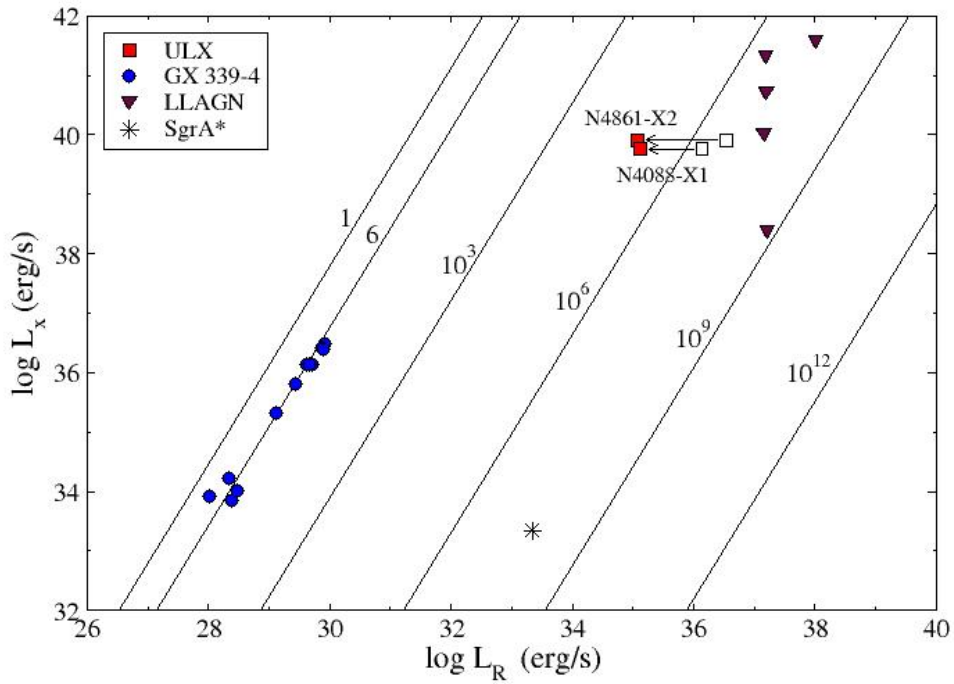


FIGURE 4.4— Old (Sánchez-Sutil et al. 2006, open squares) and new (this work, filled squares) location of the ULX sources NGC 4088-X1 and NGC 4861-X2 in the fundamental plane of accreting black holes. The parallel lines correspond to the labeled black hole mass relative to that of the Sun. We show for comparison the Corbel et al. 2003 data for the X-ray binary GX 339-4 (filled circles), the Merloni et al. (2003) data for the Low Luminosity AGN (LLAGN) NGC 2787, NGC 3147, NGC 3169, NGC 3226, and NGC 4143 (inverted triangles), and Sgr A\* (asterisk).

### 4.3.1 Data

A list of all the ULX sources with detected radio counterparts is presented in Table 4.6. The columns listed are: right ascension and declination J2000 coordinates (Col. 1 and 2, respectively); X-ray luminosity in the 2-10 keV band ( $L_X$ , Col. 3); integrated radio luminosity at 5 GHz ( $L_R$ , Col. 4); distance to nucleus of host galaxy (Col. 5); and references (Col. 6). All those ULXs reported in the literature to be background radio galaxies and AGN or confirmed supernova remnants (SNR) are not included in the data. The values of  $L_X$  and  $L_R$  of the sources M81-X1, NGC 5457-X1, NGC 5457-X2, NGC 5204-X1, and NGC 4736-X2 are taken from Körding et al. (2005), Table 6. Their value of the continuum radio luminosity instead of the flaring luminosity is taken as  $L_R$ , since the radio/X-ray correlation (Falcke et al. 2004) should not be valid for flares. For the sources NGC 4736-X2, NGC 5204-X1, NGC 5457-X1 and NGC 5457-X2 an upper limit to the radio luminosities is given. The X-ray luminosity of NGC 5408-X1 derived from Cseh et al. (2011a) has been scaled to the 2-10 keV band using a photon index ( $\Gamma$ ) of 2.36. The X-ray luminosities of NGC 4395-X2, NGC 4490-X1, and NGC 5194-X2 have been scaled to 2-10 keV using  $\Gamma=5.11$ , 3.38, and 1.86, respectively (Swartz et al. 2004). For NGC 4395-X2, NGC 4559-X4, NGC 5457-X9, NGC 5457-X17, NGC 5457-X26, NGC 4088-X1 and NGC 4861-X2, the  $L_X$  and  $L_R$  have been scaled to the 2-10 keV band and to 5 GHz using a power-law index of -0.6 and 0.15, respectively (Falcke et al. 2004).

The six ULXs located in the Chandra Deep Fields and with detected radio counterparts (see Sect. 5.6), as well as the sources NGC 4088-X1 and NGC 4861-X2 are also included in the analysis.

### 4.3.2 Analysis

Using the values of  $L_X$  and  $L_R$  given in Table 4.6 and the fundamental plane of accreting black holes (Eq. 4.1), an estimate of the ULXs black hole mass is derived. Locations of the ULXs in the fundamental plane are shown with squares in Fig. 4.5 and the estimated values of the  $M_{BH}$  are listed in Table 4.7. The empty squares in Fig. 4.5 correspond to those ULXs found in the Chandra Deep Fields (Lehmer et al. 2006) whose radio counterparts do not solely belong to the ULXs but include also host galaxy contribution. They are thus included in the plot as a separate sample.

To further disentangle the possible nature of the ULXs, we use the ratio of 6 cm radio emission to 2-10 keV X-ray emission  $R_X \equiv L_R/L_X =$

TABLE 4.6— ULX sources with detected radio counterparts

Name	RA (J2000)	DEC (J2000)	$L_X$ [erg s <sup>-1</sup> ]	$L_R$ [erg s <sup>-1</sup> ]	Distance [kpc]	References
(1)	(2)	(3)	(4)	(5)	(6)	(7)
CXOCDFS J033230.01-274404.0	03:32:30.01	-27:44:04.0	$2 \times 10^{40}$	$< 1 \times 10^{38}$	1.31	1,2
CXOCDFS J033234.73-275533.8	03:32:34.73	-27:55:33.8	$2 \times 10^{39}$	$< 1 \times 10^{37}$	3.55	1,2
CXOECDFS J033143.46-275527.8	03:31:43.46	-27:55:27.8	$8 \times 10^{39}$	$< 9 \times 10^{37}$	3.49	1,2
CXOECDFS J033143.48-275103.0	03:31:43.48	-27:51:03.0	$2 \times 10^{41}$	$< 6 \times 10^{38}$	9.28	1,2
CXOECDFS J033316.29-275040.7	03:33:16.29	-27:50:40.7	$2 \times 10^{40}$	$< 9 \times 10^{37}$	5.47	1,2
CXOHDFN J123641.81+621132.1	12:36:41.81	+62:11:32.1	$5 \times 10^{39}$	$(6-100) \times 10^{35 a}$	2.04	3
Holmberg II	08:19:28.8	+70:42:20.3	$8 \times 10^{39}$	$5 \times 10^{34}$	2.04	4
IC 342-X1	03:45:55.61	+68:04:55.3	$6 \times 10^{39}$	$6 \times 10^{33}$	4.83	5
M82-X1	09:55:51.0	+69:40:45	$6 \times 10^{39}$	$3 \times 10^{35}$	0.16	6
NGC 3256-X13	10:27:52.9	-43:54:11.8	$1 \times 10^{39}$	$1 \times 10^{37}$	–	7
NGC 3877 (near nuclear ULX)	11:46:08.0	+47:29:39	$8 \times 10^{38}$	$4 \times 10^{36}$	0.58	8
NGC 4088-X1	12:05:32.02	+50:32:48.8	$6 \times 10^{39}$	$1 \times 10^{35}$	2.29	9
NGC 4395-X2	12:25:32.31	+33:25:34.0	$3 \times 10^{38}$	$6 \times 10^{35}$	18.87	10
NGC 4490-X1	12:30:36.47	+41:38:39.8	$9 \times 10^{38}$	$1 \times 10^{36}$	0.66	11
NGC 4559-X4	12:35:56.57	+27:59:22.4	$2 \times 10^{38}$	$2 \times 10^{36}$	0.87	1
NGC 4736-X2	12:50:53.3	+41:07:14	$1 \times 10^{39}$	$< 9 \times 10^{33}$	2.82	6
NGC 4861-X2	12:59:00.45	+34:50:41.3	$8 \times 10^{39}$	$1 \times 10^{35}$	4.95	9
NGC 5194-X2	13:29:50.67	+47:11:55.0	$2 \times 10^{39}$	$6 \times 10^{35}$	–	12
NGC 5204-X1	13:29:38.6	+58:25:06	$2 \times 10^{39}$	$< 7 \times 10^{33}$	0.40	6
NGC 5408-X1	14:03:19.62	-41:23:00.2	$3 \times 10^{38}$	$4 \times 10^{34}$	1.14	13,14
NGC 5457-X1	14:03:32.4	+54:21:03	$2 \times 10^{39}$	$< 9 \times 10^{33}$	4.15	6
NGC 5457-X17	14:02:28.43	+54:16:24.0	$9 \times 10^{38}$	$2 \times 10^{35}$	11.36	6
NGC 5457-X2	14:04:14.3	+54:26:04	$1 \times 10^{39}$	$< 9 \times 10^{33}$	15.03	10
NGC 5457-X26	14:04:29.41	+54:23:56.7	$6 \times 10^{38}$	$6 \times 10^{35}$	16.77	10
NGC 5457-X9	14:03:41.19	+54:19:02.5	$3 \times 10^{38}$	$1 \times 10^{36}$	6.63	10

**Column designation:** (1) – ULX name ; (2) – right ascension (J2000 coordinates) ; (3) – declination (J2000 coordinates) ; (4) – Integrated X-ray luminosity in the (2-10 keV) band ; (5) – Integrated radio luminosity at 5 GHz ; (6) – distance to the nucleus of the ULX host galaxy ; (7) – references for the X-ray and radio luminosity. **Notes:** *a* – Radio luminosities scaled to 5 GHz using a power-law index  $-2.76 < \alpha < -0.56$ .

REFERENCES.– (1) Lehmer et al. (2006); (2) Kellermann et al. (2008); (3) Bauer et al. (2002); (4) Miller et al. (2005a); (5) Cseh et al. (2011b); (6) Körding et al. (2005); (7) Neff et al. (2003); (8) Miller et al. (2005b); (9) this thesis; (10) Sánchez-Sutil et al. (2006); (11) Mushotzky (2004); (12) Pérez-Ramírez et al. (2011); (13) Cseh et al. (2011a); (14) Lang et al. (2007).

$\nu L_\nu(5 \text{ GHz})/L_X(2-10 \text{ keV})$ , as defined by Terashima & Wilson (2003). Values of this ratio for all the ULXs and for different comparison objects (i.e., flaring X-ray transients, a cluster of hot stars, the galactic supernova remnant Cas A, and several LLAGNs) are given in Table 4.7, col. 3 (see as well Neff et al. 2003).

### 4.3.3 Discussion

All the ULXs whose radio counterpart have no contribution from the host galaxy (filled squares in Fig. 4.5) lay in the range of BH masses  $10^3 - 10^8 M_\odot$  (19 ULXs). This conclusion is obtained under the assumption that the ULX radio emission comes from a black hole accreting at sub-Eddington rate ( $0.1\dot{M}_{\text{Edd}}$ ). The range of masses would shift by an order of magnitude if the accretion were near-Eddington, e.g.,  $10^2 < M_{\text{BH}} < 10^7 M_\odot$  at  $\sim 0.9\dot{M}_{\text{Edd}}$ . Of the 19 sources, 58% (11 sources) lay in the range of masses expected for IMBHs. The ratio  $R_X$  of these 11 sources spans  $10^{-7} < R_X < 10^{-4}$ , similar to the ratio of Galactic X-ray binaries in a transient outburst phase from a quiescent state to an either high/soft or low/hard state (Fender & Kuulkers 2001). The values obtained suggest that these ULXs might be either beamed X-ray binaries (microblazar scenario) or unbeamed binaries harboring IMBHs. The later would be in agreement with the results obtained from the fundamental plane of accreting black holes, which is valid for both low/hard state and quiescent (low luminosity hard) state X-ray binaries (Falcke et al. 2004).

The sample of ULX sources whose radio counterparts are contaminated by the host galaxy radio emission (empty squares in Fig. 4.5) are located in late-type and irregular galaxies and two of them (CXOCDFS J033230.01-274404.0 and CXOHDFN J123641.81+621132.1) are coincident with optical knots of emission (Lehmer et al. 2006). For the ULX CXOHDFN J123641.8+621132, an estimated BH mass range of  $10^5 < M_{\text{BH}} < 10^7 M_\odot$  was derived in Sect. 5.6 and is in agreement with the classification of this source as an emission-line galaxy. The  $R_X \sim 10^{-3}$  found for this ULX is similar to the typical value of LLAGN and is thus in agreement with such a classification. For the other 5 ULX sources in the CDFs (CXOECDFS J033143.46-275527.8, CXOECDFS J033143.48-275103.0, CXOCDFS J033230.01-274404.0, CXOCDFS J033234.73-275533.8, and CXOECDFS J033316.29-275040.7) a range of BH masses of  $(7-40) \times 10^7 M_\odot$  was estimated in Sect. 5.6. For CXOECDFS J033143.46-275527.8 we find a  $R_X \sim 10^{-2}$  very similar to Cas A, which suggests a supernova remnant origin for the high X-ray luminosity of this ULX. If the radio emission comes from the SNR shell, the assumption of

TABLE 4.7— Estimated  $M_{\text{BH}}$  and radio/X-ray ratio of ULXs and comparison objects

Name	$M_{\text{BH}}(M_{\odot})^a$	$R_{\text{X}}^b$	Comments
CXOCDFS J033230.01-274404.0	$< 4 \times 10^8$	$1 \times 10^{-2}$	Host galaxy contribution
CXOCDFS J033234.73-275533.8	$< 7 \times 10^7$	$5 \times 10^{-3}$	Host galaxy contribution
CXOECDFS J033143.46-275527.8	$< 4 \times 10^8$	$1 \times 10^{-2}$	Host galaxy contribution
CXOECDFS J033143.48-275103.0	$< 4 \times 10^8$	$4 \times 10^{-3}$	Host galaxy contribution
CXOECDFS J033316.29-275040.7	$< 2 \times 10^8$	$5 \times 10^{-3}$	Host galaxy contribution
CXOHDFN J123641.81+621132.1	$(9 - 300) \times 10^5$	$(0.1 - 2) \times 10^{-3}$	Host galaxy contribution
Holmberg II	$2 \times 10^4$	$6 \times 10^{-6}$	-
IC 342-X1	$2 \times 10^3$	$1 \times 10^{-6}$	-
M82-X1	$3 \times 10^5$	$5 \times 10^{-5}$	-
NGC 3256-X13	$1 \times 10^8$	$1 \times 10^{-2}$	-
NGC 3877 (near nuclear ULX)	$4 \times 10^7$	$5 \times 10^{-3}$	-
NGC 4088-X1	$1 \times 10^5$	$2 \times 10^{-5}$	-
NGC 4395-X2	$8 \times 10^6$	$2 \times 10^{-3}$	-
NGC 4490-X1	$2 \times 10^8$	$1 \times 10^{-3}$	-
NGC 4559-X4	$4 \times 10^7$	$9 \times 10^{-3}$	-
NGC 4736-X2	$< 1 \times 10^4$	$< 9 \times 10^{-6}$	-
NGC 4861-X2	$7 \times 10^4$	$1 \times 10^{-5}$	-
NGC 5194-X2	$2 \times 10^6$	$3 \times 10^{-4}$	-
NGC 5204 -X1	$< 6 \times 10^3$	$< 4 \times 10^{-6}$	-
NGC 5408-X1	$2 \times 10^5$	$1 \times 10^{-4}$	-
NGC 5457-X1	$< 8 \times 10^3$	$< 5 \times 10^{-6}$	-
NGC 5457-X2	$< 1 \times 10^4$	$< 9 \times 10^{-6}$	-
NGC 5457-X9	$2 \times 10^7$	$5 \times 10^{-3}$	-
NGC 5457-X17	$1 \times 10^6$	$3 \times 10^{-4}$	-
NGC 5457-X26	$4 \times 10^6$	$9 \times 10^{-4}$	-
X-ray transients	-	$< 2 \times 10^{-5}$	Neff et al. (2003), Table 2
$10^5$ O stars at 37 Mpc	-	$\sim 3$	Neff et al. (2003), Table 2
Cas A	-	$2 \times 10^{-2}$	Neff et al. (2003), Table 2
LLAGN at 20 Mpc	$(1 - 10) \times 10^7$	$\sim 1 \times 10^{-3}$	Neff et al. (2003), Table 2

**Notes:**  $a$  – Black hole mass estimated from the fundamental plane of accreting black holes;

$b$  –  $R_{\text{X}} = \nu L_{\nu}(5 \text{ GHz})/L_{\text{X}}(2\text{-}10 \text{ keV})$ , as defined by Terashima & Wilson (2003).

sub-Eddington accretion rate would then not be valid and the source should be removed from the fundamental plane. For the other 4 ULXs we find  $R_{\text{X}} \sim 10^{-3}$ , which is of the order of magnitude found for LLAGN.

#### 4.3.3.1 Notes on individual sources

##### *Holmberg II*

The variability and fit to the X-ray spectrum of the ULX found in the dwarf galaxy Holmberg II (or UGC 4305) suggests that a black hole binary is the origin of the high X-ray emission observed (Dewangan et al. 2004). The

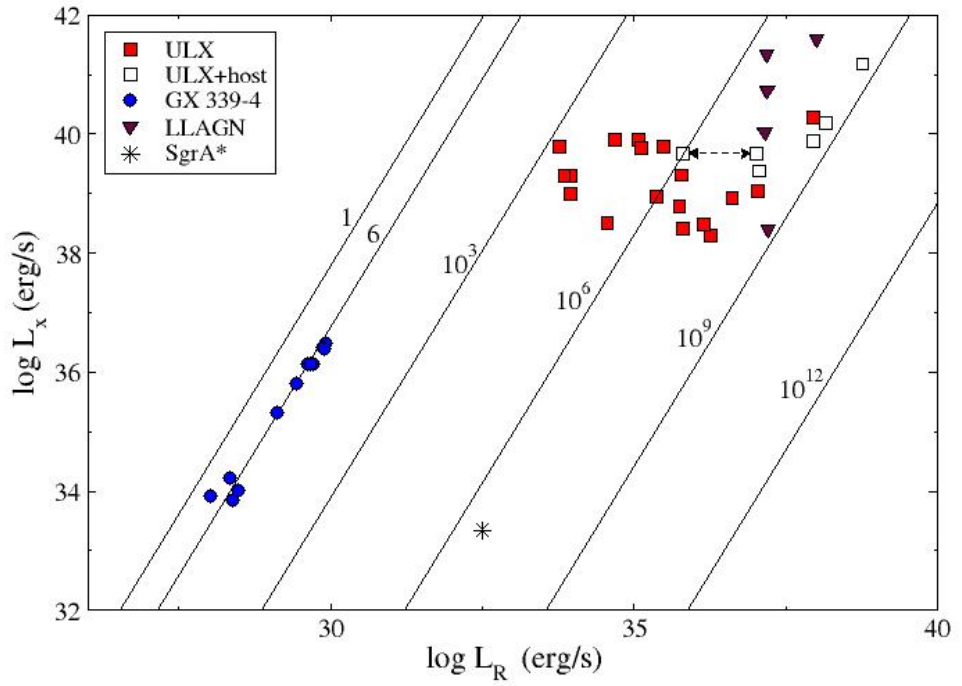


FIGURE 4.5— Location of the ULXs with radio counterparts in the fundamental plane of accreting black holes. Open squares: the six ULX sources with VLA radio counterparts detected by Bauer et al. (2002) and Kellermann et al. (2008). For these sources, the radio emission seems to come both from the ULX and its host galaxy. The double arrow indicates an estimated BH mass range of  $10^5 < M_{\text{BH}} < 10^7 M_{\odot}$  for the ULX CXOHDFN J123641.8+621132. The parallel lines correspond to the labeled black hole mass relative to that of the Sun. We show for comparison the Corbel et al. (2003) data for the X-ray binary GX 339-4 (filled circles), the Merloni et al. (2003) data for some Low Luminosity AGN (inverted triangles), and Sgr A\* (asterisk).



ULX is associated with an optical nebula (Pakull & Mirioni 2003) and shows resolved radio emission, with an effective size of  $2'' \times 1.4''$  (Mushotzky 2004), covering the same physical size as the ionized gas of the nebula ( $\sim 35$  pc; Miller et al. 2005a). The flat radio spectral index of  $-0.29$  (Mushotzky 2004) is indicative of either thermal bremsstrahlung or synchrotron emission and rather unusual for a SNR. The value of  $R_X \sim 10^{-6}$  (Miller et al. 2005b) also rules out the SNR or star-forming region origin but is consistent with microquasar sources and IMBHs. Using the radio flux from Miller et al. (2005b) and a distance of 3.4 Mpc to the host galaxy (Calzetti et al. 2010), we derive a  $M_{\text{BH}} \sim 2 \times 10^4 M_{\odot}$ . Thus, this ULX could harbor an IMBH powering a surrounding nebula as in the case of the ULXs NGC 5408-X1 and IC 342-X1.

#### *IC 342-X1*

The nearby spiral galaxy IC 342 hosts two ULXs suggested to be BH candidates from their X-ray spectra (Kubota et al. 2001). The ULX source X-1 was found to be in the X-ray hard state (Feng & Kaaret 2009) and to be associated with a radio nebula powered by  $9 \times 10^{50}$  erg (similar to NG 5408-X1; Cseh et al. 2011a). The BH mass we have derived from the fundamental plane assuming a distance to IC 342 of 3.3 Mpc (Calzetti et al. 2010) is in agreement with the order of magnitude of  $M_{\text{BH}} \sim 10^4 M_{\odot}$  derived from the shift of the HeII emission line (Cseh et al. 2011b), suggesting that IC 342-X1 would be another potential IMBH candidate.

#### *M82-X1*

The ULX M82-X1 or X41.4+60 (Kaaret et al. 2001) is located in the starburst galaxy M82 at a distance of 3.6 Mpc. The source lays very close to a very dense stellar cluster, shows strong variability, exhibits low-frequency QPOs, and experienced a major X-ray outburst with a duration of 79 days (Kaaret et al. 2009). With a spectrum power-law photon index of 1.6, the ULX is identified as being in the hard state both before and during the outburst. The properties of the detected QPOs are consistent with this state, which validates locating M81-X1 in the fundamental plane for accreting black holes. Scaling the mass with the QPO frequency, an upper limit on the mass of the compact object of  $2.7 \times 10^4 M_{\odot}$  was derived (Kaaret et al. 2009). Using a *Chandra* 2-10 keV luminosity of  $3 \times 10^{40}$  erg  $\text{s}^{-1}$  and an upper limit on the radio flux density (Paragi et al. 2006), these authors obtained an upper bound on the BH mass of  $M_{\text{BH}} < 10^4 M_{\odot}$ . These upper limits are in agreement with the  $M_{\text{BH}} \sim 10^5 M_{\odot}$ .

found by other authors (Körding et al. 2005) and suggests an IMBH nature for this ULX.

#### *NGC 3256-X13*

The merging galaxy NGC 3256 hosts an off-nuclear ULX source whose radio counterpart coincides with the X-ray point source within the *Chandra* positional error (Neff et al. 2003). The radio counterpart is partially resolved and shows a steep radio spectrum (Neff et al. 2003). The radio/X-ray ratio of  $\sim 0.01$  is consistent with a supernova  $\sim 200$  times more powerful than Cas A, a hypernova, or a collection of many SNe (Neff et al. 2003). The location of X13 in the fundamental plane does thus not provide any clue on its nature.

#### *NGC 3877*

The spiral galaxy NGC 3877, located 17 Mpc away, hosts a near-nuclear ULX  $\sim 7''$  away from the optical nucleus (Mushotzky 2004). The position of the ULX at 5 GHz coincides with the *Chandra* position within  $0.5''$  and is resolved with a physical size of  $150 \times 300$  pc, suggesting that its origin could be a giant HII region. However, a flat spectral index of  $\alpha \sim -0.13$  (Mushotzky 2004) and the  $R_X \sim 5 \times 10^{-3}$  suggest a LLAGN rather than an HII region. If the high X-ray luminosity of this ULX comes from a LLAGN, the fundamental plane of accreting black holes can be used to derive an estimate of its BH mass. We obtain  $M_{\text{BH}} \sim 4 \times 10^7 M_{\odot}$ , supporting thus the nature of this source as a LLAGN.

#### *NGC 4088-X1*

The radio counterpart to this ULX has been found to be compact both in the VLA images at 1.4 GHz (Sánchez-Sutil et al. 2006) and in the VLBI (see Sect. 5.5). The location of this ULX in the fundamental plane (see Sect. 5.6) yielded a  $M_{\text{BH}} \sim 10^5 M_{\odot}$ . This value classified NGC 4088-X1 as an IMBH, which is in agreement with the  $R_X \sim 10^{-5}$ .

#### *NGC 4395-X2*

The outskirts of the nearby Sc/Irr galaxy NGC 4395 hosts a ULX located  $\sim 19''$  from the nucleus (Sánchez-Sutil et al. 2006). Its radio counterpart is very compact (Sánchez-Sutil et al. 2006) and the X-ray spectrum is fitted by a very steep power-law index ( $\Gamma > 5$ ; Swartz et al. 2004). The  $M_{\text{BH}} \sim 10^6 M_{\odot}$

estimated from the fundamental plane and the  $R_X \sim 10^{-3}$  suggest that NGC 4395-X2 could be associated with a LLAGN. Given the large ULX-nuclear separation, the possibility that NGC 4395-X2 is a background AGN cannot be ruled out.

#### *NGC 4490-X1*

The spiral galaxy NGC 4490, at a distance of 8 Mpc, shows a distorted morphology in the optical maps due to its interaction with NGC 4485. The ULX X1 is located in a dusty region in NGC 4490 and its X-ray spectrum is fitted by a steep power-law ( $\Gamma > 3$ ; Swartz et al. 2004). Its radio counterpart is resolved with a size of  $75 \times 150$  pc and has a flat spectral index  $\alpha = -0.13$  (Mushotzky 2004). These results, together with the  $R_X \sim 10^{-3}$  and its estimated BH mass of  $\sim 10^8 M_\odot$ , suggest that NGC 4490-X1 could be a LLAGN. Given that the source is located in an interacting galaxy, this ULX could be a secondary BH in the course of a galactic merger with NGC 4490 and NGC 4485.

#### *NGC 4559-X4*

The ULX NGC 4559-X4 is located within a blue HII region in one arm of the nearby spiral galaxy NGC 4559 (Sánchez-Sutil et al. 2006). It has a faint radio counterpart that does not show any extended emission in the VLA image at 1.4 GHz (Sánchez-Sutil et al. 2006). Both the estimated BH mass and  $R_X$  are suggestive of a LLAGN nature for this ULX.

#### *NGC 4736-X2*

NGC 4736 is a spiral galaxy located 4.3 Mpc away and that hosts two ULX sources. For the ULX X2 an upper limit on the radio flux density at 5 GHz was reported (Körding et al. 2005) and is here used to locate this ULX in the fundamental plane of accreting black holes. We find an upper limit on the BH mass of  $10^4 M_\odot$ , thus in the range of IMBH masses, which is in agreement with the  $R_X < 10^{-6}$ .

#### *NGC 4861-X2*

Assuming that this ULX is solely formed by a compact radio component (see Sect. 5.5) yields an estimated BH mass of  $\sim 10^5 M_\odot$  and a ratio  $R_X \simeq 10^{-5}$ , similar to the ratio of Galactic X-ray binaries in a transient outburst phase from

a quiescent state to an either high/soft or low/hard state (Fender & Kuulkers 2001). The compact radio emission of NGC 4861-X2 could be coming from an IMBH.

#### *NGC 5194-X2*

NGC 5194 or the Whirlpool Nebula is an starburst spiral galaxy that forms an interacting system with the galaxy NGC 5195. NGC 5194 is located at a distance of 8.4 Mpc and hosts a total of 7 ULX sources (Swartz et al. 2004). The ULX X2 shows a steep power-law X-ray spectrum (Swartz et al. 2004) and is coincident with a peak of radio emission within  $0.4''$  (Pérez-Ramírez et al. 2011). The location of this ULX in the fundamental plane of accreting black holes yields an estimate of the BH mass of  $\sim 10^6 M_\odot$ . The close location of the ULX to the nucleus of the host galaxy discards a possible background AGN as the origin of the radio emission, but the  $R_X \sim 10^{-4}$  is more indicative of an IMBH or X-ray binary nature.

#### *NGC 5204-X1*

The Magellanic irregular galaxy NGC 5204 is located 4.8 Mpc away and hosts a ULX source offset  $17''$  from the optical nucleus. Both the observed high X-ray variability and the ULX optical counterpart (Roberts et al. 2001; Liu et al. 2004) indicate a HMXB. The radio/X-ray ratio of  $\sim 10^{-6}$  and the upper limit on the BH mass derived using an upper limit on the radio luminosity (Körding et al. 2005) are in agreement with this scenario.

#### *NGC 5408-X1*

This ULX is found in the dwarf irregular galaxy NGC 5408 at a distance of 4.8 Mpc. It is variable and exhibits low-frequency quasi-periodic X-ray oscillations (Strohmayer et al. 2007), which suggests that it is formed by a binary system in the hard state containing a compact object of either stellar-mass with beamed or super-Eddington emission or an IMBH. Its resolved radio emission, with a physical size of 35–46 pc, and radio spectral index of  $-0.8$  indicate optically thin synchrotron emission coming from a radio nebula surrounding the ULX (Lang et al. 2007). This rules out the beamed jet scenario as being the origin of the radio emission and makes NGC 5408-X1 one of the best IMBH candidates. The  $M_{\text{BH}} \sim 10^5 M_\odot$  derived from the fundamental plane is in agreement with this scenario as well as with the X-ray/radio ratio of  $R_X \sim 10^{-4}$ , reinforcing the possible IMBH nature of this

source. Optical observations of this ULX (Cseh et al. 2011a) revealed a shift in the broad component of the HeII line that might be due to the orbital motion of a secondary star. Under this assumption, the compact object would have a maximum BH mass of  $1800 M_{\odot}$  (Cseh et al. 2011a). Although this mass is two orders of magnitude smaller than the one estimated from the radio/X-ray correlation, it falls within the range of masses expected for IMBHs.

#### NGC 5457

M101 or NGC 5457 is a nearby spiral galaxy located 4.97 Mpc away that hosts more than 20 ULXs as detected by *ROSAT* (Liu & Bregman 2005). A radio counterpart to five of the ULX sources has been found with the VLA (Körding et al. 2005; Sánchez-Sutil et al. 2006) and we report here each of them with detail: The ULXs NGC 5457-X1 and NGC 5457-X2 (Körding et al. 2005) found in the *Chandra* ACIS data of February 2003 correspond to the ULX sources X5 and X23, respectively, in the catalog of Liu & Bregman (2005). The upper limits on their radio luminosities (Körding et al. 2005) locate both sources in an upper range of masses of  $M_{\text{BH}} < 10^3 - 10^4 M_{\odot}$  in the fundamental plane for accreting black holes. An IMBH nature for these two ULXs can thus be suggested, although given the upper limit on the masses an association of young stars and SNe could also be possible. The upper limit on the X-ray ratio being  $< 10^{-6}$ , however, discards the stellar cluster scenario and supports an X-ray binary or IMBH origin. Such scenario would be in agreement in the case of NGC 5457-X2 with the fit to its X-ray spectrum, which shows variability and a high photon index indicative of the presence of thermal plasma surrounding the source (Jenkins et al. 2004). This thermal plasma is suggested to come from a HMXB via stellar winds (Jenkins et al. 2004).

NGC 5457-X9 and NGC 5457-X17 (Liu & Bregman 2005) seem to be coincident in the optical with extended regions within the spiral arms of the host galaxy, suggesting that these sources might be associated with star formation. In particular, X17 seems to be coincident with a giant HII region and its X-ray spectrum shows both short-term and long-term variability (Jenkins et al. 2004). This, together with the hard spectrum detected by *ROSAT* (Wang et al. 1999), suggests that the X-ray emission is coming from an X-ray binary embedded in the HII region. On the other hand, the  $M_{\text{BH}}$  of X17 as derived from the  $L_X - L_R$  diagram lies within the range of masses expected for IMBHs. Both an IMBH or a beamed X-ray binary in this ULX would be in agreement with its location within the star-forming region and the fit to the X-ray spectrum. The value of  $R_X \sim 10^{-4}$  does agree as well with the IMBH

or HMXB nature. The ULX X9 is as well coincident with a giant HII region in M101 and, as in X17, the X-ray spectrum fit indicates the presence of an IMBH or a X-ray binary (Jenkins et al. 2004). The values of the BH mass and radio/X-ray ratio found for X9, however, do not match with this scenario but are closer to the ones of LLAGN.

The ULX NGC 5457-X26 is located in the outskirts of the host galaxy and was found to coincide with the optical position of the SNR NGC 5471B (Chu & Kennicutt 1986). Both the thermal plasma energy estimated from the ULX X-ray spectrum (Wang et al. 1999) and optical imaging and spectroscopy with the *HST* (Chen et al. 2002) suggested that the source could be a hypernova remnant (HNR). The lack of variability of its X-ray spectrum lends further support to this scenario, although the very soft spectrum shown by *ROSAT* indicates that the source could be as well a supersoft source (SSS) associated to an X-ray binary as the ones found in other galaxies (Di Stefano & Kong 2004). A sub-Eddington accreting black hole as the origin of the observed X-ray luminosity is not supported in any of the two scenarios, but the value of the  $R_X \sim 10^{-4}$  seems to support the X-ray binary nature rather than the HNR for this ULX.

#### **4.4 The shell-like structure of the extragalactic supernova remnant SNR 4449-1**

The young and ultraluminous supernova remnant (SNR) SNR 4449–1 was discovered in the late 1970s (radio, Seaquist & Bignell 1978; optical, Balick & Heckman 1978) in the star-forming galaxy NGC 4449. NGC 4449 is a barred Magellanic-type irregular galaxy hosting a number of areas of extensive star formation (Reines et al. 2008). The galaxy is located at an estimated distance of  $3.82 \pm 0.18$  Mpc (Annibali et al. 2007).

The SNR 4449–1 was identified as a young and very luminous oxygen-rich SNR embedded in an HII region (Blair & Fesen 1998), based on observations in several different wavebands. It was first discovered as a bright, unresolved nonthermal radio source ( $\sim 10$  mJy at 2.7 GHz; Seaquist & Bignell 1978) located approximately  $1'$  North of the nucleus of NGC 4449. A steep spectral index  $\alpha = -0.95 \pm 0.27^1$  (Seaquist & Bignell 1978) in the radio band and observations of both broad and narrow lines in the optical spectrum (Balick & Heckman 1978) indicated that the source was a SNR.

The SNR 4449–1 is one of the few known intermediate-age SNRs, with an age between that of Cas A ( $\sim 330$  yrs; Thorstensen et al. 2001) and those of the oldest known extragalactic radio SNe, like SN 1923A in M83 (83 yrs;

---

<sup>1</sup>The spectral index  $\alpha$  was here defined from  $S_\nu \propto \nu^\alpha$ , where  $S$  is the flux density at frequency  $\nu$

Eck et al. 1998) and SN 1957D, also in M83 (49 yrs; Pennington & Dufour 1983). The SNR in NGC 4449 is also notable as the most luminous and most distant member of the class of oxygen-rich SNRs (Blair et al. 1983). The nature of such a bright luminosity was long suspected to be due to interaction with a surrounding HII region, but *HST* observations (Milisavljevic & Fesen 2008) suggested that the remnant is instead interacting with a very dense circumstellar material from the SNR's progenitor star of mass  $\geq 20 M_{\odot}$ . The remnant possesses the characteristics of typical SNe of massive stars, since it lies inside a rich cluster of high-mass stars surrounded by a presumably SN- and wind-blown Interstellar Medium (ISM) bubble, it is interacting with the dense circumstellar material, and it exhibits the chemical properties of an hydrogen-poor envelope progenitor (Milisavljevic & Fesen 2008).

While the SNR 4449–1 is currently quite luminous, the significant decline in the remnant's X-ray and radio flux over the last three decades implies that it was even brighter in the past. Lacey et al. (2007) combined newer Very Large Array (VLA) observations of NGC 4449 with archive VLA and Westerbork Synthesis Radio Telescope (WSRT) observations to present the lightcurve of the SNR at 6 and 20 cm from 1973 to 2002. The radio flux of the SNR 4449–1 measured at 4.9 GHz has undergone a significant decline over the last three decades, dropping from 13 mJy to 4 mJy between 1973 and 2002 (Lacey et al. 2007).

The SNR 4449–1 was identified as a ULX source, NGC 4449-X4, based on *ROSAT* observations (e.g., Liu & Bregman 2005; Sánchez-Sutil et al. 2006). Application of an absorbed, non-equilibrium ionization model (e.g., Yokogawa et al. 2002) to NGC 4449-X4 yielded an X-ray temperature  $T_X \approx 2.2 \times 10^7$  K in the 0.3-8.0 keV band, a column density of  $N_H = 1.26 \times 10^{21}$  cm $^{-2}$ , and an absorption-corrected luminosity  $L_X = 2.3 \times 10^{38}$  erg s $^{-1}$  (Summers et al. 2003). The X-ray temperature measurement was used to estimate an age of  $\sim 270$  yrs and an ambient medium density of 120-200 cm $^{-3}$  for this SNR (Summers et al. 2003).

VLBI observations made in 1980 and 1981 with the EVN yielded an upper limit of  $\leq 0.07''$  (1.3 pc at 3.9 Mpc) for the angular diameter of SNR 4449–1 (de Bruyn 1983). This upper limit was obtained from interferometric visibilities, while the data were insufficient for obtaining an image. Optical observations with the *HST* in 1996 and 2005 yielded somewhat smaller upper limits of  $0.028''$  (0.5 pc) (Blair & Fesen 1998) and  $0.037''$  (Milisavljevic & Fesen 2008), respectively. The expansion velocity of 6000 km s $^{-1}$  obtained from the [OIII] optical emission line (Blair & Fesen 1998) provided an

estimated age of the remnant of  $\sim 50$  years (Milisavljevic & Fesen 2008). Recently, Bietenholz et al. (2010) reported the first resolved radio image of the remnant, obtained with the VLBA in 2008, showing two parallel ridge-like structures with an angular extent of  $65 \times 40$  mas. Using a slightly larger velocity expansion of  $6500 \text{ km s}^{-1}$ , they obtained an age estimate of  $\sim 70$  yrs for the SNR.

We made a VLBI observation of the SNR 4449–1 using the EVN at 1.6 GHz ( $\lambda = 18$  cm), as part of the larger study of milliarcsecond-scale structure of radio counterparts of ULX sources aimed at revealing the nature of ULXs and their possible connection to secondary BHs.

#### 4.4.1 Observations and data reduction

The SNR 4449–1 in NGC 4449 was observed during a 12-hour observing run, during which two other ULX sources were also observed (see Section. 4.2.2), on 1 June 2009, using the nine EVN antennas listed in Table 4.2.

Observations were made in the phase-referencing mode, with the compact radio source J1221+4411, located  $\sim 1$  degree away from the target, used as a phase calibrator. Observing scans on J1221+4411 and SNR 4449-1 were interleaved, with a calibrator-target cycle time of 8 min (2 min on the phase calibrator and 6 min on the source). This resulted in a total integration time of 2 hours spent on SNR 4449-1. A bright and compact radio source, 4C +39.25, was observed as a fringe finder and bandpass calibrator.

As it was done for NGC 4088-X1 and NGC 4861-X2 (Sect. 4.2.2), the data were recorded in dual-circular polarization, at a rate of 1024 Megabit per second (Mbps), resulting in a total bandwidth of 256 MHz (comprising 8 intermediate frequency bands, each covering a 16 MHz band split into 32 spectral channels). After the observations, the data were correlated at the EVN Correlator Facility at JIVE using a correlator averaging time of 2 seconds. This ensured that the target source could be effectively detected within the  $3\sigma$  error box of the VLA FIRST position measurement.

The correlated data were fringe-fitted using the AIPS and phase solutions obtained on the phase-reference calibrator J1221+4411 were applied to the target source. No ionospheric corrections were applied. The target was subsequently imaged using AIPS task IMAGR. The resulting image is shown in Fig. 4.7.



TABLE 4.8— Radio components of the SNR in NGC 4449

Component	RA (J2000)	DEC (J2000)	Integrated flux [mJy]	$\bar{T}_B$ [ $10^6$ K]
A	$12^h28^m10.94738^s \pm 0.00006^s$	$44^\circ06'48.5181'' \pm 0.0008''$	0.524	3.8
B	$12^h28^m10.94691^s \pm 0.00006^s$	$44^\circ06'48.5200'' \pm 0.0008''$	0.423	3.1
C	$12^h28^m10.94611^s \pm 0.00003^s$	$44^\circ06'48.5223'' \pm 0.0004''$	0.648	5.6
D	$12^h28^m10.94444^s \pm 0.00005^s$	$44^\circ06'48.5146'' \pm 0.0007''$	0.592	3.5
E	$12^h28^m10.94481^s \pm 0.00003^s$	$44^\circ06'48.5008'' \pm 0.0005''$	0.424	4.5
F	$12^h28^m10.94588^s \pm 0.00004^s$	$44^\circ06'48.5423'' \pm 0.0007''$	0.269	3.0

#### 4.4.2 Results

The phase-referenced image of the SNR 4449-1 shown in Fig. 4.7 is obtained by applying CLEAN deconvolution to the naturally weighted data. The cleaning is done without self-calibration. The resulting restoring beam (CLEAN beam) is  $7.9 \times 3.5$  mas, oriented at a P.A. of  $25.8^\circ$ . The image has an off-source rms noise of  $42 \mu\text{Jy beam}^{-1}$  and a peak flux density of  $287 \mu\text{Jy beam}^{-1}$ , thus corresponding to a detection  $S/N \approx 6$ .

The remnant is clearly resolved, showing a typical shell-like morphology expected for a young radio supernova. The structure detected is breaking apparently into several “spot-like” components. This appearance is likely to be caused by an incomplete uv-coverage due to the short integration time on the source (see Fig. 4.6). Six distinct regions (labeled A through F in Fig. 4.7) can be identified in the image. The basic properties of components A-F (coordinates, total flux densities, and brightness temperatures) have been obtained from fits by two-dimensional gaussian components to the image plane (see Sect. 2.2.3, model fitting). Table 4.8 lists the parameters obtained. The errors are taken from the covariance matrix of the fits.

The integrated flux density of the components identified varies from 0.269 to 0.648 mJy while the brightness temperature ranges from  $3.0 \times 10^6$  K to  $5.6 \times 10^6$  K. While components A to E can be also clearly identified in the map of Bietenholz et al. (2010), component F has a lower flux and cannot be confirmed as real. An even fainter component of 0.150 mJy of integrated flux seems to be also detected in the North-West of the image, but we cannot consider it as real given its low S/N. The whole structure has a total flux of  $6.1 \pm 0.6$  mJy, from which we derive a radio luminosity at 1.6 GHz of  $1.74 \times 10^{35}$  erg  $\text{s}^{-1}$ .

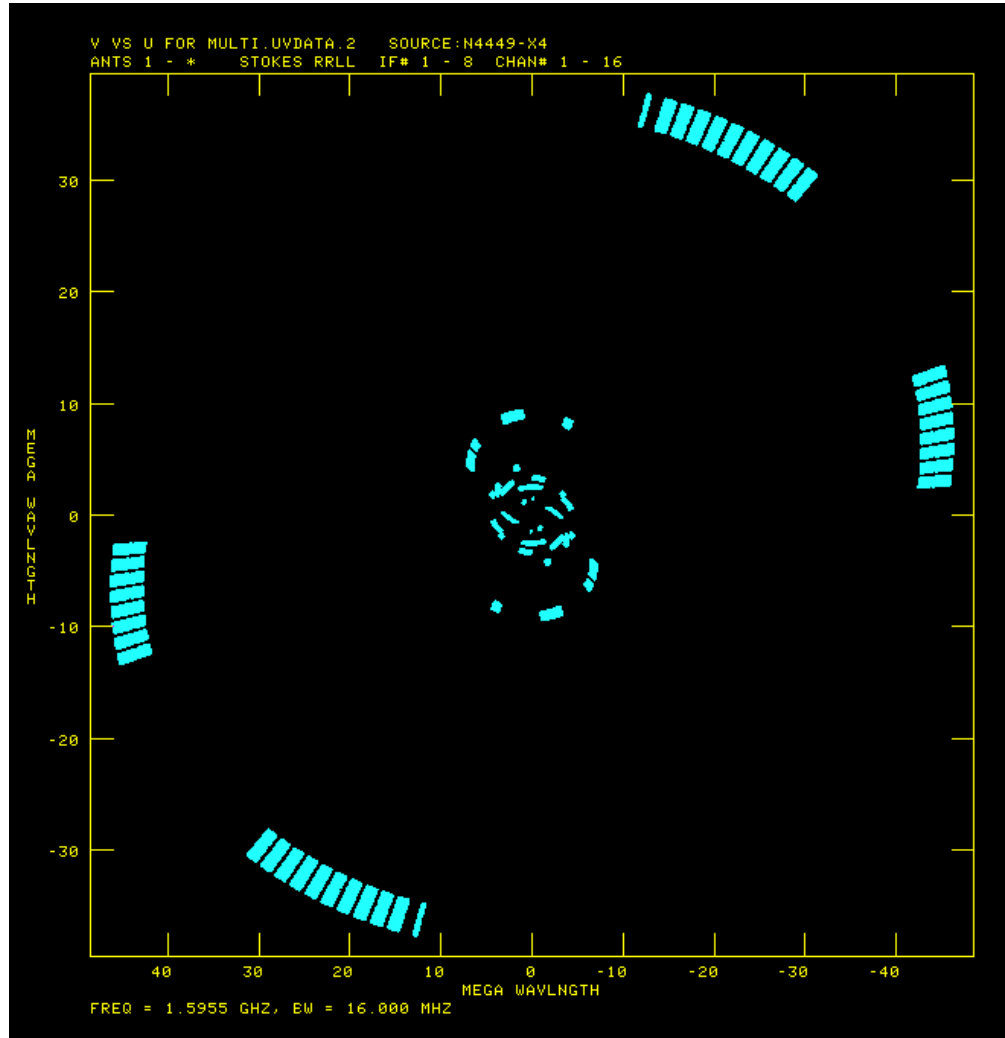


FIGURE 4.6— uv-coverage for an integration time of 2 hours on SNR 4449-1.

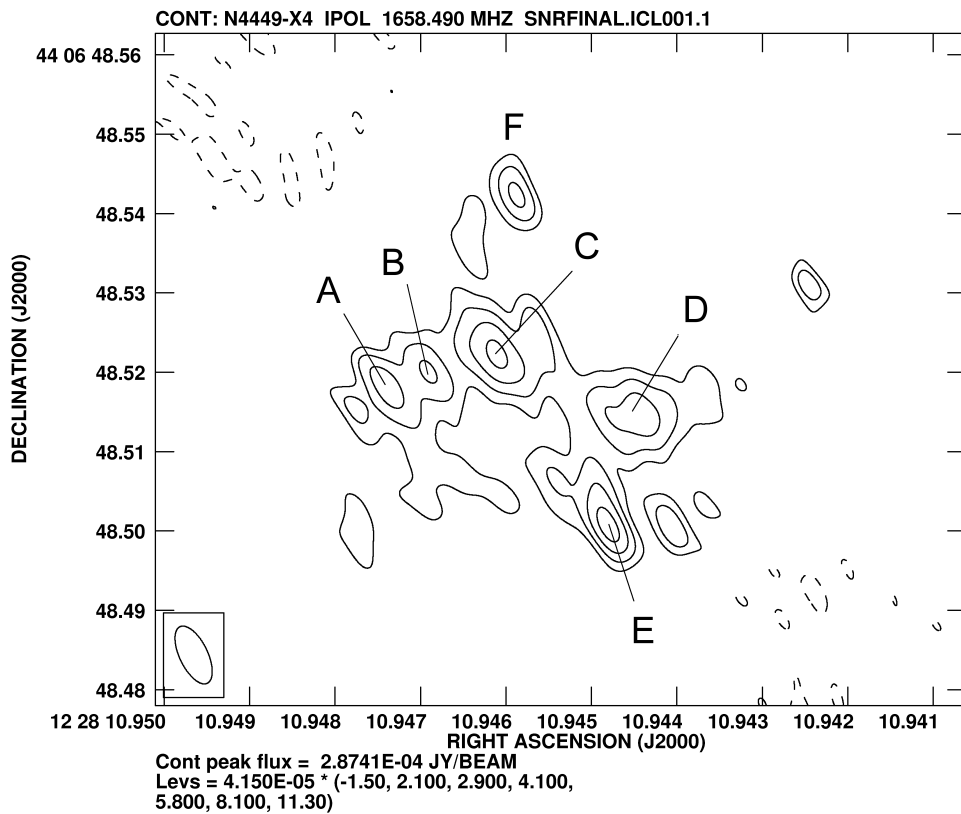


FIGURE 4.7— Radio resolved structure of the SNR in NGC 4449 using the EVN at 1.6 GHz. The rms noise off-source is  $42\mu\text{Jy beam}^{-1}$ . Contours start at  $-1.5$  times the rms and increase with factors of  $\sqrt{2}$ . The six components detected are labeled A, B, C, D, E, and F. The brightness peak of the map corresponds to component E and is  $0.287\text{ mJy beam}^{-1}$ . The dimensions (full width at half maximum) of the restoring beam are  $7.9 \times 3.5\text{ mas}$ , with the major axis of the beam oriented along a position angle of  $25.8^\circ$ . North is up and east is to the left.

#### 4.4.2.1 Positional center and size of the remnant

The positional center and an estimate of the SNR diameter size can be determined from the resolved structure. The fit of an ellipse to the structure formed by the peak of the five brightest components A-E (Fig. 4.8) yields the best position for the SNR center at:

$$\text{RA} = 12^{\text{h}}28^{\text{m}}10.9463^{\text{s}} \pm 0.0001^{\text{s}},$$

$$\text{DEC} = 44^{\circ}06'48.508'' \pm 0.001'',$$

and a SNR size of major axis  $b = 0.058'' \pm 0.002''$  and minor axis  $a = 0.028'' \pm 0.002''$ , corresponding to  $1.1 \times 0.5$  pc at the distance of the galaxy. This estimate is limited by the uncertainty in the distance to NGC 4449. In order to compare the radio diameter to the one derived from optical images, we derive a mean value of  $0.043'' \pm 0.001''$ . This size is larger than the values of  $0.028''$  (Blair & Fesen 1998) and  $0.037''$  (Milisavljevic & Fesen 2008) estimated from *HST* images, suggesting that the outer layers of SNR 4449-1 do not emit at optical wavelengths. The SNR mean diameter of 43 mas is larger, as well, than the  $\sim 30$  mas peak-to-peak separation between the two bright parallel ridges of emission found by Bietenholz et al. (2010). If component F is real, the size of the remnant can be determined from the distance between components A-D and F-E. This yields a size of  $32 \times 43$  mas, more similar to the two-part radio morphology obtained by Bietenholz et al. (2010). Deviations from the expected circular or elliptical morphology reported by Bietenholz et al. (2010) for SNR 4449-1 are not likely to result from deconvolution errors or gaps in the uv-coverage, but peculiar non-circular structures have also been observed in other supernova remnants (e.g., 41.95+575 in M82; McDonald et al. 2001).

### 4.4.3 Discussion

#### 4.4.3.1 Lightcurve

Using archival radio observations of NGC 4449, Lacey et al. (2007) presented the lightcurves of the SNR at 6 and 20 cm from 1972 to 2002, revealing a remarkable decline in its radio emission. An up-to-date version of the lightcurves, including the new flux densities from Bietenholz et al. (2010) and this work, is presented in Fig. 4.9.

Our flux-density measurement is in agreement with the radio decline and we use it to estimate the decay rate of the emission from a power-law fit of the form

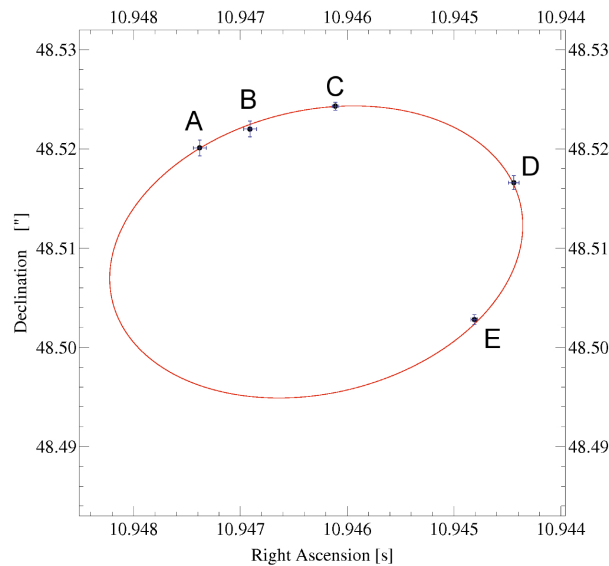


FIGURE 4.8— Elliptical fit to the peak of the five components detected. The ellipse has a major axis of  $0.058'' \pm 0.002''$ , a minor axis of  $0.028'' \pm 0.002''$ , and a position angle of  $208^\circ$ . This corresponds to an ellipse of  $1.1 \text{ pc} \times 0.5 \text{ pc}$ .

$$S = S_0(t - t_0)^\beta \nu^\alpha, \quad (4.2)$$

where  $t_0$  is the date of the supernova explosion,  $S_0$  is a scaling factor,  $\nu$  is the observing frequency,  $\alpha$  is the spectral index, and  $\beta$  is the index of the power-law decay (see, e.g., Weiler et al. 2002). From a combined fit to the lightcurves at 20 cm, 18 cm, and 6 cm (solid and dashed lines, Fig. 4.9), we obtain  $S_0 = 922 \pm 307 \text{ Jy}$ ,  $t_0 = 1956 \pm 2 \text{ yr (A.D.)}$ ,  $\beta = -1.19 \pm 0.07$ , and  $\alpha = -0.620 \pm 0.004$ , with a  $\chi^2 = 9$ .

The value of  $\beta$  obtained from this fit yields a secular decline rate of the radio emission of  $2.2 \pm 0.1 \%$  per year. This decline rate is similar to the ones found for SN 1970G in the periods 1973-1991 and 1991-2001 (Stockdale et al. 2001; Cowan et al. 1991), and it is slightly lower than the value  $2.8 \%$  obtained by Lacey et al. (2007) under assumption of the SNR age of  $\sim 100$  yrs.

Lacey et al. (2007) report as well variations of the spectral index,  $\alpha$ , observed over the time period 1972-2002. The spectral index remains relatively constant from 1982 to 1996, with an average value of  $\alpha \approx -0.65$  obtained largely from 1.4 and 4.8 GHz measurements. This value is in good agreement with the spectral index derived from our combined fit to the lightcurves at 6

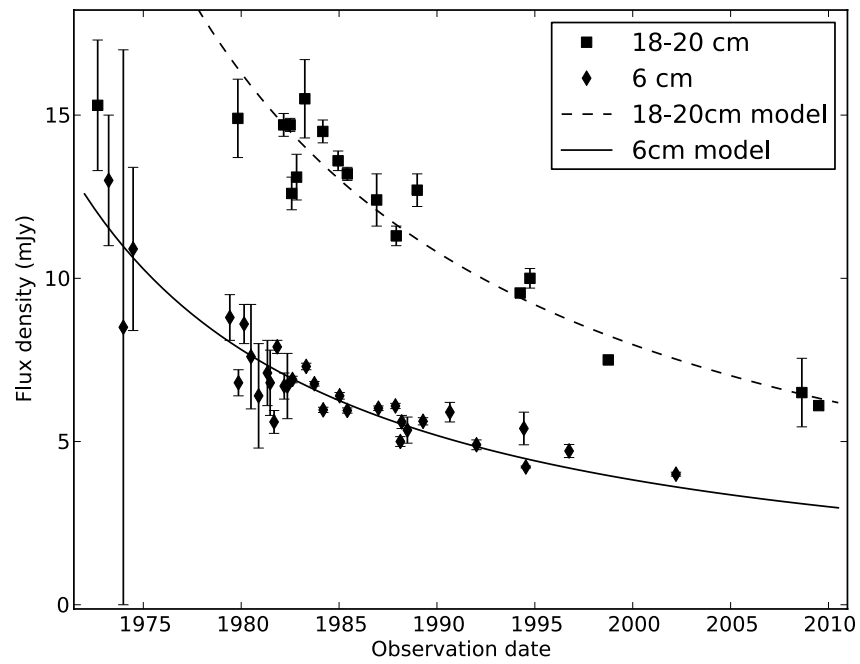


FIGURE 4.9— Lightcurve of SNR 4449-1 at 18 cm and 20 cm (squares), and 6 cm (diamonds). Data taken from Lacey et al. (2007), Bietenholz et al. (2010), and this work. Dashed line (thick line), is our best-fit model to the 18-20 cm (6 cm) data using Eq. 4.2. The fit takes into account the different frequencies of each flux, but for visual purposes the same symbol (square) is used for both the 18 cm and 20 cm fluxes.

cm and 20 cm. It steepens later to  $\alpha \approx -1$ , albeit in measurements involving 22 GHz where spectral aging is more pronounced.

#### 4.4.3.2 *Constraining the age of SNR 4449-1*

The estimate of  $t_0 \sim 1956$  yr (A.D.) indicates that the supernova should have exploded  $\sim 55$  years ago. This age agrees with the upper limit of 100 years (Milisavljevic & Fesen 2008) and with the  $\sim 70$  years suggested by Bietenholz et al. (2010). It is as well in agreement with the detections of the SNR on optical plates (see Milisavljevic & Fesen 2008 for a discussion), which indicated that the supernova explosion must have taken place in 1961 or before.

Using the [OIII] optical emission line of the SNR spectrum, a range of expansion speeds of the SNR of  $3000\text{--}6000 \text{ km s}^{-1}$  was found (Blair & Fesen 1998). An estimated maximum expansion velocity of  $\sim 6500 \text{ km s}^{-1}$  was later provided (Bietenholz et al. 2010). This velocity range can be used to derive a lower limit on the age of SNR 4449-1. Adopting the SNR radius of  $14\text{--}29$  mas, as given by the semimajor and semiminor axes of the elliptical fit shown in Fig. 4.8, and an expansion speed of  $\sim 6500 \text{ km s}^{-1}$ , we estimate an age of the SNR between 39 and 78 years (assuming a constant expansion speed). The supernova explosion would thus have taken place between 1932-1961, which is in agreement with the  $t_0 \sim 1956$  found from the fit to the radio lightcurves.

We note, though, that this estimate is made under the assumption that the radio shell is expanding together with the optical [OIII] emitting gas, at a constant speed of  $\sim 6500 \text{ km s}^{-1}$ . However, we have seen that the shell-like structure observed at 1.6 GHz is much larger than the one in the optical, suggesting that the outer shock front is moving faster than  $6500 \text{ km s}^{-1}$ . The age estimated using this expansion speed constitutes thus an upper limit to the remnant's age.

#### *Decelerated expansion*

A deceleration in the shock front, produced by the interaction of the ejecta with a dense circumstellar medium (CSM), would affect as well the estimated age of the SNR. Chevalier (1982a,b) proposed that the relativistic electrons and enhanced magnetic field necessary to produce the observed radio synchrotron emission arise from the supernova shock wave interacting with a dense CSM, which is presumed to have been established by a very effective mass-loss wind from the supernova stellar progenitor.

According to Chevalier (1982a,b), the shock front of the supernova in the CSM expands following a power-law of time,  $r \propto t^m$ , where  $m$  is the

*deceleration parameter*, defined as

$$m = (n - 3)/(n - s). \quad (4.3)$$

The radial density profiles of the CSM and the ejecta are also described as power-laws, with indices  $n$  and  $s$ , respectively (i.e., the ejecta density is  $\propto r^{-n}$  and the CSM density is  $\propto r^{-s}$ ). The deceleration parameter,  $m$ , can also be written in terms of the spectral index,  $\alpha$ , and the flux-density decay rate,  $\beta$ , in the form (see Martí-Vidal et al. 2011b)

$$m = \frac{2(3 + \alpha + \beta)}{3(s - 4) + \alpha(s - 2)}. \quad (4.4)$$

Taking the values of  $\alpha = -0.62$  and  $\beta = -1.19$ , estimated from our fit to the radio lightcurves, Eq. 4.4 results in a deceleration parameter  $m = 0.80$ , if we use a radial CSM profile with  $s = 2$  (i.e., if we assume a constant mass-loss rate for the progenitor star). This value is in agreement with the typical values reported in other supernovae (where the expansion has been monitored during several years). It is found in all cases that  $0.7 \leq m \leq 0.9$  (Weiler et al. 2002; Bietenholz et al. 2002; Marcaide et al. 2009; Martí-Vidal et al. 2011a; and references therein).

The constraint of the explosion date of SNR 4449-1 places this source in a unique position as being the youngest known supernova remnant (Cas A is the youngest Galactic SNR with an age of  $\sim 330$  yrs; Thorstensen et al. 2001).

On the other hand, the present luminosity of SNR 4449-1 of  $1.74 \times 10^{35}$  erg s $^{-1}$  is comparable to the peak luminosity of SN 1970G, and higher than the current luminosities of the Galactic SNRs Cas A and the Crab (see Lacey et al. 2007 for further discussion). This makes SNR 4449-1 an interesting link between SNe and their remnants and calls for classifying this object as a transition-type source that links supernova explosions and supernova remnants (Lacey et al. 2007), or as an intermediate age SNR with exceptional radio luminosity (the so-called ‘radio hypernova remnant’; Wilkinson & de Bruyn 1990).

## 4.5 Summary

Several scenarios have been suggested to explain the nature of ULX sources: intermediate-mass black holes (Colbert & Mushotzky 1999); X-ray binaries with peculiar features such as being in an ultraluminous state (Gladstone & Roberts 2009), with super-Eddington accretion (e.g., Begelman 2002), or with



strong beaming effects (e.g., Körding et al. 2002); or secondary black holes in the course of a galactic merger (Lobanov 2007). The determination of the black hole mass of those ULXs being powered by accretion is crucial in order to clarify which is the origin of the high X-ray emission in these sources. The detection of a ULX radio counterpart offers the possibility to derive an estimate of the BH mass by means of the fundamental plane of accreting BHs (e.g., Falcke et al. 2004). Obtaining a radio spectral index provides, in addition, a hint on the ULX nature while high-resolution radio observations allow to spatially resolve in some cases the ULX radio counterpart.

In order to clarify the nature of ULX sources and their possible link to secondary black holes in post-merger galaxies, two samples of ULXs have been analyzed in this chapter. The first sample consisted of 24 ULX sources located in late-type galaxies in the Chandra Deep Fields. Analysis of archival GMRT data for the CDFs at 235, 325 & 610 MHz have not yielded any radio counterparts for these sources but upper limits on their flux densities. Six ULX sources out of the 24 were detected in images from more sensitive radio surveys (e.g., Bauer et al. 2002; Kellermann et al. 2008). In all these cases the radio emission seems to come from both the ULX and its host galaxy. Radio observations at a higher resolution would thus be needed to disentangle both contributions and characterize the radio emission of these ULX sources.

On the other hand, a number of ULX sources was cross-identified by other authors in the existing radio catalogs, and some of these sources are well suited for VLBI studies. We have initiated an EVN program to detect and study milliarcsecond-scale emission in ULX objects with known radio counterparts. EVN observations of three ULXs yielded mas-scale images of all three objects, with the following results:

1. N4449-X1. We confirm the earlier identification of this object with a SNR and obtain the most accurate estimates of its size and age.
2. NGC 4088-X1. We detect a compact component with a radio luminosity of  $3.8 \times 10^{34}$  erg s<sup>-1</sup> and brightness temperature in excess of  $7 \times 10^4$  K. This ULX could harbor a  $10^5 M_{\odot}$  black hole accreting at about  $0.1 \dot{M}_{\text{Edd}}$ .
3. NGC 4861-X2. We detect a compact component with  $T_{\text{B}}$  in excess of  $10^6$  K and possibly an extended emission which however can not be firmly localized with the present data. If the extended structure were confirmed, this ULX could be an HII region with a diameter of 8.6 pc and  $T_{\text{B}} \geq 10^5$  K. The compact radio emission may be coming from a  $\sim 10^5 M_{\odot}$  black hole accreting at  $0.1 \dot{M}_{\text{Edd}}$ .

For NGC 4088-X1 and NGC 4861-X2, the EVN measurements have provided improved estimates of the compact radio flux, yielding better localizations of these objects in the  $L_X - L_{\text{radio}}$  diagram. If the compact radio emission indeed comes from accreting black holes, we expect it to have a rather flat spectral index. The suggested nature of these objects can be best verified with more sensitive observations at 5 GHz aimed at both improving the brightness temperature estimates and obtaining spectral index information. The success of the EVN observations also calls for expanding this study to more ULX objects.

This chapter also presents a compilation of those ULX sources for which a radio counterpart candidate has been detected and is not suggested to come from a background AGN. The radio and X-ray luminosities are used to locate the ULXs in the fundamental plane for accreting black holes and to derive the ratio  $R_X$  of radio to X-ray luminosity (Terashima & Wilson 2003). More than 50% of the ULXs are found to possibly host an IMBH of  $10^3 < M_{\text{BH}} < 10^5 M_{\odot}$ , while the suggested nature of the rest of the sources varies from XRBs and an association of SNe to low-luminosity AGN. For those ULXs with an optical counterpart detected, the BH mass estimated from the fundamental plane is in agreement with the one derived from optical spectroscopy measurements, supporting thus the  $L_X - L_R$  correlation as an excellent tool for obtaining a  $M_{\text{BH}}$  estimate in the case of sub-Eddington accretion.

It is thus clear that there is not a unique scenario able to explain the high X-ray luminosities of all ULX sources. The IMBH scenario is a likely explanation for the most powerful ULXs, with  $L_X > 10^{41}$  erg s<sup>-1</sup>, but an effort to combine optical-UV, X-ray, and radio studies of individual ULX sources is needed to disentangle their nature.

# 5

---

## Double nucleus galaxies

*Arguably, the best way to study how galaxies form and grow, and how their evolution is linked to the evolution of their nucleus is to investigate those galaxies that are undergoing a merger event. This chapter presents the study of a sample of galaxies that are in the last stages of a minor merger event (i.e., post-merger galaxies) and that are suggested to host a double nucleus. Using the PSF fitting technique, the optical luminosity of each of the nuclei and their relative separation is derived. According to the current models for binary black hole evolution, the luminosity of each of the nuclei is expected to be affected by an enhancement of the accretion rate owing to tidal effects and by the disruption of the accretion disk surrounding the central black hole. Such models are applied to the luminosity trends observed in the sample of post-merger galaxies, fitting them satisfactorily. The results reveal that the nuclear luminosity is indeed affected both by tidal enhancement of the accretion rate as well as accretion disk disruption, and that the accretion disk stripping takes place both in the primary and the secondary nucleus. Moreover, some of the sources studied are found to have double nucleus at a separation  $< 1$  kpc and are, thus, potential candidates for sub-kpc AGN pairs.*

### 5.1 Introduction

A galaxy merger, understood as a pair of galaxies that are gravitationally bound and whose orbits will dynamically decay and their nuclei merge, is a process that lasts a few Gyr (e.g., 1–3 Gyr for major mergers with mass ratios  $> 1:3$ ) and passes through different stages (Lotz et al. 2008; see Fig. 5.1). Numerical simulations show that there is an enhancement of star formation during the merger, when the system shows as well clear morphological distortions,  $\sim 2$  Gyr after the pre-merger state (Lotz et al. 2008). The SMBHs at the center of each galaxy are close enough to become gravitationally bound in the ‘post-merger’ stage,  $\sim 0.5$  Gyr after the merger. Finally, the two BH would

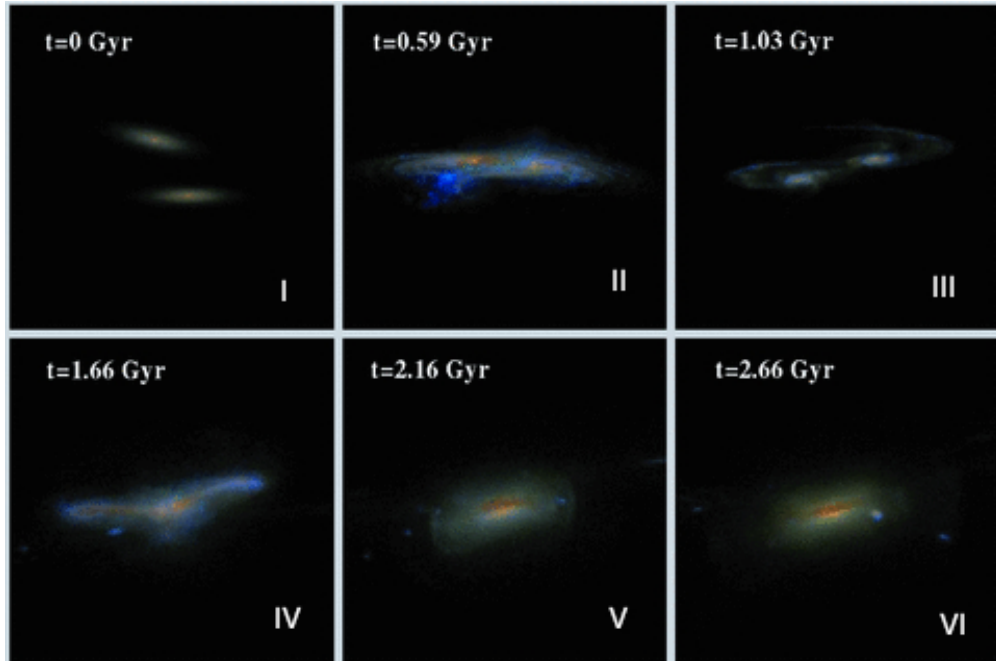


FIGURE 5.1— Color images (composite of SDSS  $u$ ,  $r$ , and  $z$  bands) including dust extinction for the high-resolution prograde-prograde simulation of an equal-mass and gas rich galaxy merger viewed face-on (Lotz et al. 2008). The time passed since the start of the simulation is shown in the upper-left corner of each image. The different merger states, in a sequence from (I) to (VII) are: initial pre-merger galaxies, first pass, maximal separation after first pass, merger of the nuclei, post-merger at 0.5 Gyr after the merger, and remnant at 1 Gyr after the merger. The field of view for the initial pre-merger system and the maximal separation is 200 kpc, while the field of view for the other images is 100 kpc. The merger morphologies are most disturbed at the first pass and merger states. Star-forming regions in the initial discs, tidal tails, and outer regions of the remnant are shown in blue, while the dust-enshrouded star-forming nuclei appear red. Figure and caption reproduced from Lotz et al. (2008).

coalesce within a time scale of  $\sim 10^8$  years (see Sect. 1.7) and a single remnant galaxy is formed. An increase of the accretion rate and potential triggering of nuclear activity in post-merger galaxies is expected from numerical simulations (e.g., Di Matteo et al. 2005; Springel et al. 2005a) and is indicated by direct observations of on-going galaxy mergers (e.g., Tadhunter et al. 2005; Emonts et al. 2006; Letawe et al. 2007; see also Sect. 1.2).

Despite the wide recognition of the hierarchical galaxy evolutionary model described in Sect. 1.2, the role of mergers in galaxy assembly is not yet clear and direct observations of galaxy mergers are needed to constrain the galaxy evolutionary models. Several catalogs of merging galaxies (e.g., Mazzarella

et al. 1991; Mazzarella & Boroson 1993; Gimeno et al. 2004; De Propriis et al. 2007; Bridge et al. 2010; Lintott et al. 2011 and references therein) and classifications of AGN into the merger states of Fig. 5.1 (e.g., Karouzos et al. 2010; Schawinski et al. 2011) exist, while many studies aimed at detecting double nuclei and BBH systems inferred from peculiar AGN properties such as double-peaked emission lines (e.g., Liu et al. 2010a,b) and helical jet structures (e.g., Lobanov & Roland 2005) have also been done. The evolution of binary SMBH systems was suggested to be closely related to the nuclear activity in post-merger galaxies (Lobanov & Roland 2005; Lobanov 2007, 2008), but it has not yet been tested in observational data.

In this chapter the luminosity and distance between the two nuclei of a sample of double nucleus post-merger galaxies is analyzed with the aim of studying the possible connection between the strength of the nuclear activity and the evolution of a BBH system. Because the double nuclei are in most cases not spatially resolved, a PSF (Point Spread Function) fitting is used to determine the brightness of each of the nuclei. We present a model, based on the evolution of a BBH system, that explains the observed trends between the luminosity of each nucleus and the separation between them.

The BBH model and the sample of post-merger galaxies analyzed are presented in Sect. 5.2 and 5.3, respectively. The description of the PSF fitting technique and of the analysis performed is explained in Sect. 5.4. Finally, the results obtained are presented in Sect. 5.5 and discussed in Sect. 5.6.

## 5.2 The binary black hole evolution-luminosity relation

In a post-merger galaxy where each of the two central black holes have an accretion disk around them and there is a central stellar cluster, the peak luminosity of each AGN (the primary and the secondary, from now on labeled 1 and 2) can be estimated from Eq. (1.19) (Lobanov 2007; Lobanov 2008):

$$L_{1,2} = L_0 \left( 1 + \frac{\tilde{M}}{2 - \tilde{M}} \frac{\tilde{M}}{\tilde{r}^2} \right),$$

where  $L_0$  is the luminosity of a typical single inactive galactic nucleus,  $\tilde{M}$  is the reduced mass of the binary BH system, and  $\tilde{r}$  is its reduced separation (see Sect. 1.7). This expression is valid for  $\tilde{r} \geq \tilde{r}_{d1,2}$ , where  $\tilde{r}_{d1,2}$  are the distances at which the outer part of the accretion disk of the primary and secondary black hole start being disrupted (see Eqs. 1.17-1.18). In the case of  $\tilde{r} < \tilde{r}_{d1,2}$ , a decline of the AGN luminosity will occur due to the disruption of the accretion disk. A

factor  $\xi$  should then be introduced to account for the decrease of AGN power:  $\xi = L_{d1,2}/L_d$ , where  $L_d$  is the luminosity of the undisturbed disk and  $L_{d1,2}$  is the luminosity of the disturbed disk of the primary and secondary black hole, respectively. The accretion disk luminosity can be derived from Eq. (1.12):

$$L_d \propto \int_{r_{\text{in}}}^{r_{\text{out}}} F(r) r dr, \quad (5.1)$$

where  $F(r) \propto r^{-\beta}$  is the radial distribution of spectral intensity of the accretion disk, which extends from  $r_{\text{in}}$  to  $r_{\text{out}} = \kappa_d r_{\text{in}} \simeq 10^4 r_{\text{in}}$  (Ivanov et al. 1998), and  $\beta$  is the spectral index.

The undisturbed disk has thus a luminosity:

$$L_d \propto \frac{1}{2-\beta} r^{2-\beta} \Big|_{r_{\text{in}}}^{r_{\text{out}}} = \kappa_d^{2-\beta} - 1, \quad (5.2)$$

after setting  $r_{\text{in}}=1$ . On the other hand, the disturbed disk extends to:

$$r_{\text{out}} = \kappa_d r_{\text{in}} \frac{\tilde{r}}{\tilde{r}_{d1,2}} = \kappa_d \frac{\tilde{r}}{\tilde{r}_{d1,2}}. \quad (5.3)$$

The disturbed disk of each nuclei has thus a luminosity:

$$L_{d1,2} \propto \left( \frac{\kappa_d \tilde{r}}{\tilde{r}_{d1,2}} \right)^{2-\beta} - 1. \quad (5.4)$$

The factor  $\xi$  can then be expressed as:

$$\xi = \frac{\left( \frac{\kappa_d \tilde{r}}{\tilde{r}_{d1,2}} \right)^{2-\beta} - 1}{\kappa_d^{2-\beta} - 1} \quad (5.5)$$

The peak luminosity of each AGN in the case of  $\tilde{r} < \tilde{r}_{d1,2}$  will thus be:

$$L_{1,2} = L_0 \left( 1 + \frac{\tilde{M}}{2-\tilde{M}} \frac{\tilde{M}}{\tilde{r}^2} \right) \left[ \frac{\left( \frac{\kappa_d \tilde{r}}{\tilde{r}_{d1,2}} \right)^{2-\beta} - 1}{\kappa_d^{2-\beta} - 1} \right] \quad (5.6)$$

### 5.3 The sample

The sources analyzed in this chapter are drawn from a catalog of double nucleus disk galaxies suggested to be in the course of a minor merger event (Gimeno et al. 2004). The catalog comprises 107 double nucleus galaxies selected from older catalogs under the following three requirements: 1) galaxies with redshift  $z < 0.05$  (or apparent B magnitude  $m_B < 18$ ), to ensure that the morphology can be resolved with 2-4-meter telescopes; 2) galaxies showing disk-like morphology (i.e., elliptical and cD galaxies are excluded), to avoid the inclusion of major merger remnants and include only possible minor merger events; 3) galaxies not exhibiting strong tidal distortions or tails, as these features are expected in major merger events.

Of the 107 double nucleus disk galaxies (Gimeno et al. 2004), 60 are found to have imaging data in the Sloan Digital Sky Survey Data Release 8 (Eisenstein et al. 2011, and references therein; SDSS DR8 hereafter). FITS images of these 60 objects in the  $u$ ,  $g$ , and  $r$  bands (centered at 3551Å, 4686Å, and 6166Å, respectively) are retrieved by coordinates from the Science Archive Server (SAS) of the SDSS. When searching for RA and DEC, SAS returns the field image at that location with a size of  $2048 \times 1489$  pixels and a pixel scale of  $0.396''/\text{pixel}$ . The retrieved images are calibrated and have a sky-subtraction applied that serves as a good sky subtraction for large objects (see Eisenstein et al. 2011 for a more detailed description).

For the objects MCG +06-07-020 and Mrk 1341, the coordinates reported in Gimeno et al. (2004) do not provide the SDSS field image where these sources should be located. The corrected coordinates are found in NED by name and are, for MCG +06-07-020:

$$\text{RA(J2000)} = 02^{\text{h}}55^{\text{m}}29^{\text{s}}, \text{DEC(J2000)} = 36^{\circ}12'0.2'',$$

and for Mrk 1341:

$$\text{RA(J2000)} = 13^{\text{h}}00^{\text{m}}59^{\text{s}}, \text{DEC(J2000)} = -00^{\circ}01'39''.$$

### 5.4 Data analysis

#### 5.4.1 PSF fitting

The analysis of the images is done using the IRAF software and the PSF fitting code *imfitfits* (McLeod et al. 1998), which fits a model convolved with a PSF image. The model is optimized by computing the  $\chi^2$  to fit the observed image. In order to determine the brightness of each individual nucleus, the field images are first cropped to a size of  $64 \times 64$  pixels around the nucleus of each target galaxy using the IRAF task *imcopy*. In most of the target galaxies these new

‘nuclear’ images are dominated by the nucleus of the galaxy so that most of the host galaxy contribution is cut out. An isolated, bright, but not saturated (less than 15,000 counts) star is chosen from the field image and a region of  $64 \times 64$  pixels around it is cut. The nuclear images are then fit as point sources by `imfitfits` using the stellar images as PSFs. The parameters of the model are the positions and intensities of each of the nuclei and the background level of the image. Initial values of the position and intensity of the nuclei are estimated from the nuclear images using the IRAF task `imexam`. The position of one of the two nuclei (the brightest one) is set as the origin of the coordinates system and is allowed to vary in steps of 0.01, while the X and Y location of the second nucleus is set to vary in steps of 0.001. The intensities of the brightest and the secondary nuclei are set to vary in steps of 10 and 1, respectively. The background level is allowed to vary in steps of 1. Since the images are already background-subtracted, the values of the fitted background are not significant and do not affect the resulting intensities. The uncertainty of the intensities fitted are given by the residual image created after subtraction of the model image from the data (see Fig. 5.2), and are  $<10\%$ . The global astrometric precision of the SDSS DR8 is of  $0.1''$ , therefore the error in the relative separation between the two nuclei is  $<0.1''$ . `Imfitfits` allows as well to fit the galaxy luminosity profile with a de Vaucouleurs model or an exponential disk. The addition of these profiles to the model does not improve the fitting of the intensities.

#### 5.4.2 Nuclear and host galaxy luminosities

The images retrieved from the SDSS are calibrated in nanomaggies (nmg) per pixel<sup>1</sup>. The intensities obtained from `imfitfits` for each of the two nuclei are converted to nmg using the count conversion factor specified in the header of each SAS image. The nmg are then converted to magnitudes, which are corrected for Galactic dust extinction using the reddening corrections at the position of each object provided by SDSS (following Schlegel et al. 1998). After converting these magnitudes to absolute AB magnitudes (Oke & Gunn 1983), the  $r$ -band luminosities of the nuclei are derived using:

$$\frac{L}{L_{\odot}} = 10^{(M - M_{\odot})/2.5}, \quad (5.7)$$

---

<sup>1</sup>A nmg corresponds to  $3.361 \times 10^{-6}$  Jy or 22.5 mag in any band



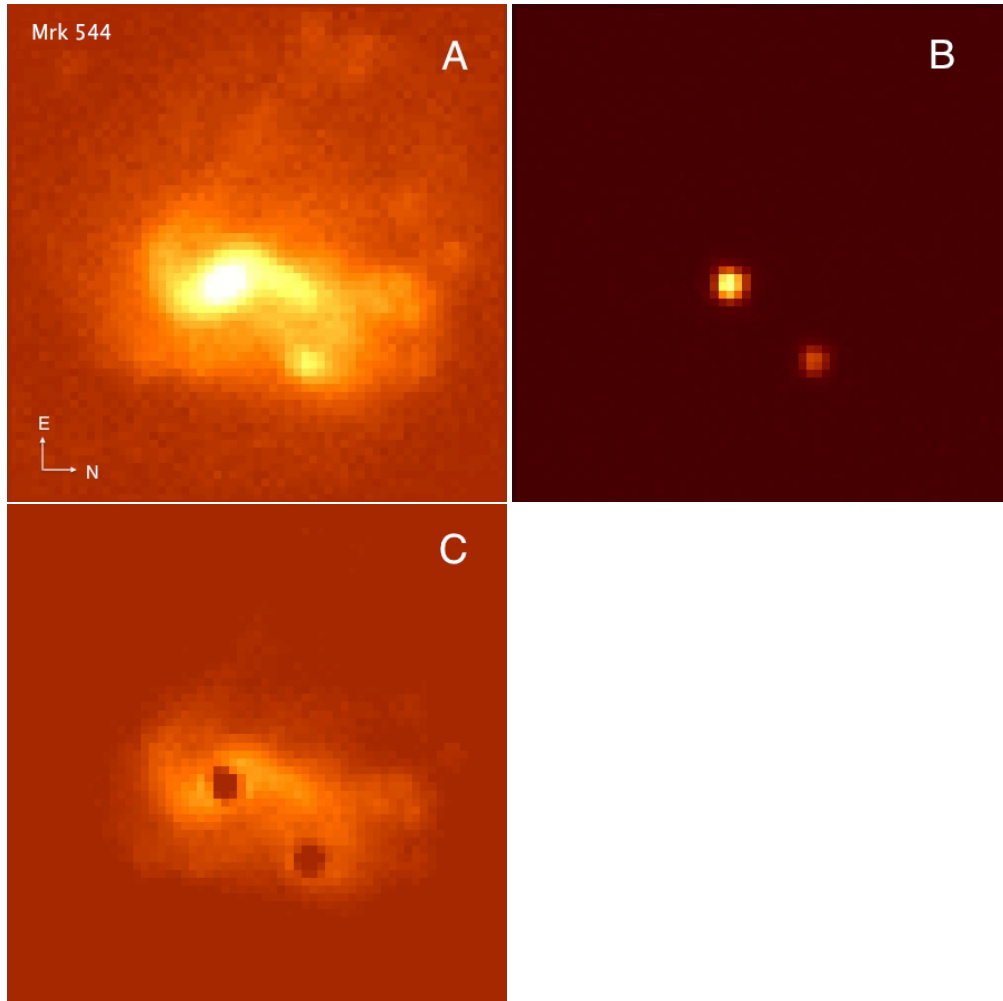


FIGURE 5.2— *R*-band image of Mrk 544 from SDSS DR8. Figures A–C show the observed image, model image, and the residual image, respectively. Images of the fit for all sources can be found in Appendix C, page 203.

where  $M$  is the absolute magnitude of the target and  $M_{\odot}$  and  $L_{\odot}$  are, respectively, the absolute bolometric magnitude and bolometric luminosity of the Sun. Their values, used here, are  $M_{\odot}=4.74$  and  $L_{\odot}=3.85\times 10^{26}$  W. The same expression is used to derive the host galaxy luminosity from the model magnitude of the  $r$ -band provided by the SDSS DR8 photometry. Model magnitudes are fiber magnitudes that reflect the flux contained within the spectroscopic fiber of  $3''$  in diameter (SDSS DR8 website), and are the result of fitting a Vaucouleurs profile and an exponential profile to the resolved extended galaxy.

#### 5.4.3 Parameters of the model

In order to find a possible connection between disk disruption and AGN luminosity, as described by Eq. (5.6), the reduced mass and separation of the binary BH system must be determined. The reduced mass  $\tilde{M}$  of each system can be derived from Eq. (1.15) assuming that  $M_{1,2} \propto L_{1,2}$  (e.g.,  $M_{\text{BH}} \propto L_{\text{bulge}}^{0.90\pm 0.11}$ , Wandel 2002;  $M_{\text{BH}} \propto L_{\text{bulge}}^{0.80\pm 0.09}$ , Bentz et al. 2009). The reduced distance  $\tilde{r}$  defined in Eq. (1.16) is a function of the separation  $r$  between the two nuclei and the distance  $r_c$  at which the two BHs become gravitationally bound. While  $r$  is obtained from the relative position of the two nuclei fitted by `imfitfits`,  $r_c$  is left as a free parameter when applying Eq. (5.6) to the data.  $L_0$  and the power-law index  $\beta$ , in the case of Eq. (5.6), are also left as free parameters. The disruption distances  $\tilde{r}_{d1}$  and  $\tilde{r}_{d2}$  can be derived from Eqs. (1.17) and (1.18), respectively, assuming that  $\varepsilon_1 = M_1/M_{\text{eq}}=0.1$  (corresponding roughly to  $M_1 \sim 10^9 M_{\odot}$ ; Lobanov 2008).

### 5.5 Results

The results of the PSF fitting (i.e., luminosities of the primary and secondary nuclei, and their relative separation) together with the name and distances of the post-merger galaxies analyzed are listed in Table 5.1. Columns 1 to 7 list the object name (Col. 1), luminosity distance provided by NED (Col. 2),  $r$ -band host galaxy luminosity (Col. 3),  $r$ -band primary nucleus luminosity (Col. 4),  $r$ -band secondary nucleus luminosity (Col. 5), and separation between the two nuclei in arcsec (Col. 6) and kpc (Col. 7). Of the 60 objects for which SDSS DR8 images are available, three do not have any spectroscopical identification nor redshift available and thus their nuclear and host galaxy luminosities could not be derived. These objects are therefore excluded from the analysis and are not included in Table 5.1. The `imfitfits` code is not able to find a double nucleus in three other targets, which are thus also removed from the analysis.

Therefore, the total number of objects included in Table 5.1 and considered for further analysis is 54.

### 5.5.1 The AGN-host connection

The nuclear luminosity of the primary and secondary nucleus versus their host galaxy luminosity are plotted in Fig. 5.3, top and bottom, respectively. For both the primary and secondary nucleus, a clear trend between nuclear luminosity and host luminosity is observed above  $L_{\text{host}} \sim 5 \times 10^{41} \text{ erg s}^{-1}$  (corresponding to  $\log L_{\text{R}} \geq 8 L_{\odot}$ , where  $L_{\text{R}}$  is the  $r$ -band luminosity). This trend should be described by the  $M_{\text{BH}} - L_{\text{bulge}}$  correlation obtained typically for bulge luminosities  $\log L_{\text{bulge}} > 8 L_{\odot}$  (e.g., Wandel 2002; Marconi & Hunt 2003; Bentz et al. 2009). In order to test this, a trendline to  $L_1$  vs.  $L_{\text{host}}$  and  $L_2$  vs.  $L_{\text{host}}$  is fitted for those sources with  $L_{\text{host}} > 5 \times 10^{41} \text{ erg s}^{-1}$ . The fits obtained indicate that  $L_1 \propto L_{\text{host}}^{1.0 \pm 0.1}$  and  $L_2 \propto L_{\text{host}}^{0.9 \pm 0.1}$ . These correlations are in agreement with the  $M_{\text{BH}} \propto L_{\text{bulge}}^{0.9}$  correlation derived both for inactive and active galaxies (Wandel 2002), which has an scatter of 0.1 dex. From now on we will thus consider that  $M_{1,2} \propto L_{1,2}$ .

### 5.5.2 Tidal enhancement

In post-merger galaxies, the evolution of the nuclear luminosity is expected to be affected by an increase of the accretion rate proportional to tidal forces acting on gas and stars and by accretion disk stripping. To test which is the effect of the tidal enhancement of the accretion rate on the nuclear luminosity, Eq. (1.19) (valid for  $\tilde{r} \geq \tilde{r}_{\text{d}1,2}$ ) is applied to the data. Defining

$$\delta_{\text{L}} = 1 + \frac{\tilde{M}}{2 - \tilde{M}} \frac{\tilde{M}}{\tilde{r}^2},$$

the Eq. (1.19) can be written as  $L_{\text{peak}} = L_0 \delta_{\text{L}}$ .  $\tilde{M}$  and  $\tilde{r}$  can be obtained from Eqs. (1.15)-(1.16), respectively, using  $M_{1,2} \propto L_{1,2}$  and assuming an initial gravitationally bound radius  $r_{\text{c}}=0.1 \text{ pc}$ . The peak luminosity can be set as the sum of the primary and secondary nuclear luminosities,  $L_{\text{peak}} = L_1 + L_2$ , while the unit luminosity  $L_0$  of an inactive nuclei can be initially taken as the luminosity of the secondary nucleus obtained in the previous section:  $L_0 = L_2 = 3.25(L_{\text{host}}/10^{42})^{0.9}$ . The values of  $L_0 \delta_{\text{L}}/L_{\text{peak}}$  can be then derived and plotted against  $L_{\text{peak}}$  (see Fig. 5.4, top), where a weak trend is observed.

TABLE 5.1— Double nucleus galaxies

Name	$D_L$ [Mpc]	$\log L_{\text{host}}$ [erg s $^{-1}$ ]	$\log L_1$ [erg s $^{-1}$ ]	$\log L_2$ [erg s $^{-1}$ ]	$r$ [ $''$ ]	$r$ [kpc]
(1)	(2)	(3)	(4)	(5)	(6)	(7)
MCG +00-04-098	228	44.37	41.31	40.68	1.8	1.8
MCG +00-12-073	68	40.88	40.24	40.08	17.1	5.5
MCG +00-27-041	83	41.25	39.30	38.89	7.1	2.7
MCG +01-02-017	173	40.74	40.31	39.84	8.0	6.2
MCG +01-02-045	67	41.90	39.27	39.67	4.1	1.3
MCG +01-32-049	18	42.38	38.15	37.98	7.4	0.6
MCG +02-31-088	39	40.64	38.72	38.55	12.7	2.3
MCG +02-32-078	12	41.86	37.31	37.24	8.1	0.5
MCG +05-06-015	79	43.66	39.70	39.83	5.0	1.8
MCG +06-07-20	119	43.86	40.53	40.06	4.5	2.5
MCG +06-21-031	29	42.49	37.94	37.84	2.1	0.3
MCG +07-29-061	111	43.49	39.83	39.43	4.5	2.3
MCG +10-19-089	30	39.51	38.10	37.82	6.4	0.9
MCG +10-21-040	32	38.59	38.13	37.90	12.0	1.8
Mrk 104	33	42.63	39.54	39.04	5.0	0.8
Mrk 1114	137	43.82	40.57	40.09	4.0	2.5
Mrk 1134	66	41.84	40.01	39.66	4.7	1.4
Mrk 116	12	41.10	38.24	37.89	5.5	0.3
Mrk 1230	26	43.06	39.05	39.01	2.0	0.3
Mrk 1263	25	41.81	38.87	38.59	7.1	0.8
Mrk 1307	20	42.28	38.85	38.70	8.1	0.8
Mrk 1341	21	43.14	39.07	38.91	12.3	1.2
Mrk 1431	93	43.61	40.16	39.68	4.8	2.1
Mrk 147	100	43.48	39.99	39.72	4.1	1.9
Mrk 153	36	38.94	39.64	39.13	4.2	0.7
Mrk 19	59	42.94	39.91	39.68	4.4	1.2
Mrk 212	99	43.61	40.70	40.83	11.7	5.4
Mrk 219	47	42.61	39.24	38.76	10.5	2.3
Mrk 22	24	42.10	38.80	38.46	4.5	0.5
Mrk 224	15	41.71	38.28	38.11	3.7	0.3
Mrk 306	73	43.62	39.97	39.82	4.8	1.7
Mrk 35	15	42.23	39.00	39.20	4.0	0.3
Mrk 365	68	43.70	40.75	39.65	6.9	2.2
Mrk 38	155	42.96	40.66	40.09	4.1	2.9
Mrk 423	140	41.43	41.25	40.29	9.2	5.9
Mrk 544	94	40.47	40.18	39.75	5.7	2.5
Mrk 553	58	42.89	39.35	39.32	2.6	0.7
Mrk 66	89	40.96	40.34	39.64	8.3	3.4
Mrk 712	68	43.70	40.15	40.12	4.8	1.5
Mrk 721	140	41.26	40.36	40.07	5.5	3.5
Mrk 729	186	44.29	40.93	40.92	6.0	5.0
Mrk 731	25	43.25	39.56	39.49	3.9	0.5
Mrk 777	134	42.80	39.94	39.80	4.0	2.4
Mrk 789	137	43.80	41.11	40.68	4.2	2.6
Mrk 799	42	41.22	40.14	40.13	20.0	4.0
Mrk 930	71	42.56	40.20	39.88	5.0	1.7
NGC 3049	25	43.20	39.68	38.93	10.7	1.3
NGC 3758	130	44.23	41.16	40.81	6.2	3.7
NGC 3773	18	42.86	39.32	39.32	2.8	0.2
NGC 4509	17	42.03	38.73	38.22	8.3	0.7
NGC 5058	17	42.42	38.59	38.57	2.4	0.2
NGC 5256	119	44.11	40.87	40.55	10.2	5.6
NGC 5860	77	43.45	40.40	40.19	9.1	3.3
NGC 7468	24	41.16	39.08	39.06	7.6	0.9

**Column designation:** (1) – object name ; (2) – luminosity distance provided by NED; (3) –  $r$ -band host galaxy luminosity; (4) –  $r$ -band primary nucleus luminosity; (5) –  $r$ -band secondary nucleus luminosity; (6) – separation, in arcsec; (7) – separation, in kpc.

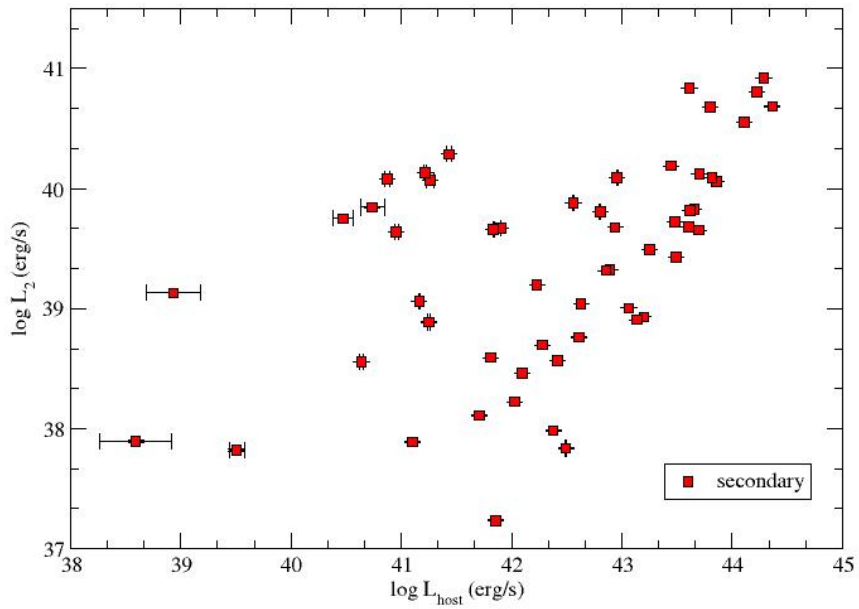
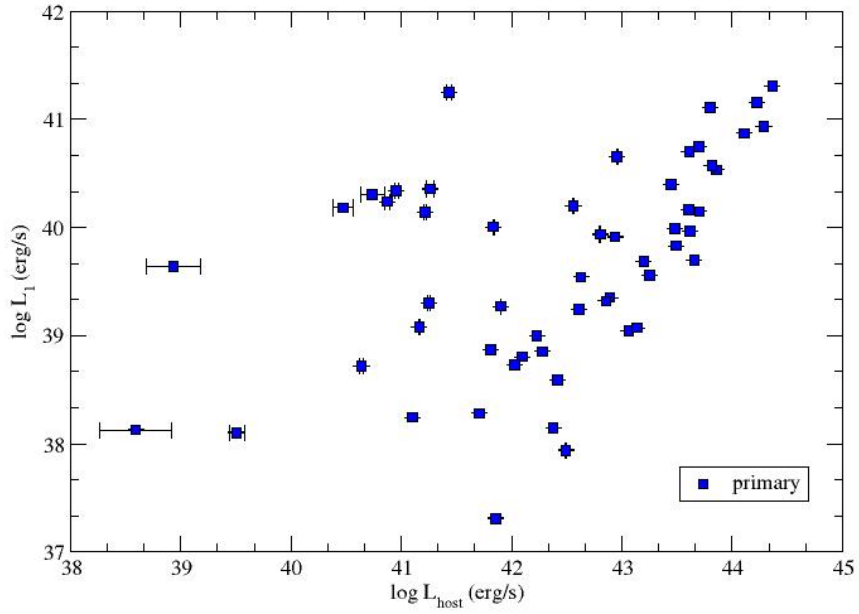


FIGURE 5.3— Luminosity of the primary (top) and secondary (bottom) nucleus versus host luminosity. In both plots, a correlation between nuclear and host luminosity is observed for  $\log L_{\text{host}} > 41.7$ , which is in agreement with the black hole-bulge correlation.

This trend can be described as:

$$\frac{L_0 \delta_L}{L_{\text{peak}}} = C_2 L_{\text{peak}}^\alpha \quad (5.8)$$

$$L_0 \delta_L = C_2 L_{\text{peak}}^{\alpha+1} = 9 \times 10^{17} L_{\text{peak}}^{-0.46+1} \quad (5.9)$$

Using  $L_0 = C_1 L_{\text{host}}^\gamma$ , where  $C_1 = 3.25 \times 10^{38} / 10^{42 \times 0.9}$ , and:

$$\delta_L = C_3 L_{\text{peak}}^\beta = 501.22 L_{\text{peak}}^{-0.06} \quad (5.10)$$

(see Fig. 5.4, bottom), a value of  $\gamma$  can be derived from Eq. 5.8 so that the correlation in Fig. 5.4 (top) is as flat and good as possible:

$$\gamma = \frac{\log(C_2/C_1 C_3) + (\alpha + 1 - \beta) \log L_{\text{peak}}}{\log L_{\text{host}}} \quad (5.11)$$

The new values of  $L_0$  calculated using  $\gamma$  are inserted in  $L_0 \delta_L / L_{\text{peak}}$ . Using the new values, the plot of  $L_0 \delta_L / L_{\text{peak}}$  vs.  $L_{\text{peak}}$  becomes tighter, with a slope of  $\alpha = -0.46$  and a correlation coefficient  $R^2 = 0.93$  (see Fig. 5.5, top). The luminosity trend provided by tidal enhancement of the accretion rate can therefore be greatly de-trended, proving that tidal enhancement is indeed present. The residual trend indicates that the evolution of the nuclear luminosity must be also affected by another process. The disruption of the accretion disk is the other mechanism expected to contribute to the nuclear luminosity evolution.

The analysis done under the assumption that  $r_c = 0.1 \text{ kpc}$  is repeated for different values of binding radii,  $r_c = 1$  and  $r_c = 3 \text{ kpc}$ , shown in Fig. 5.5 (middle and bottom, respectively). The plots show that the slope increases with  $r_c$  while the correlation decreases, indicating that the effect of accretion disk stripping is stronger at these binding radii.

### 5.5.3 Accretion disk disruption

In the course of the merger, it is expected that the accretion disks of the two AGN will disrupt at distances  $\tilde{r}_{d1}$  and  $\tilde{r}_{d2}$  (Eqs. 1.17- 1.18, respectively). The disk stripping should then be reflected in the evolution of the nuclear luminosities, which can be described by Eq. (5.6). Average values of  $\tilde{M}$ ,  $\tilde{r}_{d1}$  and  $\tilde{r}_{d2}$  are calculated:

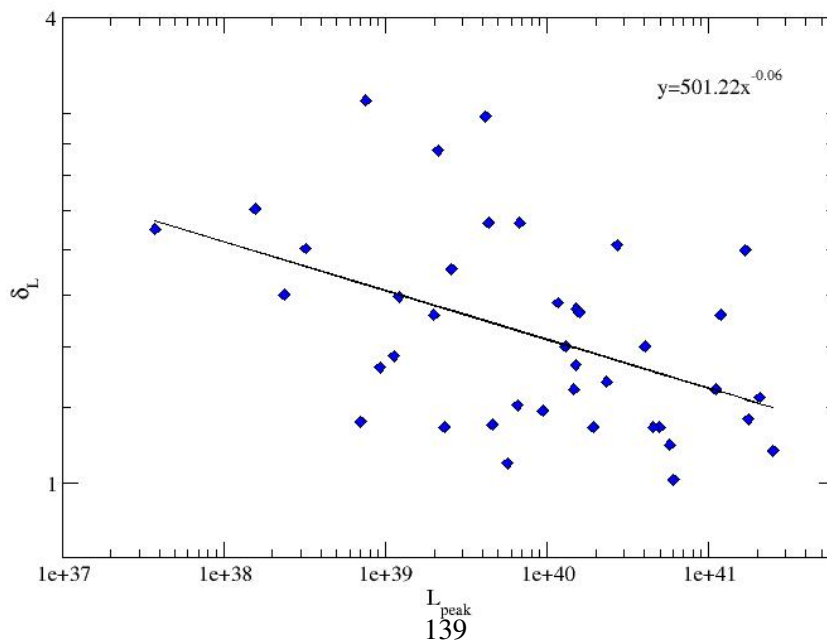
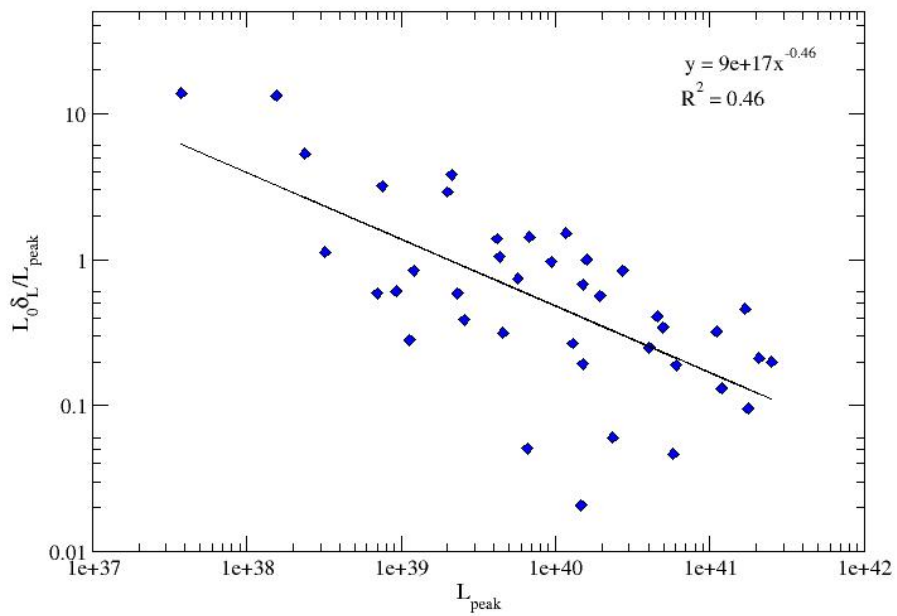


FIGURE 5.4— Ratio of  $L_0 \delta_L / L_{\text{peak}}$  vs.  $L_{\text{peak}}$  (top) and dependence of  $\delta_L$  on  $L_{\text{peak}}$  (bottom) for those sources that follow the black hole-bulge correlation. The regression fitted for  $\delta_L$  vs.  $L_{\text{peak}}$  is shown on the top right corner (right plot). The nuclear luminosity of the secondary ( $L_2 \propto L_{\text{host}}^{0.9}$ ) is taken as  $L_0$  and a value of  $r_c=100$  pc is assumed.

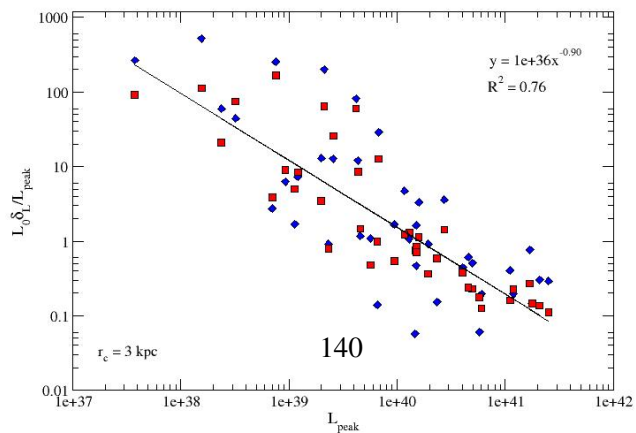
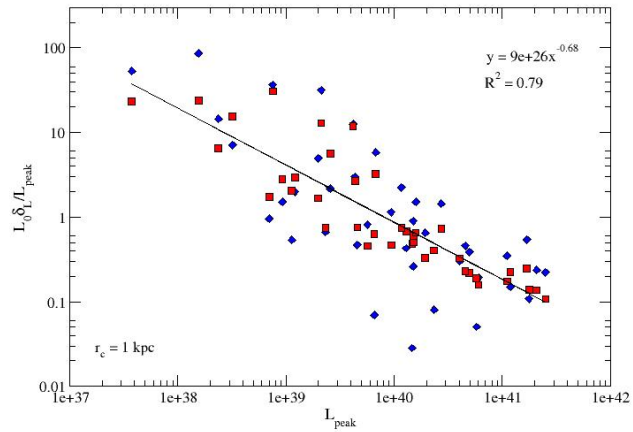
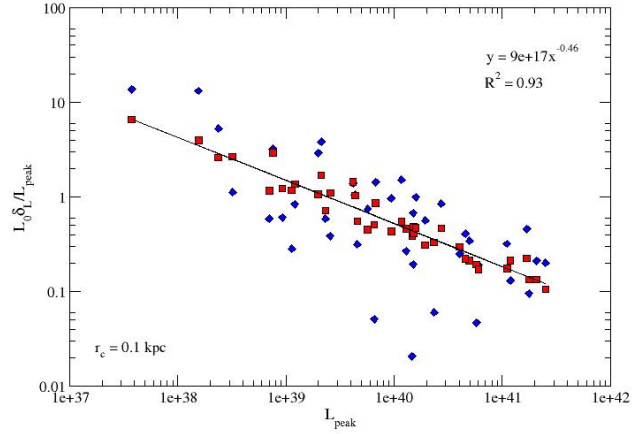


FIGURE 5.5— Ratio of  $L_0\delta_L/L_{\text{peak}}$  vs.  $L_{\text{peak}}$  after using  $L_0 = C_1L_{\text{host}}^\gamma$  (see text), where  $\gamma$  is given by Eq. (5.11) (red squares). The fitted regression (solid line) and correlation coefficients are shown on the top right corner of each plot. The initial values of the ratio are also shown for comparison (blue diamonds). Plots from top to bottom correspond to binding radius  $r_c=0.1, 1,$  and  $3$  kpc, respectively.



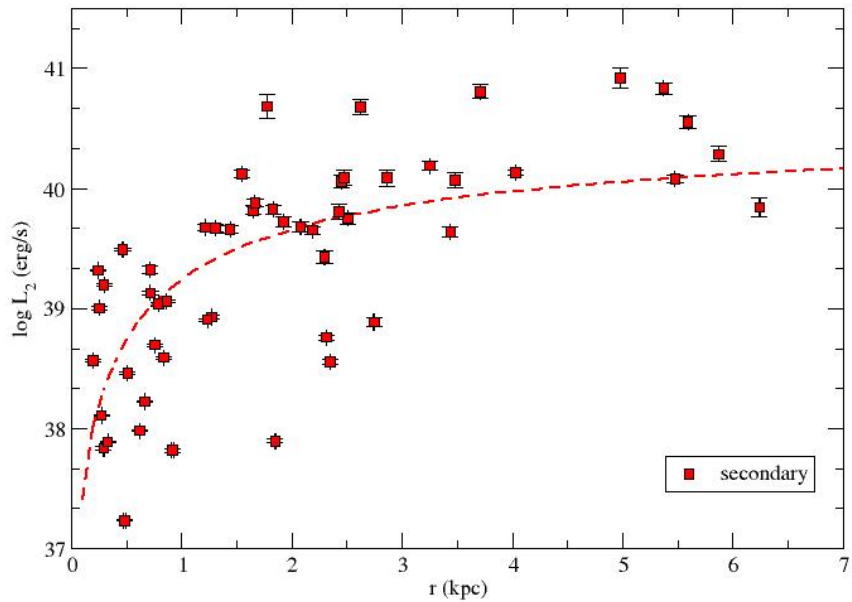
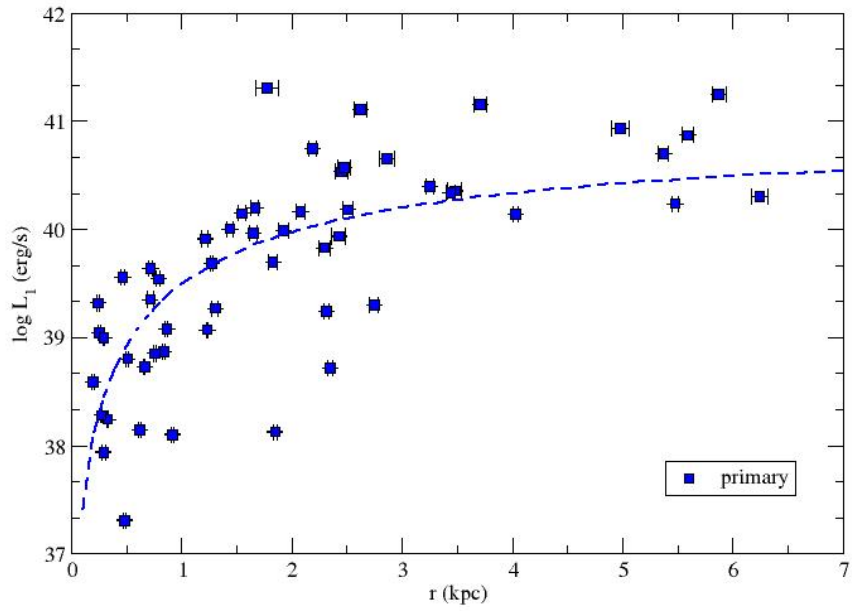
$$\begin{aligned}\langle \tilde{M} \rangle &= 0.72 \pm 0.04, \\ \langle \tilde{r}_{d1} \rangle &= 0.83 \pm 0.02, \\ \langle \tilde{r}_{d2} \rangle &= 0.94 \pm 0.01,\end{aligned}$$

and these values are inserted in Eq. (5.6). This equation is then applied to the luminosity dependence of each nucleus with the separation between the two, using  $L_0$ ,  $r_c$ , and  $\beta$  as free parameters. The luminosity of the primary and secondary nuclei versus their separation are shown in Fig. 5.6, top and bottom, respectively. The best fits obtained for each nucleus are also plotted (dashed lines) and have a non-reduced  $\chi^2$  of 22. The computed values of the fit are:  $\log L_0 = 39.9 \pm 0.2 \text{ erg s}^{-1}$ ,  $r_c = 2.27 \pm 0.01 \text{ kpc}$ ,  $\beta = -2.3 \pm 0.2$ .

The two nuclei become thus gravitationally bound when they are at a projected separation of 2.27 kpc. An average inclination angle of  $\sim 69^\circ$  can be derived from the axial ratio of the host galaxies provided in Gimeno et al. (2004). This yields a physical separation between the two nuclei of 2.4 kpc, which is larger than the separations obtained from the PSF fitting for 60% of the post-merger galaxies analyzed. Therefore the primary and secondary nucleus are gravitationally bound in 60% of the sources studied. Using this value of  $r_c$ , the reduced separation  $\tilde{r}$  is calculated for all sources and is found to be always  $< \tilde{r}_{d1,2}$ . The accretion disk of both nuclei have thus already started being disrupted in all sources.

#### 5.5.4 Extinction

To ensure that the results obtained are not affected by different degrees of extinction in each of the nuclei, the  $u$  and  $g$ -band images of each target are retrieved from the SDSS DR8 and PSF fitting is performed in these bands in the same way as for the  $r$ -band. In the  $u$  band, `imfitfits` fails to fit the positions of the double nuclei in 10 of the targets. For the remaining 44 sources, the fitted fluxes are converted from nmg to magnitudes and the  $u-g$  colors of the primary against the secondary nuclei are plotted (see Fig. 5.7). Both nuclei are affected by the same extinction, and thus they both have the same environment. The results obtained in the previous sections are thus not affected by extinction or by differences in the ambient medium in which the nuclei are embedded.



142

FIGURE 5.6— Luminosity of the primary (top) and secondary (bottom) nucleus versus separation between the two nuclei. The dashed line in each plot is the fit to the data given by Eq. (5.6).

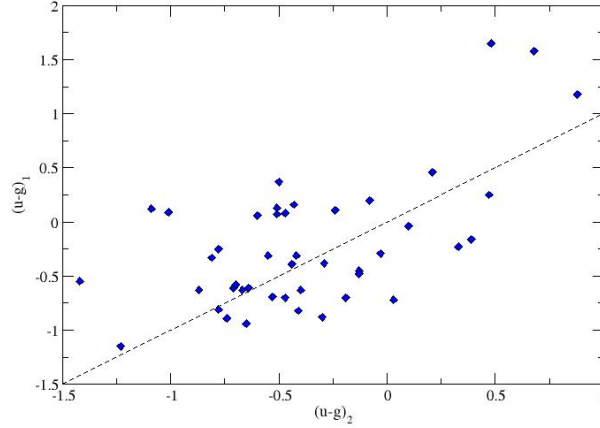


FIGURE 5.7— Color-color diagram of  $u-g$  magnitudes of the primary vs. the  $u-g$  magnitudes of the secondary nucleus. A one-to-one correlation indicating no extinction differences between the two nuclei is also plotted (dashed line).

## 5.6 Discussion

In the cold dark matter paradigm for structure formation, the stellar mass and the size of local massive galaxies is built up via assembly processes such as major mergers and satellite accretion (e.g., Williams et al. 2011 and references therein). Major mergers have been shown to be responsible for only  $\sim 20\%$  of the mass growth (López-Sanjuan et al. 2011 and reference therein), which is a significant but not dominant contribution. Minor merger processes could lead to a significant increase in both mass and size, as they have been found to be more efficient at increasing galaxy radii than major mergers (e.g., Naab et al. 2009; Trujillo et al. 2011). Evidence for minor merging have been often reported in the literature (e.g., as recent star formation in early-type galaxies; Kaviraj et al. 2007, 2009; Fernández-Ontiveros et al. 2011) and confirmed by simulations (e.g., Mihos & Hernquist 1994; Bournaud et al. 2007; Callegari et al. 2011). In this chapter, evidence that minor mergers play a role in BH growth and, possibly, in galaxy hierarchical assembly is provided by investigating the evolution of the nuclear luminosity of the primary and secondary nucleus in a sample of 54 post-merger galaxies.

### 5.6.1 The black hole-bulge correlation

The results obtained indicate that the luminosity of each of the nucleus is correlated with the host galaxy luminosity ( $L_1 \propto L_{\text{host}}^{1.0 \pm 0.1}$  for the primary, and  $L_2 \propto L_{\text{host}}^{0.9 \pm 0.1}$  for the secondary), thus following the  $M_{\text{BH}} - L_{\text{bulge}}$  correlation (e.g., Wandel 2002; Marconi & Hunt 2003; Bentz et al. 2009). There has been a major concern regarding a different value of the slope in the  $M_{\text{BH}} - L_{\text{bulge}}$  correlation for quiescent and for active galaxies (see Bentz et al. 2009 for a discussion). The slopes obtained here for the primary and the secondary nucleus are in agreement with the  $M_{\text{BH}} \propto L_{\text{bulge}}^{1.0}$  found for quiescent galaxies (Graham 2007) and with the slope of  $0.9 \pm 0.1$  found for both active and quiescent galaxies (Wandel 2002), but steeper than the value of 0.8 found for nearby AGN (Bentz et al. 2009). The finding that both the primary and secondary nuclei are AGN (e.g., via X-ray observations), would lend further support to a common black hole-bulge correlation for active and inactive galaxies.

### 5.6.2 Tidal enhancement and accretion disk disruption

In the binary black hole evolutionary model (Lobanov 2008 and references therein), the nuclear luminosity of post-merger galaxies is expected to be affected both by a tidal enhancement of the accretion rate as well as the disruption of the accretion disk. The analysis performed in Sect. 5.5.2 shows that there is a significant contribution to the observed luminosity trend from tidal enhancement, indicating that an increase of the accretion rate is present. This enhancement of the accretion rate due to tidal effects is also expected from simulations of unequal-mass mergers (e.g., Callegari et al. 2011), which show that accretion rates onto the two BHs are enhanced by roughly the same factor and confirm the fundamental role that tidal stripping plays in the formation of close binary BH systems. A residual trend is still observed after removing the contribution of the tidal effects from the nuclear luminosity. These residuals are more significant at binding radii of 1-3 kpc, and are suggested to be the contribution of accretion disk disruption.

A theoretical connection between disk disruption and nuclear luminosity can be derived from the radial distribution of spectral intensity of the accretion disk (Shakura & Sunyaev 1973), after introducing a factor that accounts for the reduction of nuclear power owing to the disruption of the outer parts of the disk (see Eq. 5.6). This model is applied to the luminosity evolution of the primary and secondary nucleus with their separation, using as free parameters the power-law index of the spectral distribution  $\beta$ , the binding radius  $r_c$ , and

the undisturbed luminosity  $L_0$  of a single, inactive nucleus. The luminosity of both the primary and the secondary nuclei are satisfactorily fitted by the model, finding  $L_0=8\times 10^{39}$  erg s<sup>-1</sup>,  $\beta = -2.3$ , and that the nuclei become gravitationally bound at  $r_c=2.27$ . These results show, for the first time, that the accretion disk of both the primary and the secondary nuclei are being stripped in the course of the merger, and that they become gravitationally bound at a separation of  $\sim 2.3$  kpc.

According to the standard disk model (Shakura & Sunyaev 1973), the spectrum at each radius of the accretion disk is assumed to be blackbody radiation with a local effective temperature. The power-law spectral index  $\beta$  can be then approximately taken as  $\alpha+1$  (Shakura & Sunyaev 1973), where  $\beta > 0$  and  $F_\nu \propto \nu^{-\alpha}$ . From the computed value of  $\beta$ , a spectral power-law index  $\alpha=1.27$  is obtained. This power-law decline is steeper than the canonical  $\alpha$  of the Shakura-Sunyaev disk, but consistent with the disk model. The spectral energy distribution (SED) of AGN shows a “big blue bump” that peaks in the ultraviolet (UV; 912-2000Å) and is thought to be thermal emission from an optically thick accretion disk around a SMBH (e.g., Shields 1978; Malkan & Sargent 1982). The far-ultraviolet (FUV; 912-2000Å) spectral region of AGN with UV-bump exhibits  $\alpha_{\text{FUV}} \sim 1-2.2$  (e.g., Ross et al. 1992; Zheng et al. 1997), while in the 1200-5500Å range (UVO) values of  $\alpha_{\text{UVO}} \sim 0.5-1.7$  are inferred from the data (Shang et al. 2005). These values are also in agreement with the spectral power-law index  $\alpha$  derived from the modeling presented in Sect. 5.5.3.

All the results obtained for the sample of 54 double nucleus post-merger galaxies indicate therefore that both the tidal enhancement of the accretion rate during the merger and the accretion disk disruption affect the evolution of the nuclear luminosity of the black holes.

### 5.6.3 Sub-kpc AGN pairs

Of the 54 double nucleus systems analyzed, *imfitfits* finds 19 sources with projected nuclear separations  $< 1$  kpc (corresponding to  $< 9''$ ), or physical separations  $\leq 1$  kpc when considering an average inclination angle for the host galaxies of  $\sim 69^\circ$ . The closest separation AGN pair so far detected is NGC 6240 (Komossa et al. 2003; Koss et al. 2011), showing two hard X-ray cores at physical separation of 1.4 kpc, while several kpc-scale binary AGN have been found from X-ray observations (e.g., Koss et al. 2011) or suggested from double-peaked optical emission lines (Liu et al. 2010a). In all these cases no double nuclei are detected in the optical band, which could be due to a high rate of star formation (especially in ULIRGs). High-resolution optical/infrared

observations of those post-merger galaxies with the closest separated double nucleus would be pivotal in order to confirm the presence of a binary nucleus in these systems. In addition, the detection of a double core from high-resolution X-ray observations (e.g., *Chandra*) of those double-nucleus galaxies with nuclear separations  $< 1$  kpc, would indicate that the two nuclei are AGN and yield therefore the first ever detection of a sub-kpc AGN pair.

#### 5.6.4 Relation to the ULX objects

One of the possible scenarios suggested to explain the observed high X-ray luminosities of ultraluminous X-ray sources is that they are the secondary black hole of the BBH system formed in post-merger galaxies (see Chapter 4). The range of black hole masses between  $10^3 - 10^8 M_{\odot}$  estimated from the fundamental plane for the ULXs studied in Chapter 4 would be in agreement with this scenario if some of the ULXs were hosting a BH that has undergone a minor merger event with the ULX host galaxy. In this case, the luminosity of these ULXs would be affected by a tidal enhancement of the accretion rate and a disruption of the accretion disk as the nuclei of the post-merger galaxies studied here are. The dependence of the ULX luminosity with the nuclear separation to the host galaxy should then be well fitted by the binary black hole evolution-luminosity relation (see Sect. 5.2).

Given the lack of optical counterparts and accurate black hole masses for most of the ULX sources studied in Chapter 4, the detailed analysis and fit obtained for the double nucleus post-merger galaxies cannot be yet performed for these ULX sources. A first test to the BBH scenario was done by plotting the ULX luminosity against the nuclear separation for a sample of ULX objects located in the Chandra Deep Fields (Lobanov 2008). We include also to this plot the ULX sources with detected radio counterparts reported in Chapter 4. The relative distance between the two nuclei of the post-merger galaxies studied in this chapter (see Table 5.1) does not reach values greater than 8 kpc. We exclude thus from the ULX luminosity vs. distance those ULXs with nuclear separations much higher than 8 kpc (i.e., above 10 kpc), and which have also values of X-ray luminosity in the limit of the ULX definition (i.e., below  $10^{39}$  erg  $s^{-1}$ ). The ULX sources excluded are: NGC 3256-X13, NGC 4395-X2, NGC 5457-X2, NGC 5457-X17, and NGC 5457-X26. The  $L_X$  vs. nuclear distance plot for the rest of ULXs is shown in Fig. 5.8. There seems to be a similar trend to the one observed for the post-merger galaxies, and the trend seems to follow quite satisfactorily the BBH model obtained for the primary nucleus of the post-merger systems (dashed line in Fig. 5.8).

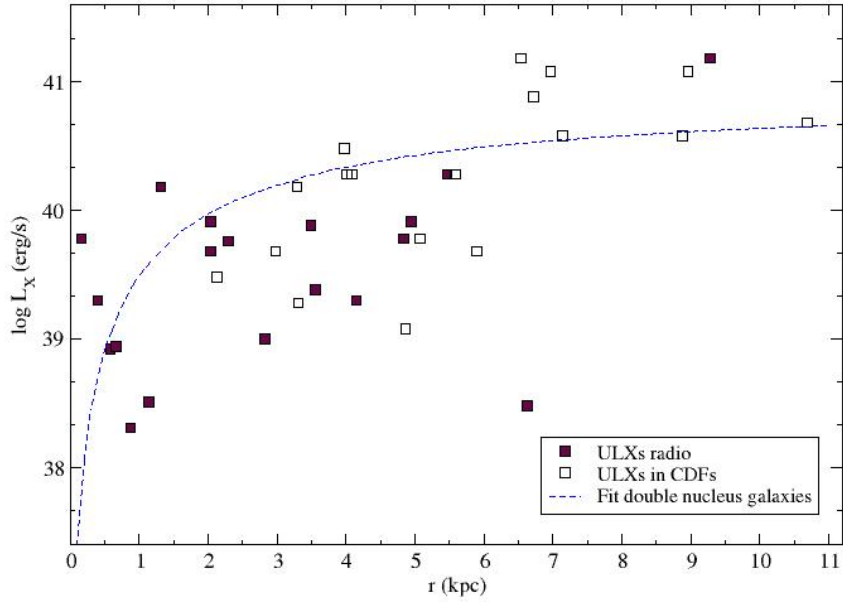


FIGURE 5.8— X-ray luminosity of the ULX sources studied in Chapter 4 versus their separation to the nucleus of the host galaxy. Filled squares: ULXs with detected radio counterparts (see Table 4.6). Open squares: ULXs located in the Chandra Deep Fields (Lehmer et al. 2006). The BBH fit obtained for the primary nucleus in the post-merger galaxies is also shown (dashed line).

A correlation between X-ray luminosity and nuclear distance is not expected from the other scenarios proposed to explain the ULX nature (e.g., super-Eddington accretion, microblazars, etc.), but is expected if ULXs do indeed harbor secondary black holes in post-merger galaxies. The trend observed, thus, supports the presence of secondary BHs in some ULX sources. A more detailed analysis and application of the BBH model is needed and will be pursued when optical counterparts and more accurate estimates of the ULX BH mass are available.





# 6

---

## Conclusions and future work

*The end is where we start from.  
Thomas Stearns Elliot (1888-1965)*

Understanding how galaxies form and grow is one of the major challenges that astronomy faces today. The currently most recognized evolutionary model suggests that galaxies grow hierarchically through mergers, building larger and more massive galaxies from smaller systems (Toomre 1977). Alternative models such as secular evolution or cold accretion are also gaining strength nowadays.

According to the hierarchical evolutionary model, star formation and quasar activity are enhanced during the galactic merger, triggering the growth of the central supermassive black hole (SMBH; e.g., Hopkins et al. 2006). If nearly all galaxies host a SMBH in their center (Richstone et al. 1998) and galaxies grow through merging, it is expected that a pair of SMBHs will be found in the center of those galaxies that have recently undergone a merger. The detection and estimate of the number of binary SMBHs is thus pivotal for constraining the existing models of galaxy formation and evolution.

This thesis has presented three lines of observational evidence of binary black hole (BBH) systems: X-shaped radio galaxies, ultraluminous X-ray sources, and double nucleus galaxies. A brief description of the analysis performed and the main results obtained are summarized in this chapter.

## 6.1 Summary of results

### *X-shaped radio galaxies*

X-shaped radio galaxies exhibit two pairs of misaligned radio lobes associated to the same parent galaxy, giving these galaxies a peculiar X-shaped morphology. It was suggested that the black hole coalescence as a result of a galactic merger could be responsible for the flip of the black hole spin axis, thus driving the reorientation of the jet (Merritt & Ekers 2002). In this thesis, we have carried out a statistical study of the BH mass and starburst activity of a sample of 38 X-shaped radio galaxies, and compared the results obtained to those in a control sample of 36 radio-loud active nuclei with redshifts and optical and radio luminosities in the same range as for the X-shaped galaxies. The optical spectra of the X-shaped and control sources have been modeled using a stellar population synthesis code that yields the stellar velocity dispersion, light fraction, mass fraction, age, and metallicity of the stellar populations used in the fit. These parameters have been used to derive the starburst histories of these objects, and the stellar velocity dispersion has been used to derive the mass of the central SMBH. An estimate of the dynamic age of the radio lobes has been also derived from their angular size measured in the radio maps. The results obtained have revealed that:

- All the X-shaped radio galaxies studied are hosted by early-type galaxies, as indicated by their Ca II break values and the color-color diagram (Sect. 3.4.3). This supports the merger hypothesis as the origin of the X-shaped radio sources, since early-type galaxies are expected to have undergone at least one merger during their evolution (Toomre 1977).
- The X-shaped radio galaxies tend to have statistically higher BH mass than the objects in the control sample, as shown by the histograms of the BH mass distribution (Figs. 3.8–3.9). The average BH mass of the X-shaped sample is  $2.89^{+0.62}_{-0.51}$  times higher than the one of the control sample in a tight common range of radio and optical luminosities. This higher mean BH mass could be the result of a major merger event, which could be the cause of the X-shaped morphology observed in the radio maps.
- The most recent bursts of star formation in the X-shaped sample are statistically older than those of the control sample, with 50% of the X-shaped sources having starburst ages older than  $10^8$  years, and occurred

before the active lobes were formed. Moreover, a peak at ages of 1-3 Gyr is observed in the distribution of the most recent starburst age of the X-shaped sample (Fig. 3.10). This peak suggests enhanced star formation due to a merger event, and is in agreement with the time delay between the peak of starburst activity and the end of the merger expected from simulations of galaxy mergers (Lotz et al. 2008) and observations of individual objects (e.g., Tadhunter et al. 2005; Emonts et al. 2006). The dynamic age of  $10^6$  yrs derived for the X-shaped radio lobes is also in agreement with the time delay between the merger event and the onset of the radio-AGN activity triggered by the merger (e.g., Emonts et al. 2006).

All these results do not only strengthen the merger scenario as the suggested origin of the X-shaped radio sources, but also yield further support to the hierarchical evolutionary model where galaxies grow by mergers, triggering star formation and AGN activity.

#### *Ultraluminous X-ray sources*

Ultraluminous X-ray sources (ULX) are extragalactic, off-nuclear, and very bright X-ray sources with luminosities exceeding  $10^{39}$  erg s<sup>-1</sup>. It has been suggested that ULXs are sub-Eddington accreting intermediate mass black holes (IMBH) of  $10^2$ - $10^5 M_{\odot}$  (Colbert & Mushotzky 1999), which are the missing link between stellar mass BHs and SMBHs. Alternatively, ULXs could be super-Eddington accreting stellar-mass BHs (e.g., Begelman 2002; King et al. 2001), X-ray binaries in an ultraluminous state (Gladstone & Roberts 2009), or young X-ray luminous supernovae (Colbert & Mushotzky 1999). ULXs have also been suggested to harbor the secondary BH of the BBH systems formed in post-merger galaxies (Lobanov 2007), being thus of particular interest for this thesis.

With the aim of revealing the nature of ULX sources and their possible connexion to BBH systems, we have: (1) analyzed archival images of the Chandra Deep Fields (CDF) taken with the Giant Meterwave Radio Telescope (GMRT) looking for faint radio counterparts of the ULX sources located in these fields; (2) observed three ULX objects with known radio counterparts with the European VLBI Network (EVN) at 1.6 GHz in a program initiated to detect and study milliarcsecond-scale emission from ULXs; and (3) compiled all the ULX sources for which a radio counterpart is reported in the literature. The radio and X-ray luminosities of the ULX objects studied are used for estimating the ULX BH mass from their location in the fundamental plane

of accreting black holes (Corbel et al. 2003; Gallo et al. 2003; Merloni et al. 2003; Falcke et al. 2004), and to derive the ratio  $R_X$  of radio to X-ray luminosity (Terashima & Wilson 2003).

The results obtained are the following:

- No radio counterparts of the 24 ULXs located in the CDFs are found in the archival GMRT images. The upper limits on their radio flux densities obtained are used to locate these sources in the black hole fundamental plane. For six of the sources, radio counterparts were detected by more sensitive surveys (e.g., Bauer et al. 2002; Kellermann et al. 2008). The BH mass of these six objects estimated from the fundamental plane ranges between  $10^5$ – $10^8 M_\odot$  (Fig. 4.3).
- The EVN radio observations of the ULX N4088-X1 yield the detection of a compact component with a radio luminosity of  $3.8 \times 10^{34} \text{ erg s}^{-1}$  and brightness temperature  $T_B \geq 7 \times 10^4 \text{ K}$  (Fig. 4.2, left). The EVN measurements have provided a better localization of this ULX in the fundamental plane, and yielded an estimate of the BH mass of  $10^5 M_\odot$ . This ULX could thus be harboring an IMBH accreting at sub-Eddington rate.
- For the ULX N4861-X2, a compact component with  $T_B \geq 10^6 \text{ K}$  and possible extended emission are detected with the EVN at 1.6 GHz (Fig. 4.2, right). This ULX could be an HII region with a diameter of 8.6 pc and  $T_B \geq 10^5 \text{ K}$  if the extended structure were confirmed. If the radio emission comes only from the compact component, the ULX could be a sub-Eddington accreting IMBH of  $\sim 10^5 M_\odot$ .
- The EVN observations of the third target, N4449-X1, confirm the earlier identification of this object with a supernova remnant (SNR) and yield the resolved shell-like structure of this SNR (Fig. 4.7). We obtain the most accurate estimates of its size ( $0.058'' \times 0.028''$ ;  $1.1 \text{ pc} \times 0.5 \text{ pc}$ ) and age ( $\sim 55$  years), making this object one of the largest extragalactic SNRs imaged with VLBI.
- The location in the fundamental plane of all those ULX for which a radio counterpart has been detected (including the six ULXs in the CDFs, N4088-X1, and N4861-X2) and is not suggested to come from background AGN or SNRs, yields a range of BH masses between  $10^3$ – $10^8 M_\odot$  (Fig. 4.5). More than 50% of the ULXs have estimated BH

masses ranging  $10^3 < M_{\text{BH}} < 10^5 M_{\odot}$ , and are thus potential candidates for being IMBHs.

The range of BH masses obtained for all the ULX located in the fundamental plane would be in agreement with the BBH scenario (Lobanov 2007) if some the ULXs hosted a BH that has undergone a minor merger event with the ULX host galaxy. The BBH evolutionary model should then fit the evolution of the ULX nuclear luminosity with the nuclear separation to the host galaxy, as it is observed in Sect. 5.6.4.

#### *Double nucleus galaxies*

According to the BBH evolutionary model (Lobanov 2008 and references therein), the luminosity of each of the nucleus of the BBH system is affected by an enhancement of the accretion rate due to tidal disruption and by accretion disk stripping. A tidal enhancement of the accretion rate is also expected from simulations of un-equal mass mergers (Callegari et al. 2011), but had not yet been tested observationally until now.

We have applied this model to a sample of 54 double nucleus post-merger galaxies undergoing a minor merger event. We have applied the PSF fitting technique to the  $g$ ,  $r$ , and  $u$ -band optical images of the nuclear center of these galaxies and obtained, as a result, the brightness of each of the nucleus and the relative separation between the them. The host galaxy luminosity has also been derived from SDSS photometry. Finally, the BBH model (Eq. 5.6) has been applied to the data using as free parameters the reduced separation of the two nuclei ( $r_c$ ), the canonical luminosity of a single inactive nuclei ( $L_0$ ), and the the power-law index of the radial distribution of spectral intensity ( $\beta$ ).

The PSF fitting and consequent study of a connection between nuclear and host luminosity have yielded the following results:

- A trend between the nuclear luminosity of each of the nuclei and the host galaxy luminosity is observed. This trend is in agreement with the  $M_{\text{BH}} - L_{\text{bulge}}$  correlation (e.g., Wandel 2002) for  $r$ -band luminosities above  $8 L_{\odot}$  (Fig. 5.3).
- A deeper study of this luminosity trend shows that tidal enhancement is indeed present and that another process (i.e., accretion disk disruption) must be responsible for the residual trend. These residuals are stronger at a binding radius in the range  $r_c=1-3$  kpc, and are suggested to be due to accretion disk stripping.

- The primary and the secondary nuclei are found in the same environment and affected by the same extinction (Fig. 5.7). The results obtained are thus not extinction-dependent.
- Of the 54 galaxies analyzed, 19 are found to have a double nucleus with separation  $\leq 1$  kpc. If both nuclei were confirmed as AGN (e.g., via X-ray observations), these sources would be the closest separation AGN pair so far detected (the closest one is NGC 6240, with a physical separation of 1.4 kpc; Koss et al. 2011).

From the fit of the BBH model to the data we have obtained that:

- The luminosity of the primary and the secondary nuclei are satisfactorily fitted by the model, with  $L_0=8 \times 10^{39}$  erg s<sup>-1</sup>,  $\beta = -2.3$ , and  $r_c=2.3$ . The two nuclei become thus gravitationally bound when they are at a projected separation of 2.3 kpc. This value is larger than the separations of the two nuclei obtained from the PSF fitting in 60% of the galaxies analyzed.
- The reduced separation derived from the value of  $r_c$  obtained from the fit is found to be always smaller than the distance at which the accretion disk of the primary and the secondary nuclei are disrupted. The accretion disk of the two nuclei are thus already being disrupted in all sources.
- The value of  $\beta$  is used to derive an accretion disk power-law spectral index  $\alpha=1.27$ , where  $F_\nu \propto \nu^{-\alpha}$ . This value is in agreement with the  $\alpha$  found in the spectral region of AGN with a peak in the optical-UV band (the “big blue bump”; e.g., Shang et al. 2005).

The study of the nuclear luminosity of double nucleus galaxies has proved, for the first time, the BBH model on post-merger galaxies. The results indicate that both the tidal enhancement of the accretion rate and disk disruption are at play there, and that the accretion disk of both the primary and secondary nuclei are being disrupted during a minor merger event.

The results of the BBH fit have also been applied to the luminosity dependence of the ULX sources of Chapter 3 on the nuclear separation to their host galaxy, obtaining that the observed trend between luminosity and distance for the ULX objects is also in agreement with the BBH model (Fig. 5.8).

To summarize, this thesis has shown that the hierarchical evolutionary model is capable of explaining the origin of X-shaped radio galaxies and that

the evolution of binary systems of supermassive black holes, forming during galactic mergers, determines at large the luminosity evolution of the brightest ULX sources and the primary and secondary nuclei of post-merger galaxies.

## **6.2 Future work**

The results obtained in this thesis have laid a broad foundation for further observational programs and tests aimed at detecting supermassive secondary black holes in post-merger galaxies, studying their physical properties, and understanding their relation to the evolution of their galactic hosts.

### **X-shaped radio galaxies**

The results obtained for the X-shaped radio galaxies call for special attention to studies of the star formation history and stellar and gas kinematics that could potentially confirm the merger event in X-shaped radio sources. No systematic studies of star formation and host kinematics in X-shaped radio sources have been done so far. A new project has been initiated in this area of study, combining integral field spectroscopy (IFS) studies, observations of the neutral HI gas, and high- resolution VLBI radio observations.

#### *Integral field spectroscopy*

The IFS technique would allow us to spatially resolve the X-shaped sources and, for the first time in this type of sources, distinguish the spectrum of the host galaxy from the one of the active nucleus. The immediate goals of such a project would be:

- Obtain the velocity field structure and 2-D velocity dispersion maps for the gas, the stellar component, and the neutral interstellar medium using different optical absorption and emission lines.
- Model the rotation pattern to determine possible merger-induced deviations in the kinematics.
- Obtain accurate dynamical mass estimates and recover the properties of putative binary black hole systems in these galaxies.

#### *Neutral HI gas*

The main objectives are to quantify the amount of neutral gas in these galaxies, to trace any evidence for merging (indicated by the HI kinematics) and to

investigate possible AGN-induced outflows. The HI gas is the best tracer of galaxy-galaxy interactions, as its distribution is usually several times larger than the optical extent of the galaxy, and thus more easily disrupted by external forces (e.g., Emonts et al. 2006; Koribalski & López-Sánchez 2009; English et al. 2010). HI gas observations of radio galaxies offer, in addition, the chance to investigate AGN fueling/feedback mechanisms and radio jet interactions with the host galaxy.

#### *High-resolution radio observations*

We have been granted observing time at the EVN at 1.6 GHz to study the parsec-scale radio emission of a small sample of X-shaped sources. The goal of the project is to search for compact, weak AGN-like components and present or relic extended jets that may be associated with active (or recently active) SMBHs, while investigating if X-shaped sources do harbor binary SMBH systems with two pairs of jets associated with two unresolved AGN. No studies of this kind have been done so far in X-shaped sources.

#### **Ultraluminous X-ray sources**

Given the importance of intermediate-mass or seed BHs in the growth of more massive ones (Georgakakis et al. 2011) and the possible link of ULXs with IMBHs and secondary BHs in the course of a minor merger event (Sect. 5.6.4), finding a significant number of IMBHs and secondary BHs would yield important constraints on the models for galaxy formation and evolution. Such finding can only be achieved via studies of the ULX black hole mass and properties of their closest surroundings. With this in mind, a new study has been initiated, targeting a sample of ULXs with detected radio counterparts and combining archival photometric data and spectroscopic observations of their optical counterparts with VLBI radio observations.

#### *Hubble Space Telescope optical images*

Archival *HST* images of the galaxies hosting ULXs with detected radio counterparts can be analyzed to search for optical counterparts. The immediate results would be:

- An estimate of the X-ray to optical flux ratio ( $\log f_X/f_o$ ). This would allow us to discern between background AGN or an accreting system within the host galaxy (e.g., X-ray binary, IMBH), even in the case that



the ULX optical counterpart is not detected. The optical flux (or an upper limit in the case of no detection) can be further used to estimate the BH mass (e.g., Jithesh et al. 2011).

- The observed magnitudes (if different filters available) can be used to locate the source in the color-magnitude diagram and constrain the spectral type of a possible stellar companion in an XRB.

#### *Optical spectroscopic observations*

Follow-up spectroscopic observations can be applied for those ULX sources with optical counterparts detected. This would allow finding out if the optical emission arises from a companion star in an XRB (indicated by the detection of continuum emission with a series of absorption lines), an accretion disk surrounding a compact object (indicated by a blue continuum and emission lines), or a nebula surrounding the ULX (indicated by the presence of forbidden lines, e.g., Kaaret et al. 2009). If the optical emission comes from an accretion disk, the radial velocities of the emission lines (or width in the case of broad emission lines) can be used to constrain the mass of the BH and estimate the size of the line-emitting region (e.g., Cseh et al. 2011a).

#### *Milliarcsec-scale radio emission*

As a continuation of the EVN program started in this thesis, the milliarcsec-scale radio emission of those ULX sources with radio counterparts will be studied in order to distinguish between compact radio emission (i.e., coming from a compact accreting object) and possible extended structure (i.e., coming from a radio nebula or a supernova remnant), and to find out which is the physical mechanism responsible for the radio emission (e.g., synchrotron, bremsstrahlung). We have already been granted observing time with the EVN at 1.6 and 5 GHz of a sample of ULXs.

#### **Double nucleus galaxies**

For the sample of post-merger galaxies analyzed in Chapter 5, the estimates of the brightness of the primary and secondary nuclei and their relative separation are the result of fitting a PSF to the nuclear region of these objects. These estimates could be better constrained by means of high-resolution optical observations of the nucleus of these sources. This, together with spectroscopic observations, would allow us to rule out that one of the nuclei is a giant III

region, as it has been the case for other double nucleus galaxy candidates (e.g., Gimeno et al. 2007).

Milliarcsec-scale radio observations with VLBI would also be an excellent tool to confirm the existence of a binary black hole system in the center of these galaxies and the presence (or absence) of jets with peculiar morphologies. The existence of an AGN pair can be also confirmed by X-ray observations with the *Chandra* satellite. Of particular interest would be the observation of those double nucleus with separations  $< 1$  kpc. Detecting a double X-ray core in these systems would yield the first detection of a sub-kpc AGN pair.

# Appendices



# A

---

## Kinematic black hole mass estimates from motions of ionized gas

### A.1 Introduction

In Chapter 3, the black hole mass of the X-shaped radio galaxies and control sources was obtained using the empirical correlation between BH mass and stellar velocity dispersion (e.g., Gebhardt et al. 2000; Tremaine et al. 2002) as represented by stellar absorption lines in the optical spectra. A second method can be employed to obtain kinematic estimates of the central BH masses, which is based on the motions of ionized gas near the SMBH (e.g., Peterson & Wandel 1999; Kaspi et al. 2000; Onken et al. 2004; Peterson et al. 2004) and the relation between the width of broad emission lines emitted by this gas, the BH mass, and the size of broad line regions (BLR) estimated from the continuum luminosity (Kaspi et al. 2000, 2005).

Both methods are based on the assumption of virialized motions in the nuclear regions of galaxies, but the broad line emission reflects gas motions only around presently active black holes, while the stellar absorption lines can probe both active and inactive black holes. Therefore, the determination and comparison of the masses obtained using these two methods can provide a useful tool (together with the results from Chapter 3) for distinguishing between the different scenarios proposed for the X-shaped objects.

## A.2 Analysis

### A.2.1 Black hole masses

If the FWHM of the broad emission lines reflects a Keplerian motion of ionized gas in the BLR, the mass of the central black hole can be estimated from

$$M_{\text{BH}} = \frac{R_{\text{BLR}} V_{\text{BLR}}^2}{G}, \quad (\text{A.1})$$

where  $G$  is the gravitational constant,  $R_{\text{BLR}}$  is the radius of the BLR and  $V_{\text{BLR}}$  is the velocity of the line-emitting gas, traditionally estimated from the *FWHM* of the  $\text{H}\beta$  emission line (or  $\text{H}\alpha$  in the absence of  $\text{H}\beta$ ). The  $R_{\text{BLR}}$  is correlated with the monochromatic continuum luminosity  $\lambda L_{\lambda}$  at  $5100\text{\AA}$  of the host galaxy (Kaspi et al. 2000), and this continuum luminosity is correlated with the luminosity of the  $\text{H}\alpha$  ( $L_{\text{H}\alpha}$ ) and  $\text{H}\beta$  ( $L_{\text{H}\beta}$ ) emission lines (Greene & Ho 2005). The black hole mass can then be expressed in terms of the observed  $L_{\text{H}\beta}$  (or  $L_{\text{H}\alpha}$ ) and the *FWHM* of the broad  $\text{H}\beta$  (or  $\text{H}\alpha$ ) lines, respectively (Greene & Ho 2005):

$$M_{\text{BH}} = 3.6 \pm 0.2 \times 10^6 \left( \frac{\lambda L_{\text{H}\beta}}{10^{42} \text{ erg s}^{-1}} \right)^{0.56 \pm 0.02} \left( \frac{\text{FWHM}_{\text{H}\beta}}{10^3 \text{ km s}^{-1}} \right)^2 M_{\odot} \quad (\text{A.2})$$

$$M_{\text{BH}} = 2.0_{-0.3}^{+0.4} \times 10^6 \left( \frac{\lambda L_{\text{H}\alpha}}{10^{42} \text{ erg s}^{-1}} \right)^{0.55 \pm 0.02} \left( \frac{\text{FWHM}_{\text{H}\alpha}}{10^3 \text{ km s}^{-1}} \right)^{2.06 \pm 0.06} M_{\odot} \quad (\text{A.3})$$

### A.2.2 Emission lines

Some of the X-shaped radio galaxies and control sources in Chapter 3 show broad emission lines in their optical spectrum. We determine properties of these broad emission lines using the residual spectra obtained after subtracting the host galaxy contribution and AGN continuum from the STARLIGHT fits (Asari et al. 2007; Cid Fernandes et al. 2004b, 2005, 2007; Mateus et al. 2006). The  $\text{H}\beta$  and  $[\text{OIII}]$  emission lines in these spectra are modeled as a combination of narrow and broad components. We first fit three narrow Gaussian components for the oxygen  $[\text{OIII}]\lambda 4959\text{\AA}$  and  $[\text{OIII}]\lambda 5007\text{\AA}$  lines and for  $\text{H}\beta$ . Three additional constraints are applied during the fitting in order to reduce the number of free parameters and provide robust fits: 1) the central wavelengths of the narrow line components are set to their respective

laboratory wavelengths; 2) the *FWHM* of the two [OIII] narrow components are required to have the same value; 3) the 1:3 ratio of amplitudes of the [OIII] $\lambda$ 4959Å and [OIII] $\lambda$ 5007Å narrow components is fixed (see Fig. A.1, top).

After adjusting the narrow components, broad Gaussian components are added to the H $\beta$  line, and the joint fit is further adjusted until the relative residuals are reduced below 0.02-0.03 (see Fig. A.1, bottom).

Whenever the observed H $\beta$  line is too weak or absent, the same fitting method is applied to the H $\alpha$  and [NII] $\lambda$ 6548, 6583Å emission lines. We first fit a narrow Gaussian component to each line, setting the central wavelength of each component to its respective laboratory wavelength, and then constrain the *FWHM* of the two [NII] components to have the same value and a ratio [NII] $\lambda$ 6548Å/[NII] $\lambda$ 6583Å of 1:3.

### A.3 Results

Table A.1 lists the *FWHM* of the H $\beta$  broad line component (Col. 2) and the black hole mass calculated using Eq. A.2 and Eq. A.3 (Col. 3). Since there are too few objects with emission lines, only in two X-shaped sources could the *FWHM* of the H $\beta$  broad line be measured. In the case of the control sample, fourteen *FWHM*s were measured. The BH mass obtained from the *FWHM* ( $M_{\text{BH}} \text{FWHM}$ ) reflects the presence of an active black hole, while the mass derived from the stellar velocity dispersion (see Tables 3.2–3.3) probes both active and inactive black holes. However, the low number of X-shaped sources that show broad emission lines does not allow us to statistically compare these BH masses.

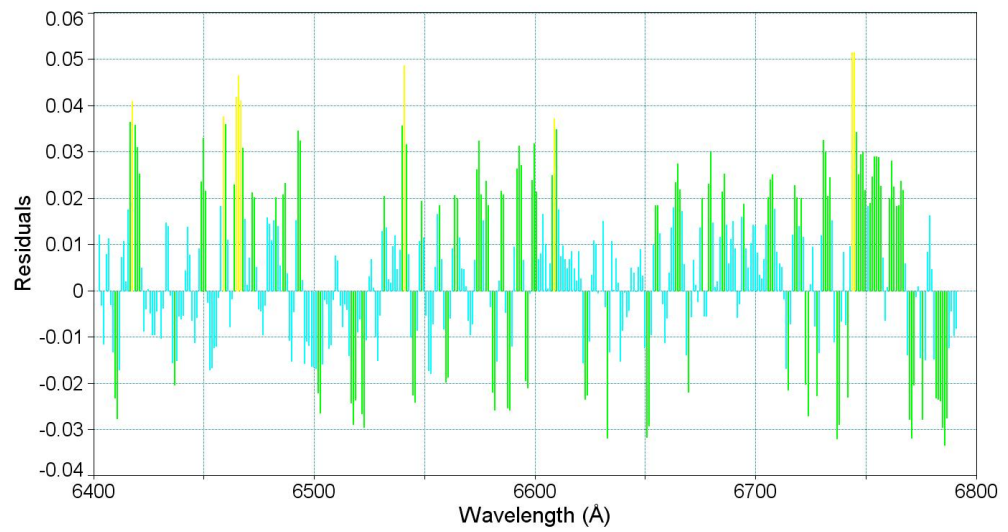
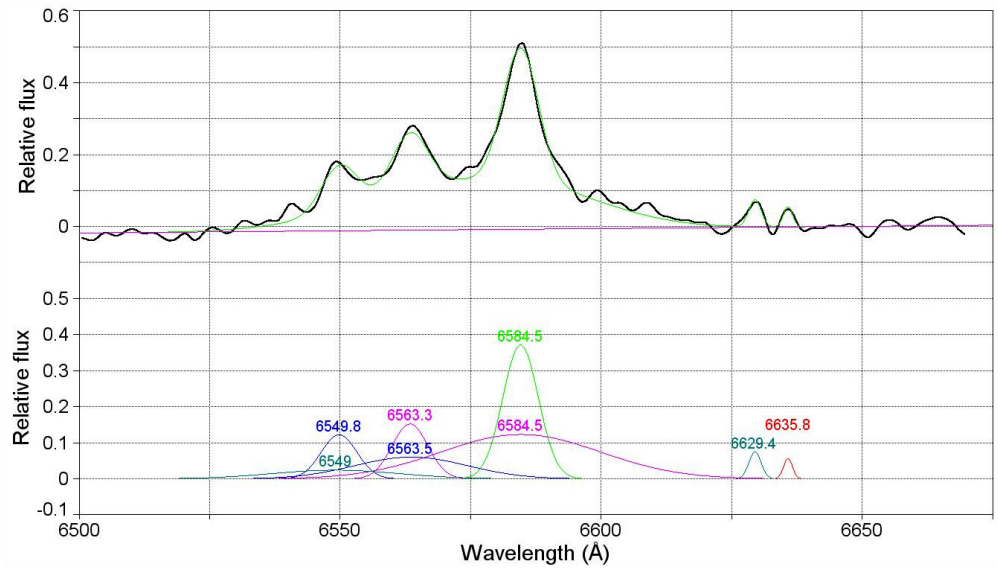


FIGURE A.1— Top: broad and narrow fitting components for the [NII] $\lambda\lambda$ 6548, 6583Å and H $\alpha$  emission lines of the source J1043+3131. Bottom: fit residuals.



TABLE A.1 — Emission lines and black hole masses

Name	$FWHM\ H\beta$ (km s $^{-1}$ )	$\log\left(\frac{M_{\text{BH}}\ FWHM}{M_{\odot}}\right)$
(1)	(2)	(3)
X-shaped objects		
J1043+3131	$1716.89^a \pm 65.29$	$5.82^b \pm 0.03$
4C+01.30	$2670.16^a \pm 253.99$	$7.20^b \pm 0.09$
Control sample		
J0758+3747	$921.70^a \pm 128.51$	$5.33^b \pm 0.13$
J0821+4702	$4824.11 \pm 2109.38$	$7.64 \pm 0.39$
J0921+4538	$2217.94 \pm 119.11$	$6.90 \pm 0.05$
J0947+0725	$4646.74 \pm 85.90$	$7.80 \pm 0.02$
J1007+1248	$6234.56 \pm 76.99$	$8.81 \pm 0.01$
J1031+5225	$1341.75 \pm 74.25$	$6.22 \pm 0.05$
J1114+4037	$5861.77 \pm 229.82$	$9.15 \pm 0.03$
J1154+0238	$1504.63^a \pm 28664.31$	$6.52^b \pm 17.04$
J1220+0203	$3817.45 \pm 128.00$	$8.45 \pm 0.03$
J1332+0200	$2001.11 \pm 34.53$	$6.95 \pm 0.02$
J1341+5344	$1154.92 \pm 93.32$	$5.88 \pm 0.07$
J1512+0203	$1257.47 \pm 233.92$	$6.11 \pm 0.16$
J1617+3222	$4349.66 \pm 156.76$	$7.76 \pm 0.03$
J2351-0109	$6114.47 \pm 178.05$	$8.71 \pm 0.03$

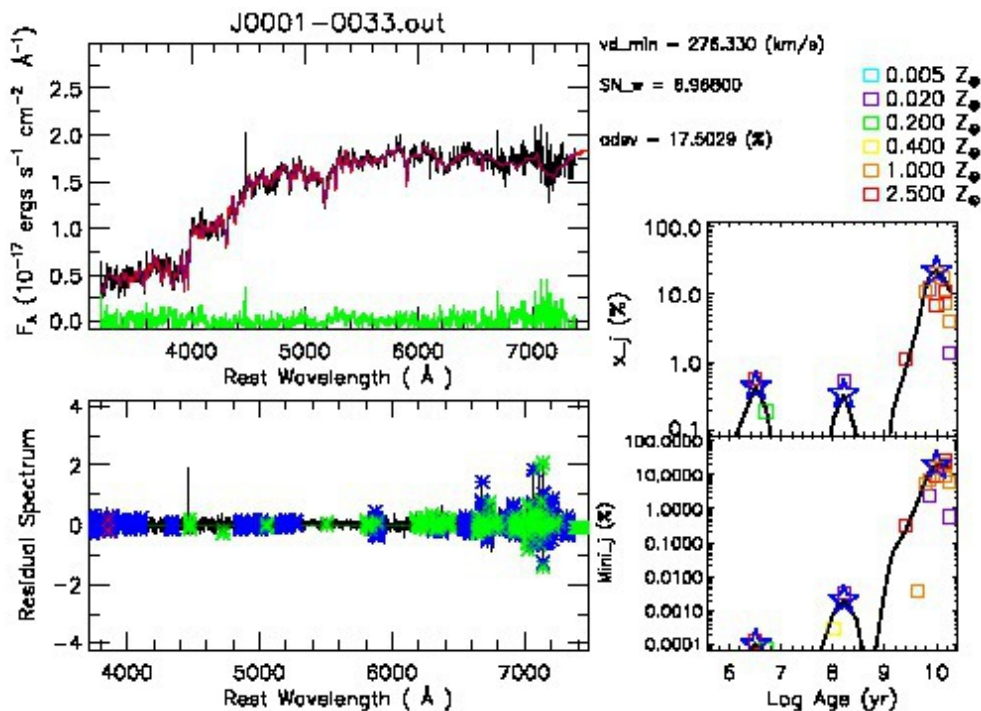
**Notes:**  $a$  –  $FWHM$  of the  $H\alpha$  line;  $b$  – Mass determined using the  $L_{H\alpha}$  and  $FWHM_{H\alpha}$

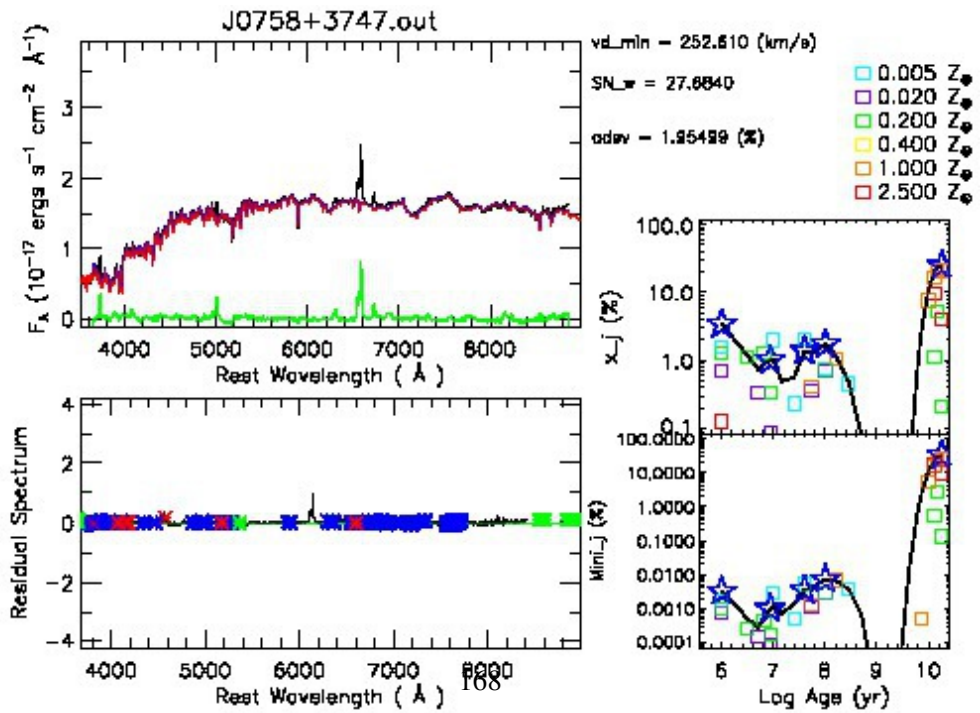
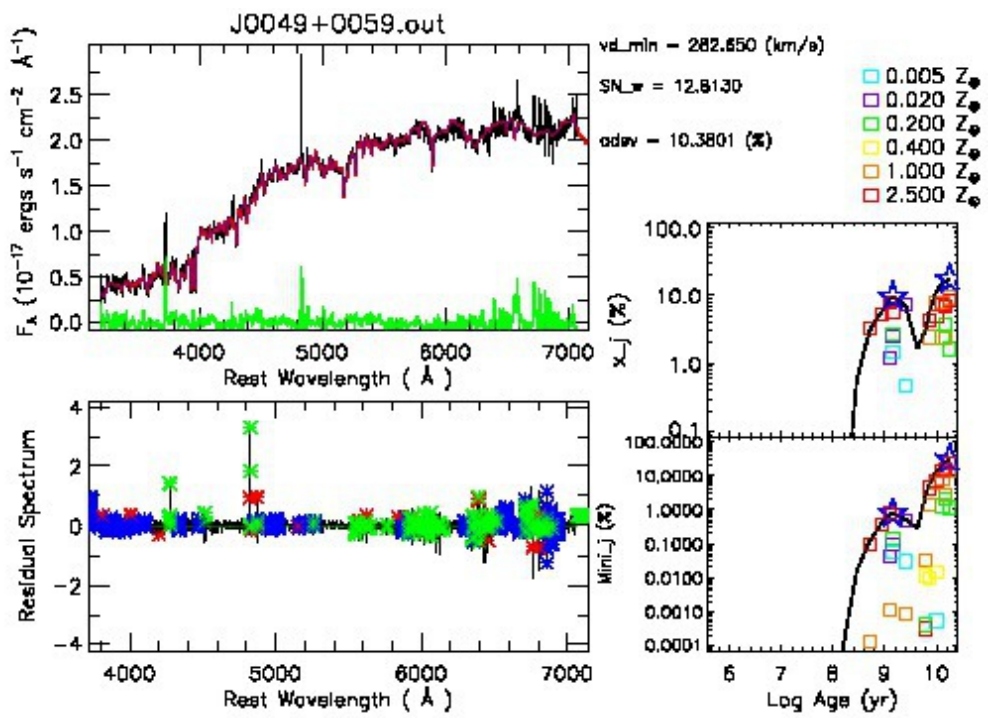


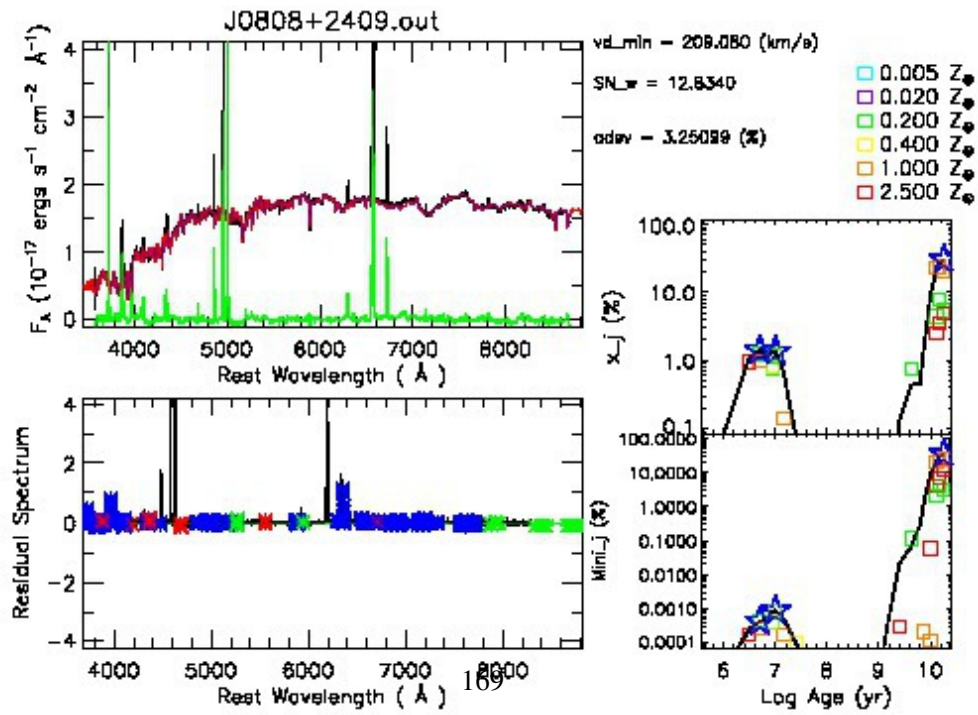
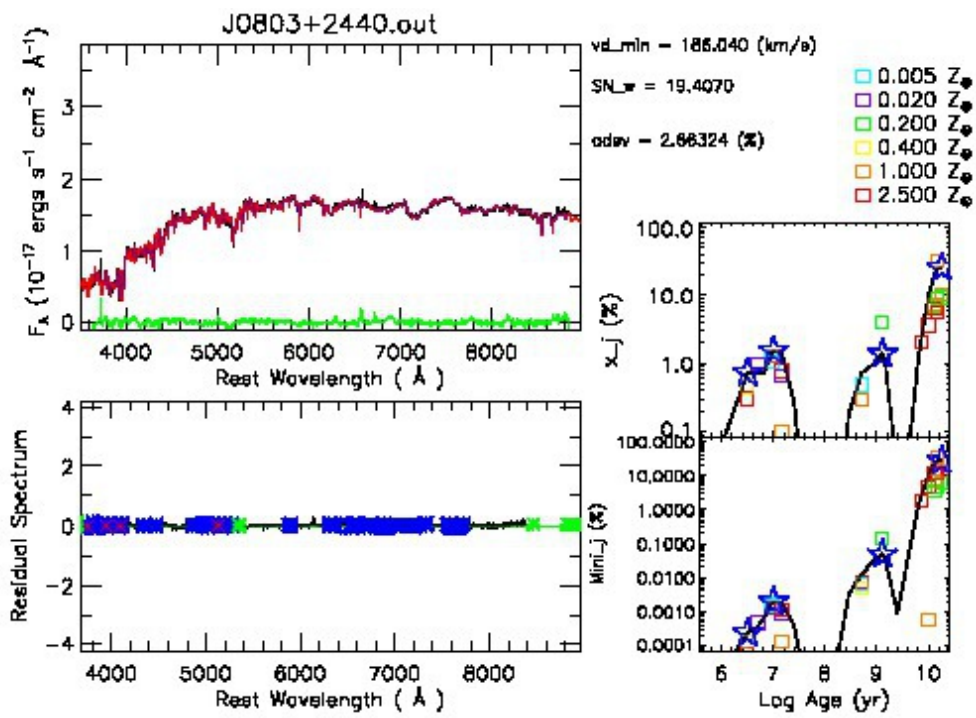
# B

## Atlas of stellar population analysis and starburst histories

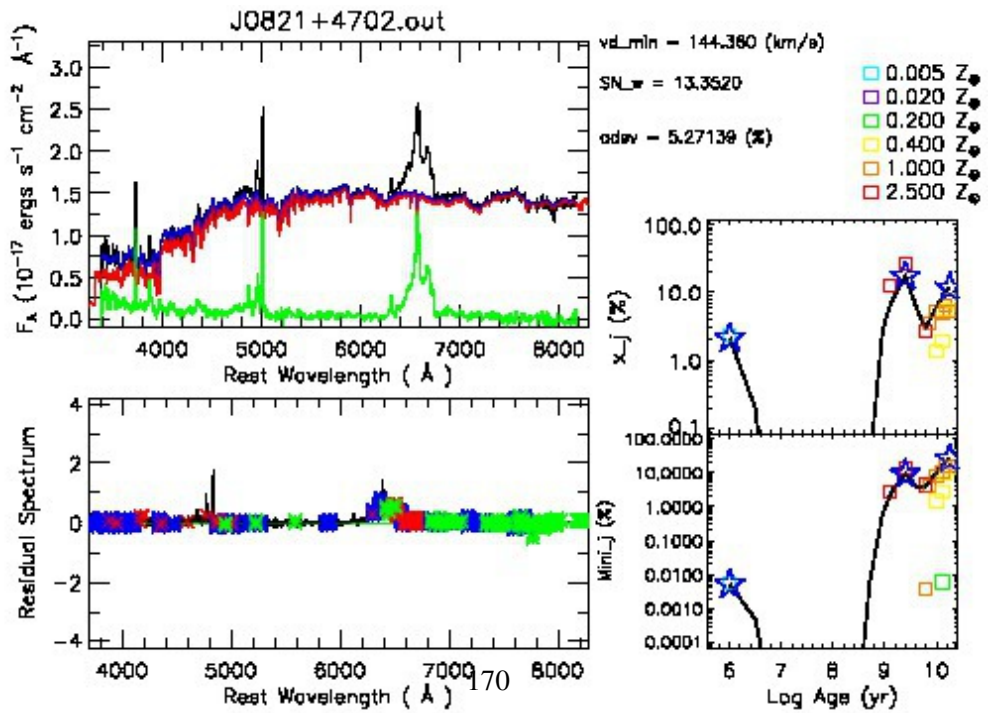
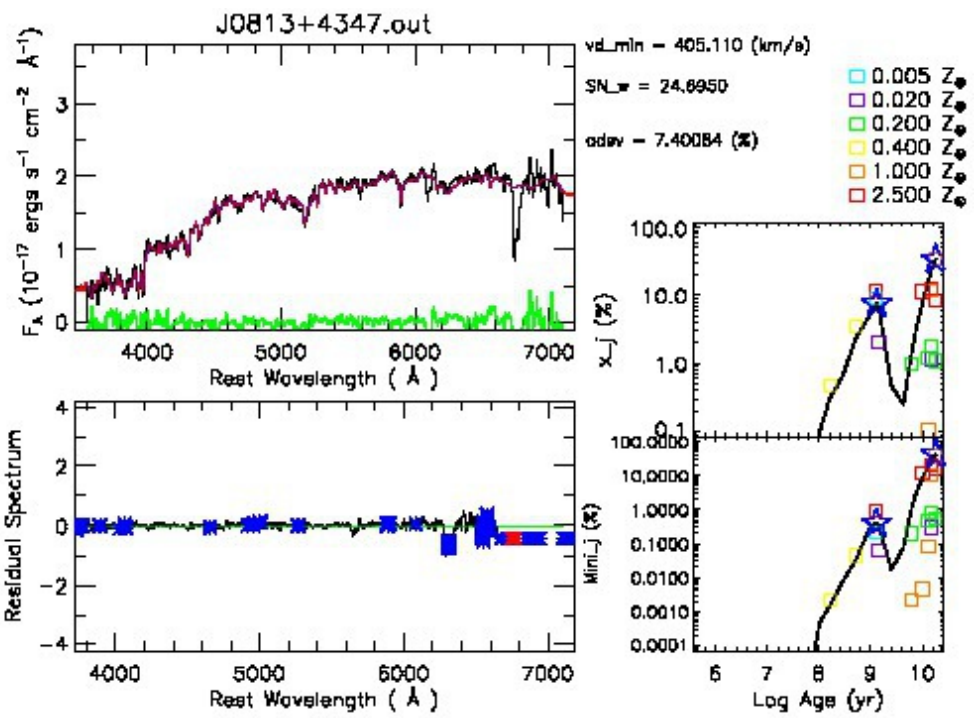
For all the X-shaped radio galaxies and control sources fitted with STARLIGHT, each figure shows: the STARLIGHT fit (top left), the residuals of the fit (bottom left), and the Gaussian smoothing applied to the mass and light fraction distributions of individual starbursts (right). In each plot, the source name is found above the STARLIGHT fit as 'name.out'.



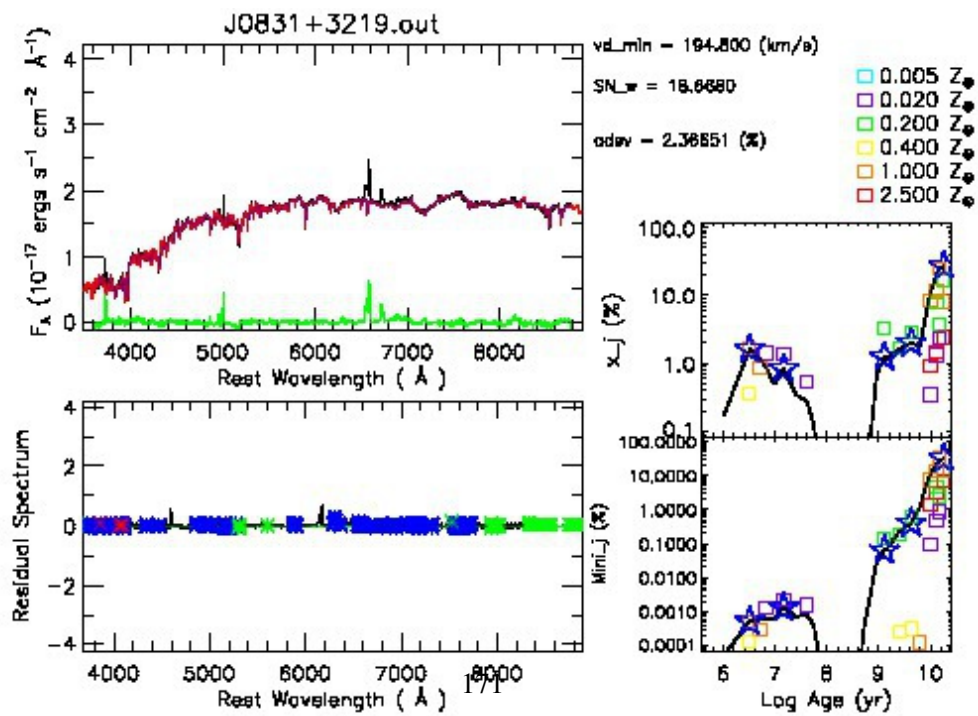
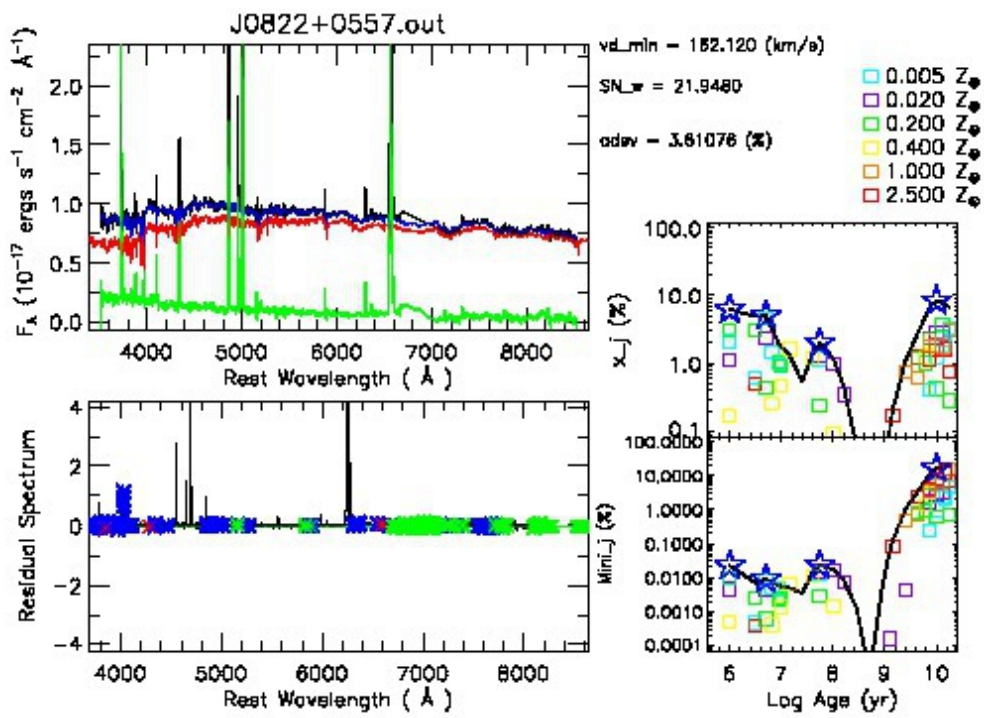


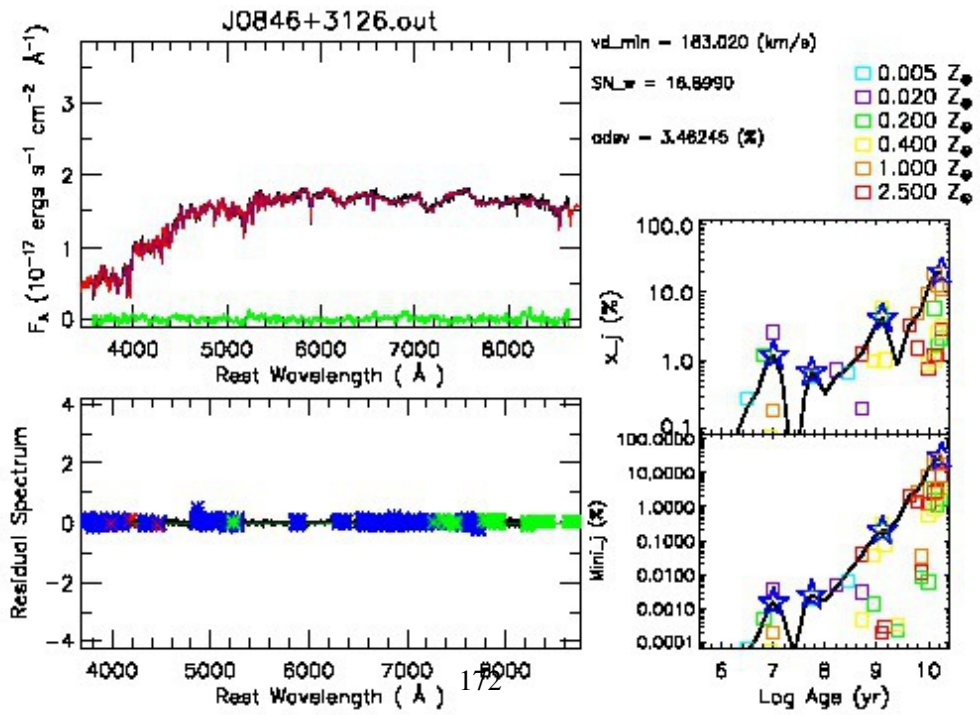
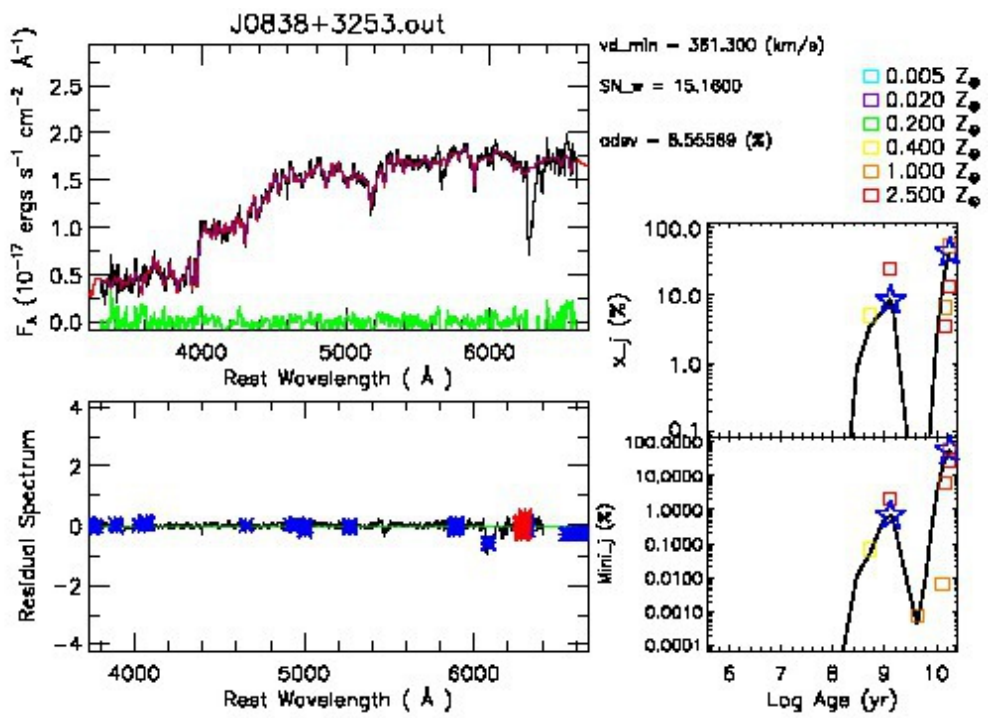


109

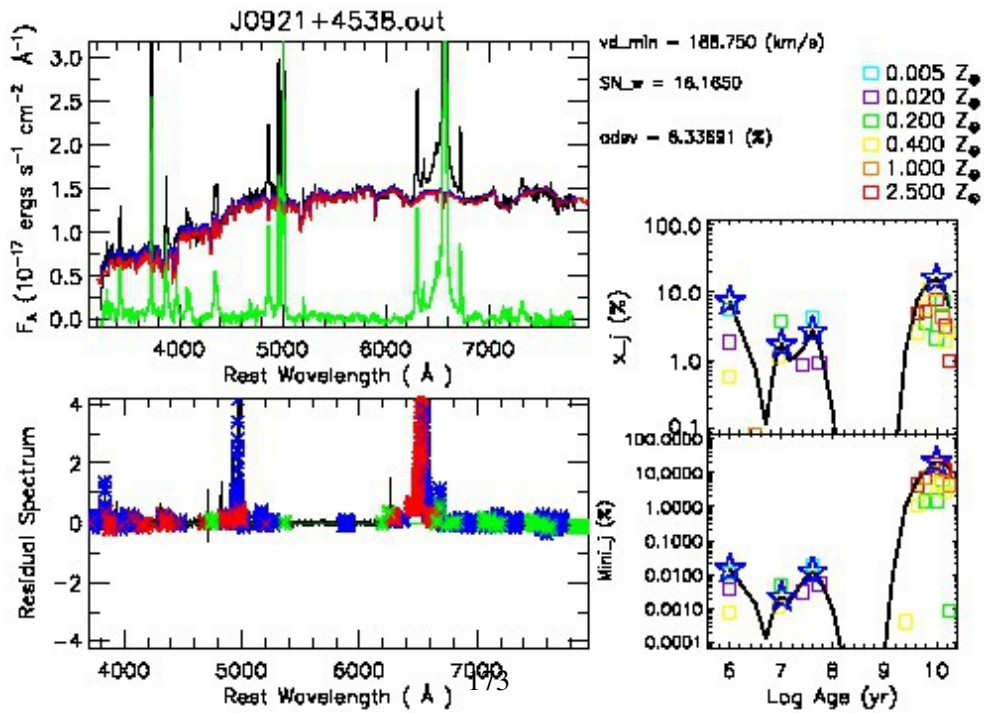
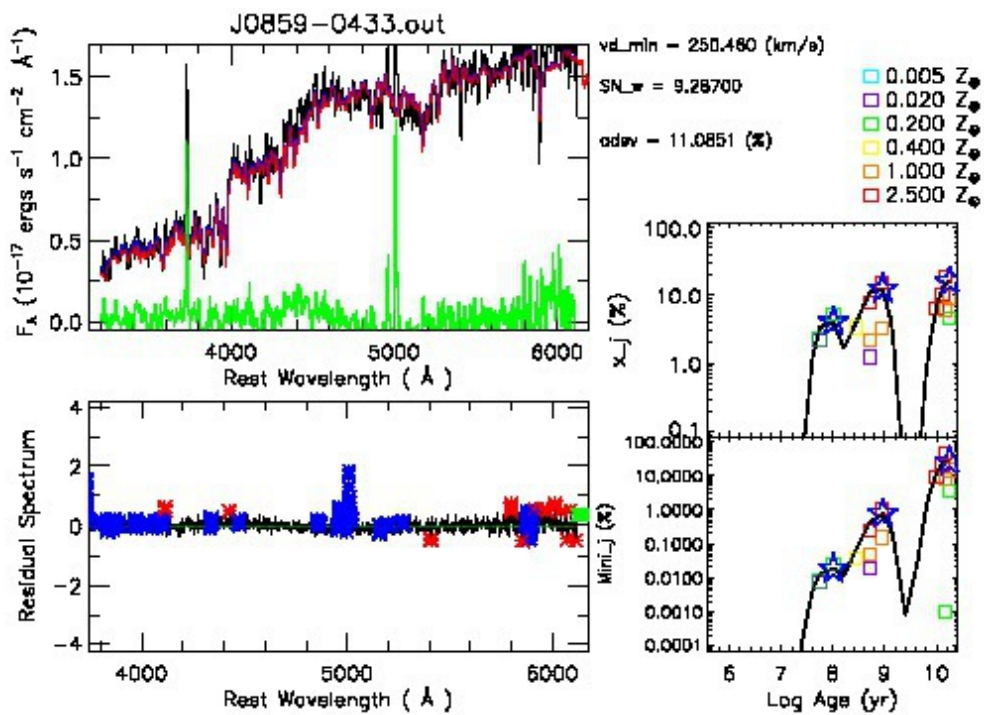


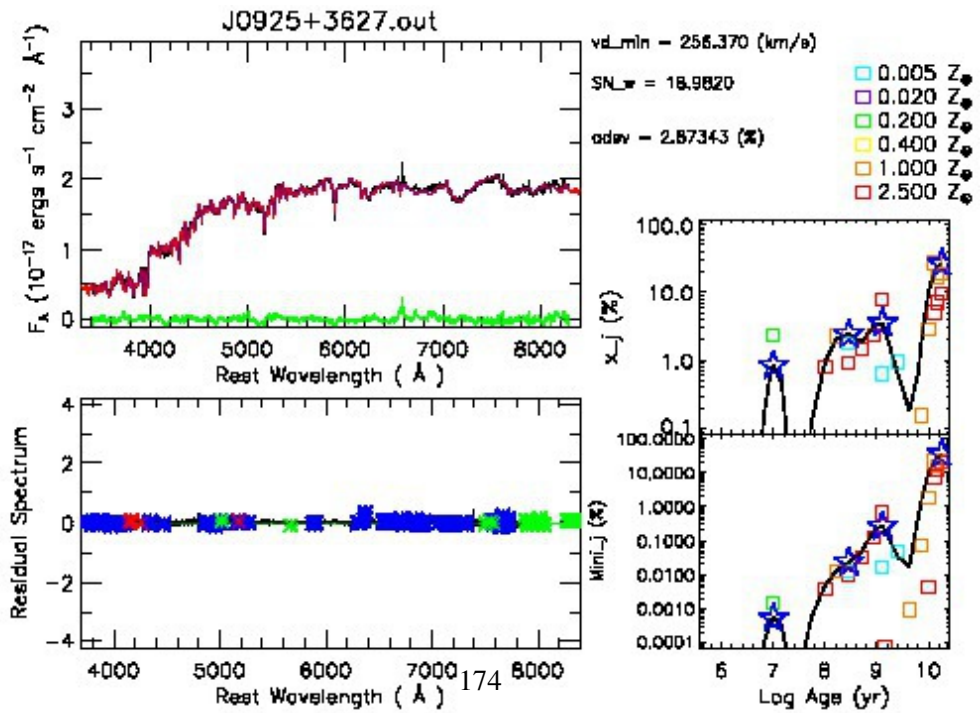
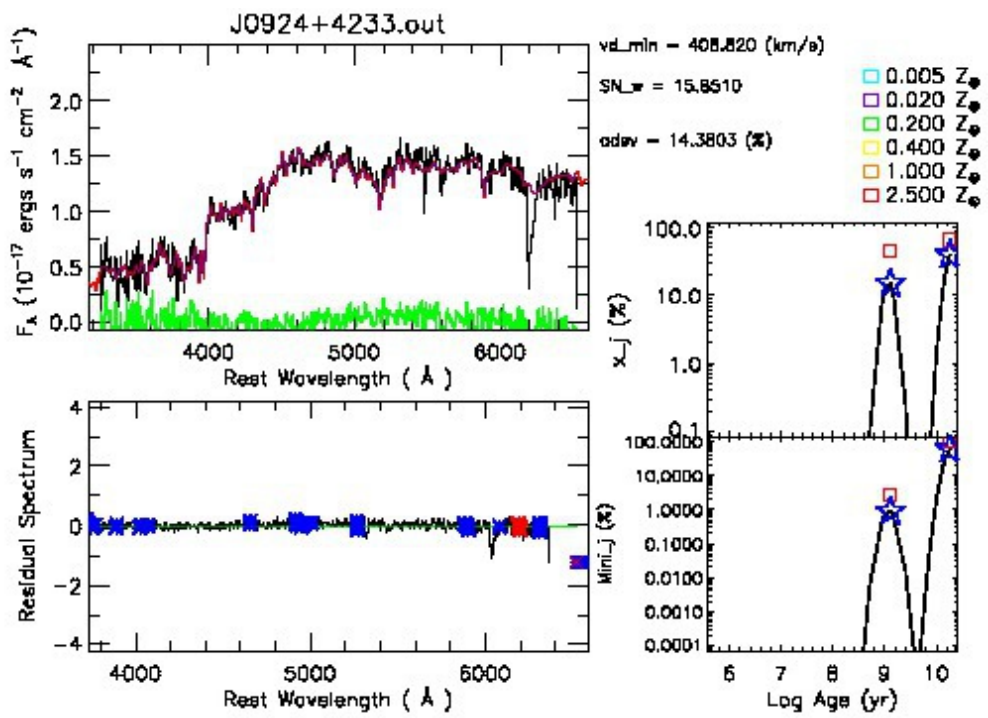


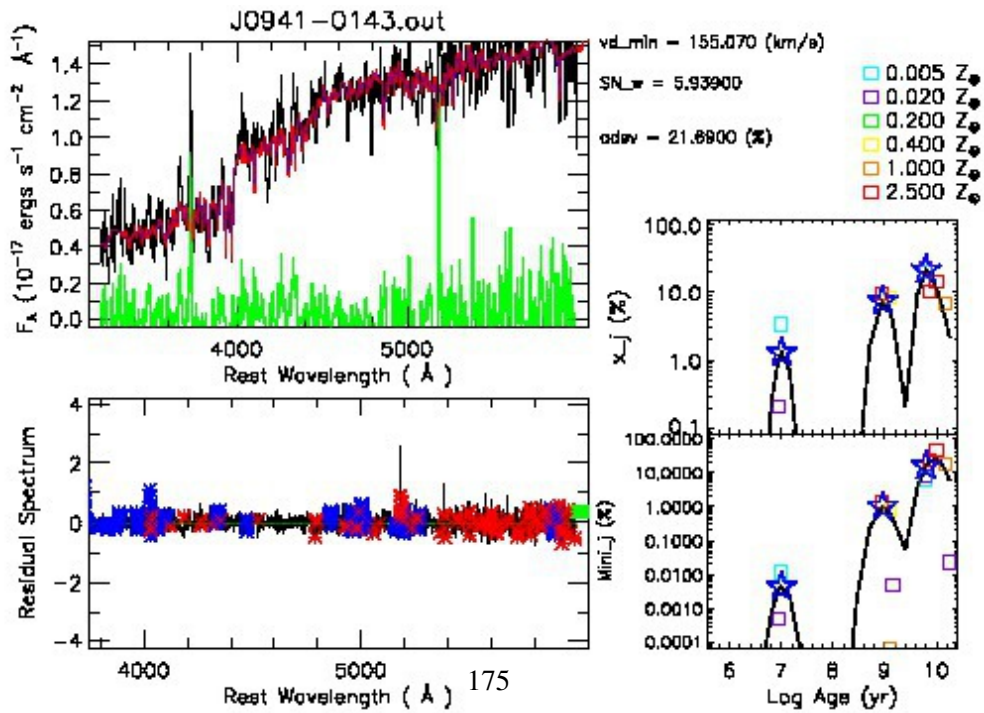
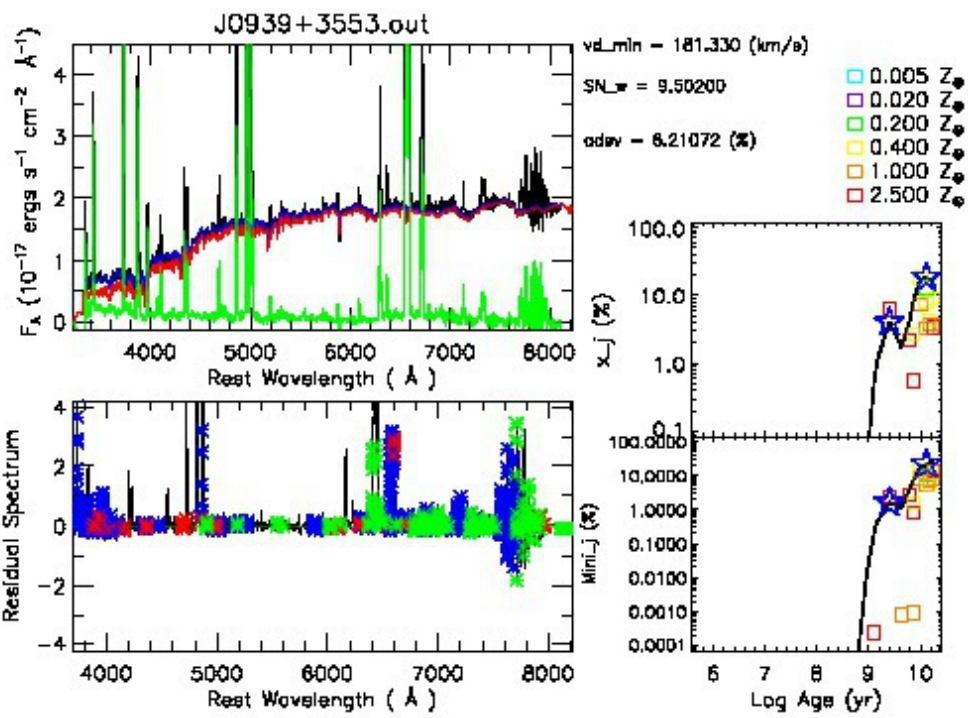


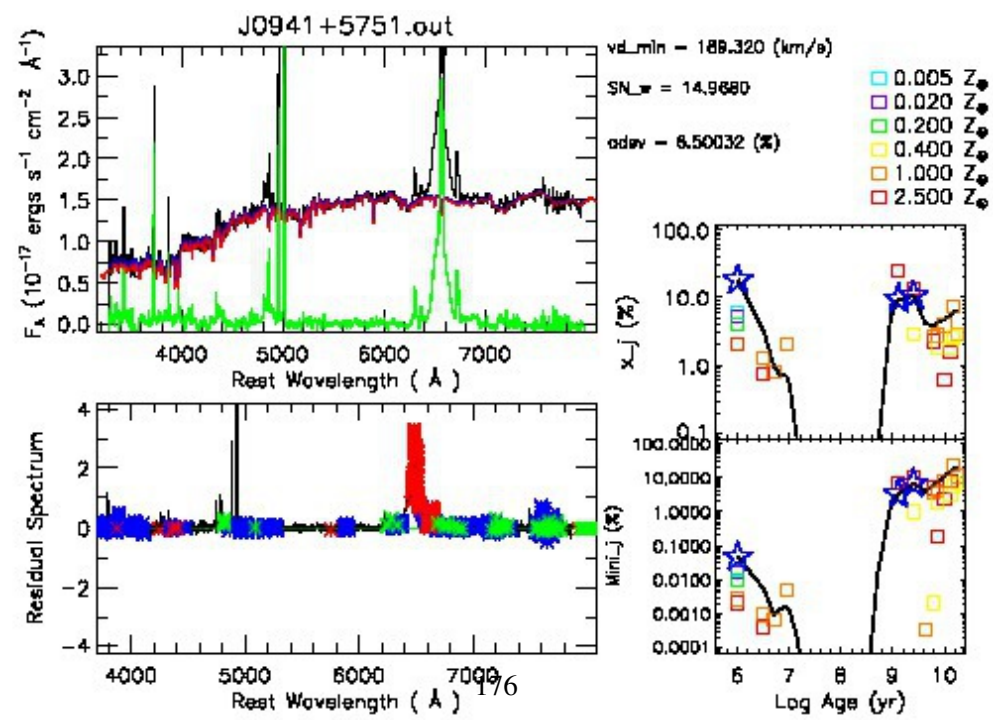
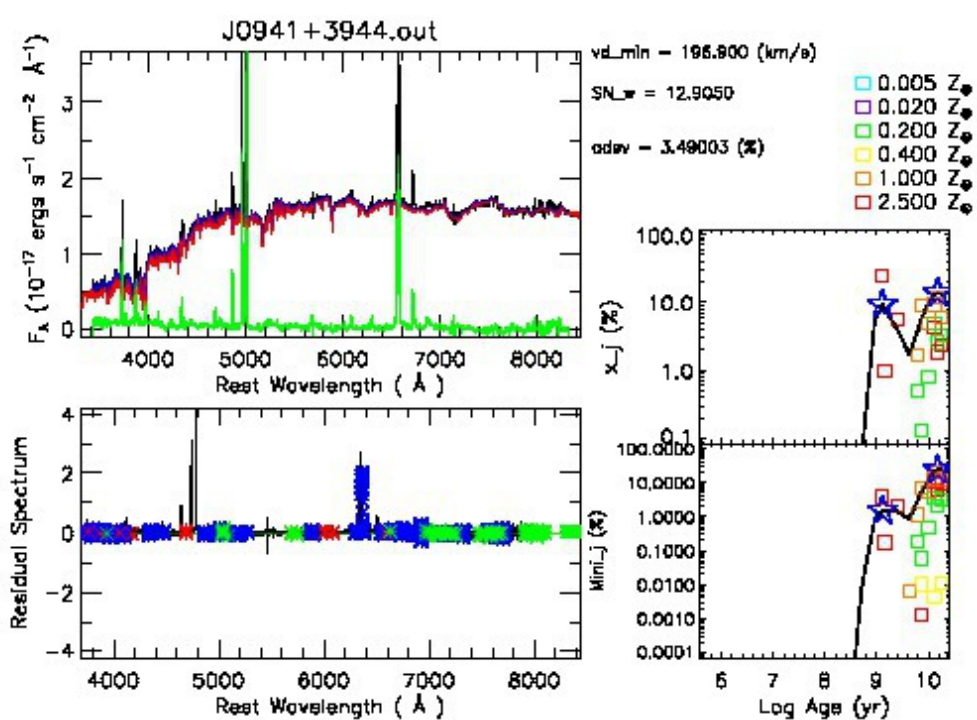




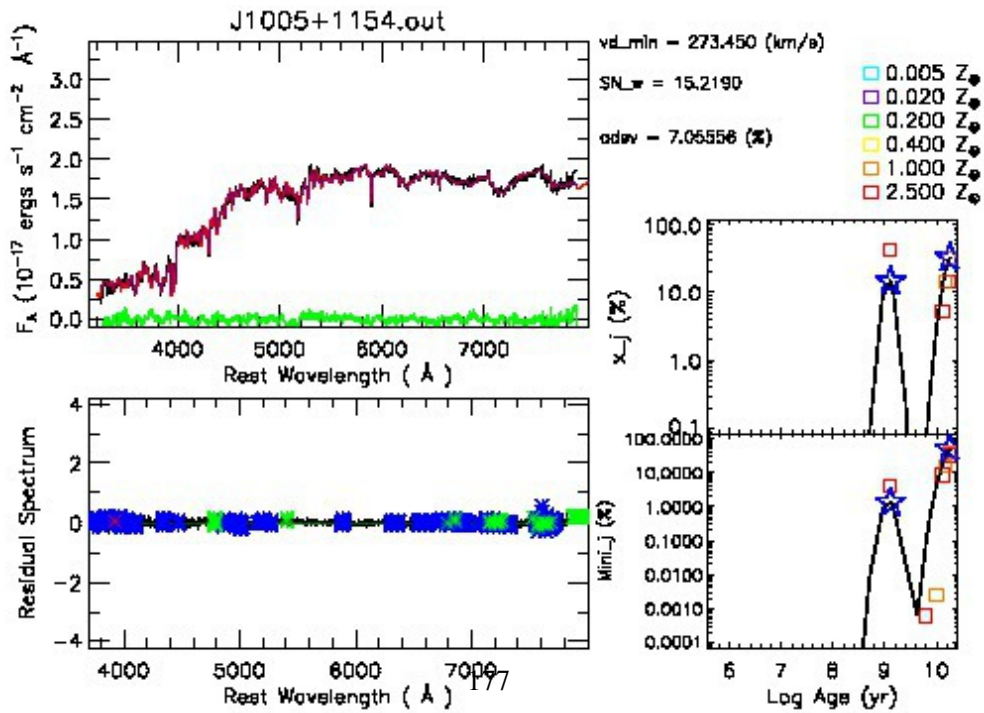
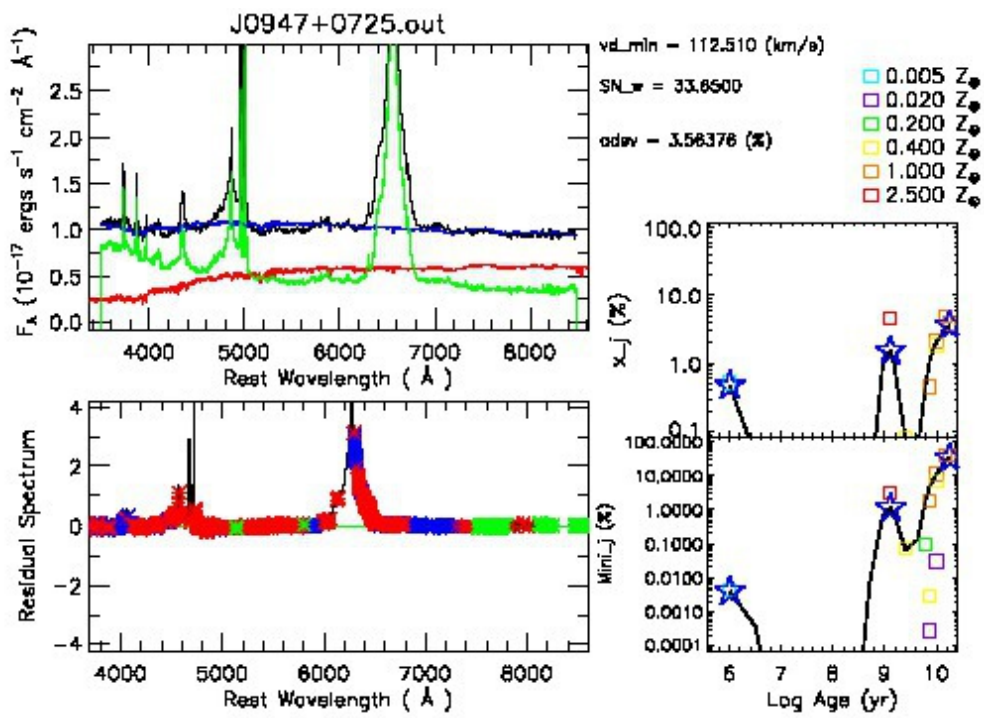


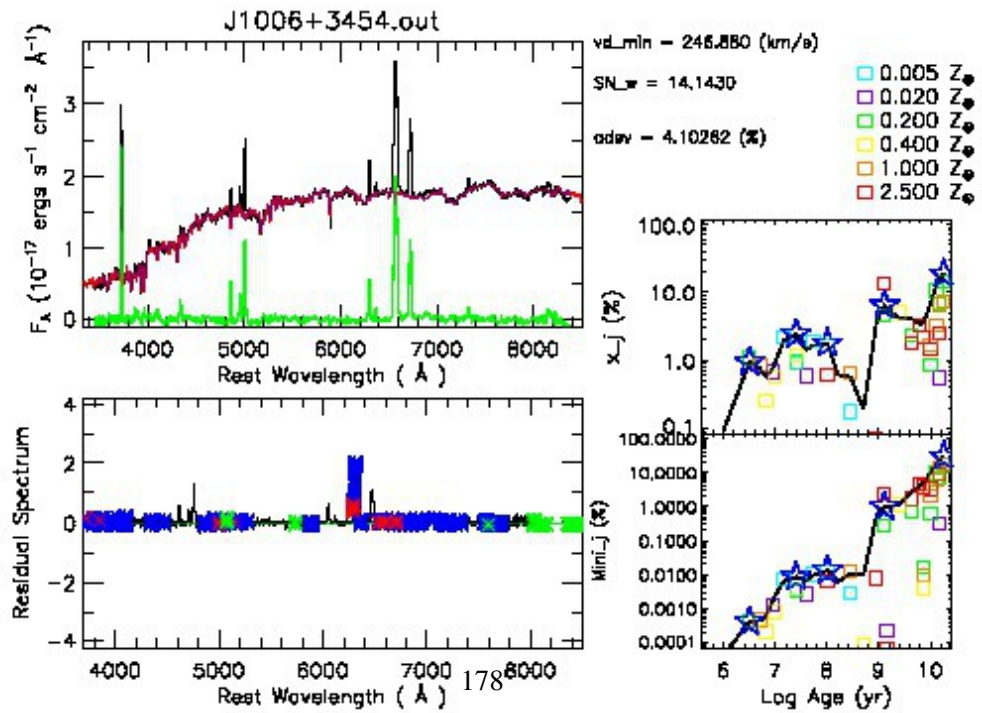
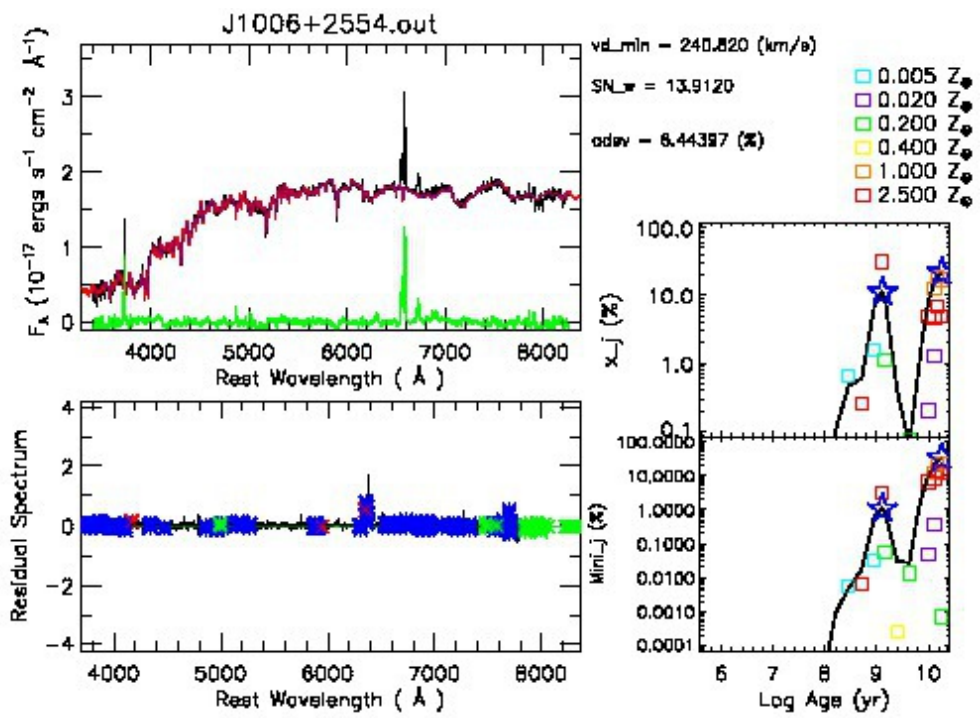


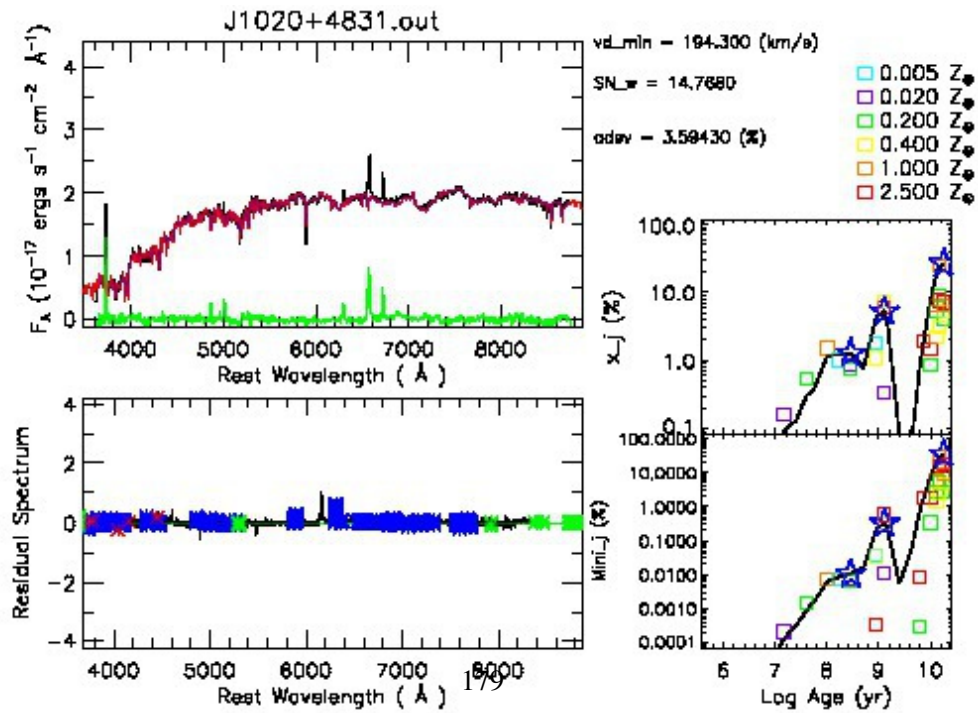
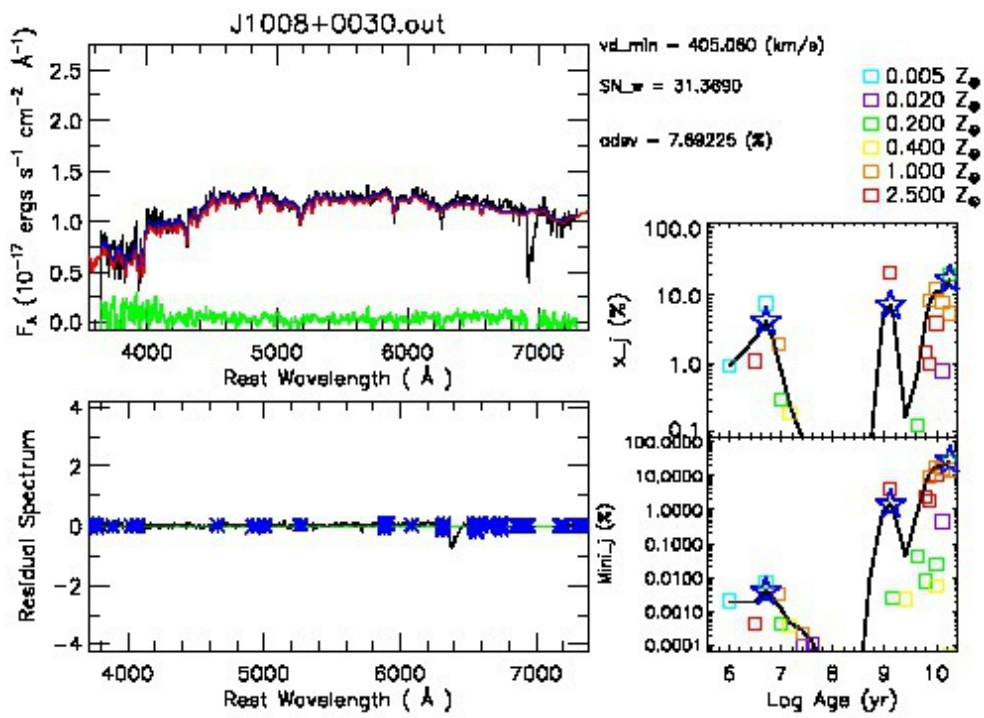


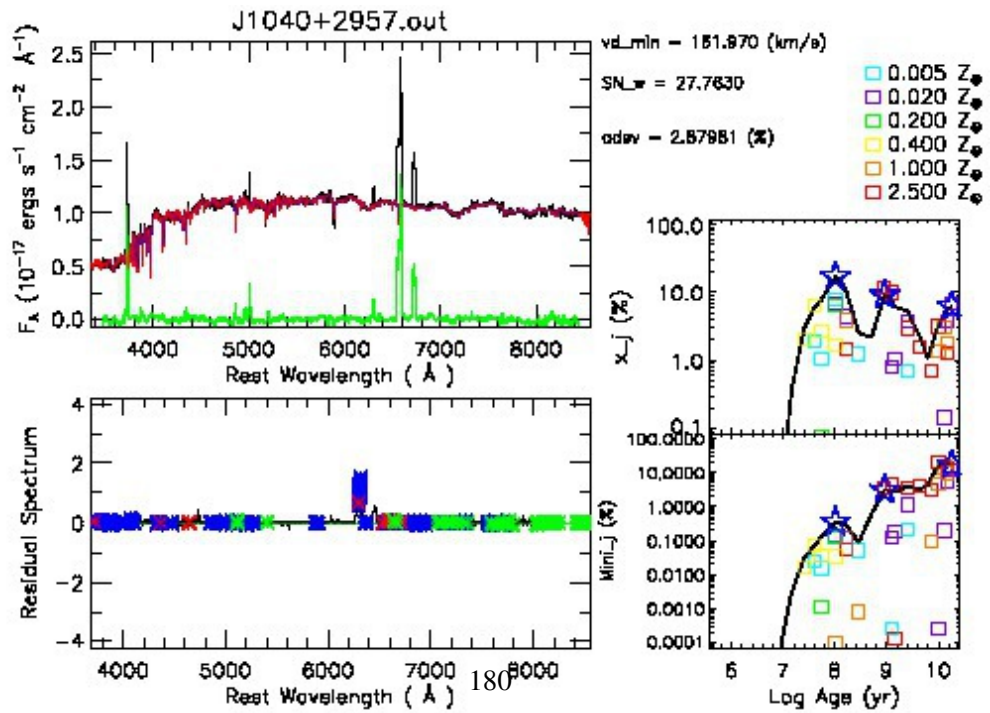
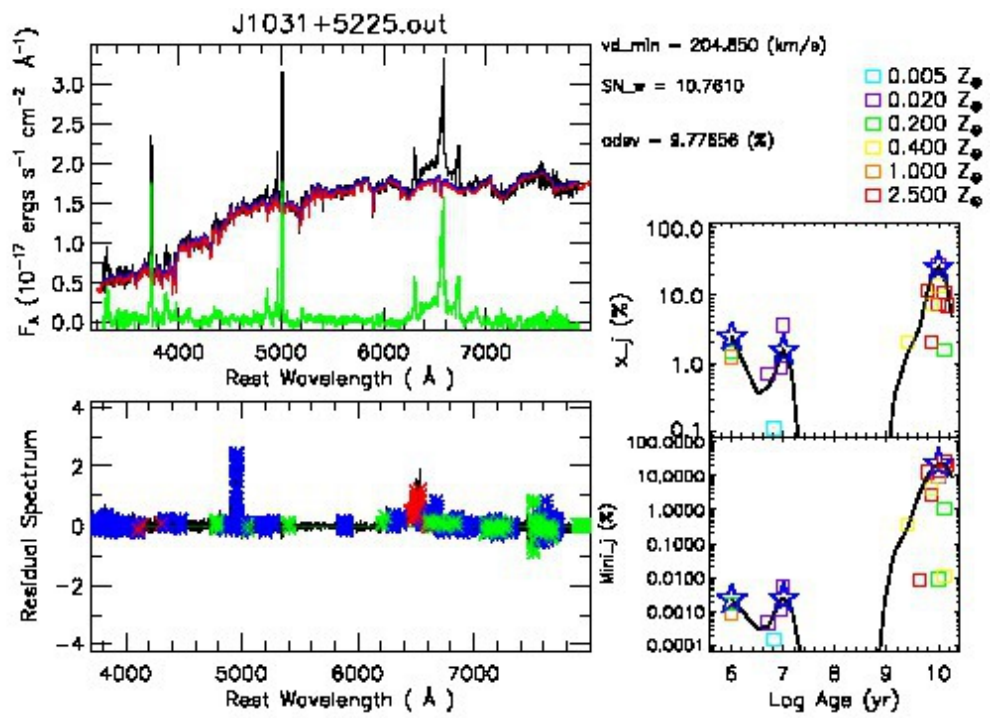




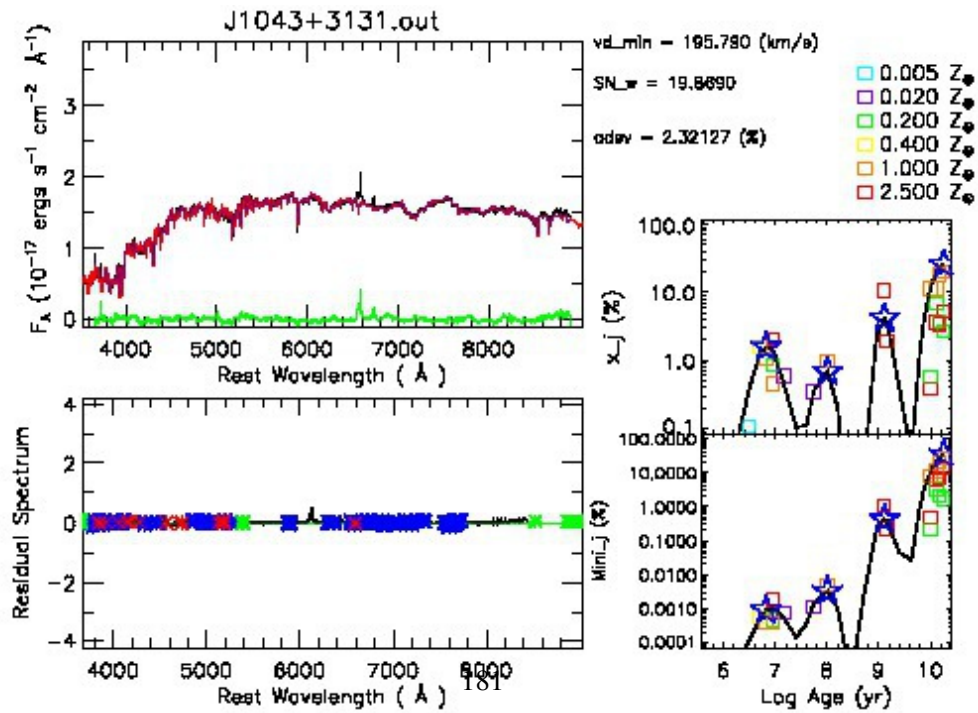
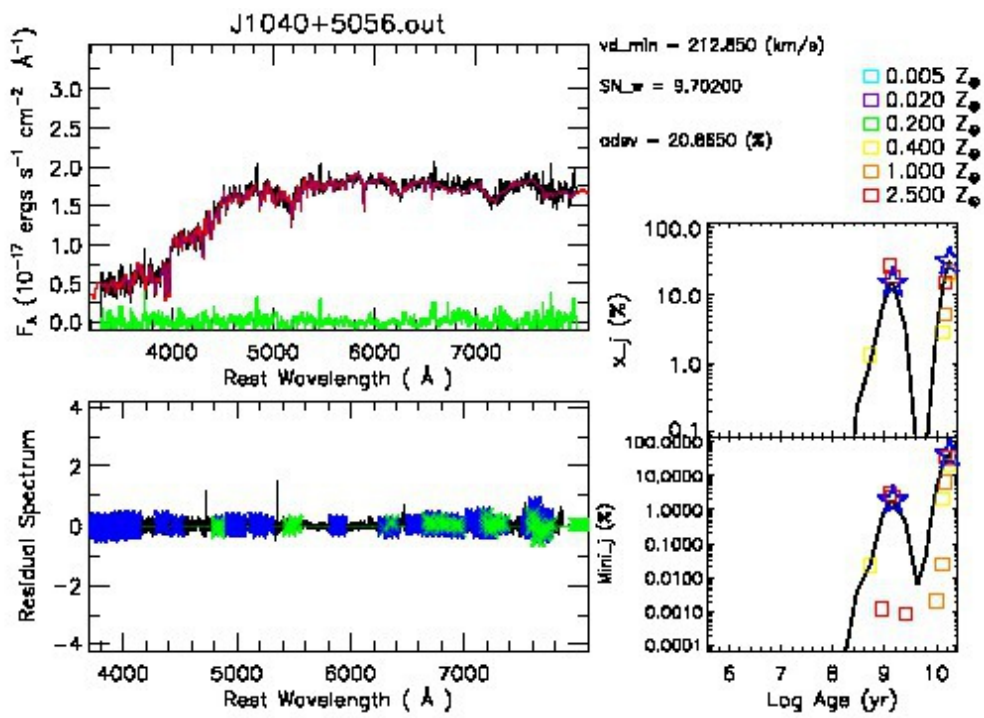


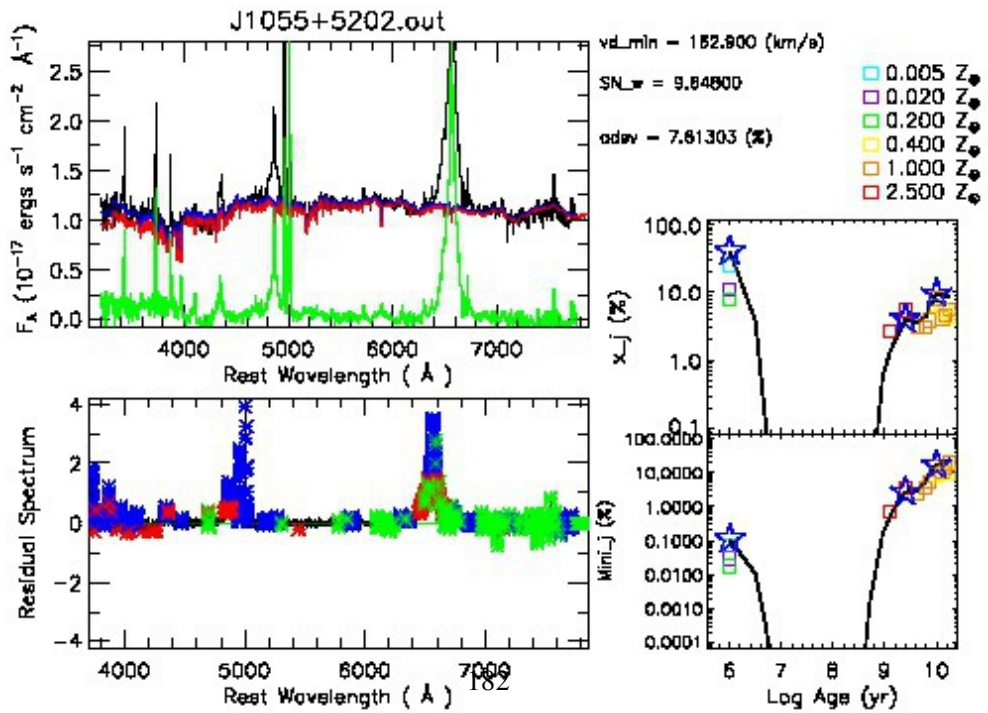
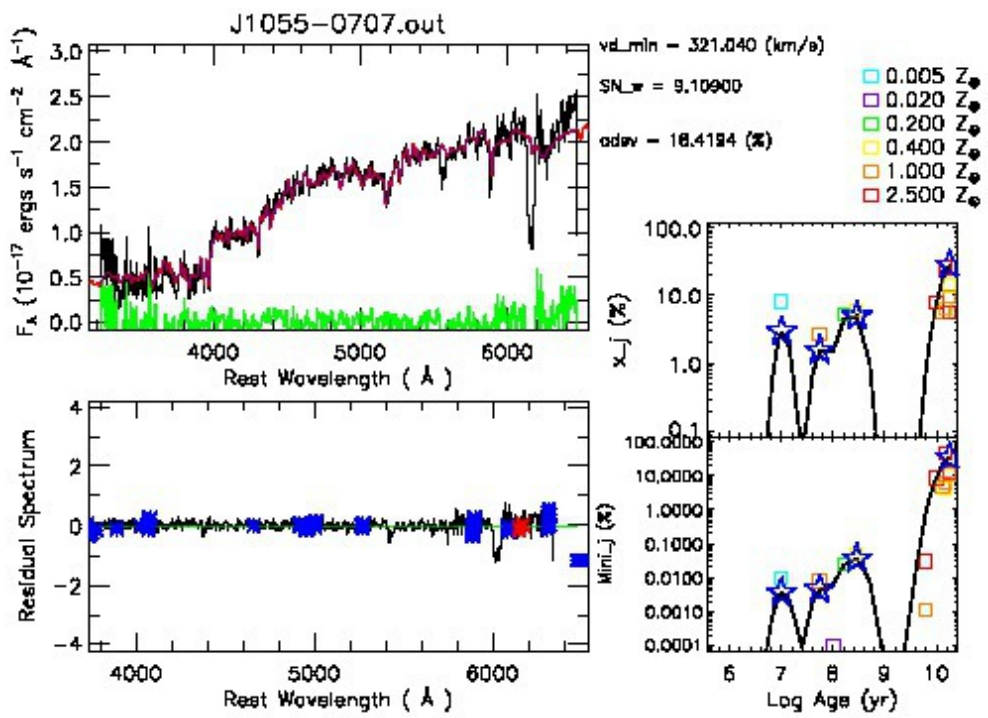


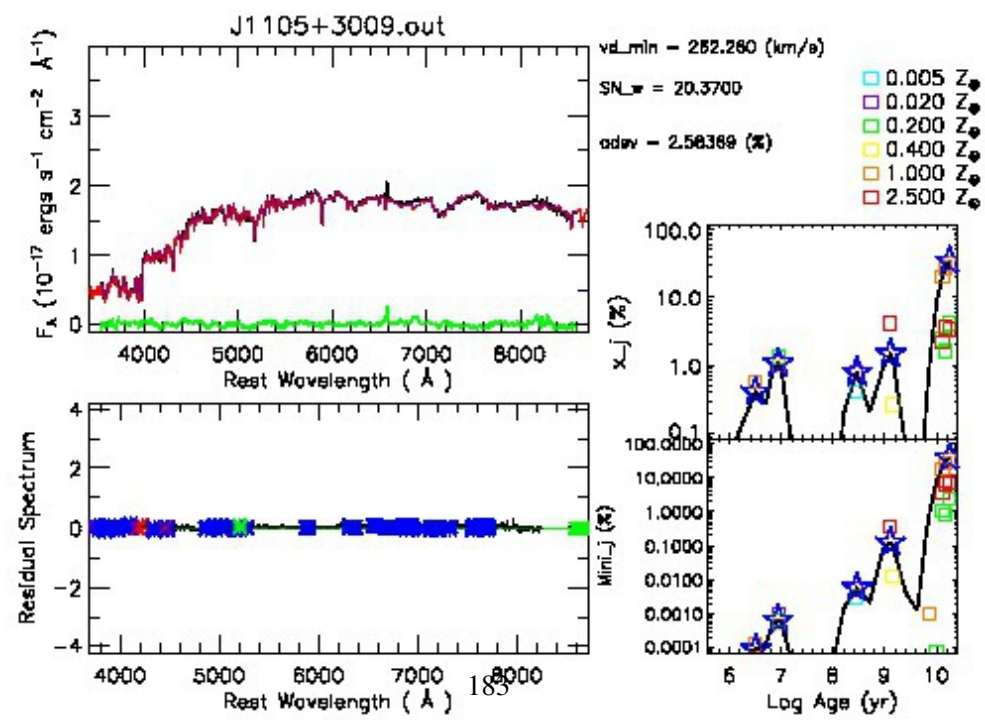
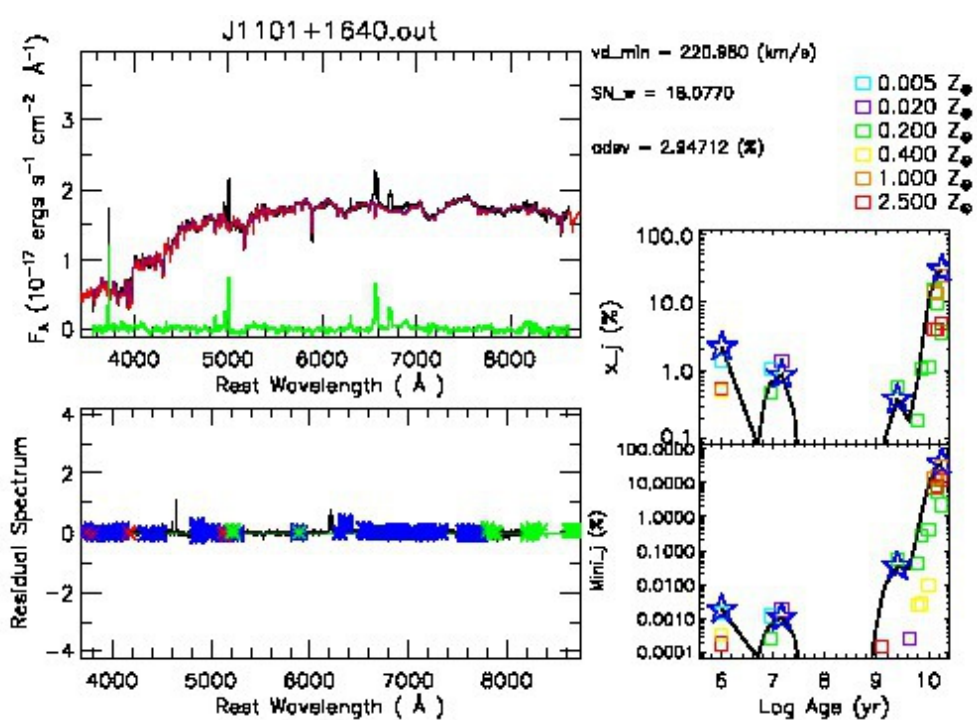


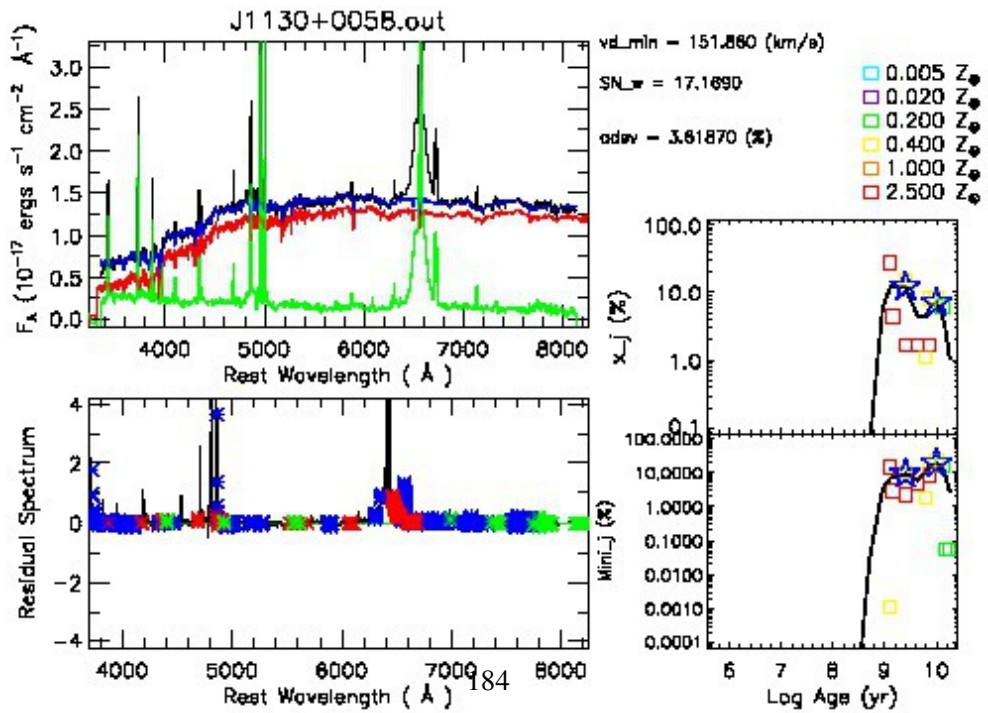
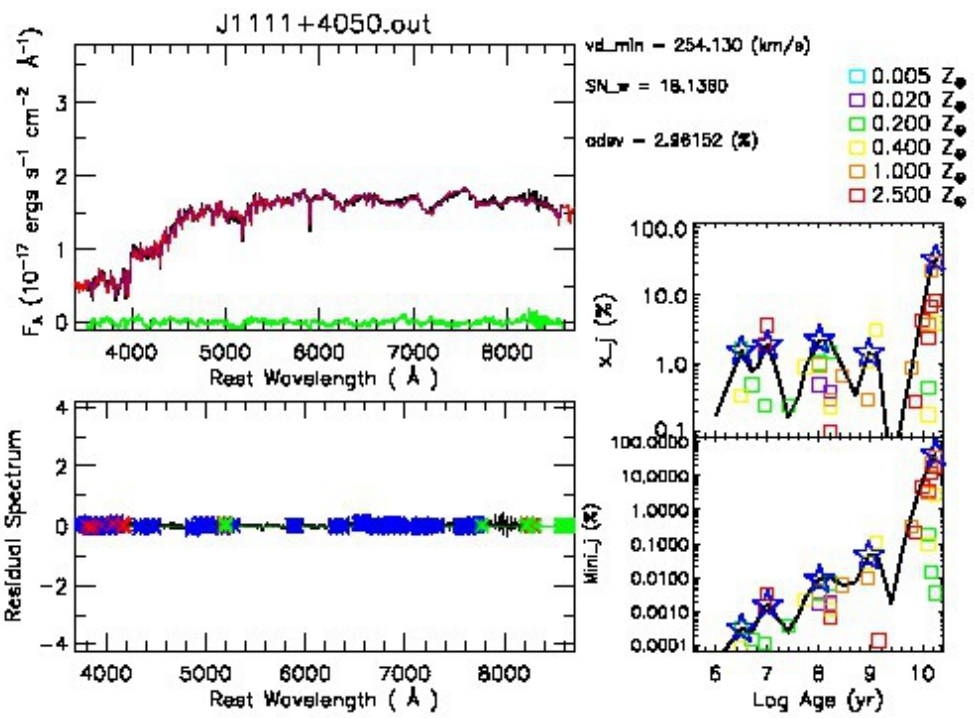










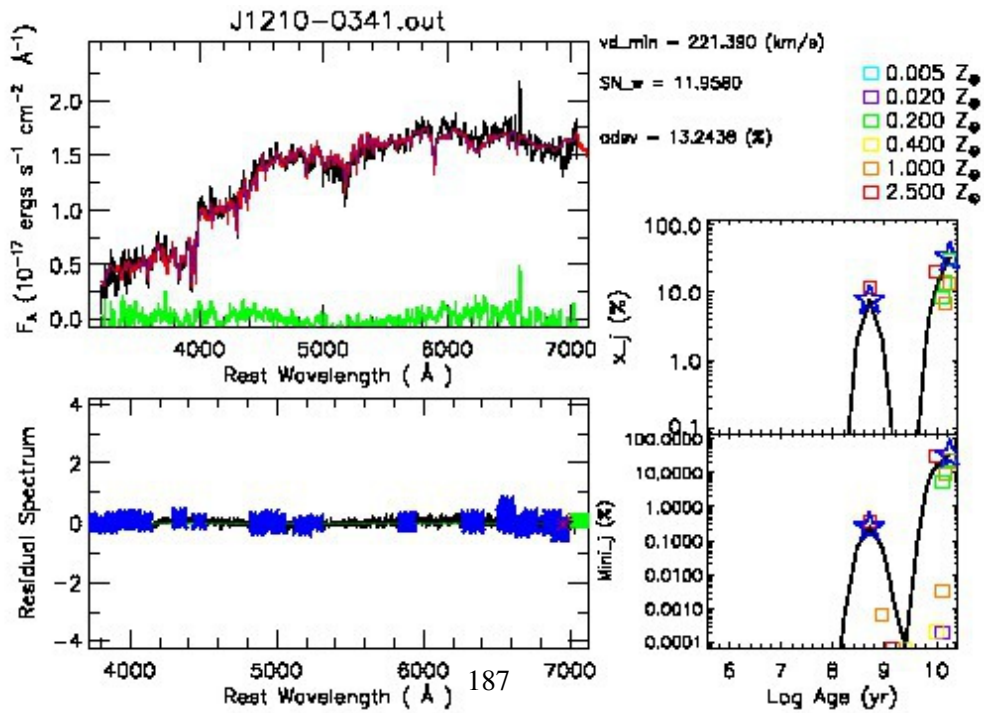
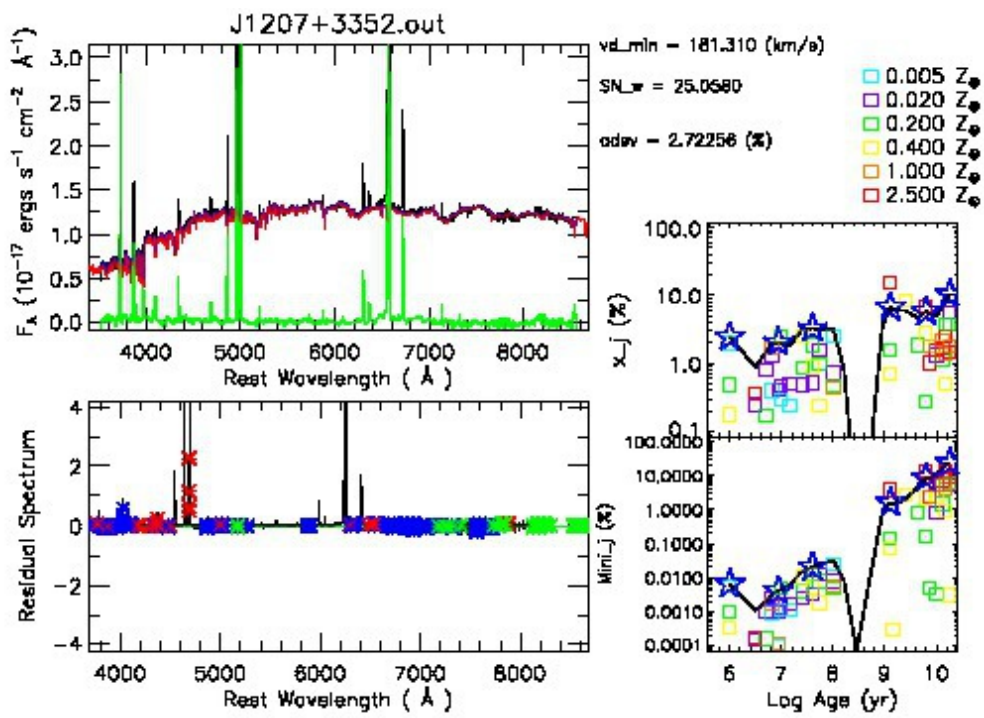


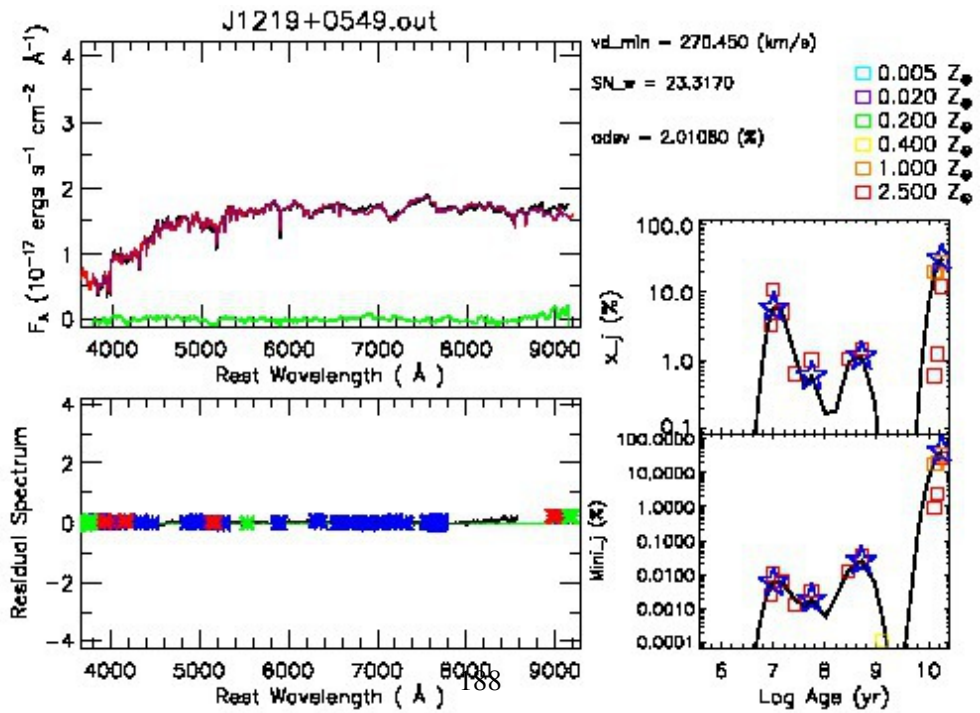
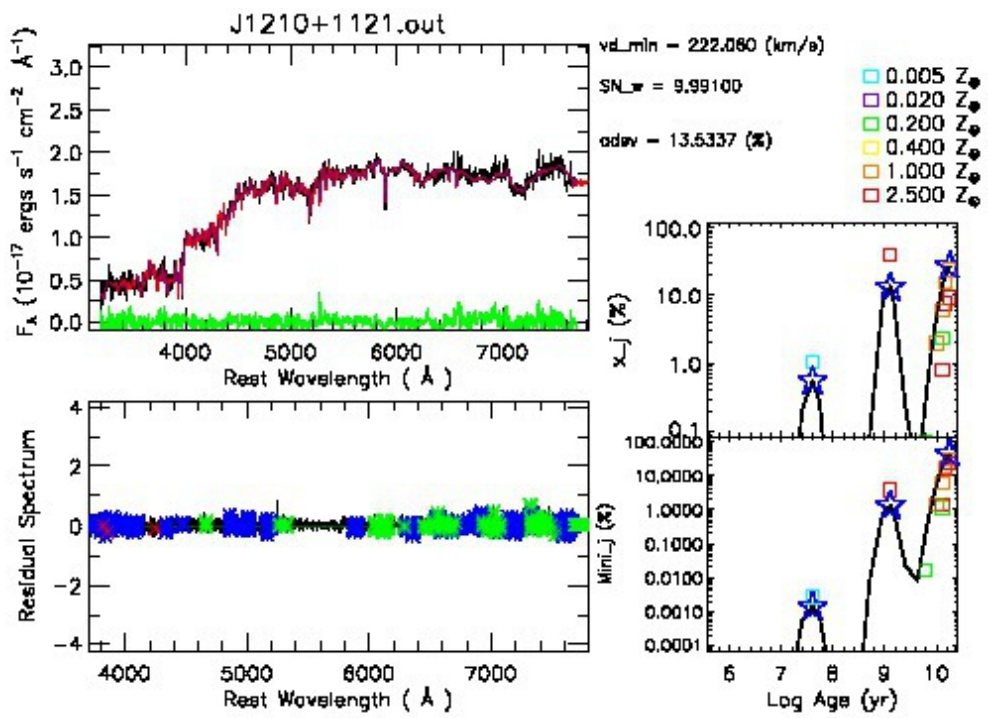
184



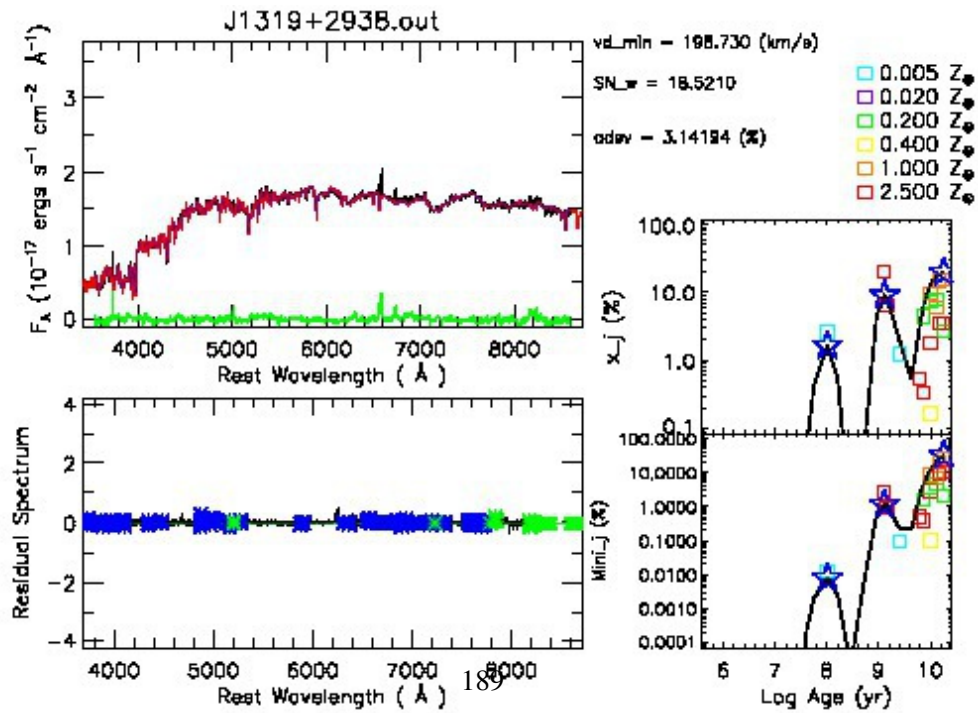
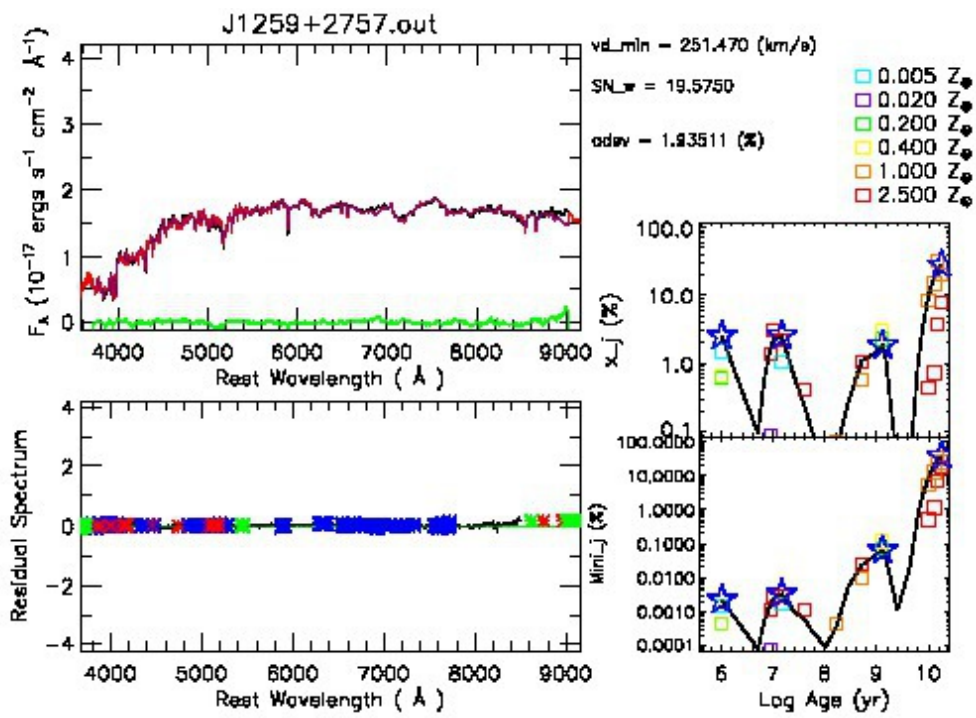


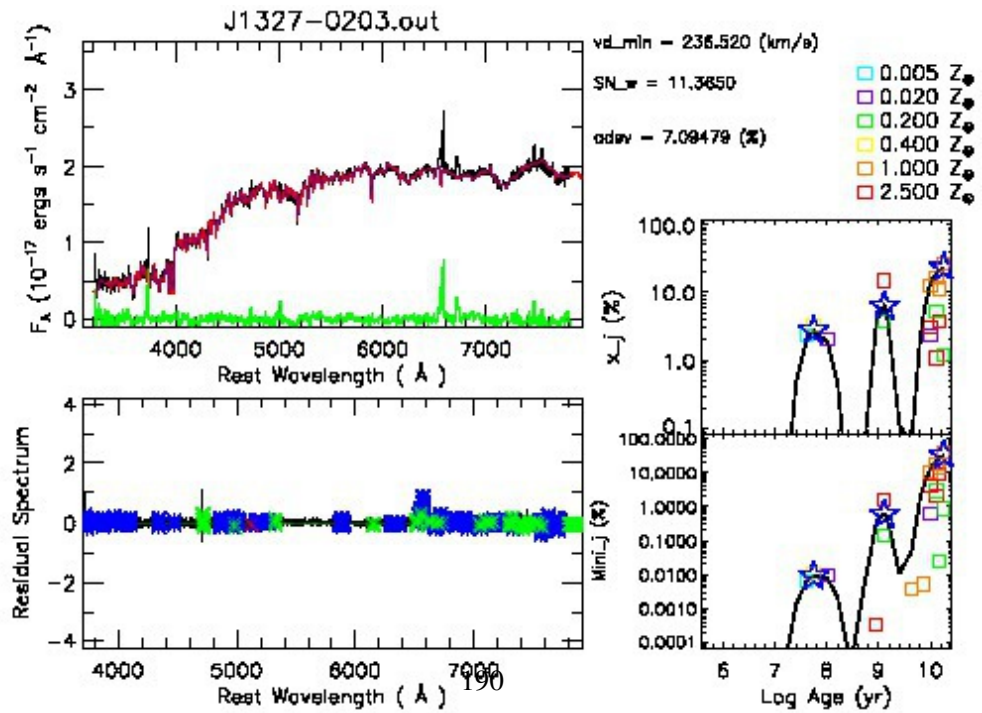
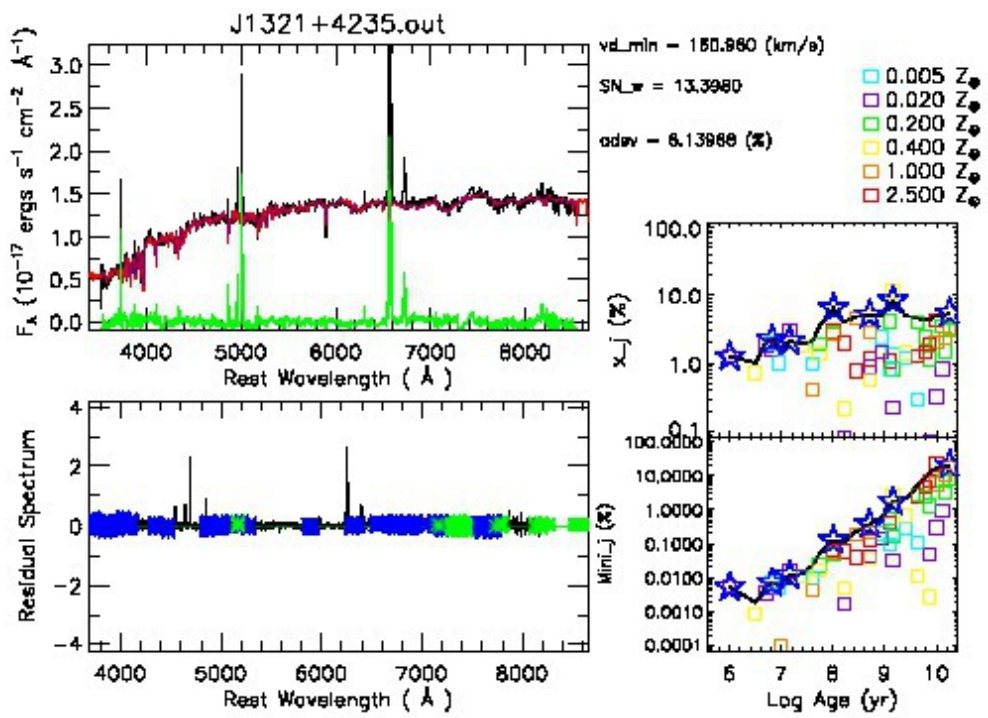


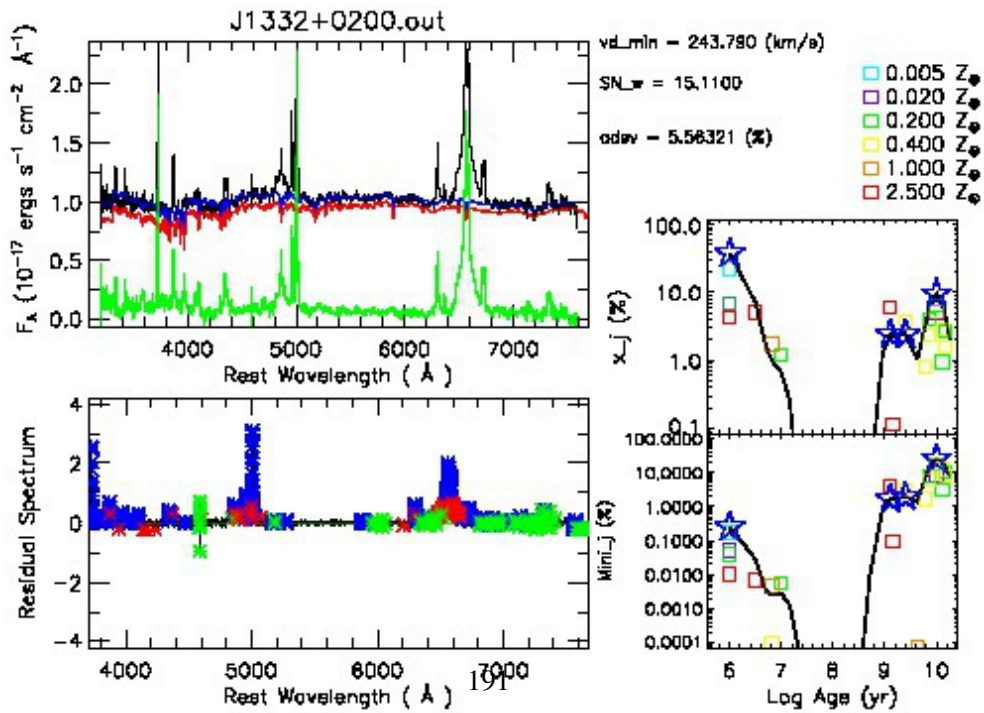
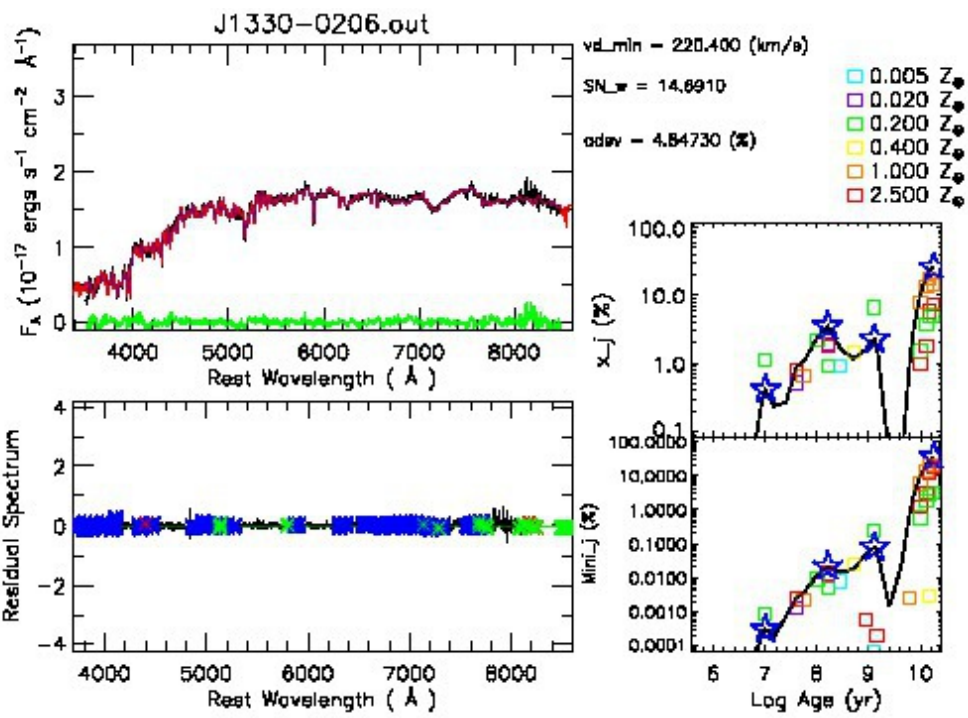


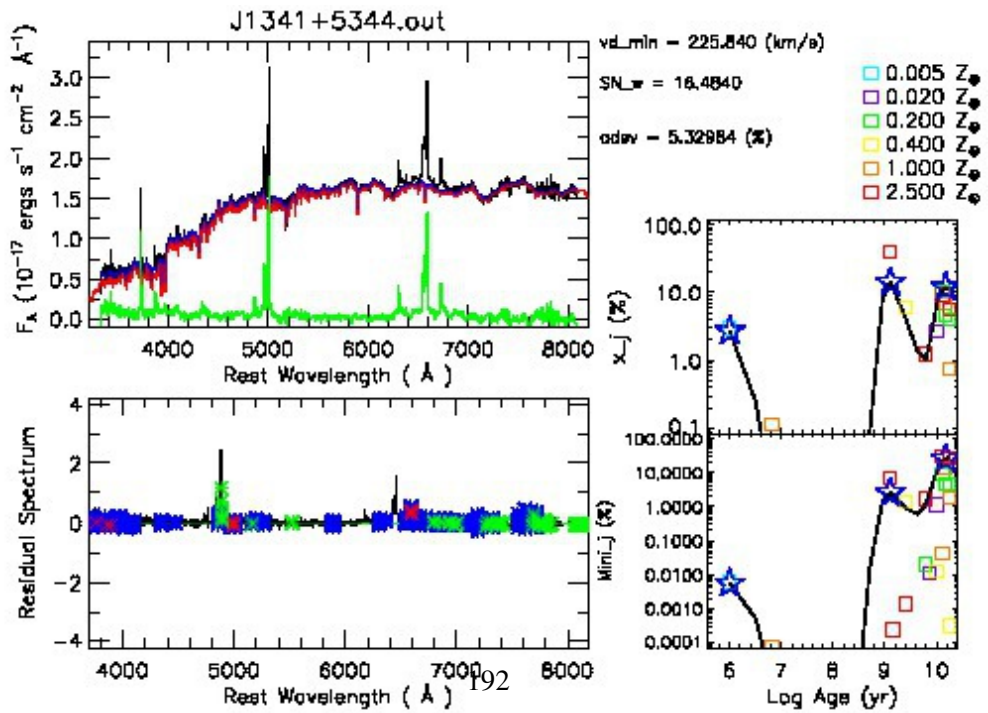
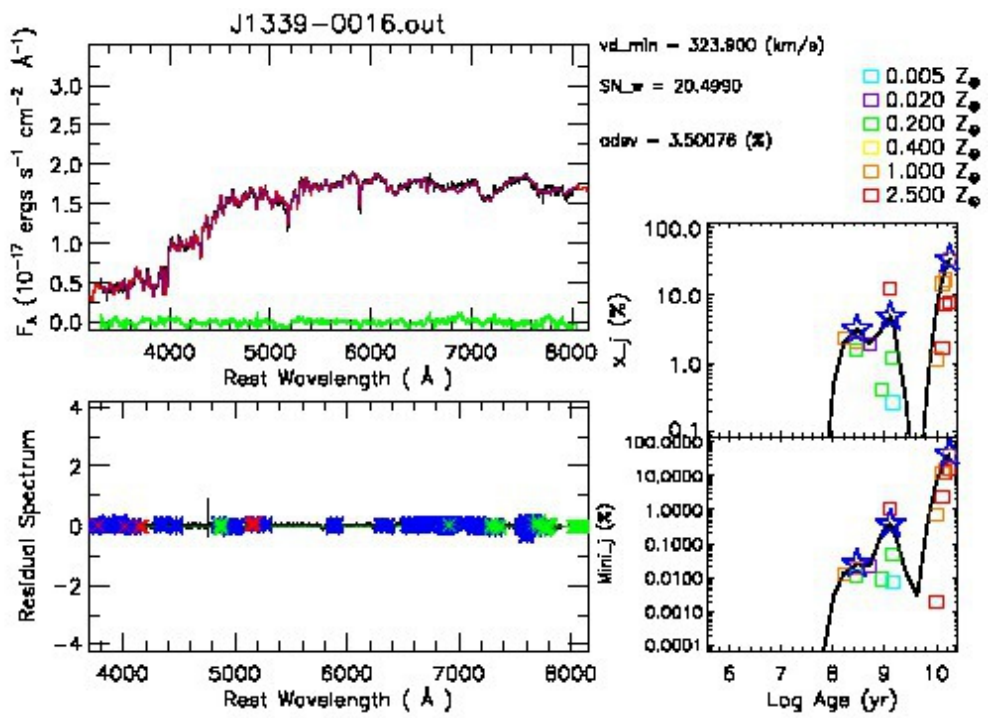




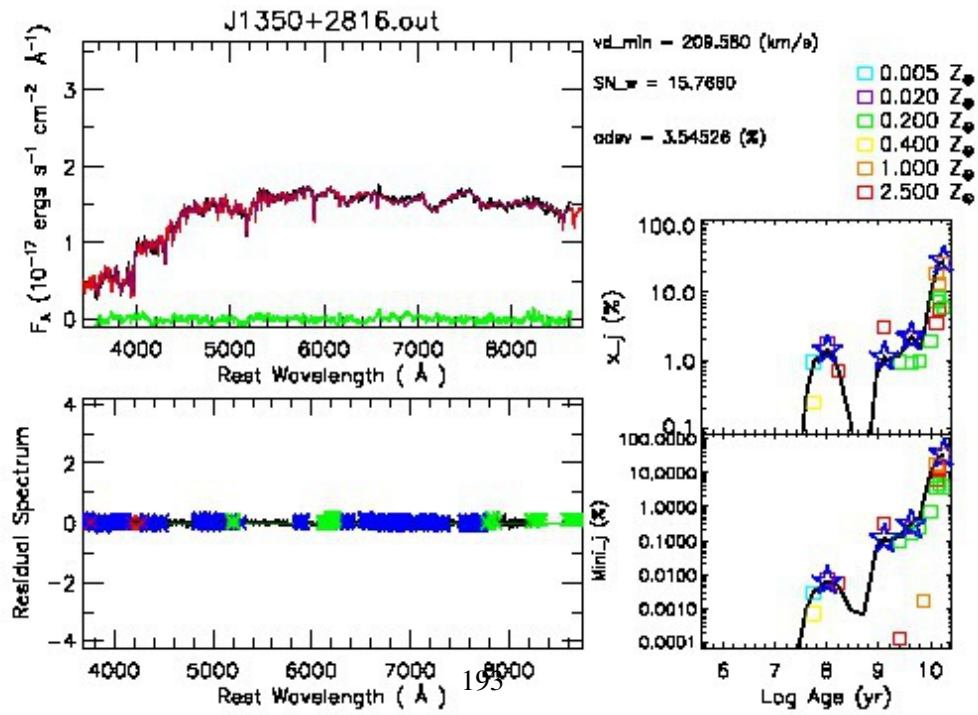
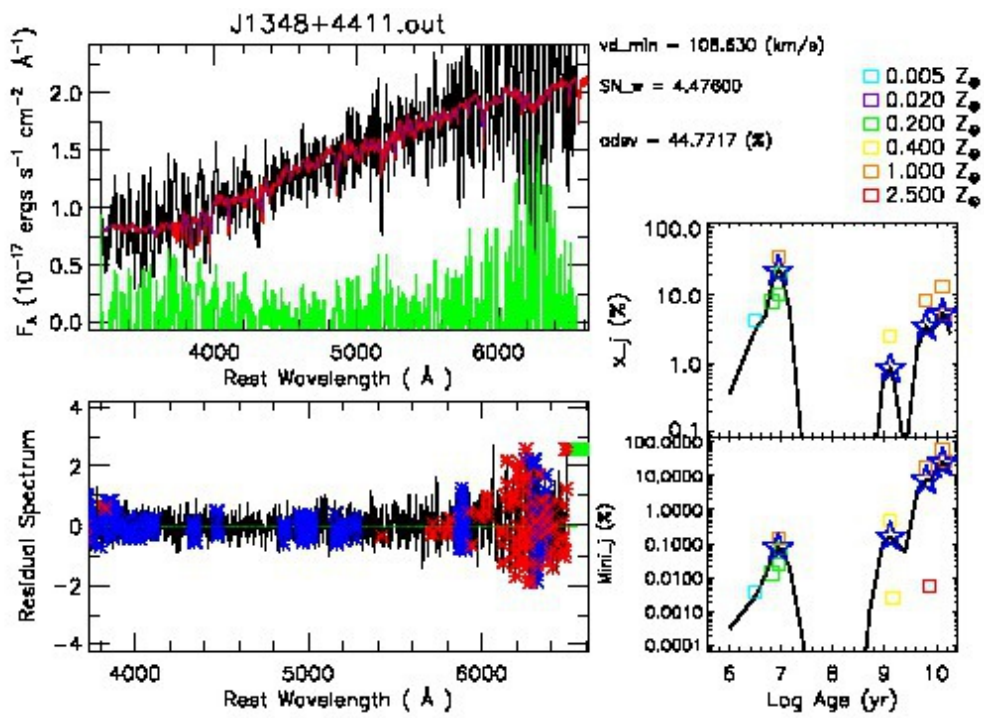


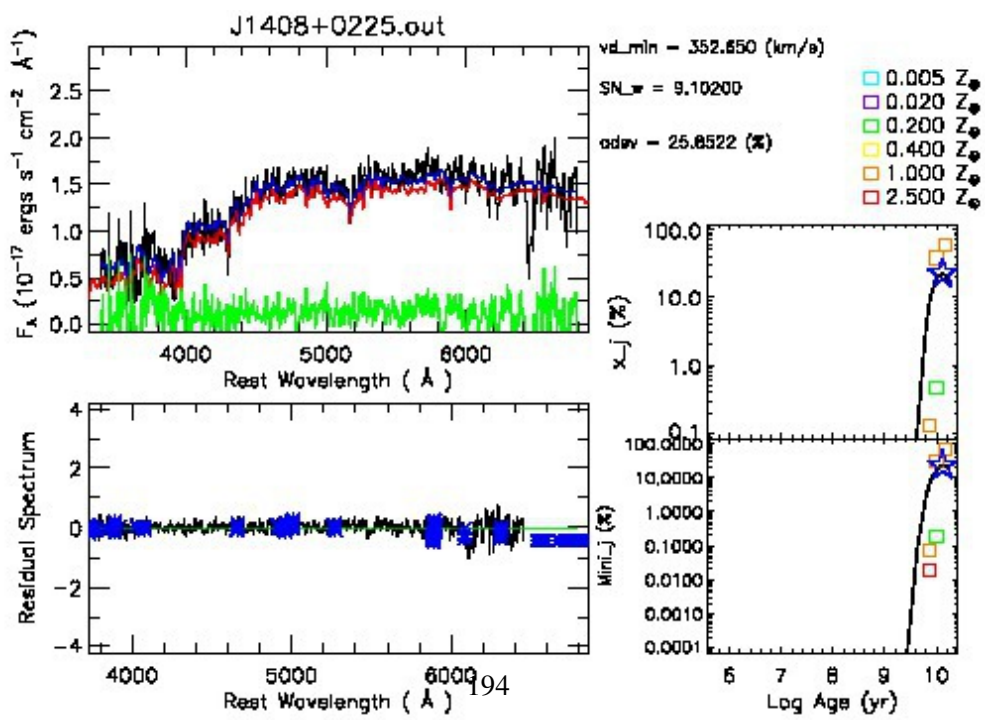
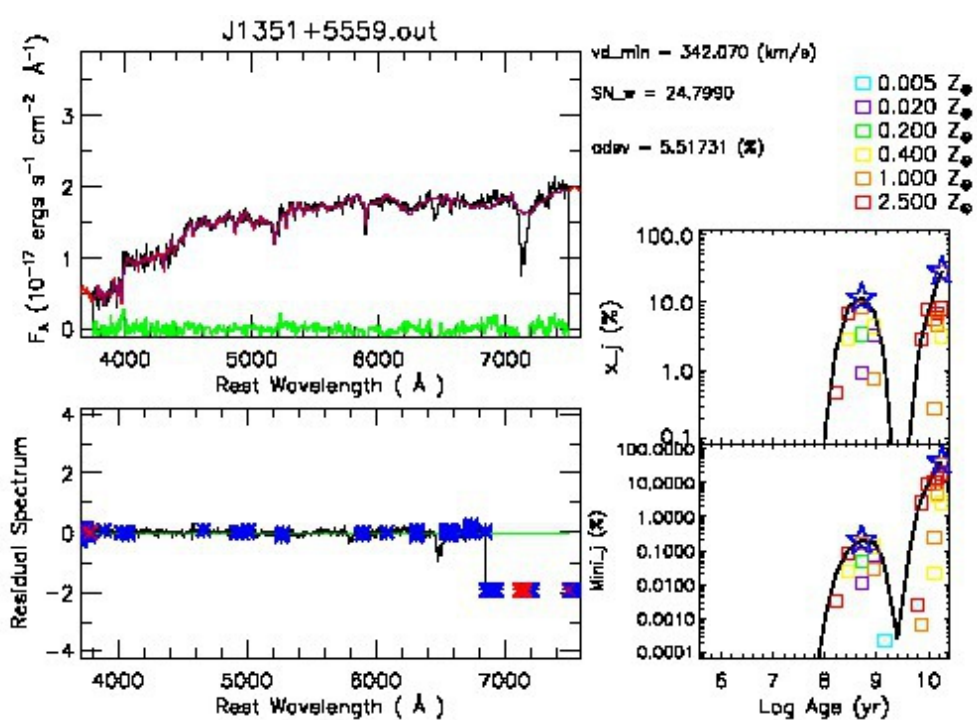


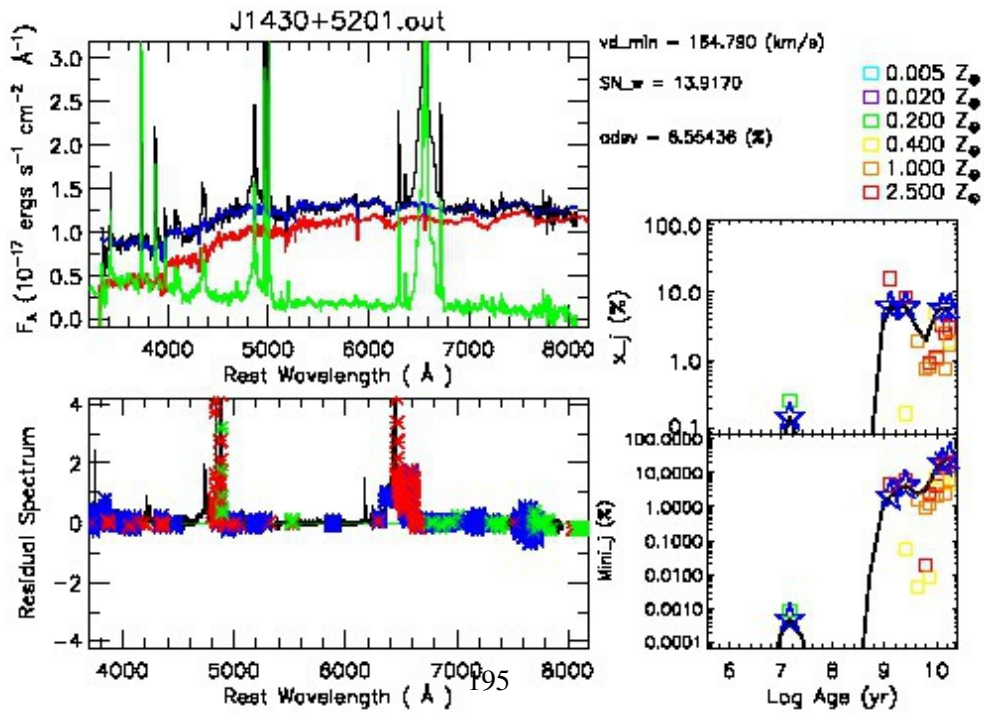
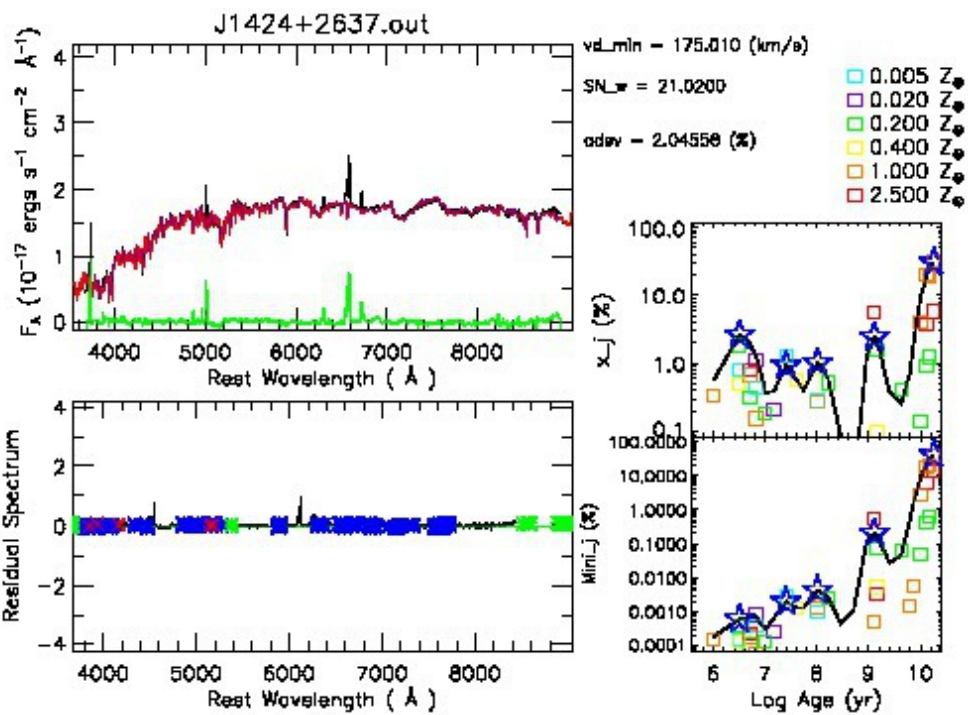


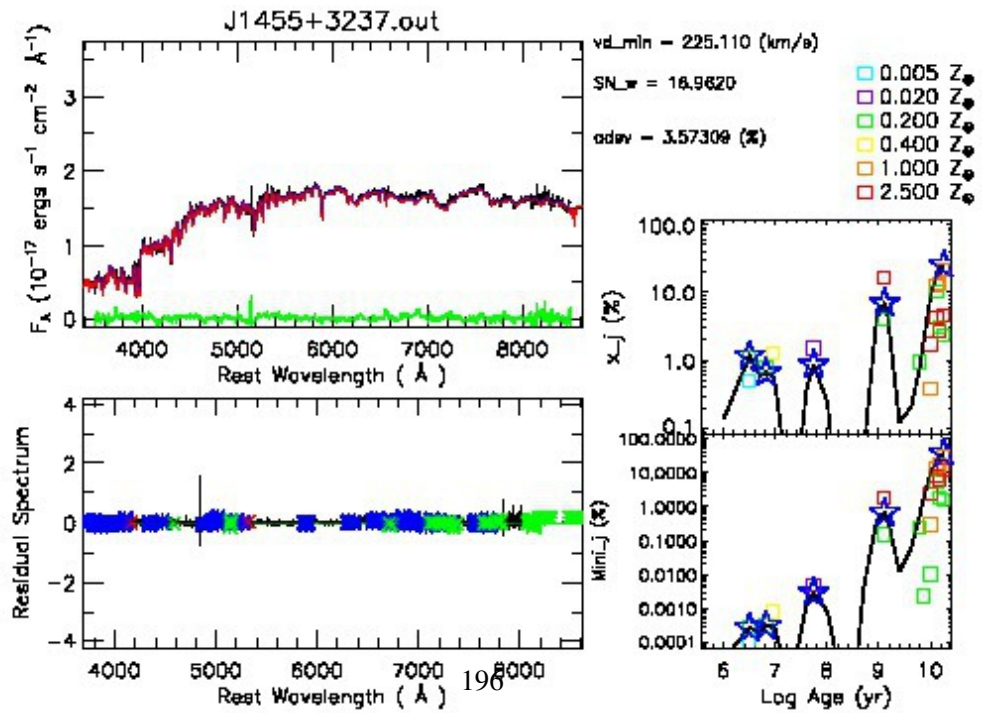
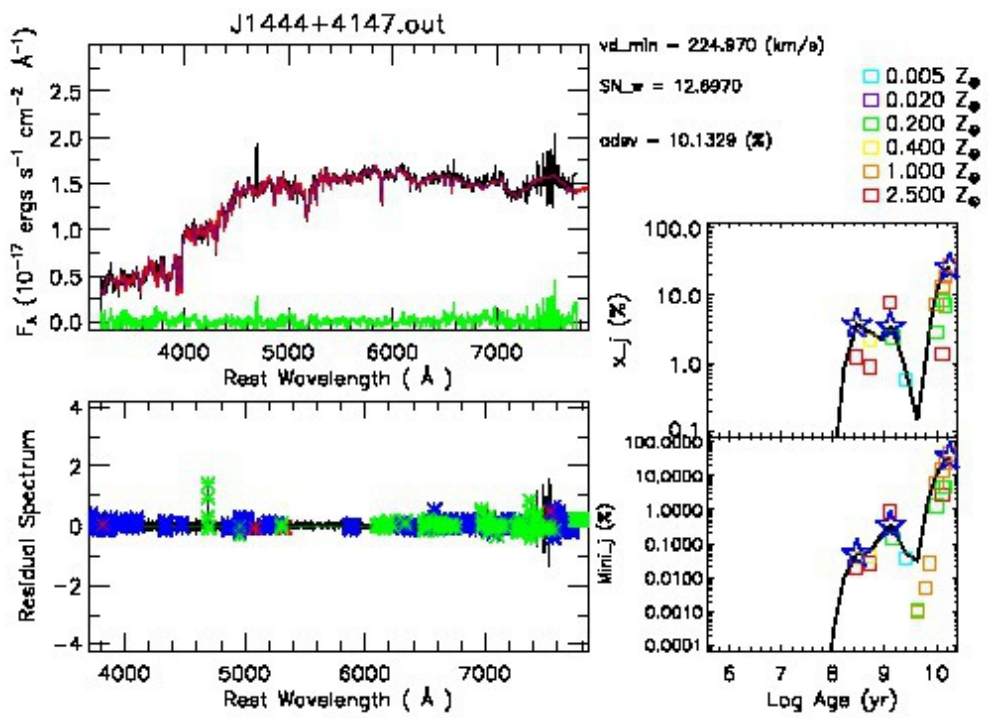




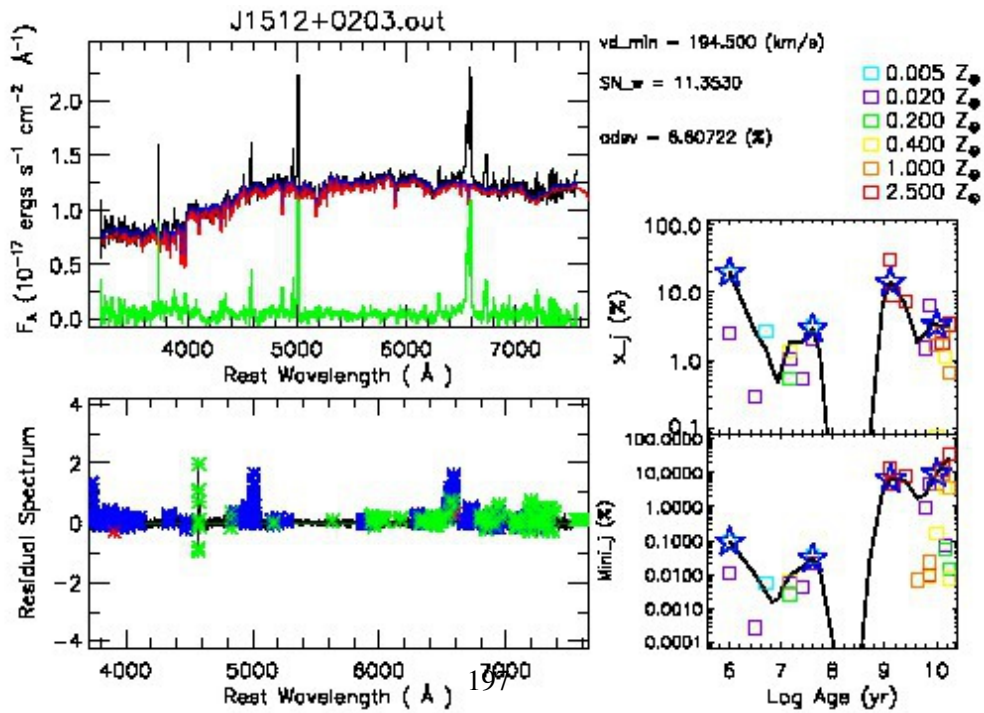
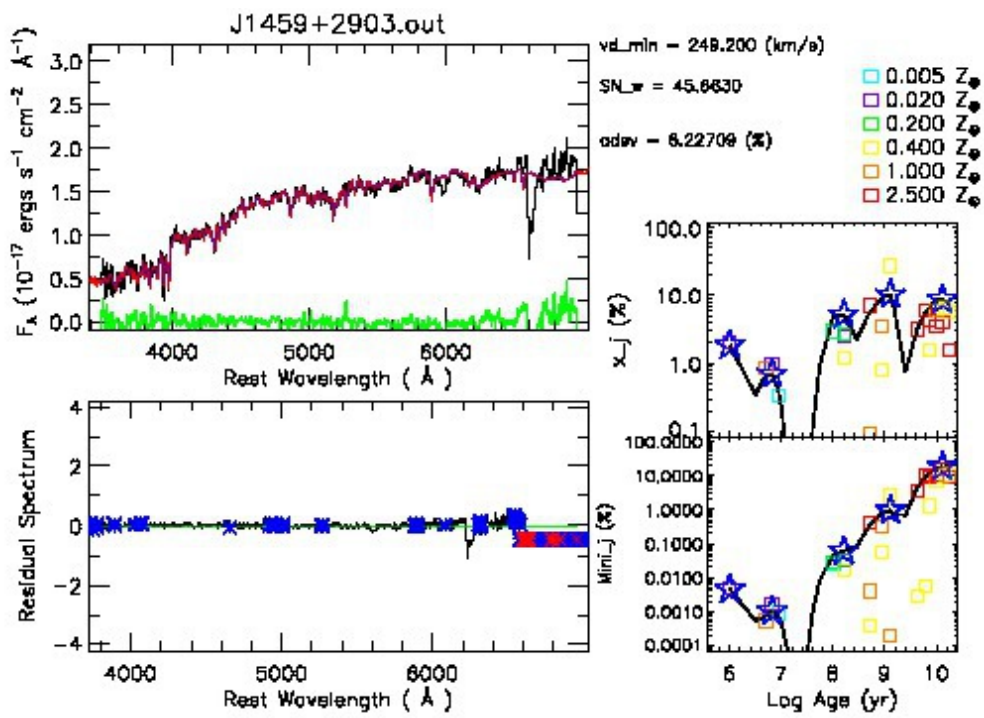


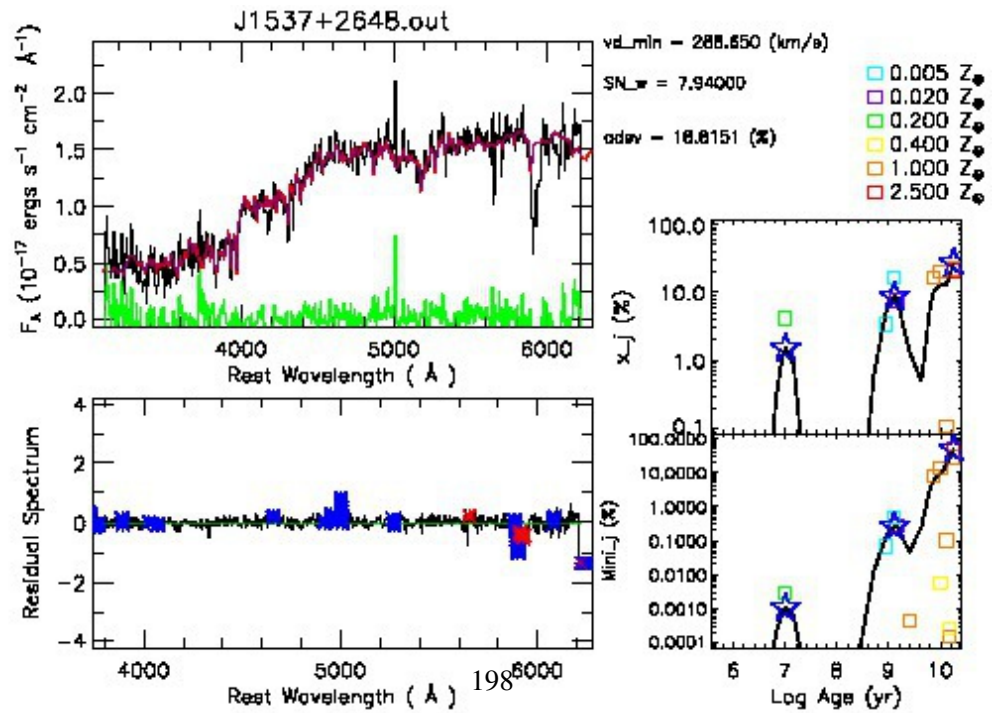
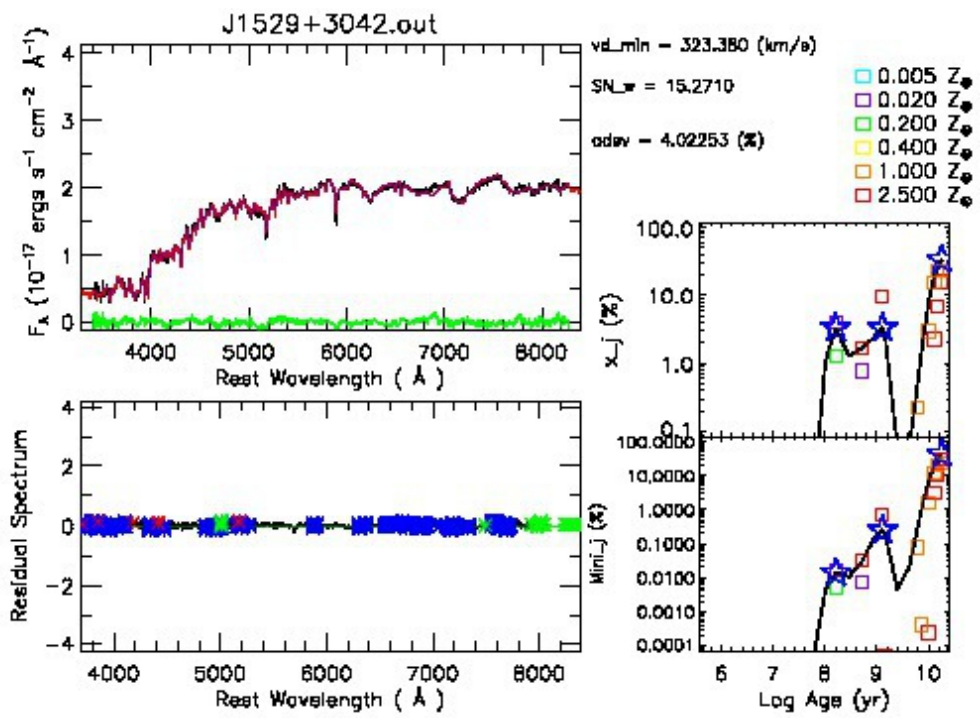


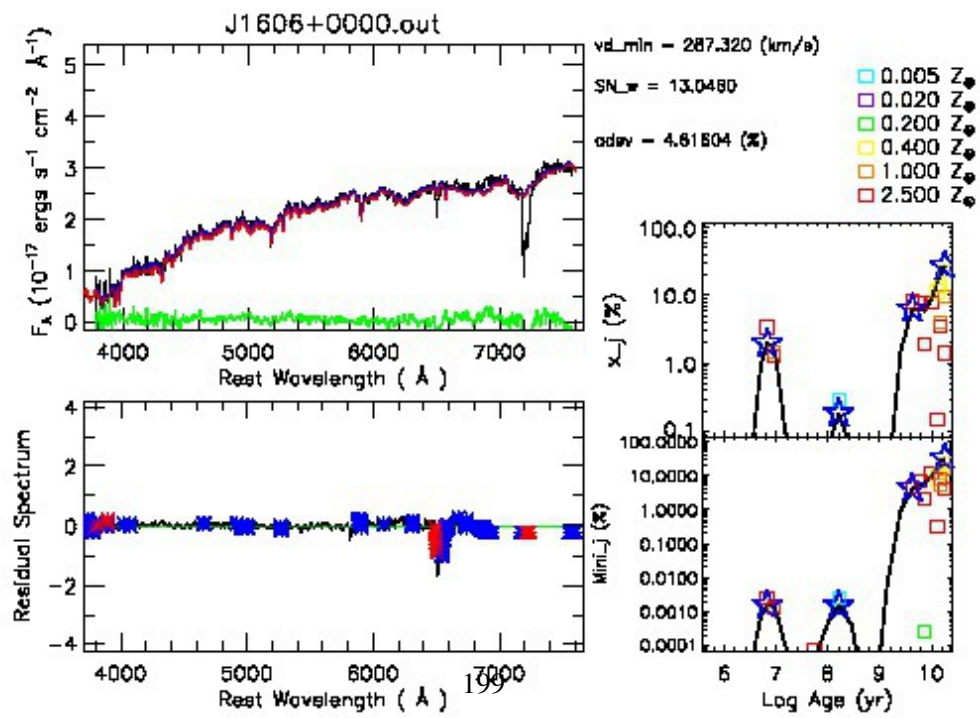
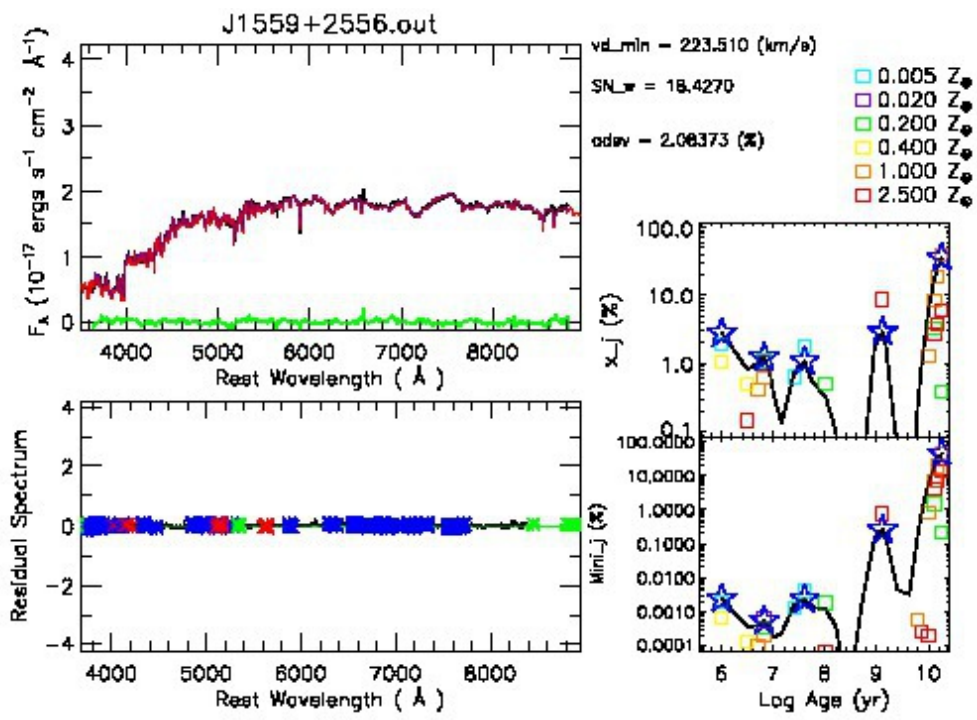


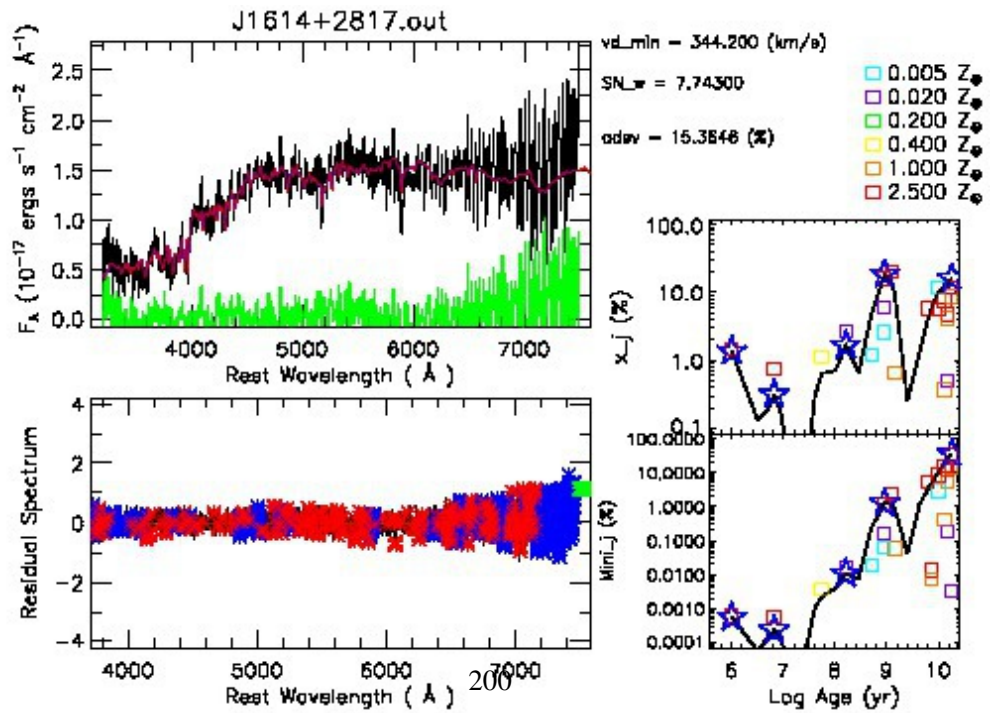
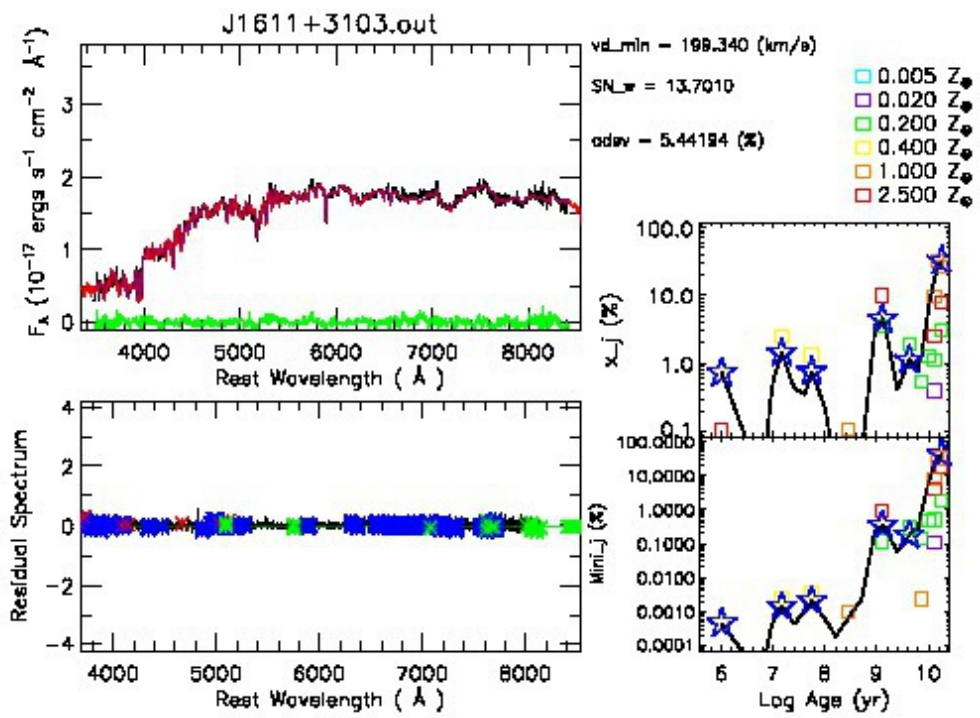




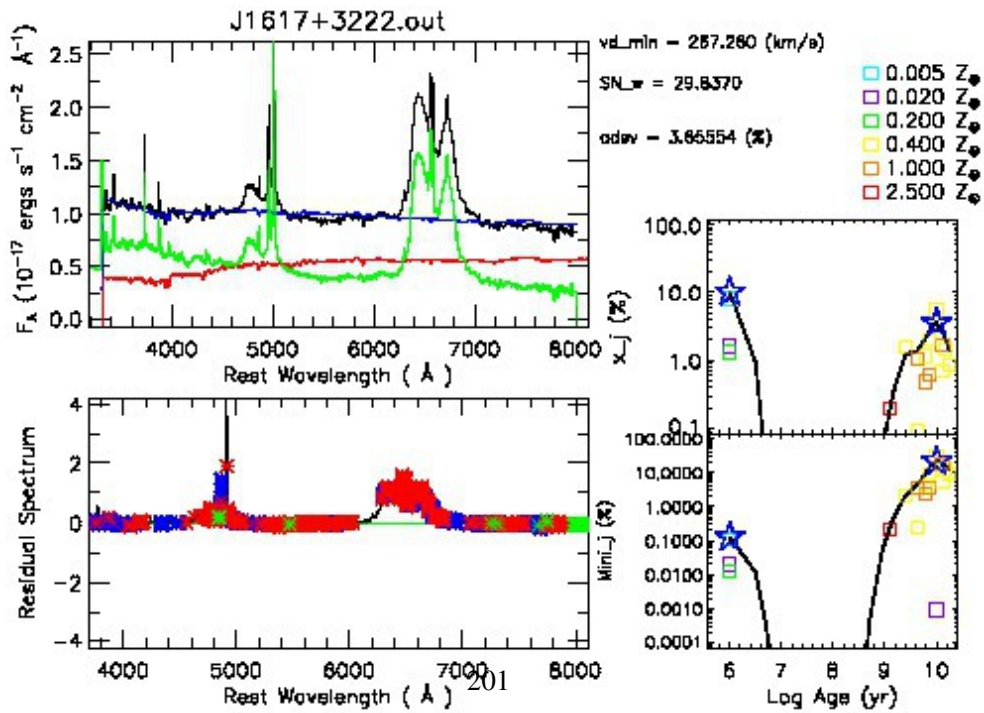
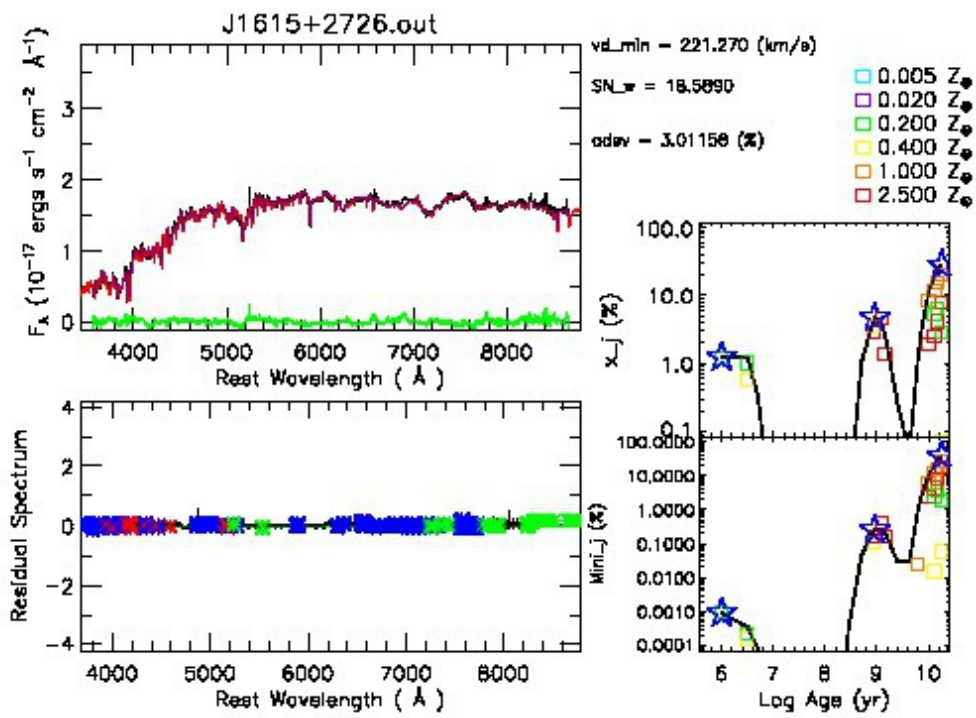












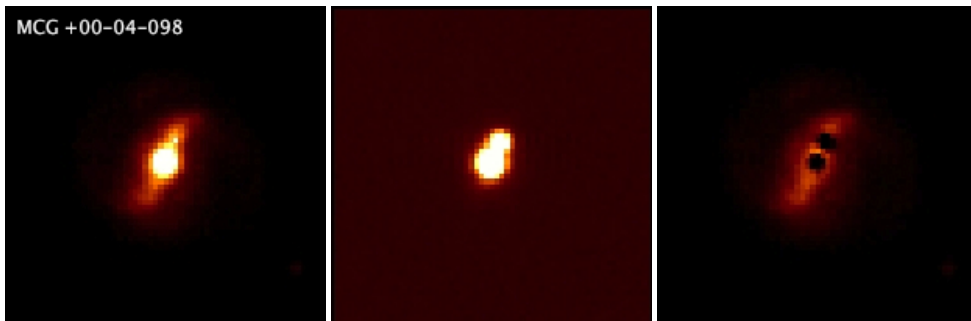


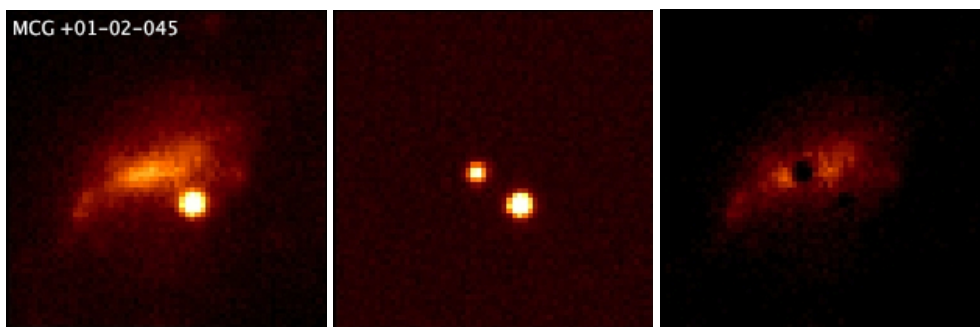
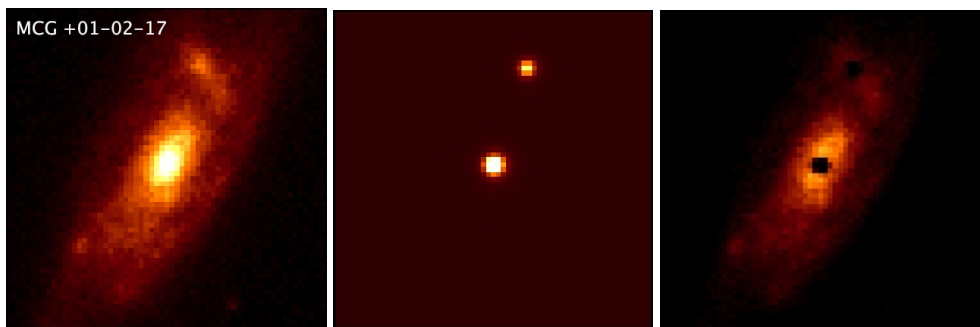
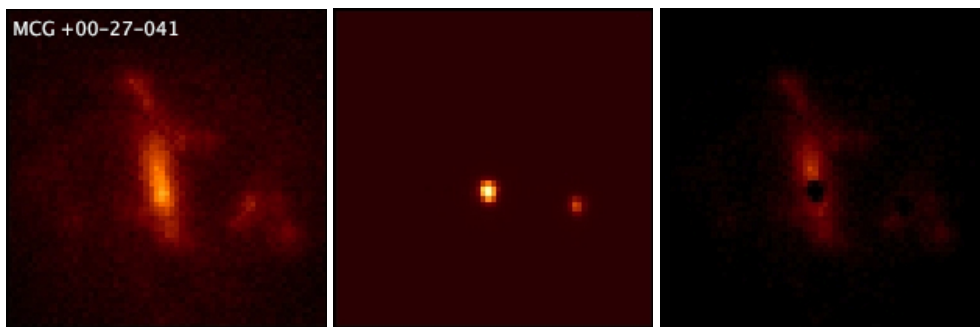
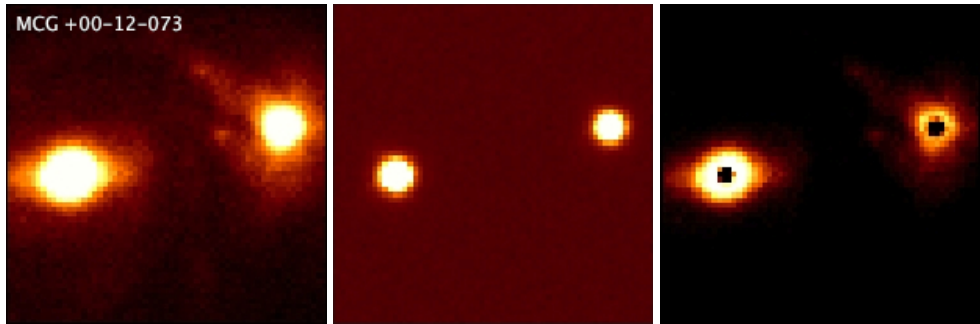
# C

---

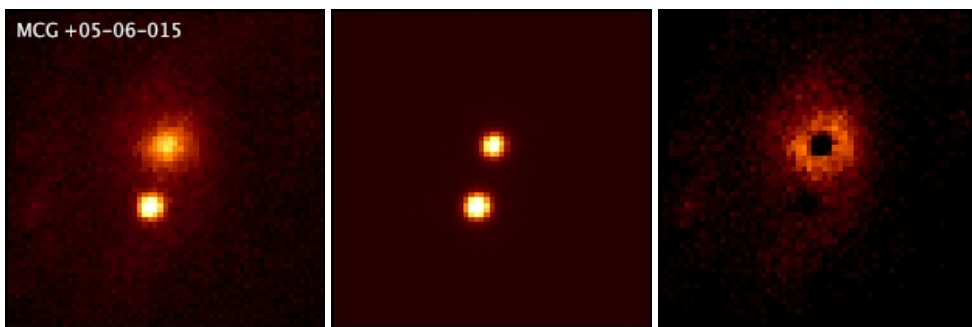
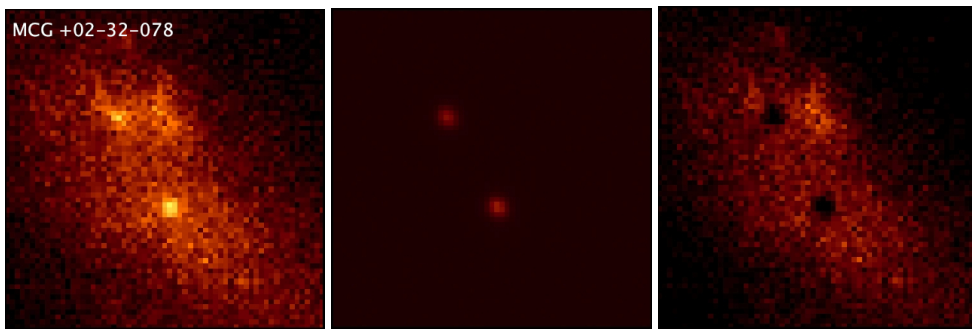
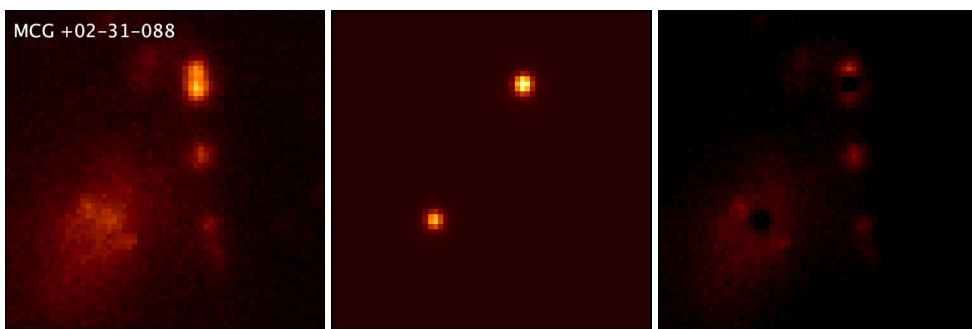
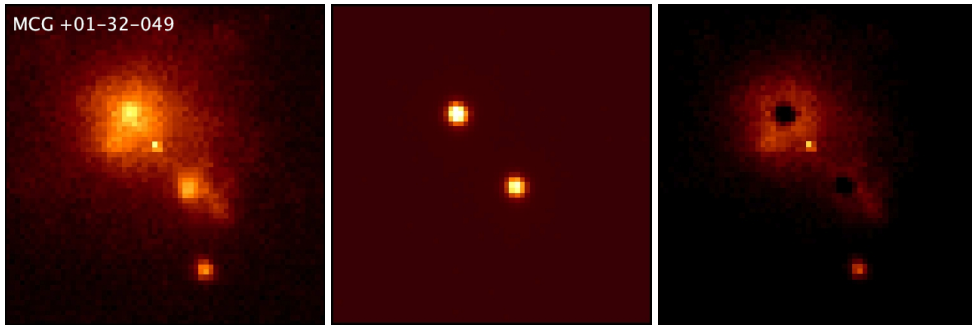
## PSF fitting of double nucleus post-merger galaxies

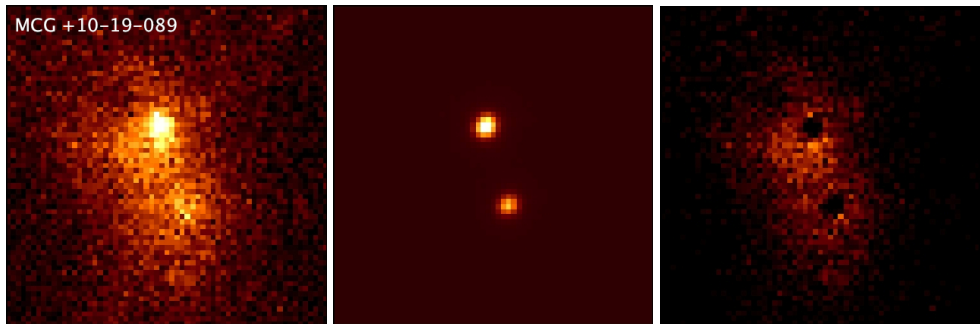
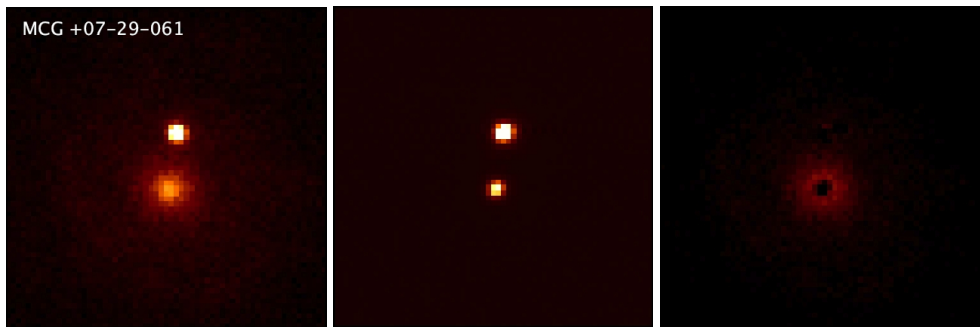
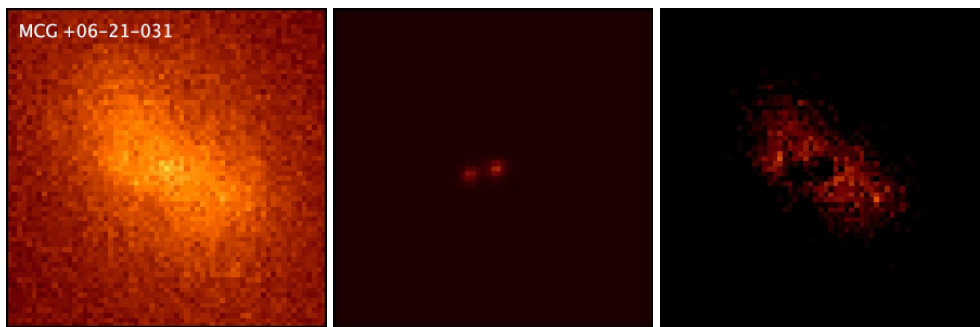
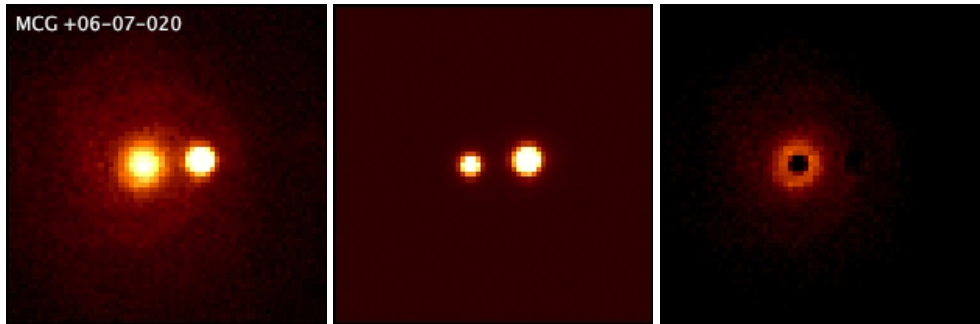
*R*-band image from SDSS DR8 (left), model image obtained from the PSF fitting (center), and residual image created after subtraction of the model image from the observed image (right). The name of the double nucleus galaxy is indicated on top of the left image.

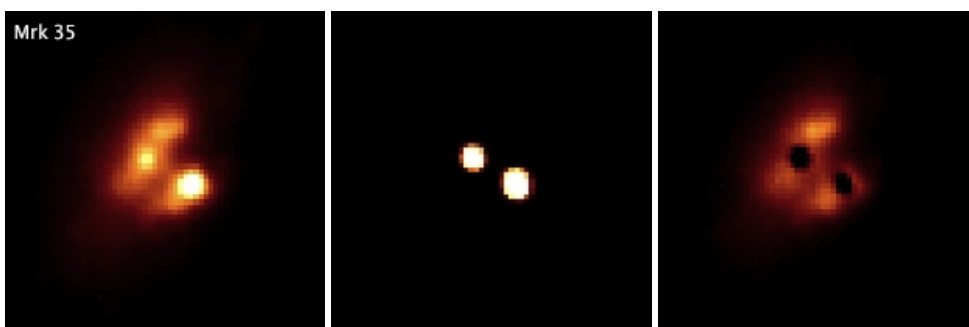
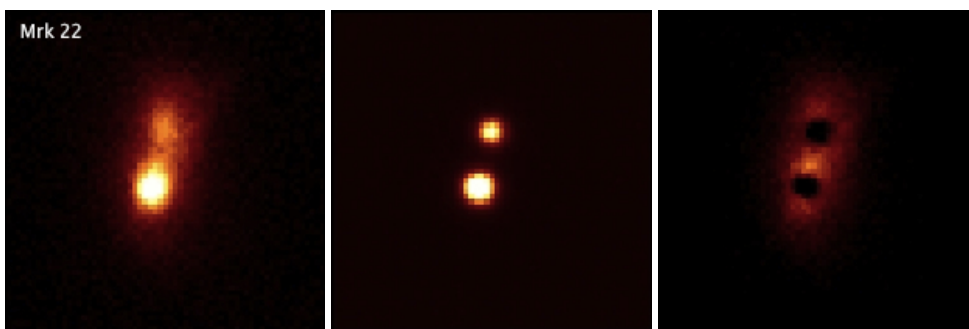
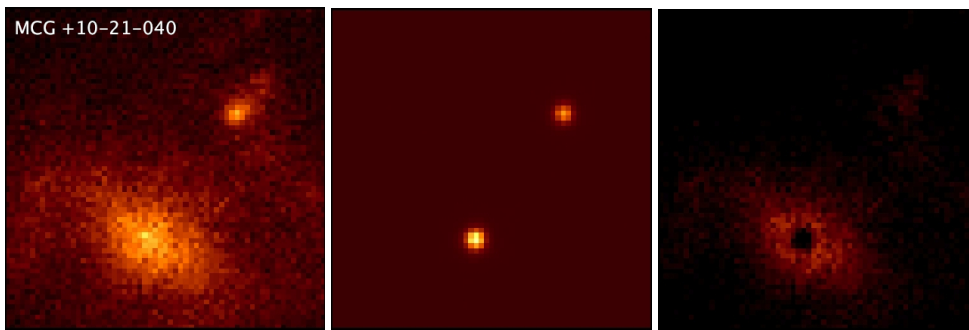


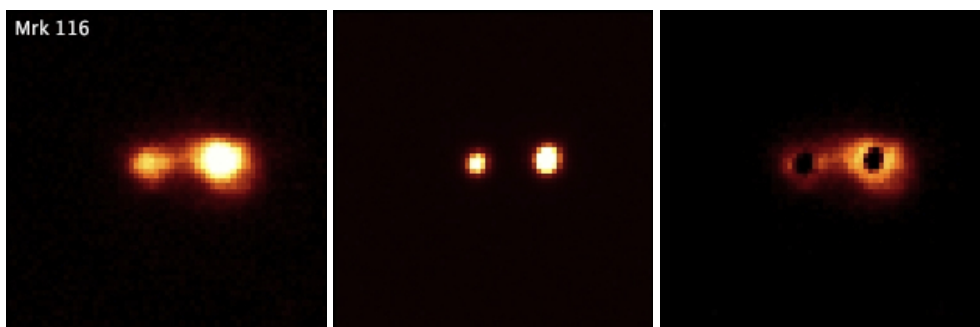
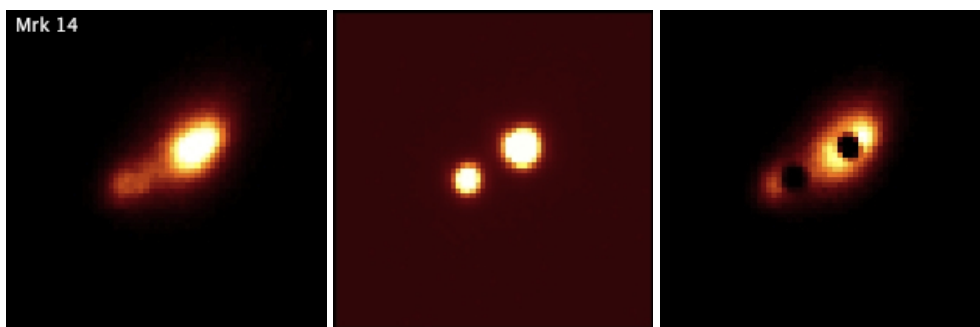
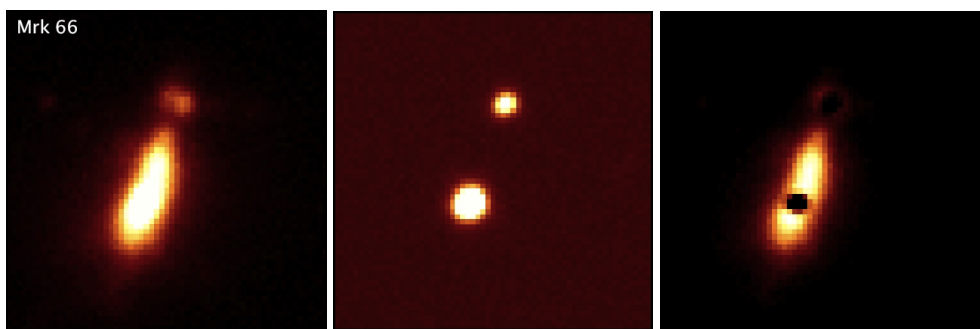
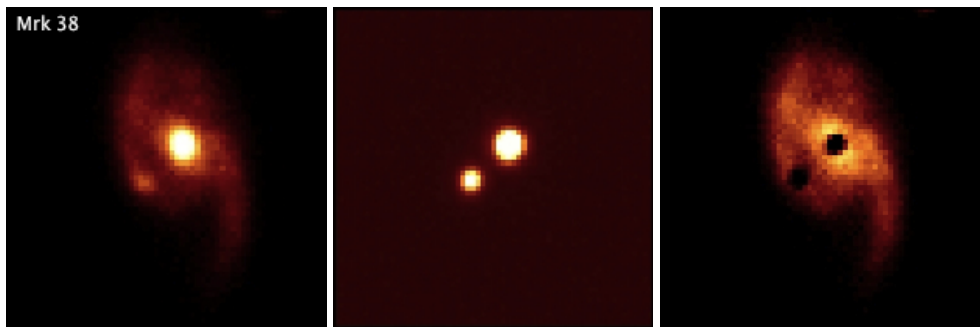


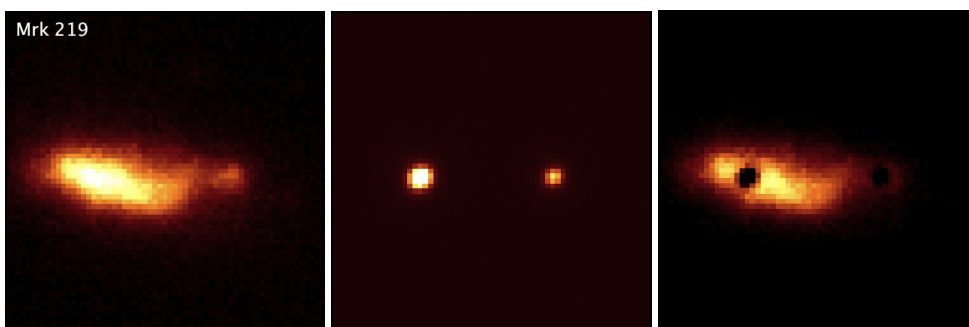
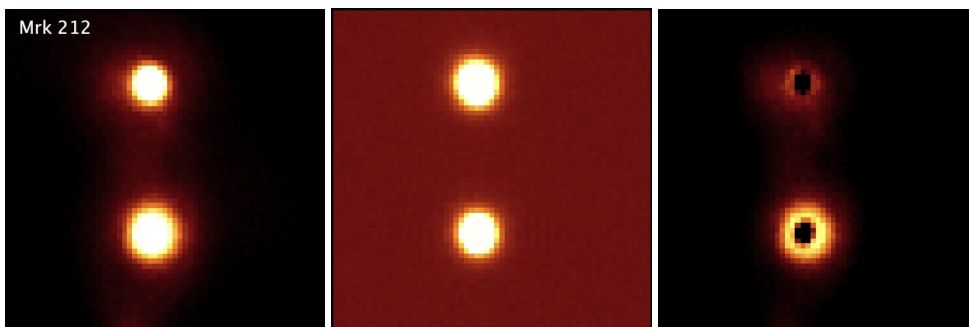
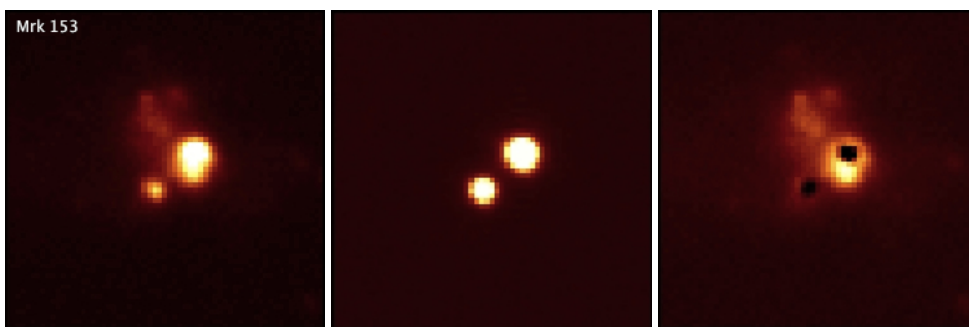
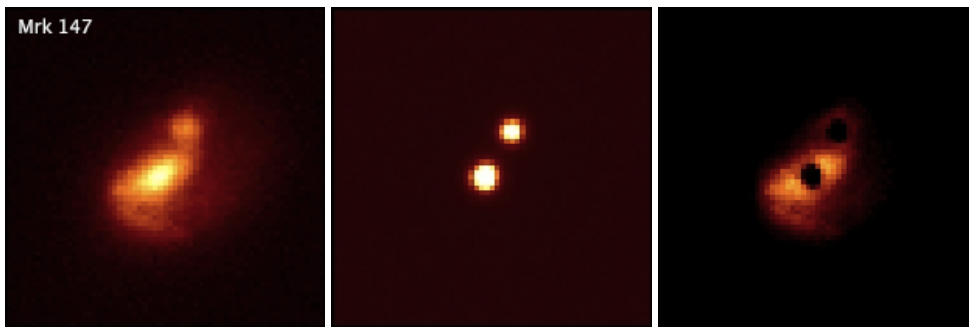


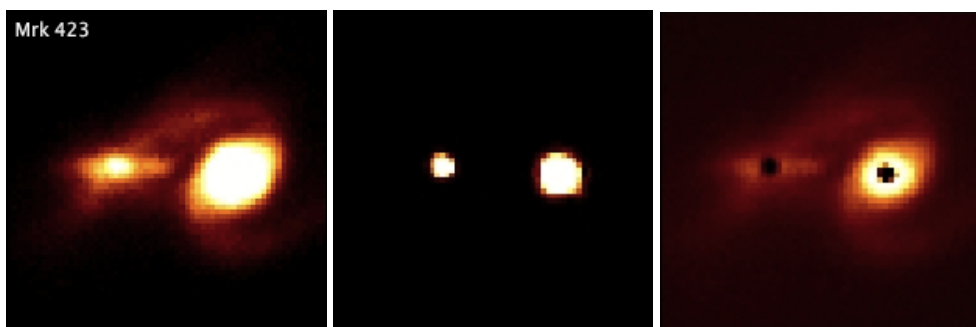
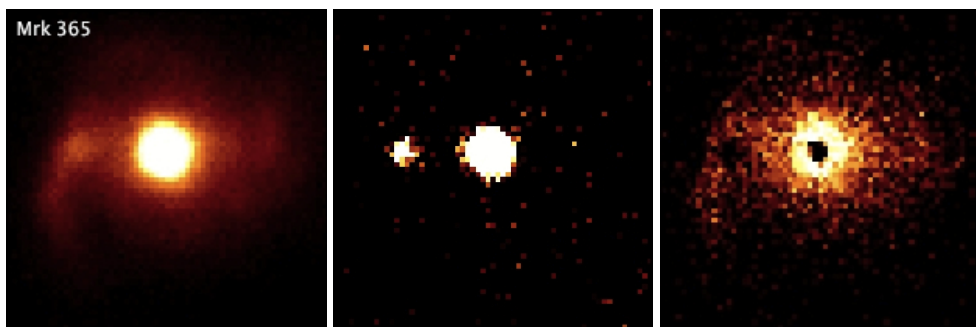
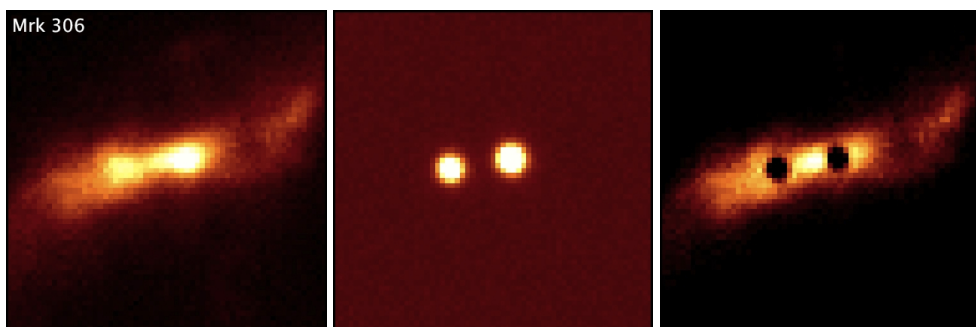
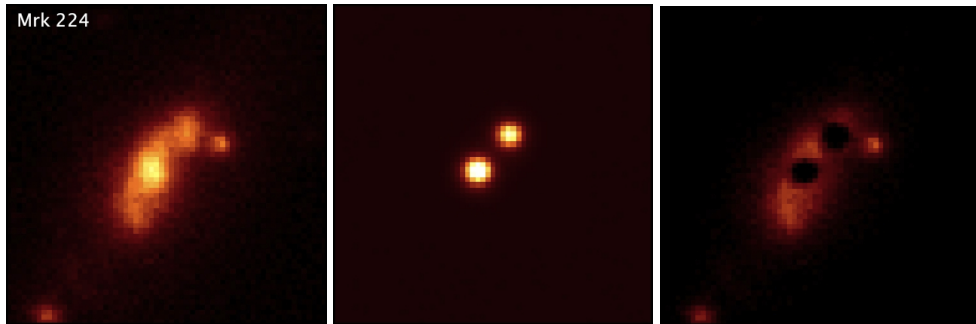




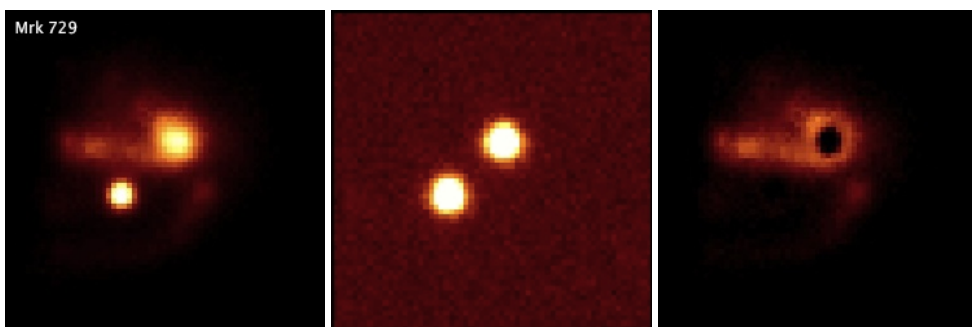
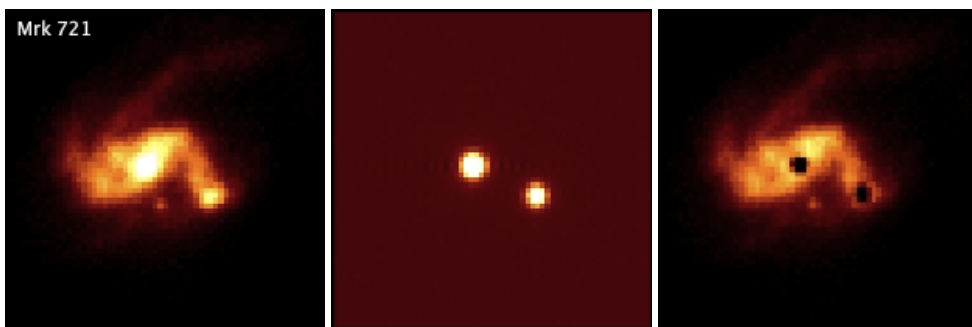
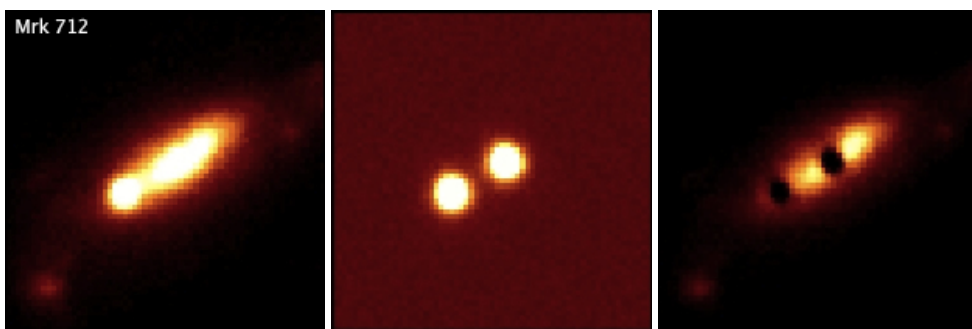
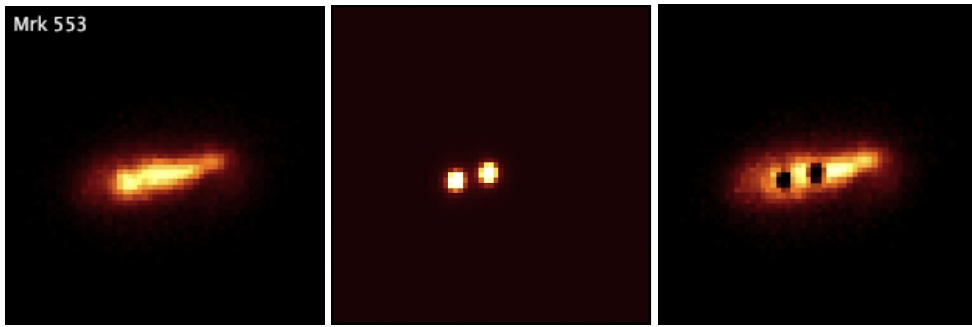


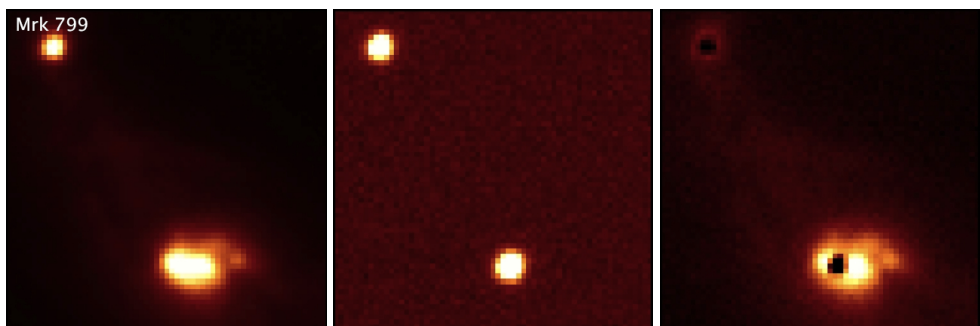
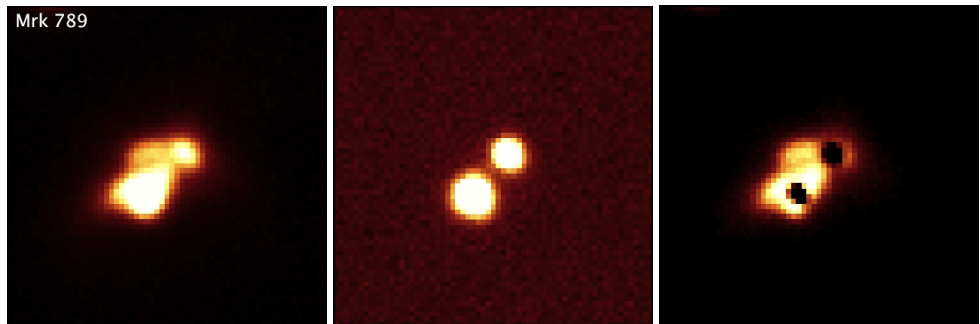
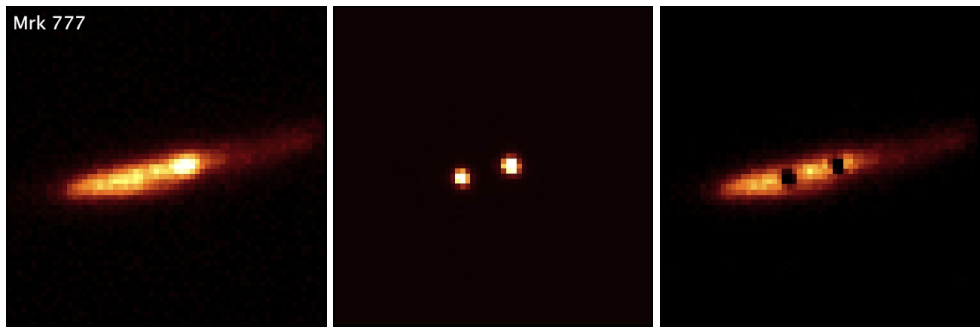
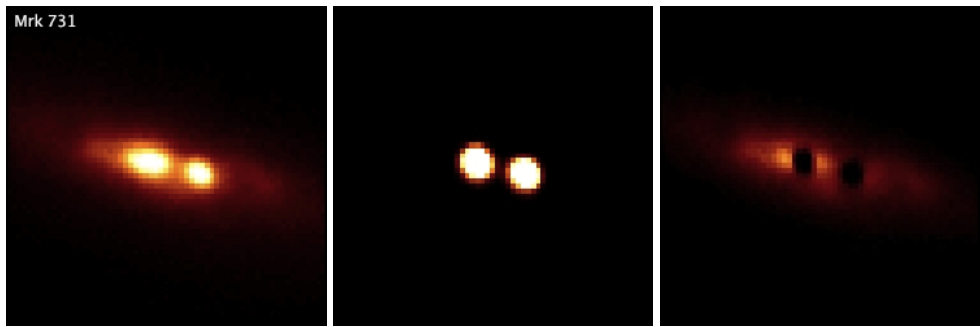




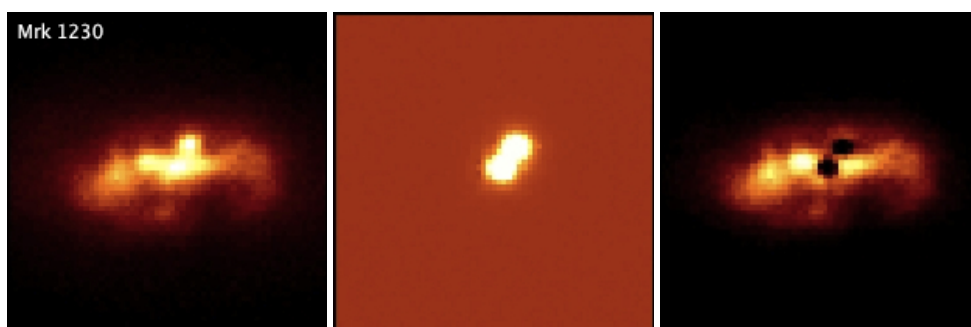
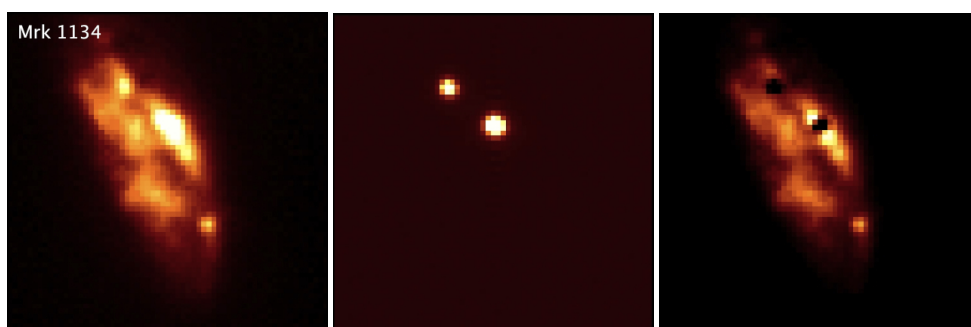
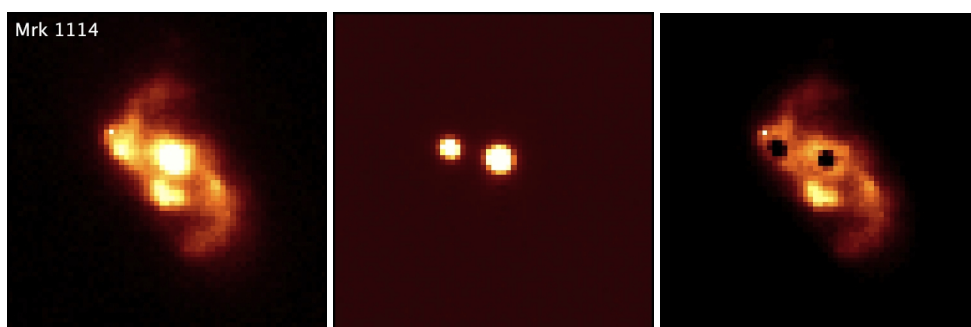
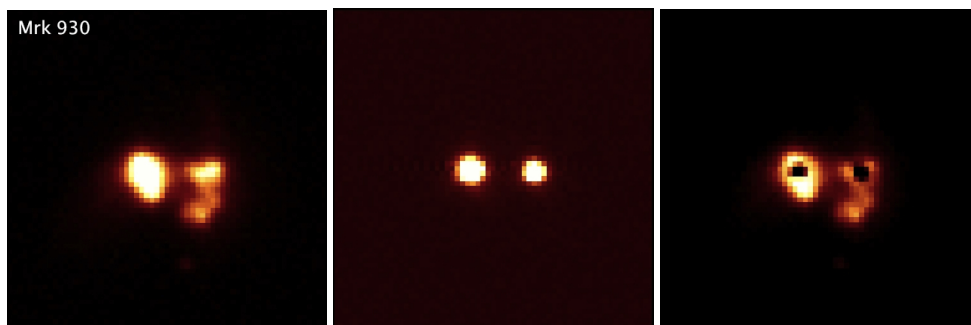


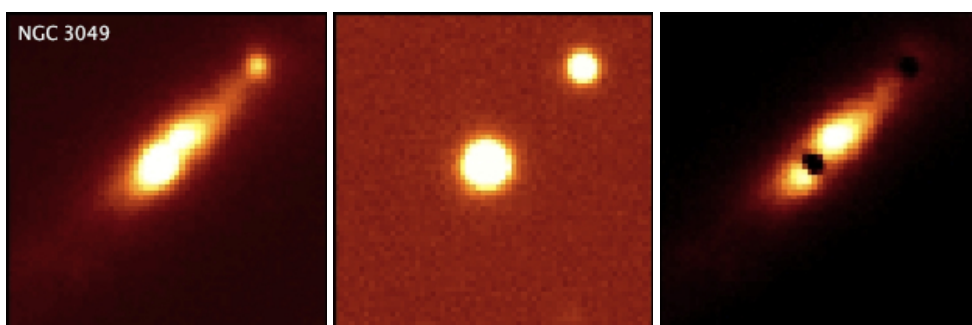
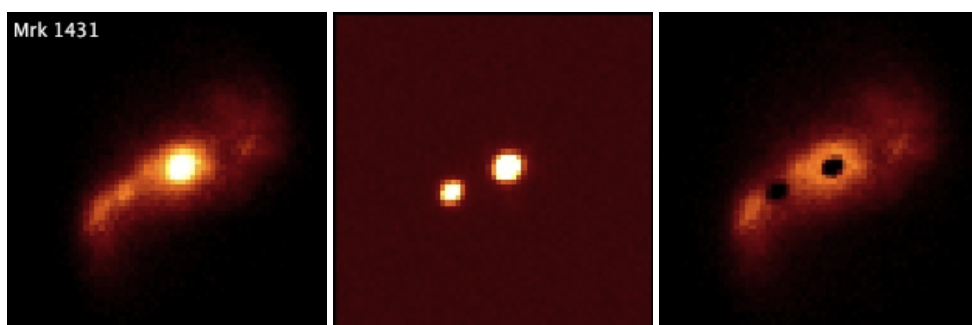
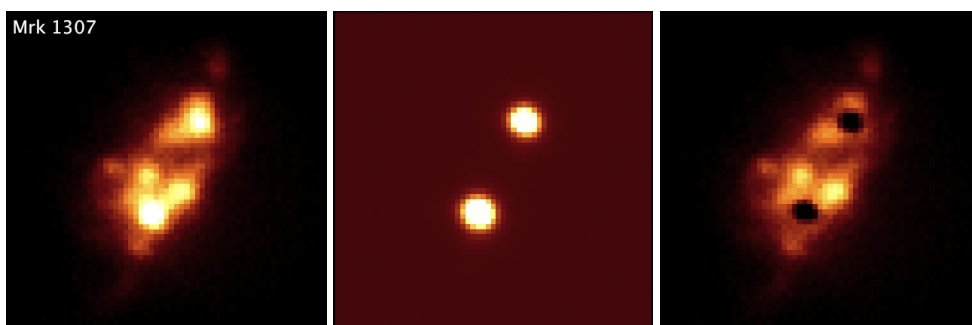
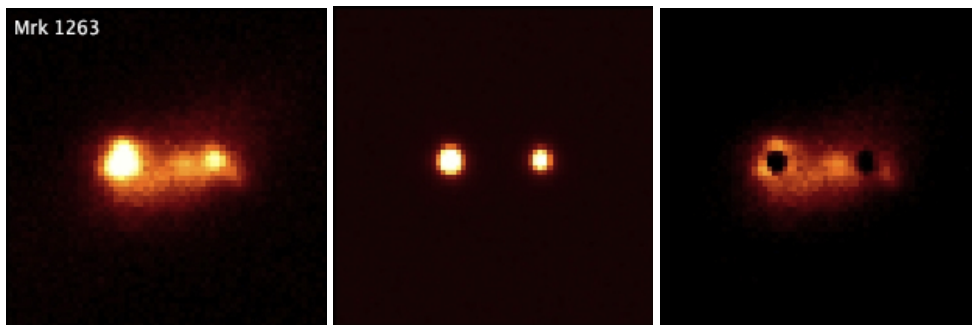


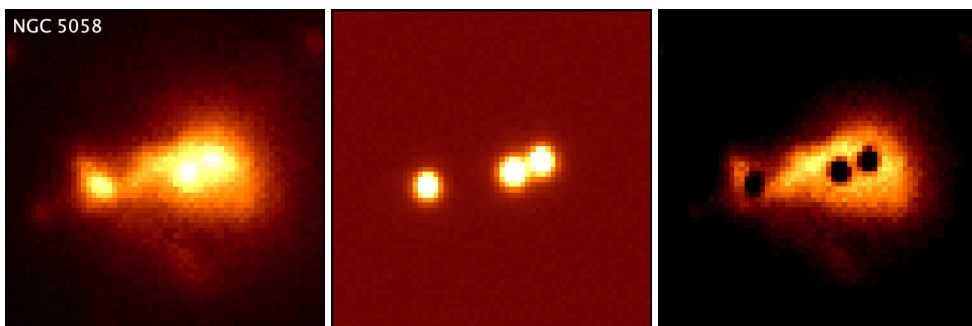
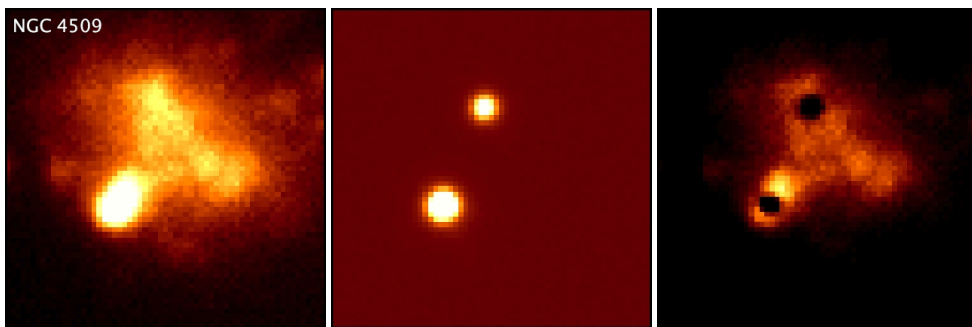
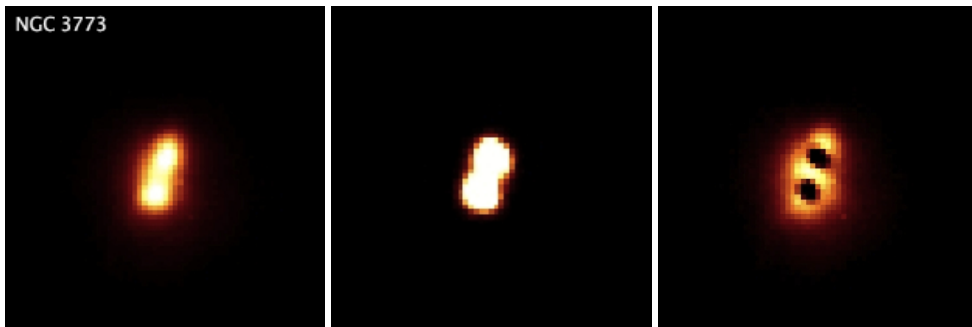
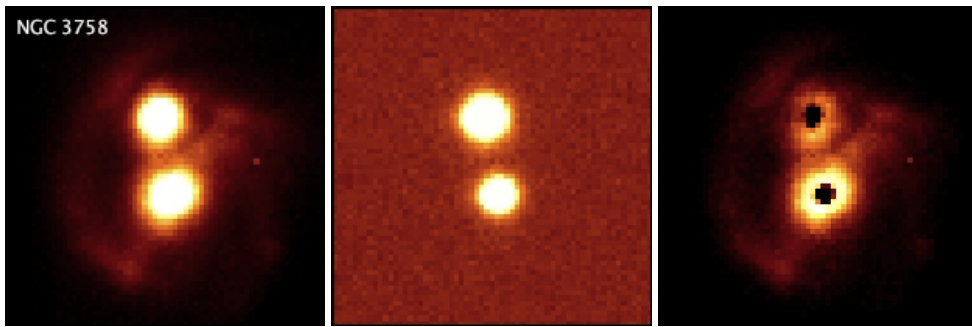


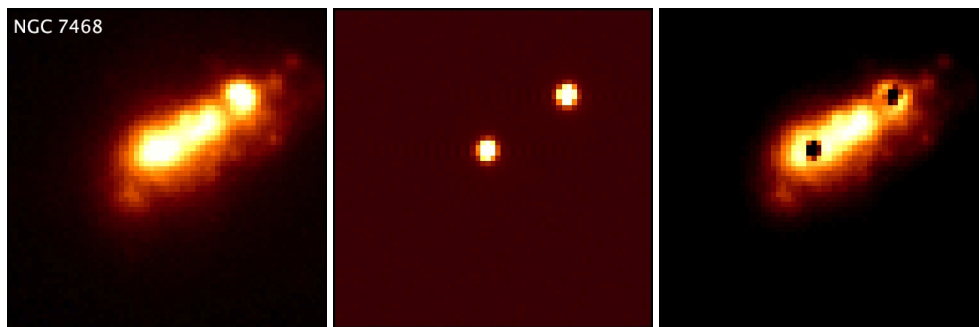
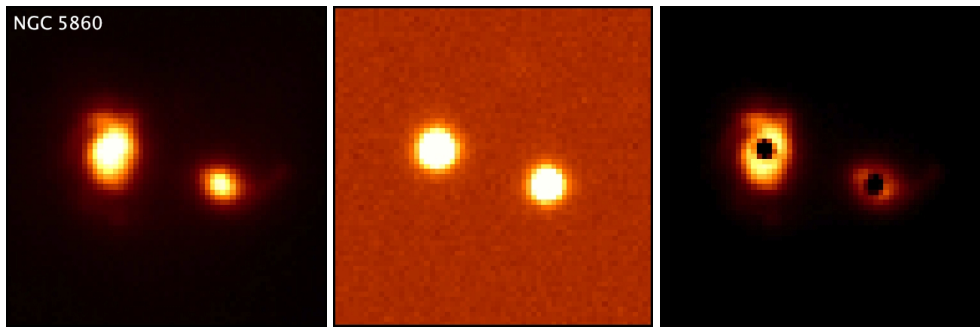
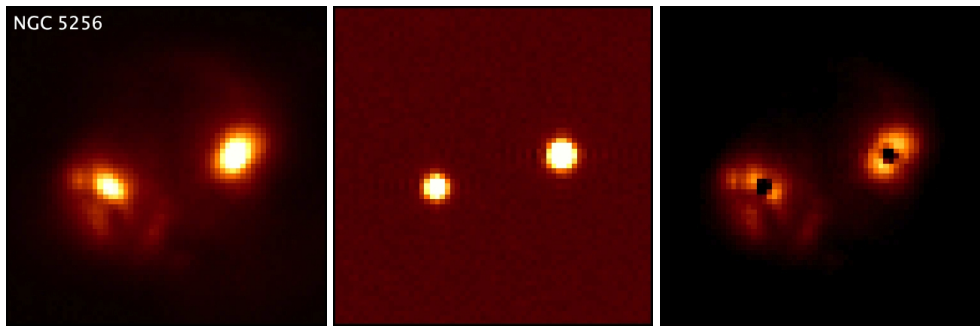












# Bibliography

- Adelman-McCarthy, J. K., Agüeros, M. A., Allam, S. S., et al. 2008, *ApJS*, 175, 297
- Adelman-McCarthy, J. K., Agüeros, M. A., Allam, S. S., et al. 2007, *ApJS*, 172, 634
- Alfvén, H. & Herlofson, N. 1950, *Physical Review*, 78, 616
- Annibali, F., Aloisi, A., Mack, J., et al. 2007, *ArXiv e-prints*
- Antonucci, R. 1993, *ARA&A*, 31, 473
- Armitage, P. J. & Natarajan, P. 2002, *ApJ*, 567, L9
- Asari, N. V., Cid Fernandes, R., Stasińska, G., et al. 2007, *MNRAS*, 381, 263
- Backer, D. C., Jaffe, A. H., & Lommen, A. N. 2004, *Coevolution of Black Holes and Galaxies*, 438
- Balick, B. & Heckman, T. 1978, *ApJ*, 226, L7
- Barnes, J. E. & Hernquist, L. 1992, *ARA&A*, 30, 705
- Barvainis, R. 1987, *ApJ*, 320, 537
- Basu, D., Valtonen, M. J., Valtonen, H., & Mikkola, S. 1993, *A&A*, 272, 417
- Bauer, F. E., Alexander, D. M., Brandt, W. N., et al. 2002, *AJ*, 124, 2351
- Becker, R. H., White, R. L., & Helfand, D. J. 1995, *ApJ*, 450, 559
- Beckert, T. 2005, *Mem. Soc. Astron. Italiana*, 76, 150
- Beckwith, K., Hawley, J. F., & Krolik, J. H. 2009, *ApJ*, 707, 428
- Begelman, M. C. 2002, *ApJ*, 568, L97
- Begelman, M. C., Blandford, R. D., & Rees, M. J. 1980, *Nature*, 287, 307

- Begelman, M. C., King, A. R., & Pringle, J. E. 2006, MNRAS, 370, 399
- Bentz, M. C., Peterson, B. M., Pogge, R. W., & Vestergaard, M. 2009, ApJ, 694, L166
- Best, P. N., Röttgering, H. J. A., & Lehnert, M. D. 1999, MNRAS, 310, 223
- Bietenholz, M. F., Bartel, N., Milisavljevic, D., et al. 2010, MNRAS, 409, 1594
- Bietenholz, M. F., Bartel, N., & Rupen, M. P. 2002, ApJ, 581, 1132
- Blair, W. P. & Fesen, R. A. 1998, in Bulletin of the American Astronomical Society, Vol. 30, American Astronomical Society Meeting Abstracts, 1365–+
- Blair, W. P., Kirshner, R. P., & Winkler, Jr., P. F. 1983, ApJ, 272, 84
- Blecha, L., Cox, T. J., Loeb, A., & Hernquist, L. 2011, MNRAS, 412, 2154
- Bolton, J. G. & Stanley, G. J. 1948, Nature, 161, 312
- Bolton, J. G., Stanley, G. J., & Slee, O. B. 1949, Nature, 164, 101
- Bondi, H. 1952, MNRAS, 112, 195
- Boroson, T. A. & Lauer, T. R. 2009, Nature, 458, 53
- Bournaud, F., Jog, C. J., & Combes, F. 2007, A&A, 476, 1179
- Brassington, N. J., Ponman, T. J., & Read, A. M. 2007, MNRAS, 377, 1439
- Bridge, C. R., Carlberg, R. G., & Sullivan, M. 2010, ApJ, 709, 1067
- Britzen, S., Roland, J., Laskar, J., et al. 2001, A&A, 374, 784
- Bruzual, G. & Charlot, S. 2003, MNRAS, 344, 1000
- Burke, B. F. & Graham-Smith, F. 2002, An Introduction to Radio Astronomy: Second Edition, ed. Burke, B. F. & Graham-Smith, F.
- Callegari, S., Kazantzidis, S., Mayer, L., et al. 2011, ApJ, 729, 85
- Calzetti, D., Wu, S.-Y., Hong, S., et al. 2010, ApJ, 714, 1256
- Capetti, A., Zamfir, S., Rossi, P., et al. 2002, A&A, 394, 39
- Cardelli, J. A., Clayton, G. C., & Mathis, J. S. 1989, ApJ, 345, 245
- Chen, C.-H. R., Chu, Y.-H., Gruendl, R., Lai, S.-P., & Wang, Q. D. 2002, AJ, 123, 2462
- Chen, K. & Halpern, J. P. 1989, ApJ, 344, 115
- Cheung, C. C. 2007, AJ, 133, 2097

- Cheung, C. C., Healey, S. E., Landt, H., Verdoes Kleijn, G., & Jordán, A. 2009, *ApJS*, 181, 548
- Chevalier, R. A. 1982a, *ApJ*, 259, L85
- Chevalier, R. A. 1982b, *ApJ*, 259, 302
- Chornock, R., Bloom, J. S., Cenko, S. B., et al. 2010, *ApJ*, 709, L39
- Chu, Y.-H. & Kennicutt, Jr., R. C. 1986, *ApJ*, 311, 85
- Cid Fernandes, R., Asari, N. V., Sodré, L., et al. 2007, *MNRAS*, 375, L16
- Cid Fernandes, R., González Delgado, R. M., Schmitt, H., et al. 2004a, *ApJ*, 605, 105
- Cid Fernandes, R., Gu, Q., Melnick, J., et al. 2004b, *MNRAS*, 355, 273
- Cid Fernandes, R., Mateus, A., Sodré, L., Stasińska, G., & Gomes, J. M. 2005, *MNRAS*, 358, 363
- Colbert, E. J. M. & Mushotzky, R. F. 1999, *ApJ*, 519, 89
- Colina, L., Borne, K., Bushouse, H., et al. 2001, *ApJ*, 563, 546
- Corbel, S., Nowak, M. A., Fender, R. P., Tzioumis, A. K., & Markoff, S. 2003, *A&A*, 400, 1007
- Cornwell, T. 1995, in *Astronomical Society of the Pacific Conference Series*, Vol. 82, *Very Long Baseline Interferometry and the VLBA*, ed. J. A. Zensus, P. J. Diamond, & P. J. Napier, 39–+
- Cornwell, T. & Fomalont, E. B. 1999, in *Astronomical Society of the Pacific Conference Series*, Vol. 180, *Synthesis Imaging in Radio Astronomy II*, ed. G. B. Taylor, C. L. Carilli, & R. A. Perley, 187–+
- Cowan, J. J., Goss, W. M., & Sramek, R. A. 1991, *ApJ*, 379, L49
- Cox, T. J. 2004, PhD thesis, University of California, Santa Cruz, California, USA
- Croton, D. J., Springel, V., White, S. D. M., et al. 2006, *MNRAS*, 365, 11
- Cseh, D., Grisé, F., Corbel, S., & Kaaret, P. 2011a, *ApJ*, 728, L5+
- Cseh, D., Lang, C., Corbel, S., Kaaret, P., & Grisé, F. 2011b, in *IAU Symposium*, Vol. 275, *IAU Symposium*, ed. G. E. Romero, R. A. Sunyaev, & T. Belloni, 325–326
- Cuadra, J., Armitage, P. J., Alexander, R. D., & Begelman, M. C. 2009, *MNRAS*, 393, 1423
- de Bruyn, A. G. 1983, *A&A*, 119, 301
- De Propriis, R., Conselice, C. J., Liske, J., et al. 2007, *ApJ*, 666, 212

- de Vries, W. H., Becker, R. H., & White, R. L. 2006, *AJ*, 131, 666
- Dennett-Thorpe, J., Scheuer, P. A. G., Laing, R. A., et al. 2002, *MNRAS*, 330, 609
- Dewangan, G. C., Miyaji, T., Griffiths, R. E., & Lehmann, I. 2004, *ApJ*, 608, L57
- Di Matteo, P., Bournaud, F., Martig, M., et al. 2008, *A&A*, 492, 31
- Di Matteo, P., Combes, F., Melchior, A.-L., & Semelin, B. 2007, *A&A*, 468, 61
- Di Matteo, T., Springel, V., & Hernquist, L. 2005, *Nature*, 433, 604
- Di Stefano, R. & Kong, A. K. H. 2004, *ApJ*, 609, 710
- Dunlop, J. S. 2001, in *QSO Hosts and Their Environments*, ed. I. Márquez, J. Masegosa, A. del Olmo, L. Lara, E. García, & J. Molina, 3–4
- Eck, C. R., Roberts, D. A., Cowan, J. J., & Branch, D. 1998, *ApJ*, 508, 664
- Eisenstein, D. J., Weinberg, D. H., Agol, E., et al. 2011, *ArXiv e-prints*
- Eliche-Moral, M. C., Balcells, M., Aguerri, J. A. L., & González-García, A. C. 2006, *A&A*, 457, 91
- Emonts, B. H. C., Morganti, R., Tadhunter, C. N., et al. 2006, *A&A*, 454, 125
- English, J., Koribalski, B., Bland-Hawthorn, J., Freeman, K. C., & McCain, C. F. 2010, *AJ*, 139, 102
- Eracleous, M. & Halpern, J. P. 1994, *ApJS*, 90, 1
- Eracleous, M. & Halpern, J. P. 2003, *ApJ*, 599, 886
- Eracleous, M., Halpern, J. P., Gilbert, A. M., Newman, J. A., & Filippenko, A. V. 1997, *ApJ*, 490, 216
- Fabbiano, G. 1989, *ARA&A*, 27, 87
- Falcke, H., K rding, E., & Markoff, S. 2004, *A&A*, 414, 895
- Fanaroff, B. L. & Riley, J. M. 1974, *MNRAS*, 167, 31P
- Fath, E. A. 1909, *Lick Observatory Bulletin*, 5, 71
- Fender, R. P. & Kuulkers, E. 2001, *MNRAS*, 324, 923
- Feng, H. & Kaaret, P. 2009, *ApJ*, 696, 1712
- Fern ndez-Ontiveros, J. A., L pez-Sanju n, C., Montes, M., Prieto, M. A., & Acosta-Pulido, J. A. 2011, *MNRAS*, 411, L21



Ferrarese, L. & Merritt, D. 2000, *ApJ*, 539, L9

Frieden, B. R. 1972, *Journal of the Optical Society of America (1917-1983)*, 62, 511

Fu, H., Myers, A. D., Djorgovski, S. G., & Yan, L. 2011, *ApJ*, 733, 103

Fuerst, E., Reich, W., Reich, P., Handa, T., & Sofue, Y. 1987, *A&AS*, 69, 403

Gallo, E., Fender, R. P., & Pooley, G. G. 2003, *MNRAS*, 344, 60

Gaskell, C. M. 1996, *ApJ*, 464, L107+

Gebhardt, K., Bender, R., Bower, G., et al. 2000, *ApJ*, 539, L13

Genzel, R., Tacconi, L. J., Rigopoulou, D., Lutz, D., & Tecza, M. 2001, *ApJ*, 563, 527

Georgakakis, A., Tsamis, Y. G., James, B. L., & Aloisi, A. 2011, *MNRAS*, 413, 1729

Gergely, L. Á. & Biermann, P. L. 2009, *ApJ*, 697, 1621

Ghisellini, G., Padovani, P., Celotti, A., & Maraschi, L. 1993, *ApJ*, 407, 65

Gimeno, G. N., Díaz, R. J., & Carranza, G. J. 2004, *AJ*, 128, 62

Gimeno, G. N., Dottori, H. A., Díaz, R. J., Rodrigues, I., & Carranza, G. J. 2007, *AJ*, 133, 2327

Gladstone, J. C. & Roberts, T. P. 2009, *MNRAS*, 397, 124

Gonçalves, A. C. & Soria, R. 2006, *MNRAS*, 371, 673

Gong, B. 2008, *MNRAS*, 389, 315

Gong, B. P., Li, Y. P., & Zhang, H. C. 2011, *ApJ*, 734, L32+

González-Serrano, J. I. & Carballo, R. 2000, *A&AS*, 142, 353

Gopal-Krishna, Biermann, P. L., Gergely, L. Á., & Wiita, P. J. 2010, *ArXiv e-prints*

Gopal-Krishna, Biermann, P. L., & Wiita, P. J. 2003, *ApJ*, 594, L103

Graham, A. W. 2007, *MNRAS*, 379, 711

Graham, A. W. & Driver, S. P. 2007, *ApJ*, 655, 77

Graham, A. W., Erwin, P., Caon, N., & Trujillo, I. 2001, *ApJ*, 563, L11

Greene, J. E. & Ho, L. C. 2004, *ApJ*, 610, 722

Greene, J. E. & Ho, L. C. 2005, *ApJ*, 630, 122

Greene, J. E. & Ho, L. C. 2007, *ApJ*, 656, 84

- Hanbury Brown, R., Jennison, R. C., & Gupta, M. K. D. 1952, *Nature*, 170, 1061
- Heil, L. M., Vaughan, S., & Roberts, T. P. 2009, *MNRAS*, 397, 1061
- Hernquist, L. 1989, *Nature*, 340, 687
- Ho, L. C. 2008, *ARA&A*, 46, 475
- Hodges-Kluck, E. J., Reynolds, C. S., Cheung, C. C., & Miller, M. C. 2010a, *ApJ*, 710, 1205
- Hodges-Kluck, E. J., Reynolds, C. S., Miller, M. C., & Cheung, C. C. 2010b, *ApJ*, 717, L37
- Högbom, J. A. 1974, *A&AS*, 15, 417
- Hönig, S. F., Beckert, T., Ohnaka, K., & Weigelt, G. 2006, *A&A*, 452, 459
- Hopkins, P. F., Cox, T. J., Dutta, S. N., et al. 2009, *ApJS*, 181, 135
- Hopkins, P. F., Cox, T. J., Kereš, D., & Hernquist, L. 2008a, *ApJS*, 175, 390
- Hopkins, P. F., Hernquist, L., Cox, T. J., et al. 2006, *ApJS*, 163, 1
- Hopkins, P. F., Hernquist, L., Cox, T. J., & Kereš, D. 2008b, *ApJS*, 175, 356
- Hubble, E. P. 1936, *Realm of the Nebulae*, ed. Hubble, E. P.
- Hudson, D. S., Reiprich, T. H., Clarke, T. E., & Sarazin, C. L. 2006, *A&A*, 453, 433
- Ivanov, P. B., Igumenshchev, I. V., & Novikov, I. D. 1998, *ApJ*, 507, 131
- Jenkins, L. P., Roberts, T. P., Warwick, R. S., Kilgard, R. E., & Ward, M. J. 2004, *MNRAS*, 349, 404
- Jesseit, R., Naab, T., Peletier, R. F., & Burkert, A. 2007, *MNRAS*, 376, 997
- Jithesh, V., Jeena, K., Misra, R., et al. 2011, *ApJ*, 729, 67
- Kaaret, P. & Corbel, S. 2009, *ApJ*, 697, 950
- Kaaret, P., Corbel, S., Prestwich, A. H., & Zezas, A. 2003, *Science*, 299, 365
- Kaaret, P., Feng, H., & Gorski, M. 2009, *ApJ*, 692, 653
- Kaaret, P., Prestwich, A. H., Zezas, A., et al. 2001, *MNRAS*, 321, L29
- Kaaret, P., Ward, M. J., & Zezas, A. 2004, *MNRAS*, 351, L83
- Kaler, J. B. 1989, *Stars and their spectra. an introduction to spectral sequence*, ed. Kaler, J. B.
- Karouzos, M., Britzen, S., Eckart, A., Witzel, A., & Zensus, A. 2010, *A&A*, 519, A62+
- Kaspi, S., Maoz, D., Netzer, H., et al. 2005, *ApJ*, 629, 61

- Kaspi, S., Smith, P. S., Netzer, H., et al. 2000, *ApJ*, 533, 631
- Kauffmann, G. & Haehnelt, M. 2000, *MNRAS*, 311, 576
- Kaviraj, S., Peirani, S., Khochfar, S., Silk, J., & Kay, S. 2009, *MNRAS*, 394, 1713
- Kaviraj, S., Schawinski, K., Devriendt, J. E. G., et al. 2007, *ApJS*, 173, 619
- Kellermann, K. I., Fomalont, E. B., Mainieri, V., et al. 2008, *ApJS*, 179, 71
- Kellermann, K. I., Sramek, R., Schmidt, M., Shaffer, D. B., & Green, R. 1989, *AJ*, 98, 1195
- Kereš, D., Katz, N., Weinberg, D. H., & Davé, R. 2005, *MNRAS*, 363, 2
- Kilgard, R. E., Kaaret, P., Krauss, M. I., et al. 2002, *ApJ*, 573, 138
- King, A. R. 2008, *MNRAS*, 385, L113
- King, A. R. 2009, *MNRAS*, 393, L41
- King, A. R., Davies, M. B., Ward, M. J., Fabbiano, G., & Elvis, M. 2001, *ApJ*, 552, L109
- Komossa, S. 2006, *Mem. Soc. Astron. Italiana*, 77, 733
- Komossa, S., Burwitz, V., Hasinger, G., et al. 2003, *ApJ*, 582, L15
- Körding, E., Colbert, E., & Falcke, H. 2005, *A&A*, 436, 427
- Körding, E., Falcke, H., & Markoff, S. 2002, *A&A*, 382, L13
- Koribalski, B. S. & López-Sánchez, Á. R. 2009, *MNRAS*, 400, 1749
- Kormendy, J. & Kennicutt, Jr., R. C. 2004, *ARA&A*, 42, 603
- Koss, M., Mushotzky, R., Treister, E., et al. 2011, *ApJ*, 735, L42+
- Krolik, J. H. 1998, *Active Galactic Nuclei: From the Central Black Hole to the Galactic Environment*, ed. Krolik, J. H.
- Krolik, J. H. & Begelman, M. C. 1988, *ApJ*, 329, 702
- Kubota, A., Mizuno, T., Makishima, K., et al. 2001, *ApJ*, 547, L119
- Labiano, A., O’Dea, C. P., Barthel, P. D., de Vries, W. H., & Baum, S. A. 2008, *A&A*, 477, 491
- Lacey, C. K., Goss, W. M., & Mizouni, L. K. 2007, *AJ*, 133, 2156
- Lal, D. V. & Rao, A. P. 2005, in *Astronomical Society of the Pacific Conference Series*, Vol. 345, *From Clark Lake to the Long Wavelength Array: Bill Erickson’s Radio Science*, ed. N. Kassim, M. Perez, W. Junor, & P. Henning, 289–+

- Lal, D. V. & Rao, A. P. 2007, MNRAS, 374, 1085
- Landt, H., Cheung, C. C., & Healey, S. E. 2010, MNRAS, 408, 1103
- Landt, H., Padovani, P., & Giommi, P. 2002, MNRAS, 336, 945
- Lang, C. C., Kaaret, P., Corbel, S., & Mercer, A. 2007, ApJ, 666, 79
- Laor, A. & Draine, B. T. 1993, ApJ, 402, 441
- Leahy, J. P. & Parma, P. 1992, in Extragalactic Radio Sources. From Beams to Jets, ed. J. Roland, H. Sol, & G. Pelletier, 307–308
- Leahy, J. P. & Williams, A. G. 1984, MNRAS, 210, 929
- Leavitt, H. S. & Pickering, E. C. 1912, Harvard College Observatory Circular, 173, 1
- Lehmer, B. D., Brandt, W. N., Hornschemeier, A. E., et al. 2006, AJ, 131, 2394
- León-Tavares, J., Lobanov, A. P., Chavushyan, V. H., et al. 2010, ApJ, 715, 355
- Letawe, G., Magain, P., Courbin, F., et al. 2007, MNRAS, 378, 83
- Li, C., Kauffmann, G., Heckman, T. M., White, S. D. M., & Jing, Y. P. 2008, MNRAS, 385, 1915
- Lintott, C., Schawinski, K., Bamford, S., et al. 2011, MNRAS, 410, 166
- Liu, F. K., Wu, X.-B., & Cao, S. L. 2003, MNRAS, 340, 411
- Liu, J.-F. & Bregman, J. N. 2005, ApJS, 157, 59
- Liu, J.-F., Bregman, J. N., & Seitzer, P. 2004, ApJ, 602, 249
- Liu, X., Greene, J. E., Shen, Y., & Strauss, M. A. 2010a, ApJ, 715, L30
- Liu, X., Shen, Y., Strauss, M. A., & Greene, J. E. 2010b, ApJ, 708, 427
- Lobanov, A. 2005, in Growing Black Holes: Accretion in a Cosmological Context, ed. A. Merloni, S. Nayakshin, & R. A. Sunyaev, 354–355
- Lobanov, A. 2007, in From Planets to Dark Energy: the Modern Radio Universe
- Lobanov, A. P. 2008, Mem. Soc. Astron. Italiana, 79, 1306
- Lobanov, A. P. & Roland, J. 2005, A&A, 431, 831
- Lodato, G. & Natarajan, P. 2006, MNRAS, 371, 1813
- López-Corredoira, M. & Gutiérrez, C. M. 2006, A&A, 454, 77

- López-Sanjuan, C., Le Fèvre, O., de Ravel, L., et al. 2011, *A&A*, 530, A20+
- Lotz, J. M., Jonsson, P., Cox, T. J., & Primack, J. R. 2008, *MNRAS*, 391, 1137
- Mack, K.-H., Gregorini, L., Parma, P., & Klein, U. 1994, *A&AS*, 103, 157
- Madau, P. & Rees, M. J. 2001, *ApJ*, 551, L27
- Malkan, M. A. & Sargent, W. L. W. 1982, *ApJ*, 254, 22
- Marcaide, J. M., Martí-Vidal, I., Perez-Torres, M. A., et al. 2009, *A&A*, 503, 869
- Marcha, M. J. M., Browne, I. W. A., Impey, C. D., & Smith, P. S. 1996, *MNRAS*, 281, 425
- Marchesini, D., Celotti, A., & Ferrarese, L. 2004, *MNRAS*, 351, 733
- Marconi, A. & Hunt, L. K. 2003, *ApJ*, 589, L21
- Martí-Vidal, I., Marcaide, J. M., Alberdi, A., et al. 2011a, *A&A*, 526, A142+
- Martí-Vidal, I., Pérez-Torres, M. A., & Brunthaler, A. 2011b, *A&A*, 529, A47+
- Mateus, A., Sodré, L., Cid Fernandes, R., et al. 2006, *MNRAS*, 370, 721
- Mazzarella, J. M. & Boroson, T. A. 1993, *ApJS*, 85, 27
- Mazzarella, J. M., Bothun, G. D., & Boroson, T. A. 1991, *AJ*, 101, 2034
- McDonald, A. R., Muxlow, T. W. B., Pedlar, A., et al. 2001, *MNRAS*, 322, 100
- McLeod, B. A., Bernstein, G. M., Rieke, M. J., & Weedman, D. W. 1998, *AJ*, 115, 1377
- McLure, R. J. & Dunlop, J. S. 2002, *MNRAS*, 331, 795
- Merloni, A., Heinz, S., & di Matteo, T. 2003, *MNRAS*, 345, 1057
- Merritt, D. & Ekers, R. D. 2002, *Science*, 297, 1310
- Merritt, D., Milosavljević, M., Favata, M., Hughes, S. A., & Holz, D. E. 2004, *ApJ*, 607, L9
- Mezcua, M., Lobanov, A. P., Chavushyan, V. H., & León-Tavares, J. 2011, *A&A*, 527, A38+
- Mihos, J. C. & Hernquist, L. 1994, *ApJ*, 425, L13
- Mihos, J. C. & Hernquist, L. 1996, *ApJ*, 464, 641
- Milislavljevic, D. & Fesen, R. A. 2008, *ApJ*, 677, 306
- Miller, J. M., Fabbiano, G., Miller, M. C., & Fabian, A. C. 2003, *ApJ*, 585, L37
- Miller, N. A., Mushotzky, R. F., & Neff, S. G. 2005a, *ApJ*, 623, L109

- Miller, N. A., Neff, S. G., & Mushotzky, R. F. 2005b, in *X-Ray and Radio Connections*, ed. L. O. Sjouwerman & K. K. Dyer
- Milosavljević, M. & Merritt, D. 2001, *ApJ*, 563, 34
- Mirabel, I. F. & Rodríguez, L. F. 1994, *Nature*, 371, 46
- Moon, D.-S., Harrison, F. A., Cenko, S. B., & Shariff, J. A. 2011, *ApJ*, 731, L32+
- Morris, D., Palmer, H. P., & Thompson, A. R. 1957, *The Observatory*, 77, 103
- Murgia, M., Parma, P., de Ruiter, H. R., et al. 2001, *A&A*, 380, 102
- Mushotzky, R. 2004, *Progress of Theoretical Physics Supplement*, 155, 27
- Naab, T., Johansson, P. H., & Ostriker, J. P. 2009, *ApJ*, 699, L178
- Naab, T., Khochfar, S., & Burkert, A. 2006, *ApJ*, 636, L81
- Neff, S. G., Ulvestad, J. S., & Champion, S. D. 2003, *ApJ*, 599, 1043
- Nelson, C. H. 2000, *ApJ*, 544, L91
- Nipoti, C., Treu, T., & Bolton, A. S. 2009, *ApJ*, 703, 1531
- Oke, J. B. & Gunn, J. E. 1983, *ApJ*, 266, 713
- Onken, C. A., Ferrarese, L., Merritt, D., et al. 2004, in *IAU Symposium, Vol. 222, The Interplay Among Black Holes, Stars and ISM in Galactic Nuclei*, ed. T. Storchi-Bergmann, L. C. Ho, & H. R. Schmitt, 109–110
- Pakull, M. W., Grisé, F., & Motch, C. 2006, in *IAU Symposium, Vol. 230, Populations of High Energy Sources in Galaxies*, ed. E. J. A. Meurs & G. Fabbiano, 293–297
- Pakull, M. W. & Mirioni, L. 2002, *ArXiv Astrophysics e-prints*
- Pakull, M. W. & Mirioni, L. 2003, in *Revista Mexicana de Astronomia y Astrofisica, vol. 27, Vol. 15, Revista Mexicana de Astronomia y Astrofisica Conference Series*, ed. J. Arthur & W. J. Henney, 197–199
- Paragi, Z., Garrett, M. A., & Biggs, A. D. 2006, in *Proceedings of the 8th European VLBI Network Symposium*
- Parma, P., Ekers, R. D., & Fanti, R. 1985, *A&AS*, 59, 511
- Patruno, A. & Zampieri, L. 2010, *MNRAS*, 403, L69
- Pearson, T. J. & Readhead, A. C. S. 1984, *ARA&A*, 22, 97
- Pennington, R. L. & Dufour, R. J. 1983, *ApJ*, 270, L7

- Pérez-Ramírez, D., Mezcua, M., Leon, S., & Caballero-García, M. D. 2011, *Astronomische Nachrichten*, 332, 384
- Peterson, B. M., Ferrarese, L., Gilbert, K. M., et al. 2004, *ApJ*, 613, 682
- Peterson, B. M. & Wandel, A. 1999, *ApJ*, 521, L95
- Plotkin, R. M., Anderson, S. F., Hall, P. B., et al. 2008, *AJ*, 135, 2453
- Popović, L. Č., Smirnova, A. A., Kovačević, J., Moiseev, A. V., & Afanasiev, V. L. 2009, *AJ*, 137, 3548
- Porcas, R. 1983, *Nature*, 302, 753
- Poutanen, J., Lipunova, G., Fabrika, S., Butkevich, A. G., & Abolmasov, P. 2007, *MNRAS*, 377, 1187
- Quataert, E. 2003, *Astronomische Nachrichten Supplement*, 324, 435
- Rappaport, S. A., Podsiadlowski, P., & Pfahl, E. 2005, *MNRAS*, 356, 401
- Reber, G. 1944, *ApJ*, 100, 279
- Rees, M. J. 1978, *Nature*, 275, 516
- Rees, M. J. 1989, *MNRAS*, 239, 1P
- Rees, M. J., Begelman, M. C., Blandford, R. D., & Phinney, E. S. 1982, *Nature*, 295, 17
- Reines, A. E., Johnson, K. E., & Goss, W. M. 2008, *AJ*, 135, 2222
- Revnivtsev, M., Gilfanov, M., Churazov, E., & Sunyaev, R. 2002, *A&A*, 391, 1013
- Richstone, D., Ajhar, E. A., Bender, R., et al. 1998, *Nature*, 395, A14+
- Roberts, T. P., Goad, M. R., Ward, M. J., et al. 2001, *MNRAS*, 325, L7
- Rodriguez, C., Taylor, G. B., Zavala, R. T., et al. 2006, *ApJ*, 646, 49
- Rogers, A. E. E., Cappallo, R. J., Hinteregger, H. F., et al. 1983, *Science*, 219, 51
- Roland, J., Britzen, S., Kudryavtseva, N. A., Witzel, A., & Karouzos, M. 2008, *A&A*, 483, 125
- Ros, E., Zensus, J. A., & Lobanov, A. P. 1998, *Ap&SS*, 263, 59
- Ross, R. R., Fabian, A. C., & Mineshige, S. 1992, *MNRAS*, 258, 189
- Rovilos, E., Georgakakis, A., Georgantopoulos, I., et al. 2007, *A&A*, 466, 119

- Rybicki, G. B. & Lightman, A. P. 1979, *Radiative processes in astrophysics*, ed. Rybicki, G. B. & Lightman, A. P.
- Ryle, M., Smith, F. G., & Elsmore, B. 1950, *MNRAS*, 110, 508
- Salpeter, E. E. 1964, *ApJ*, 140, 796
- Sánchez-Sutil, J. R., Muñoz-Arjonilla, A. J., Martí, J., et al. 2006, *A&A*, 452, 739
- Sanders, D. B. & Mirabel, I. F. 1996, *ARA&A*, 34, 749
- Sanders, D. B., Soifer, B. T., Elias, J. H., Neugebauer, G., & Matthews, K. 1988, *ApJ*, 328, L35
- Schawinski, K., Dowlin, N., Thomas, D., Urry, C. M., & Edmondson, E. 2010, *ApJ*, 714, L108
- Schawinski, K., Treister, E., Urry, C. M., et al. 2011, *ApJ*, 727, L31+
- Schlegel, D. J., Finkbeiner, D. P., & Davis, M. 1998, *ApJ*, 500, 525
- Schoenmakers, A. P., de Bruyn, A. G., Röttgering, H. J. A., van der Laan, H., & Kaiser, C. R. 2000, *MNRAS*, 315, 371
- Sequist, E. R. & Bignell, R. C. 1978, *ApJ*, 226, L5+
- Searle, L. & Zinn, R. 1978, *ApJ*, 225, 357
- Sesana, A., Haardt, F., Madau, P., & Volonteri, M. 2005, *ApJ*, 623, 23
- Seyfert, C. K. 1943, *ApJ*, 97, 28
- Shakura, N. I. & Sunyaev, R. A. 1973, *A&A*, 24, 337
- Shang, Z., Brotherton, M. S., Green, R. F., et al. 2005, *ApJ*, 619, 41
- Shapovalova, A. I., Popović, L. Č., Burenkov, A. N., et al. 2010, *A&A*, 517, A42+
- Shemmer, O., Brandt, W. N., Netzer, H., Maiolino, R., & Kaspi, S. 2008, *ApJ*, 682, 81
- Shen, Y. & Loeb, A. 2010, *ApJ*, 725, 249
- Shields, G. A. 1978, *Nature*, 272, 706
- Shields, J. C. 1992, *ApJ*, 399, L27
- Silk, J. & Norman, C. 2009, *ApJ*, 700, 262
- Sillanpaa, A., Haarala, S., Valtonen, M. J., Sundelius, B., & Byrd, G. G. 1988, *ApJ*, 325, 628
- Sillanpaa, A., Takalo, L. O., Pursimo, T., et al. 1996, *A&A*, 305, L17+



- Slipher, V. M. 1917, *Lowell Observatory Bulletin*, 3, 59
- Smith, K. L., Shields, G. A., Bonning, E. W., et al. 2010, *ApJ*, 716, 866
- Soria, R., Motch, C., Read, A. M., & Stevens, I. R. 2004, *A&A*, 423, 955
- Springel, V., Di Matteo, T., & Hernquist, L. 2005a, *ApJ*, 620, L79
- Springel, V., White, S. D. M., Jenkins, A., et al. 2005b, *Nature*, 435, 629
- Stockdale, C. J., Goss, W. M., Cowan, J. J., & Sramek, R. A. 2001, *ApJ*, 559, L139
- Stocke, J. T., Morris, S. L., Gioia, I. M., et al. 1991, *ApJS*, 76, 813
- Strateva, I., Ivezić, Ž., Knapp, G. R., et al. 2001, *AJ*, 122, 1861
- Strateva, I. V., Brandt, W. N., Eracleous, M., Schneider, D. P., & Chartas, G. 2006, *ApJ*, 651, 749
- Strateva, I. V. & Komossa, S. 2009, *ApJ*, 692, 443
- Strateva, I. V., Strauss, M. A., Hao, L., et al. 2003, *AJ*, 126, 1720
- Strohmayer, T. E. & Mushotzky, R. F. 2003, *ApJ*, 586, L61
- Strohmayer, T. E., Mushotzky, R. F., Winter, L., et al. 2007, *ApJ*, 660, 580
- Struve, C., Oosterloo, T., Sancisi, R., Morganti, R., & Emons, B. H. C. 2010, *A&A*, 523, A75+
- Summers, L. K., Stevens, I. R., Strickland, D. K., & Heckman, T. M. 2003, *MNRAS*, 342, 690
- Swartz, D. A., Ghosh, K. K., Tennant, A. F., & Wu, K. 2004, *ApJS*, 154, 519
- Tadhunter, C., Robinson, T. G., González Delgado, R. M., Wills, K., & Morganti, R. 2005, *MNRAS*, 356, 480
- Terashima, Y. & Wilson, A. S. 2003, *ApJ*, 583, 145
- Terlevich, R. & Melnick, J. 1985, *MNRAS*, 213, 841
- Thompson, A. R. 1999, in *Astronomical Society of the Pacific Conference Series*, Vol. 180, *Synthesis Imaging in Radio Astronomy II*, ed. G. B. Taylor, C. L. Carilli, & R. A. Perley, 11–+
- Thorstensen, J. R., Fesen, R. A., & van den Bergh, S. 2001, *AJ*, 122, 297
- Tingay, S. J., Jauncey, D. L., Reynolds, J. E., et al. 1998, *AJ*, 115, 960
- Toomre, A. 1977, in *Evolution of Galaxies and Stellar Populations*, ed. B. M. Tinsley & R. B. Larson, 401–+

- Toomre, A. & Toomre, J. 1972, *ApJ*, 178, 623
- Tremaine, S., Gebhardt, K., Bender, R., et al. 2002, *ApJ*, 574, 740
- Trujillo, I., Ferreras, I., & de La Rosa, I. G. 2011, *MNRAS*, 938
- Urry, C. M. & Padovani, P. 1995, *PASP*, 107, 803
- Valtaoja, E., Teräsranta, H., Tornikoski, M., et al. 2000, *ApJ*, 531, 744
- Valtonen, M. J. & Heinämäki, P. 2000, *ApJ*, 530, 107
- Villata, M. & Raiteri, C. M. 1999, *A&A*, 347, 30
- Virani, S. N., De Robertis, M. M., & VanDalfsen, M. L. 2000, *AJ*, 120, 1739
- Volonteri, M., Haardt, F., & Madau, P. 2003, *ApJ*, 582, 559
- Volonteri, M., Lodato, G., & Natarajan, P. 2008, *MNRAS*, 383, 1079
- Volonteri, M. & Rees, M. J. 2005, *ApJ*, 633, 624
- Walker, R. C. 1986, in *Synthesis Imaging*, ed. R. A. Perley, F. R. Schwab, & A. H. Bridle, 189–213
- Walker, R. C. 1995, in *Astronomical Society of the Pacific Conference Series*, Vol. 82, *Very Long Baseline Interferometry and the VLBA*, ed. J. A. Zensus, P. J. Diamond, & P. J. Napier, 247–+
- Wandel, A. 2002, *ApJ*, 565, 762
- Wang, Q. D. 2002, *MNRAS*, 332, 764
- Wang, Q. D., Immler, S., & Pietsch, W. 1999, *ApJ*, 523, 121
- Wang, T., Zhou, H., & Dong, X. 2003, *AJ*, 126, 113
- Weiler, K. W., Panagia, N., Montes, M. J., & Sramek, R. A. 2002, *ARA&A*, 40, 387
- Wilkinson, P. N. & de Bruyn, A. G. 1990, *MNRAS*, 242, 529
- Williams, R. J., Quadri, R. F., & Franx, M. 2011, *ArXiv e-prints*
- Wilson, A. S. & Colbert, E. J. M. 1995, *ApJ*, 438, 62
- Wu, X. & Liu, F. K. 2004, *ApJ*, 614, 91
- Yokogawa, J., Imanishi, K., Koyama, K., Nishiuchi, M., & Mizuno, N. 2002, *PASJ*, 54, 53
- Yungelson, L. R., van den Heuvel, E. P. J., Vink, J. S., Portegies Zwart, S. F., & de Koter, A. 2008, *A&A*, 477, 223

- Zel'Dovich, Y. B. 1964, *Soviet Physics Doklady*, 9, 195
- Zensus, J. A., Hough, D. H., & Porcas, R. W. 1987, *Nature*, 325, 36
- Zensus, J. A. & Pearson, T. J. 1990, *Journal of the British Astronomical Association*, 100, 316
- Zheng, W., Kriss, G. A., Telfer, R. C., Grimes, J. P., & Davidsen, A. F. 1997, *ApJ*, 475, 469
- Zheng, W., Sulentic, J. W., & Binette, L. 1990, *ApJ*, 365, 115
- Zheng, W., Veilleux, S., & Grandi, S. A. 1991, *ApJ*, 381, 418
- Zier, C. 2006, *MNRAS*, 371, L36
- Zier, C. & Biermann, P. L. 2001, *A&A*, 377, 23



# List of Figures

1.1	Hubble diagram . . . . .	14
1.2	Unified model of AGN . . . . .	17
1.3	AGN accretion disk . . . . .	24
1.4	Radiation processes in AGN jets . . . . .	26
1.5	AGN accretion disk . . . . .	27
1.6	Cosmic cycle . . . . .	29
1.7	Binary black hole evolution . . . . .	31
1.8	AGN peak luminosity evolution . . . . .	34
2.1	Slit spectrograph . . . . .	40
2.2	Raw spectrum . . . . .	43
2.3	Two-antenna interferometer . . . . .	46
2.4	Treatment of visibility data . . . . .	49
2.5	Bandpass before calibration . . . . .	51
2.6	Bandpass after calibration . . . . .	52
2.7	uv-plane . . . . .	54
2.8	European VLBI Network . . . . .	57
3.1	X-shaped radio galaxy . . . . .	61
3.2	STARLIGHT fit . . . . .	66
3.3	Starburst history . . . . .	67
3.4	New X-shaped spectra . . . . .	71
3.5	Spectrum of misidentified star . . . . .	72
3.6	Optical-radio luminosity . . . . .	77
3.7	Color-color diagram . . . . .	79
3.8	Histograms of black hole mass Region 0 . . . . .	80
3.9	Histograms of black hole mass Region 1 . . . . .	80
3.10	Histograms of starburst ages . . . . .	82
3.11	Histograms of dynamic age to starburst age ratio . . . . .	83
4.1	GMRT images of HDFN and CDFS . . . . .	95
4.2	EVN images of the ULXs NGC 4088-X1 and NGC 4861-X2 . . . . .	98

4.3	Fundamental plane for ULXs in the Chandra Deep Fields . . . . .	100
4.4	Fundamental plane for ULXs with VLBI radio counterparts . . . . .	103
4.5	Fundamental plane for ULXs with radio counterparts . . . . .	108
4.6	uv-coverage of the SNR 4449-1 . . . . .	118
4.7	Resolved radio structure of the SNR 4449-1 . . . . .	119
4.8	Elliptical fit to the SNR shell-like structure . . . . .	121
4.9	Lightcurve of SNR 4449-1 . . . . .	122
5.1	Merger states . . . . .	128
5.2	PSF fitting . . . . .	133
5.3	Nuclear vs. host luminosity . . . . .	137
5.4	Tidal enhancement . . . . .	139
5.5	Binding radius . . . . .	140
5.6	Nuclear luminosity vs. separation . . . . .	142
5.7	Color-color diagram . . . . .	143
5.8	ULX luminosity vs. nuclear separation . . . . .	147
A.1	Broad emission lines fitting . . . . .	164

# List of Tables

1.1	AGN dichotomy . . . . .	20
3.1	Observation log . . . . .	63
3.2	X-shaped objects . . . . .	73
3.3	Control sample . . . . .	75
4.1	GMRT observations of the Chandra Deep Field North (CDFN) and South (CDFS) . . . . .	91
4.2	Technical characteristics of the EVN observations . . . . .	93
4.3	EVN observations at 1.6 GHz . . . . .	93
4.4	Upper limits on the flux densities at 235.5 MHz of the ULXs in the CDFN . . . . .	94
4.5	Upper limits on the flux densities at 332MHz and 610MHz of the ULXs in the CDFS and ECDFS . . . . .	96
4.6	ULX sources with detected radio counterparts . . . . .	105
4.7	Estimated $M_{\text{BH}}$ and radio/X-ray ratio of ULXs and comparison objects . . . . .	107
4.8	Radio components of the SNR in NGC 4449 . . . . .	117
5.1	Double nucleus galaxies . . . . .	136
A.1	Emission lines and black hole masses . . . . .	165





# Acknowledgements

I could write another thesis only with names of people and the reasons why I want to thank them for, but this one is already quite long so I will try to keep it brief (I repeat: I will try). I have (I don't mean that I have, but I really want) to start these acknowledgements by thanking my supervisor, or Betreuer, or Doktorvater: Andrei Lobanov. I know it sounds kind of a topic, but this thesis wouldn't really have been possible without him. He is the one that has guided my work and progress during the last three years, helping me when I needed it, giving me his advice when I had doubts, and knowing always what to do next. I want to thank him not only for his support, his wisdom, his 'yellow ideas', his care, and his protection, but also for the freedom he has given me, for his jokes, for his funny stories about university and New Mexico, for the trip to Mexico, for the Russian lessons, and above all, for not letting this thesis be an F5<sup>1</sup>.

Next, I would like to thank those people that have also directly taken part in the thesis and to whom I owe infinite gratitude. The first one is Vahram Chavushyan, who has guided me since the first time we spoke about X-shaped radio galaxies 3 years ago, and has been always at one skype-call away when I needed advice. I have always felt he is been also my supervisor. I want to thank him for his help, collaboration, and care, for the wonderful days in INAOE and San Pedro Mártir, and, of course, for the delicious quesadillas<sup>2</sup>.

The X-shaped part of this thesis wouldn't either have been possible without the collaboration of Jonathan León Tavares. I would like to thank him for his help, comments, and suggestions, and for always replying to the hundreds of emails I have sent him during the last three years.

I am also in deep debt to Evencio Mediavilla, who has been actively participating in the study of double nucleus galaxies and has been member of my thesis committee since the beginning. I would like to thank him for his advice and suggestions, for his collaboration, and for the short stay in the IAC.

There are three other people who have also taken part in the thesis committee: Prof. Andreas Eckart, Prof. Pavel Kroupa, and Dr. Jan Pflamm-Altenburg. I would like to thank all of them for their guidance and suggestions. Specially I would like to give my sincere thanks to Prof. Andreas Eckart and Prof. Anton Zensus, who have been my official supervisors, and to Prof. Claus Kiefer, for accepting to chair the defense of my thesis.

This thesis wouldn't either have been possible without the help of the IMPRS

---

<sup>1</sup>Twister (1996)

<sup>2</sup>specially the one at 4 a.m., hehehe

board, first with Prof. Eduardo Ros as IMPRS coordinator and Gabi Breuer as IMPRS secretary, and later with Dr. Manolis Angelakis and Simone Pott overtaking, respectively, the jobs. I would like to thank their excellent work and their care for the IMPRS students, and in particular I would like to thank Manolis for our perfect coordinator-student representative interaction.

My special thanks go to Eduardo Ros, not only as IMPRS coordinator, but also as a colleague, advisor, and friend. He was the first person I met in Bonn, and the one who introduced me to the Max-Planck-Institut and the IMPRS life. He is been a source of advice, help, trust, sincerity, kindness, protection, and unmeasurable support, both scientific and personal, and a person I could (and can) always turn to, no matter what. In particular I have to thank him for the time and effort he has spent reading this thesis, as well as my proposals, papers, and applications, both in English, Spanish and Catalan. Eduardo, muchísimas gracias por todo. Tú, Ana, Marina, y Pablo habéis sido como una segunda familia.

The nobel prize goes, however, to my family, the one in Spain, in a peaceful region called Lleida, characterized by extensive fields of fruit trees, corn, and wheat, and happy cows grazing all around<sup>3</sup>.

Mama i Papa, el premi Nobel dels agraïments us l'enduieu vosaltres, per encoratjar-me sempre a estudiar el que m'agradava i ser el que volgués ser, per recolzar-me des de que quan tenia 13 o 14 anys vaig dir: "Mama, vull ser astrofísica!" (mentre miràvem un documental sobre forats negres), i per permetre'm i facilitar-me el anar on fós necessari per aconseguir-ho (Barcelona, Tenerife, Alemanya). En particular, papa et vull agrair que sempre hakis confiat en mi i mostrat lo orgullós que n'estàs, moltes gràcies pel teu suport, per venir-me a buscar a l'aeroport o a l'estació de trens o on fós necessari sense pensar-t'ho dos cops, pel teus chistes a l'hora de dinar, per fer-me empipar quan ja estic empipada, i per convertir els 'grans desastres' en incidents no tan horribles. Mama, moltes gràcies per ser sempre tan positiva, persuasiva, i convincent, per animar-me quan he estat trista i per saber sempre les paraules correctes a dir, per ser la companya d'habitació més carinyosa i pacient que ha existit mai, per les passejades d'una hora per Gerb o per Duisdorf, per la llonganissa i les tres Pes, i per una infinitat de coses que no acabaria mai d'escriure. Has sigut sens dubte un dels pilars d'aquesta tesis.

Aquesta tesis va dedicada també al meu gran petit germà<sup>4</sup>, perquè és el millor germà que tinc!! Àlex, moltes gràcies pero recolzar-me sempre i protegir-me (des de que éram ben petits), per les tormentes des del llit de la teva habitació de Castelló, pel dia que es va trencar l'ampolla d'aigua, per escoltar els meus problemes i haver compartit els teus amb mi, per estar sempre al meu costat quan t'he necessitat, i per recordar-me

---

<sup>3</sup>See <http://www.turismedelleida.com/?idioma=en> for more information.

<sup>4</sup>petit d'edad, però gran de tamany

sempre lo lluny que he arribat a la vida. Desitjo que tu també arribis fins on tu vulguis. I per últim m'agradaria també dedicar aquesta tesi al padrí, la padrina, el yayo, i la yaya. Padrí i padrina, gràcies per estimar-me i mimar-me tant, per mirar sempre al cel quan he d'agafar un avió i estar atents a les notícies de Tenerife i Alemanya, per ensenyar-me que s'ha d'estalviar i que no t'has de fiar mai de ningú, pels macarrons, i, com no, per les pastetes<sup>5</sup>. Yayo y yaya, gracias por pensar siempre en mí y estar pendientes de por dónde ando, por cuidarme y mimarme, por los bocadillos de atún, por las migas y por enseñarme a cocinarlas, por el ir a buscar fresas al huerto y guardarme siempre esos melocotones amarillos gigantes únicos en el mundo. Esta tesis os la dedico también a vosotros.

Totes les raons per les quals he agraït la tesi a la meva família les podria centrar en una sola persona: Pau. Nos conocimos en segundo de carrera, y desde entonces no has dejado nunca de estar a mi lado. Muchas gracias por todo tu amor, cuidado, paciencia (sobretudo paciencia), protección, y cariño; por hacerme sonreír en los días más tristes y hacerme reír hasta llorar; por calmar a la mar cuando hay tempestad (literalmente) y enseñarme que hay varias maneras de hacer las cosas y no sólo una; por todos los buenos momentos que hemos pasado, pero también por los no tan buenos; por entenderme sin necesidad de hablar; por los melocotones; por no dejarme sola en el mar; por empujar la marciqueta cuando hace mucha subida; por la carbonara y el tomatoli; por una vida sin berberechos; y por ser no sólo unos de los pilares de esta tesis, sino de mi vida. También quiero agradecerles a tus padres todo el cariño y ánimos que me han dado desde que estamos juntos. Montse y Luis, gracias por acogerme cada vez que voy a Rubí, por venirnos siempre a buscar y llevarnos al aeropuerto, por los yogures de fresa, los entrecots y las pechugas de pollo, por los mensajes al móvil o al Facebook, por las patadas en la espinilla, por acordaros siempre de mí y mimarme tanto, esta tesis también va dedicada a vosotros.

The third crucial pillar of this thesis has been supported by someone I met my first week in Bonn: Marios Karouzos. He's been all in one: a friend, an advisor, a teacher, and a salsa partner! I have so much to thank him that I don't know how to start. Marios, thank you very much for all your help in the last three years, for reading and correcting my thesis (and also my proposals, applications, and even papers!), for your comments and suggestions, for being always one door away (literally) when I have needed you, for coming to my office every morning to check how I was doing or simply explain me a weird dream, and, the most important, for adapting your lunch to my Spanish schedule! (sorry if you starved sometimes because of that...). Outside the institute, thank you for all the social events we have organized together, for all the dinners and movies in your place, for the Greek food, for coming with me wherever I needed to

---

<sup>5</sup>Internacionalment ja conegudes com les "home-made" grandma cookies (pastetes de la padrina de la Mar, no fetes per la padrina sinó comprades per la padrina).

go, for picking me up after a long trip, for calming down my nerves when I was mad at the world, for cheering me up when I was down, for listening to my problems and finding always solutions, and last but not the least, for the “Welcome to your second home, there are nice things to do here too”.

The last pillar, the one that has made the structure more stable and robust, belongs to all my friends both in and outside the Max-Planck-Institut. First of all, I want to thank my officemates: Chin Shin and Christian. Chin Shin, we shared the office for two years, during which you have been not only an officemate and a colleague but also a very good friend. I want to thank you for all your help and support since the day you picked me up in Bonn Hbf for the IMPRS interview, for all the time you have spent helping me with AIPS and computer stuff, for all the laughs and the fun we have had, for our long conversations about love and life, and for making me realize that Taiwanese food is also good! (although a bit spicy...). You cannot imagine how much I have missed you during the last year! The great atmosphere we had in the office was also thanks to ‘Herr Fromm’ and the hundreds of jokes we have shared. Christian, you know I am in deep debt to you for all your help in these three years. Thank you so much for solving my problems with python and idl immediately, for your suggestions every time I had a doubt, and for the hours you spent on the Zusammenfassung of the thesis. But thank you also for being always so talkative and in a good mood, for laughing with me at the people that miss the bus (oops, maybe I shouldn’t have said that), and watching together funny videos of people being hit by a lightning or eaten by sharks<sup>6</sup>. Wherever I go for a postdoc I will really miss having an officemate like you!

I would like also to thank very specially the 13.30h-lunch team: Carolina, Rebeca, Luis, Juan, Jorgito, Marios, Paisa, Amir, Charlie, and the Italian team (Gabriele, Luciando, Filomena, and Alberto). Thanks to them the lunch time was, with no doubt, the best moment of the day. Particular thanks to Luis, for reminding me every day where I come from, for the long conversations under the cherry tree, for being a ‘very strong’ climbing partner, for making me laugh at myself and being always so cheerful, and for making life so easy, gràcies petardo!! Also my sincere thanks to the ‘podó’, for his help with the thesis, proposals and applications, for laughing always at my jokes and grasping their second meaning, for las migas y los pimientos fritos, for the guitar nights in his place, and for bringing me always a bit back to my roots. Particular thanks also to Gabriele, for all his time and patience with AIPS during the second year, for the long (and fun!) board game sessions in his place, for the trip to Oxford and Belgium, and for being always available when I have needed his help. I would like to thank many more people in the institute: Yoon, for being so affectionate and loving, outgoing and fun, for her care and details, and for being one of those friends you can always trust;

---

<sup>6</sup>the shark ate only the thumb of the guy, no worries, he is alive.

Frank, for being my ‘brother’ and my link to the 2nd floor, for his daily visits to the office and the gossiping, for knowing so much about everything and sharing it with the world, and for all his help in the last stage of the thesis; Richard, for the long discussions about life and work, for his constant care about the people downstairs and his every-two-hours visits, for organizing the group meetings and the Friday nights; Ivan, for the long conversations in his office and in Penny markt, and for his help and collaboration in the last months; Laura, for being so kind and always willing to help; Arturo; Felipe C.; Felipe B.; Seungkyung; Miguel; Macarena; Konrad; Jan; the entire VLBI group; and all the institute’s ‘mitarbeiter’ (i.e., secretaries, receptionists, administrators) that have also indirectly contributed to this thesis.

Outside the MPIfR, I would like to thank my climbing friends (Herbie, Melanie, and Annika) for their support and the nice moments in and outside the climbing gym; Anne, por los findes cortos pero intensos, por ser la alemana más española que conozco y mi mejor amiga ‘no-cientista’; Carlitos, por los saludos personales y su versión colombiana de las historias; Ana H., for being so tender, protective, and organized; Rachel, for being so nice and kind, and for the French conversations; and Montse, for the long talks on Sunday evenings and making me feel on Catalan land despite of being under German sky.

Thank you all of you, and thanks also to those who I might have forgotten. Remember, in case you don’t know, that mums are 99.9999999999% of times right: *Pots arribar fins on tu vulguis.*

I was supported for this research through a stipend from the International Max Planck Research School (IMPRS) for Astronomy and Astrophysics at the Universities of Bonn and Cologne. This work was also supported by the CONACYT research grant 54480 (México). The STARLIGHT project is supported by the Brazilian agencies CNPq, CAPES and FAPESP and by the France-Brazil CAPES/Cofecub program. This research has made use of the NASA/IPAC Extragalactic Database (NED) which is operated by the Jet Propulsion Laboratory, California Institute of Technology, under contract with the National Aeronautics and Space Administration. Funding for SDSS-III has been provided by the Alfred P. Sloan Foundation, the Participating Institutions, the National Science Foundation, and the U.S. Department of Energy Office of Science. The SDSS-III web site is <http://www.sdss3.org/>. We thank the staff of the GMRT who have made these observations possible. GMRT is run by the National Centre for Radio Astrophysics of the Tata Institute of Fundamental Research. The European VLBI Network is a joint facility of European, Chinese, South African and other radio astronomy institutes funded by their national research councils.



# Erklärung

Ich versichere, daß ich die von mir vorgelegte Dissertation selbständig angefertigt, die benutzen Quellen und Hilfsmittel vollständig angegeben und die Stellen der Arbeit - einschließlich Tabellen, Karten und Abbildungen -, die anderen Werken im Wortlaut oder dem Sinn nach entnommen sind, in jedem Einzelfall als Entlehnung kenntlich gemacht habe; daß diese Dissertation noch keiner anderen Fakultät oder Universität zur Prüfung vorgelegen hat; daß sie - abgesehen von unten angegebenen Teilpublikationen - noch nicht veröffentlicht worden ist sowie, daß ich eine solche Veröffentlichung vor Abschluß des Promotionsverfahrens nicht vornehmen werde. Die Bestimmungen dieses Promotionsverfahrens sind mir bekannt. Die von mir vorgelegte Dissertation ist von Prof. Dr. Andreas Eckart betreut worden.

Köln, den 16. August 2011

Teilpublikationen:

Mezcua, M.; Lobanov, A.P.; Martí-Vidal, I.: The shell-like structure of the extragalactic supernova remnant SNR 4449-1, *Astronomy & Astrophysics*, submitted

Mezcua, M.; Chavushyan, V. H.; Lobanov, A. P.; León-Tavares, J.: Merger signatures in X-shaped radio galaxies, *Astronomy & Astrophysics*, submitted

Mezcua, M.; Lobanov, A. P.: Compact radio emission in Ultra Luminous X-ray sources, *Astronomische Nachrichten*, 2011, 332, 379M

Mezcua, M.; Lobanov, A. P.; Chavushyan, V. H.; León-Tavares, J.: Black Hole Masses and starbursts in X-shaped radio sources, *Astronomy & Astrophysics*, 2011, 527A, 38M

Mezcua, M., Lobanov, A.P., Chavushyan, V.H., & León-Tavares, J.: X-shaped radio galaxies: their black hole masses and starburst histories, *Highlights of Spanish Astrophysics VI, Proceedings of the IX Scientific Meeting of the Spanish Astronomical Society*, 2011, in press

Mezcua, M., Lobanov, A.P., Chavushyan, V.H., & León-Tavares, J.: Black Hole Masses in X-shaped radio sources, Proceedings of the Physics of Galactic Nuclei Conference, 2009, 32M



# Curriculum Vitae

## **Persönliche Daten**

Name	Mar Mezcua Pallerola
Anschrift	Auf dem Hügel 69, 53121 Bonn, Deutschland
Geburtsdatum	19. Juni 1984
Geburtsort	Lleida, Spanien
Staatsangehörigkeit	Spanisch

## **Ausbildung**

Sept. 2008 – Sept. 2011	Doktorandin der International Max Planck Research School im Max-Planck-Institut für Radioastronomie (Bonn, Deutschland)
Okt. 2007 – Juli 2008	Studium der Physik und Astrophysik an der Georg-August-Universität-Göttingen (Deutschland)
Juni 2007 – Sept. 2007	Sommer Forschung Stipendiat im Instituto de Astrofísica de Canarias (Tenerife, Spanien)
Okt. 2005 – Juni 2007	Studium der Physik und Astrophysik an der Universidad de La Laguna (Tenerife, Spanien)
Juli 2005 – Sept. 2005	Studentische Hilfskraft im Institut d'Estudis Espacials de Catalunya, Wirtschaftswissenschaftliche Fakultät der Universitat Autònoma de Barcelona (Cerdanyola del Vallès, Spanien)
Sept. 2002 – Juni 2005	Studium der Physik an der Universitat Autònoma de Barcelona (Cerdanyola del Vallès, Spanien)